



Politecnico
di Bari

Repository Istituzionale dei Prodotti della Ricerca del Politecnico di Bari

On the uncertainties in stone armor stability

This is a PhD Thesis

Original Citation:

On the uncertainties in stone armor stability / Scaravaglione, Giulio. - ELETTRONICO. - (2024).
[10.60576/poliba/iris/scaravaglione-giulio_phd2024]

Availability:

This version is available at <http://hdl.handle.net/11589/269222> since: 2024-04-22

Published version

DOI:10.60576/poliba/iris/scaravaglione-giulio_phd2024

Publisher: Politecnico di Bari

Terms of use:

(Article begins on next page)



D.R.S.A.T.E.

POLITECNICO DI BARI

10

Doctor in Risk And Environmental, Territorial And Building Development

2024

Coordinator: Prof. Vito Iacobellis

XXXVI CYCLE
Curriculum: ICAR/02

DICATECh
Department of Civil, Environmental,
Building Engineering and Chemistry

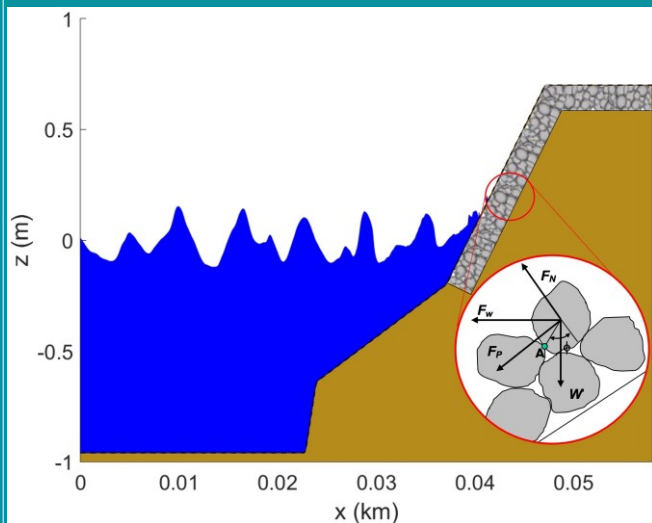
Giulio Scaravaglione

On the uncertainties in stone armor stability

Tutor:
Prof. Leonardo Damiani
Polytechnic of Bari

Supervisors:
Prof. Giuseppe Roberto Tomasicchio
University of Salento

Dr. Jeffrey A. Melby
U.S. Army Engineer Research and Development Center





Politecnico
di Bari

LIBERATORIA PER L'ARCHIVIAZIONE DELLA TESI DI DOTTORATO
Al Magnifico Rettore
del Politecnico di Bari

Il sottoscritto **GIULIO SCARAVAGLIONE** nato a **BARI (BA)** il **18/03/1996**

residente a Bari (BA) in via Melo, 78 e-mail giulio.scaravaglione@poliba.it (scaravaglione@hotmail.it)

iscritto al 3° anno di Corso di Dottorato di Ricerca in Risk and Environmental Territorial And Building Engineering and Chemistry, ciclo XXXVI

ed essendo stato ammesso a sostenere l'esame finale con la prevista discussione della tesi dal titolo:

On the uncertainties in stone armor stability

DICHIARA

- 1) di essere consapevole che, ai sensi del D.P.R. n. 445 del 28.12.2000, le dichiarazioni mendaci, la falsità negli atti e l'uso di atti falsi sono puniti ai sensi del codice penale e delle Leggi speciali in materia, e che nel caso ricorressero dette ipotesi, decade fin dall'inizio e senza necessità di nessuna formalità dai benefici conseguenti al provvedimento emanato sulla base di tali dichiarazioni;
- 2) di essere iscritto al Corso di Dottorato di ricerca in **Risk and Environmental Territorial And Building Engineering and Chemistry, ciclo XXXVI**, corso attivato ai sensi del "Regolamento dei Corsi di Dottorato di ricerca del Politecnico di Bari", emanato con D.R. n.286 del 01.07.2013;
- 3) di essere pienamente a conoscenza delle disposizioni contenute nel predetto Regolamento in merito alla procedura di deposito, pubblicazione e autoarchiviazione della tesi di dottorato nell'Archivio Istituzionale ad accesso aperto alla letteratura scientifica;
- 4) di essere consapevole che attraverso l'autoarchiviazione delle tesi nell'Archivio Istituzionale ad accesso aperto alla letteratura scientifica del Politecnico di Bari (IRIS-POLIBA), l'Ateneo archiverà e renderà consultabile in rete (nel rispetto della Policy di Ateneo di cui al D.R. 642 del 13.11.2015) il testo completo della tesi di dottorato, fatta salva la possibilità di sottoscrizione di apposite licenze per le relative condizioni di utilizzo (di cui al sito <http://www.creativecommons.it/Licenze>), e fatte salve, altresì, le eventuali esigenze di "embargo", legate a strette considerazioni sulla tutelabilità e sfruttamento industriale/commerciale dei contenuti della tesi, da rappresentarsi mediante compilazione e sottoscrizione del modulo in calce (Richiesta di embargo);
- 5) che la tesi da depositare in IRIS-POLIBA, in formato digitale (PDF/A) sarà del tutto identica a quelle **consegnate**/inviata/da inviarsi ai componenti della commissione per l'esame finale e a qualsiasi altra copia depositata presso gli Uffici del Politecnico di Bari in forma cartacea o digitale, ovvero a quella da discutere in sede di esame finale, a quella da depositare, a cura dell'Ateneo, presso le Biblioteche Nazionali Centrali di Roma e Firenze e presso tutti gli Uffici competenti per legge al momento del deposito stesso, e che di conseguenza va esclusa qualsiasi responsabilità del Politecnico di Bari per quanto riguarda eventuali errori, imprecisioni o omissioni nei contenuti della tesi;
- 6) che il contenuto e l'organizzazione della tesi è opera originale realizzata dal sottoscritto e non compromette in alcun modo i diritti di terzi, ivi compresi quelli relativi alla sicurezza dei dati personali; che pertanto il Politecnico di Bari ed i suoi funzionari sono in ogni caso esenti da responsabilità di qualsivoglia natura: civile, amministrativa e penale e saranno dal sottoscritto tenuti indenni da qualsiasi richiesta o rivendicazione da parte di terzi;
- 7) che il contenuto della tesi non infrange in alcun modo il diritto d'Autore né gli obblighi connessi alla salvaguardia di diritti morali od economici di altri autori o di altri aventi diritto, sia per testi, immagini, foto, tabelle, o altre parti di cui la tesi è composta.

Luogo e data Bari, 12/04/2024

Firma Giulio Scaravaglione

Il sottoscritto, con l'autoarchiviazione della propria tesi di dottorato nell'Archivio Istituzionale ad accesso aperto del Politecnico di Bari (POLIBA-IRIS), pur mantenendo su di essa tutti i diritti d'autore, morali ed economici, ai sensi della normativa vigente (Legge 633/1941 e ss.mm.ii.),

CONCEDE

- al Politecnico di Bari il permesso di trasferire l'opera su qualsiasi supporto e di convertirla in qualsiasi formato al fine di una corretta conservazione nel tempo. Il Politecnico di Bari garantisce che non verrà effettuata alcuna modifica al contenuto e alla struttura dell'opera.
- al Politecnico di Bari la possibilità di riprodurre l'opera in più di una copia per fini di sicurezza, back-up e conservazione.

Luogo e data Bari, 12/04/2024

Firma Giulio Scaravaglione



D.R.S.A.T.E.

POLITECNICO DI BARI

10

Doctor in Risk And Environmental, Territorial And Building Development

2024

Coordinator: Prof. Vito Iacobellis

XXXVI CYCLE
Curriculum: ICAR/02

DICATEch
Department of Civil, Environmental,
Building Engineering and Chemistry

Giulio Scaravaglione

On the uncertainties in stone armor stability

Tutor:
Prof. Leonardo Damiani
Polytechnic of Bari

Supervisors:
Prof. Giuseppe Roberto Tomasicchio
University of Salento

Dr. Jeffrey A. Melby
U.S. Army Engineer Research and Development Center

Ph.D. Candidate:
Giulio Scaravaglione
Polytechnic of Bari

Giulio Scaravaglione



D.R.S.A.T.E.

POLITECNICO DI BARI

10

Dottorato in Rischio e Sviluppo Ambientale,
Territoriale ed Edilizio

2024

Coordinatore: Prof. Vito Iacobellis

XXXVI CICLO
Curriculum: ICAR/02

DICATECh
Dipartimento di Ingegneria Civile, Ambientale,
del Territorio, Edile e di Chimica

Giulio Scaravaglione

**L'incertezza nella stabilità Idraulica delle opere a
gettata**

Tutor:
Prof. Leonardo Damiani
Politecnico di Bari

Supervisor:
Prof. Giuseppe Roberto Tomasicchio
Università del Salento

Dr. Jeffrey A. Melby
U.S. Army Engineer Research and Development Center

Candidato:
Giulio Scaravaglione
Politecnico di Bari



Politecnico
di Bari



Doctoral Thesis

ON THE UNCERTAINTIES IN STONE ARMOR STABILITY

*A thesis submitted in fulfillment of the requirements
for the degree of Doctor of Philosophy
in*

Risk and Environmental, Territorial And Building Development – XXXVI cycle
Department of Civil, Environmental, Building Engineering and Chemistry (DICA TECh)

Author:

Giulio Scaravaglione
Polytechnic of Bari

Tutor:

Prof. Leonardo Damiani
Polytechnic of Bari

Supervisors:

Prof. Giuseppe Roberto Tomasicchio
University of Salento

Dr. Jeffrey A. Melby
U.S. Army Engineer Research and Development Center

Coordinator of Ph.D. program:

Prof. Vito Iacobellis

November, 2020 - April, 2024

Abstract

The present research aims to synthesize data across a wide range of international studies to quantify and improve uncertainty understanding in stone armor stability. Data synthesis was accomplished by collecting and describing data from 7 different studies and homogenizing parametric characteristics to the extent possible considering the disparate nature of the native data. Then all 7 studies were simulated with a numerical high-fidelity phase-resolving wave transformation model (Coulwave) to better homogenize the data. Results were used to quantify hydrodynamic uncertainty and determine the relative contributions of aleatory and epistemic uncertainty and bias in damage measurements, enabling the separation and assessment of the effects of wave prediction errors on stability equations. Five of the studies produced well-known empirical stability equations. These stability equations were refit to the homogenized data illustrating weaknesses and strengths of the various empirical approaches. All formulations work well in deep water but weaknesses are illustrated in shallow and very shallow water. Improved physics are proposed that span the water depth regimes and, in concert with the quantified uncertainty, provide a significant advancement in probabilistic stone armor layer design and assessment.

Key words: Stone armor stability, epistemic uncertainty, homogenous database, Boussinesq numerical model, hydrodynamic uncertainty, wave momentum flux.

Riassunto

La presente ricerca si propone di raccogliere e sintetizzare i dati provenienti da una vasta gamma di studi internazionali al fine di quantificare e migliorare la comprensione dell'incertezza nella stabilità delle opere a gettata in massi naturali. La sintesi dei dati è stata effettuata tramite la raccolta e la descrizione dei dati provenienti da 7 diversi studi, omogeneizzando le caratteristiche parametriche per quanto possibile, tenendo conto della natura eterogenea dei dati originali. Successivamente, gli studi sono stati simulati utilizzando un modello numerico ad alta precisione per la propagazione del moto ondoso (Coulwave), al fine di migliorare l'omogeneizzazione dei dati dal punto di vista idrodinamico. I risultati ottenuti sono stati impiegati per quantificare l'incertezza idrodinamica e per determinare i contributi relativi dell'incertezza aleatoria ed epistemica e del bias nelle misurazioni del danno, consentendo così la separazione e la valutazione degli effetti degli errori di previsione sull'errore indotto dalle equazioni di stabilità. Cinque dei 7 studi analizzati hanno prodotto equazioni di stabilità ben note, le quali sono state riadattate ai nuovi dati omogeneizzati al fine di evidenziarne i punti di forza e di debolezza dei vari modelli predittivi empirici. Sebbene tutte le formulazioni funzionino bene in acque profonde, sono stati rilevati dei limiti in acque basse e molto basse. Infine, sono proposte nuove equazioni di stabilità che coprono diversi regimi di profondità, e in combinazione con l'incertezza quantificata, offrono un significativo progresso nella progettazione probabilistica delle mantellate delle opere a gettata.

Parole chiave: stabilità idraulica, incertezza epistemica, database omogeneo, modello numerico Boussinesq, incertezza idrodinamica, flusso di energia ondoso.

Extended abstract

Coastal rubble mound armor stability has historically been based on empirical equations correlating armor stone movement resistance to wave-induced forces. These equations are primarily derived from small-scale laboratory studies and exhibit considerable uncertainty. While new relationships have been introduced to broaden their applicability, little progress has made in recent decades to reduce equation uncertainty. Uncertainty in stability is primarily due to intrinsic aleatory uncertainty related to the stochastic nature of waves, stone geometry, and inter-stone contacts/interlocking, as well as epistemic uncertainty associated with knowledge limitations, modeling errors, and measurements. Here, we refer to aleatory uncertainty as inherit and epistemic uncertainty as reducible. Effects of aleatory uncertainty in hydraulic stability have often assumed dominant over epistemic uncertainty. However, the magnitude of both contributions has not yet been explicitly quantified to validate this assumption.

Modern probabilistic design and simulation methodologies demand deeper understanding of uncertainties. A clear understanding of the relative magnitudes of epistemic and aleatory uncertainty will guide studies toward improving physics research. Efforts to describe complex wave-structure interaction phenomena have prompted new experimental campaigns, generating comprehensive datasets from diverse laboratories worldwide. The present research synthesizes data across a wide range of international studies to quantify and improve uncertainty understanding in stone armor stability. Existing experimental data in the literature have been examined and synthesized, leading to the formation of a new database encompassing varied water depth regimes from deep to very shallow. Data synthesis was accomplished by collecting and describing data from 7 different studies and homogenizing parametric characteristics to the extent possible considering the disparate nature of the native data. Benefiting from this extensive database, the most widely-used armor stability formulae were compared within the framework of quantifying uncertainty. This comparison

revealed that no stability formula significantly outperforms others due to the high uncertainty in the available data. However, the raw data cannot be fully synthesized and homogenized without further modeling because of the disparate modeling approaches, non-homogeneous nature of the parametric data and the limited understanding possible of the detailed laboratory measurement techniques and data analysis.

The 7 studies were simulated with a numerical high-fidelity phase-resolving wave transformation model to better homogenize the data. To achieve this, a one-dimensional fully nonlinear Boussinesq numerical model (Coulwave) was implemented to replicate incident and reflected wave conditions for all tests in the 7 studies. Wave parameters were matched near the wave generator and the structure toe to facilitate a consistent comparison of laboratory and numerical studies. This approach enhances the understanding of hydrodynamic uncertainty, shedding light on the primary sources and magnitudes of intrinsic and epistemic uncertainty. It also enables separation of errors caused by stability formulae and wave transformation model/stability formula (combined), allowing the assessment of the effect of wave prediction errors on stability prediction errors. The stability relations associated with the experimental studies were again evaluated using the synthesized homogenized data.

The numerical model proved effective in clarifying uncertainty. A marginal reduction in hydrodynamic uncertainty was achieved compared to the total uncertainty illustrating that a majority of the uncertainty is not associated with the wave and water level conditions. Analysis of the datasets revealed a significant similarity among them, with aleatory uncertainty being predominant and closely associated with damage. Existing equations performed well in deep water conditions, but notable weaknesses were identified in shallow waters. Results suggest that incorporating depth, bathymetric slope, structure slope, and wave steepness/breaking characteristics based on bathymetry, in addition to structure slope, is crucial for improved equations. Additionally, the integration of offshore (spectral) wave period and inshore (spectral) wave height into the equations enhances predictive accuracy. In very shallow water,

the influence of wave period appears to be of minor importance compared to deep water.

Results conclusively indicate that the wave momentum flux parameter maintains a direct proportionality to the drag force exerted along the structure slope, displaying a discernible correlation with incident wave and depth parameters. Therefore, adopting such an approach enhances the understanding of physics and forces acting on stone armor units, and so appears to be a promising path forward for the optimal armor stability relationship that spans all wave and water depth regimes. In pursuit of this objective, initial attempts have been made to propose new stability equations, offering valuable insights and, in combination with uncertainty quantification, represents a significant advancement in probabilistic stone armor layer design and assessment.

Key words: stone armor stability, epistemic uncertainty, homogenous database, Boussinesq numerical model, hydrodynamic uncertainty, wave momentum flux.

Index

Abstract	I
Riassunto	II
Extended abstract	III
List of figures	XI
List of tables	XVI
List of abbreviations	XVIII
List of symbols	XIX
1. Introduction	1
1.1. Background and motivation of the research.....	1
1.2. General overview to stone armor stability	3
1.3. Statement of the problem.....	5
1.4. Research objectives	6
1.5. Methodology.....	6
1.6. Organization of the work and thesis outline	8
2. Literature review	11
3. Description of new extensive database	23
3.1. Thompson and Shuttler (1975) – TS data	24
3.2. Van der Meer (1988) – vdM data.....	27
3.3. Van Gent et al. (2003) – VSK data	29
3.4. Vidal et al. (2006) – VML data	30
3.5. Melby and Kobayashi (2011) – MK data	32
3.6. Herrera et al. (2017) – HGM data.....	33
3.7. EUMER data.....	34
3.8. Processed database.....	36
3.9. Conclusions	46

4. Data analysis.....	47
4.1. Physically based derivation of armor stability based on M_f	47
4.1.1. Instability normal to structure slope (Hudson failure)	49
4.1.1.1. Instability normal to structure slope based on drag force	50
4.1.1.2. Instability normal to structure slope based on M_f	51
4.1.2. Instability due to rolling	51
4.1.3. Instability due to sliding.....	52
4.1.4. Generalized stability	53
4.2. Wave momentum flux derivation	54
4.2.1. Stability equations based M_f with the new database.....	57
4.2.2. M_f stability equations refitting	58
4.2.3. Test series separation.....	61
4.2.4. M_f stability equations refitting using $T_{m-1,0}$	68
4.2.5. M_f refitting stability equations for each dataset.....	71
4.2.6. Discussion	77
4.3. Comparison between armor stability formulae	79
4.3.1. Discussion	82
4.4. Conclusions	89
5. Uncertainties in stone armor stability.....	91
5.1. Introduction	91
5.2. Sources of uncertainty in stone armor stability	92
5.3. Definition of uncertainty	94
5.3.1. Parameter uncertainty	96
5.3.2. Model uncertainty	96
5.4. Epistemic uncertainty.....	97
5.4.1. Data uncertainty.....	97
5.4.1.1. Hydrodynamic measurement and selected wave characteristics .	97
5.4.1.2. Damage measurement.....	108
5.4.2. Model uncertainty	118
5.4.3. Errors.....	124
5.5. Conclusion	128
6. Prediction of waves transformation using Boussinesq model.....	131
6.1. Motivation and objectives.....	131
6.2. Literature survey and choice of the numerical model.....	132

6.3.	The Coulwave	135
6.4.	Coulwave calibration and validation	137
6.4.1.	Numerical setup	137
6.4.2.	Convergence.....	139
6.4.3.	Test duration.....	143
6.4.4.	Breaking trigger and stopping	149
6.4.5.	Coulwave simulations.....	154
6.4.6.	Post-processing analyses.....	156
6.4.7.	Reflection analysis	156
6.4.8.	Wave momentum flux and IG contribution	162
6.5.	Hydrodynamic uncertainty	164
6.5.1.	Wave parameters uncertainty.....	164
6.5.2.	Hydrodynamic force uncertainty	169
6.5.3.	Wave momentum flux uncertainty	172
6.6.	Conclusions	180
7.	Results	183
7.1.	General overview on the stability equation.....	184
7.2.	Reformulation of the stability equation	186
7.2.1.	Storm duration N_w	187
7.2.2.	Damage curve.....	189
7.2.3.	Slope angle α	193
7.3.	Comparison and analysis of datasets.....	194
7.3.1.	Outliers	194
7.3.2.	Differences in datasets	196
7.3.3.	Stability equations using Coulwave data.....	199
7.4.	New stability equations based on wave momentum flux	208
7.4.1.	Refitted MK equation using $M_{f,1/3}$	209
7.4.2.	Refitted MK equation using Hughes M_f with Coulwave data	210
7.4.3.	New single stability equation.....	212
7.4.4.	Final comparison.....	214
7.5.	Conclusions	220
8.	Conclusions and future research lines	221
8.1.	Summary of the thesis.....	221
8.2.	Principal findings and conclusions.....	223

8.3. Limits of the research	225
8.4. Future research lines.....	227
Bibliography	229
Acknowledgments.....	245
Curriculum Vitae.....	249
Publications.....	250

List of figures

Figure 1.1. Projected global mean SLR under various climate scenarios (source: [12]).	2
Figure 1.2. Standard rubble mound structure failures modes (source: [26]).	4
Figure 3.1. Histogram of the water depth classification.	43
Figure 3.2. Wave characteristics of the database as a function of the relative depth.	46
Figure 4.1. Schematic free-body diagram of primary forces influencing stone stability (source: [64]).	48
Figure 4.2. Dimensionless wave momentum flux versus h/gT^2 (source: [66]).	56
Figure 4.3. Plunging (K_{m1}) and surging (K_{m2}) regression coefficients computed for $N_w=1000$, $N_w=3000$ and all damage data.	59
Figure 4.4. M_f refitted stability equations.	60
Figure 4.5. Measured vs predicted N_m and S_d .	61
Figure 4.6. Data separation in plunge and surge breaking conditions according to Eq. (20d).	62
Figure 4.7. Measured vs predicted N_m for vdM test series.	63
Figure 4.8. Measured vs predicted N_m for TS test series.	64
Figure 4.9. Measured vs predicted N_m for VSK and MK test series.	65
Figure 4.10. Measured vs predicted N_m for EUMER test series.	66
Figure 4.11. Measured vs predicted N_m for HGM test series.	67
Figure 4.12. Measured vs predicted N_m for VML test series.	68
Figure 4.13. Plunging and surging coefficients for all damage data using $T_{m-1,0}$.	69
Figure 4.14. M_f refitted stability equations using $T_{m-1,0}$.	70
Figure 4.15. Measured vs predicted N_m and S_d using $T_{m-1,0}$.	70
Figure 4.16. M_f refitted stability equation using only vdM data.	72
Figure 4.17. M_f refitted stability equation using only TS data.	73
Figure 4.18. M_f refitted stability equation using only VSK data.	74
Figure 4.19. M_f refitted stability equation using only EUMER data.	75

Figure 4.20. M_f refitted stability equation using only HGM data..... 76

Figure 4.21. Comparison between measured and predicted values of the processed dataset for the most popular stability formulae for deep, shallow and very shallow water conditions, respectively; a) van der Meer (2021) [54]; b) van der Meer modified (2003) [59]; c) van Gent (2004) [63]; d) Melby and Kobayashi (2011) [65]; e) Herrera et al. (2017) [70]; f) Eldrup and Andersen (2019) [72]; g) Etemad-Shahidi et al. (2020) [79].
..... 82

Figure 5.1. Main sources of uncertainty in stone armor stability. 94

Figure 5.2. Main sources of uncertainty in lab hydrodynamic measurements..... 98

Figure 5.3. Main sources of uncertainty in lab damage measurements. 109

Figure 5.4. Damage estimation comparison between methods (source: [136]). 111

Figure 5.5. Example of uncertainty induced by damage analysis (source: [44]). 114

Figure 5.6. Main sources of model uncertainty in stability. 120

Figure 5.7. Example of breaking classification types using vdM data. 122

Figure 5.8. Main sources of errors uncertainty. 125

Figure 6.1. Bathymetry and energy spectrum input files for Coulwave simulations (EUMER wave flume)..... 139

Figure 6.2. Convergence test results - Case 1. Spectra shape offshore, along the foreshore and at the flat bottom for $dx=0.1$ (above), $dx=0.05$ (middle) and $dx=0.04$ (below) with 600 s of simulation. 141

Figure 6.3. Convergence test results - Case 2. Spectra shape offshore, along the foreshore and at the flat bottom for $dx=0.1$ (above), $dx=0.05$ (middle) and $dx=0.04$ (below) with 600 s of simulation. 142

Figure 6.4. Duration sensitivity analysis results - Case 1. Spectra shape offshore, along the foreshore and at the flat bottom for t_r equal to 300 s, 600 s, 1200 s, 5000 s and 10,000 s with $dx=0.04$ 146

Figure 6.5. Duration sensitivity analysis results - Case 2. Spectra shape offshore, along the foreshore and at the flat bottom for t_r equal to 300 s, 600 s, 1200 s, 5000 s and 10,000 s with $dx=0.04$ 148

Figure 6.6. Lab measured (red circle) and numerical computed (solid lines) cross-shore variation of H_{m0} and $T_{m-1,0}$ along the wave flume – Case 1 ($h=0.20$ m, $H_{m0,deep}=0.20$ m, $T_{p,deep}=2.38$ s). Trigger=0.60 and stopping=0.40 (above), trigger=0.60 and stopping=0.35 (middle), trigger=0.60 and stopping=0.30 (below).151

Figure 6.7. Lab measured (red circle) and numerical computed (solid lines) cross-shore variation of H_{m0} and $T_{m-1,0}$ along the wave flume – Case 2 ($h=0.10$ m, $H_{m0,deep}=0.20$ m, $T_{p,deep}=2.38$ s). Trigger=0.60 and stopping=0.40 (above), trigger=0.60 and stopping=0.35 (middle), trigger=0.60 and stopping=0.30 (below).152

Figure 6.8. Lab measured (red circle) and numerical computed (solid lines) cross-shore variation of H_{m0} and $T_{m-1,0}$ along the wave flume – Case 3 ($h=0.05$ m, $H_{m0,deep}=0.20$ m, $T_{p,deep}=2.57$ s). Trigger=0.60 and stopping=0.40 (above), trigger=0.60 and stopping=0.35 (middle), trigger=0.60 and stopping=0.30 (below).153

Figure 6.9. Comparison between target (left) and measured (right) wave spectra offshore.155

Figure 6.10. Comparison of the wave spectra obtained using different reflection techniques - Case 1 in shallow water ($h=0.20$ m, $H_{m0,deep}=0.255$ m, $T_{p,deep}=2.78$ s). Upper left single gage analysis, upper right 3-gages Mansard and Funke and bottom 9-gages Goda and Suzuki.159

Figure 6.11. Comparison of the wave spectra obtained using different reflection techniques – Case 2 in very shallow water ($h=0.10$ m, $H_{m0,deep}=0.197$ m, $T_{p,deep}=2.38$ s). Upper left single gage analysis, upper right 3-gages Mansard and Funke and bottom 9-gages Goda and Suzuki.160

Figure 6.12. Cross-shore variation of K_R and $H_{m0,i}$ along the flume for very shallow water ($h=0.10$ m) where waves break over the foreshore.162

Figure 6.13. Cross-shore variation of u_{max} , $(h+\eta)u_{max}^2$ and $H_{m0,iG}$ along the flume. 163

Figure 6.14. Cross-shore variation of $(h+\eta)u_{max}^2$ along the flume with the structure in place.164

Figure 6.15. Comparison between numerical and laboratory incident wave parameters (H_{m0} , H_s , $H_{2\%}$, T_m , T_p , $T_{m-1,0}$) computed at the toe of the structure.166

Figure 6.16. Comparison between numerical and laboratory incident wave parameters (H_{m0} , above and $T_{m-1,0}$, below) computed at the toe of the structure. 167

Figure 6.17. Wave characteristics ratios as a function of the relative depth. 169

Figure 6.18. Top left) Probability density function for $M_f(t)$; top right) Zero-Up crossing method for M_f ; bottom left) PDF of exceedance of the crest-to-trough heights; bottom right) CDF of exceedance of the crest-to-trough heights. 171

Figure 6.19. Comparison between the M_f and drag forces PDFs (source [201]). 172

Figure 6.20. $u_{1/3}$ and $u_{1/3}^2$, $hu_{1/3}^2$, $M_{f,1/3}$, $M_{f,1/3}/gh^2$ and $((h+\eta)u^2)/gh^2)_{1/3}$ plotted against the relative depth for the entire numerical database. 173

Figure 6.21. Total and velocity and pressure M_f components plotted versus the relative depth. 174

Figure 6.22. Velocity and pressure components to M_f Hughes in percentage with respect to the relative depth for the entire numerical database. 175

Figure 6.23. Normalized $M_{f,1/3}$ plotted vs $h/H_{m0,deep}$ and $H_{m0,toe}/h$ 176

Figure 6.24. Comparison between the measured M_f vs the Hughes and LWT M_f 177

Figure 6.25. New wave stability data plotted in Hughes figure. 179

Figure 7.1. Normalized damage plotted vs. H_{m0} and $M_{f,1/3}$ 190

Figure 7.2. Normalized damage plotted vs. N_s and N_m 190

Figure 7.3. Damage curves for vdM data groups. 192

Figure 7.4. Damage curves for VSK and Melby data groups. 192

Figure 7.5. Damage curves for EUMER data groups. 193

Figure 7.6. N_m vs. normalized damage for all numerical database. 195

Figure 7.7. N_m vs. normalized damage plotted for deep, shallow, and very shallow water conditions. 196

Figure 7.8. N_m plotted vs. normalized S separated for the different laboratory experiments (i.e., EUMER, HGM and Melby, VSK and vdM). 197

Figure 7.9. Bias in the damage curve for plunging (left) and surging (right) equations between VSK and vdM data. 199

Figure 7.10. VdM stability equation for deep, shallow, and very shallow waters using laboratory data (top), Coulwave data with the inshore wave period (middle), and Coulwave data using the offshore wave period (bottom).....201

Figure 7.11. Van Gent stability equation for deep, shallow, and very shallow waters using laboratory data (top) and Coulwave data (bottom).....202

Figure 7.12. Refitted MK stability equation for deep, shallow, and very shallow waters using laboratory data (top), Coulwave data with the inshore wave period (middle), and Coulwave data using the offshore wave period (bottom).....203

Figure 7.13. EA stability equation for deep, shallow, and very shallow waters using laboratory data (top), Coulwave data with the inshore wave period (middle), and Coulwave data using the offshore wave period (bottom).....204

Figure 7.14. Etemad-Shahidi et al. stability equation for deep, shallow, and very shallow waters using laboratory data (top), Coulwave data with the inshore wave period (middle), and Coulwave data using the offshore wave period (bottom).205

Figure 7.15. Plunging (K_{m1}) and surging (K_{m2}) regression coefficients computed for all analyzed numerical data.210

Figure 7.16. Wave momentum flux stability equation using $M_{f,1/3}$210

Figure 7.17. Plunging (K_{m1}) and surging (K_{m2}) regression coefficients computed for all analyzed numerical data.211

Figure 7.18. Wave momentum flux stability equation using Hughes M_f with Coulwave numerical wave parameters.212

Figure 7.19. Single regression coefficient (K_m) computed for all numerical data.....214

Figure 7.20. New single wave momentum flux stability equation.214

Figure 7.21. Measured vs. predicted N_m for the three attempts.....215

Figure 7.22. Normalized N_m plotted versus $s_{m-1,0}$ where $a_m = 1/K_m P^{0.18}$ 217

Figure 7.23. Normalized N_m plotted versus $\xi_{m-1,0}$ where $a_m = 1/K_m P^{0.18}$ 217

Figure 7.24. Normalized N_m plotted versus $\xi_{m-1,0}$ where $a_m = 1/K_m P^{0.18} \cot\alpha^c$

List of tables

Table 3.1. Damage classification for a rubble mound breakwater [30].....	37
Table 3.2. Damage range considered in the analysis.....	37
Table 3.3. Main model characteristics of the datasets.....	40
Table 3.4. Main waves characteristics of the datasets.	41
Table 4.1. Comparison between the refitted stability equations.....	71
Table 4.2. Final comparison between datasets.....	77
Table 4.3. Comparison in terms of rmse and r^2 between the stability formulae for deep, shallow, and very shallow water conditions.....	83
Table 4.4. Comparison in terms of bias and uncertainty between the stability formulae for deep, shallow, and very shallow water conditions.....	83
Table 4.5. Main characteristics of the stability equations compared in Figure 4.21. .	88
Table 5.1. Sense of hydrodynamic uncertainty (data uncertainty) in terms of $\sigma'y$...	108
Table 5.2. Sense of damage uncertainty (data uncertainty) in terms of $\sigma'y$	118
Table 5.3. Sense of model uncertainty in terms of $\sigma'y$	123
Table 5.4. Sense of total epistemic uncertainty in stone armor stability in terms of $\sigma'y$	128
Table 6.1. Convergence test results - Case 1: $H_{m0,deep}=0.255$ m, $T_{p,deep}=2.78$ s, $h_{,deep}=0.96$ m, $h=0.20$ m, JONSWAP (3.3).....	140
Table 6.2. Convergence test results - Case 2: $H_{m0,deep}=0.197$ m, $T_{p,deep}=2.38$ s, $h_{,deep}=0.86$ m, $h=0.10$ m, JONSWAP (3.3).....	141
Table 6.3. Sensitivity analysis results of test duration - Case 1.....	145
Table 6.4. Sensitivity analysis results of test duration - Case 2.....	146
Table 6.5. Estimation of the uncertainty σ' related to the test duration.....	148
Table 6.6. Sensitivity analysis based on reflection methods – Case 1: shallow water ($h=0.20$ m, $H_{m0,deep}=0.255$ m, $T_{p,deep}=2.78$ s).	159
Table 6.7. Sensitivity analysis based on reflection methods – Case 2: very shallow water ($h=0.10$ m, $H_{m0,deep}=0.197$ m, $T_{p,deep}=2.38$ s).....	160

Table 6.8. Uncertainty σ' related to the use of reflection method in different shallowness conditions.	160
Table 6.9. Structure vs. no structure in place comparison.	164
Table 6.10. Bias and uncertainty for incident wave parameters.	166
Table 7.1. Validation for the square root function for N_w as indicated by vdM [54].	188
Table 7.2. Comparison between similar data from VSK and vdM datasets.	199
Table 7.3. Comparison in terms of rmse and r^2 between the stability formulae for deep, shallow, and very shallow water conditions using laboratory data, Coulwave data with the inshore wave period, and Coulwave data using the offshore wave period.	206
Table 7.4. Comparison in terms of bias and std between the stability formulae for deep, shallow, and very shallow water conditions using laboratory data, Coulwave data with the inshore wave period, and Coulwave data using the offshore wave period.	207
Table 7.5. Final comparison.	215
Table 7.6. Influence of parameters on stability equations.	219

List of abbreviations

Abbreviation	Name
ANN	A rtificial N eural N etworks
ARC	A ctive- R eflection- C ompensation
AWACS	A ctive W ave A bsorption C ontrol S ystem
BT	B oussinesq- T ype
CDF	C umulative D ensity F unction
CEM	C oastal E ngineering M anual
Cov	C oefficient of v ariation
EA	E ldrup and A ndersen
EUMER	E uropean M aritime E nvironmental R esearch
FEMDEM	F inite and D iscrete E lement M ethod
FV	F inite V olume
GS	G oda and S uzuki
HGM	H errera, G omez-Martin, and M edina
IG	I nfra G avity
JONSWAP	J Oint N orth S ea W ave P roject
LHS	L eft- H and S ide
LN	L og- N ormal
LWT	L inear W ave T heory
MF	M ansard and F unke
MK	M elby and K obayashi
PdMf	P ressure- b ased W ave M omentum F lux
PDF	P robability D ensity F unction
PM	P ierson- M oskowitz
RHS	R ight- H and S ide
rmse	r oot m ean s quare e rror
SLR	S ea L evel R ise
SPH	S moothed P article H ydrodynamics
SPM	S hore P rotection M anual
SSP	S urf S imilarity P arameter
std	S tandard d eviation
SWL	S ea W ater L evel
TMA	T exel M arsen A rsloe
TS	T hompson and S huttler
TVD	T otal V ariation D iminishing
VbMf	V elocity- b ased W ave M omentum F lux
vdM	v an d er M eer
VML	V idal, M edina and L omónaco
VSK	V an G ent, S male and K uiper
WCV	W ave C limate V ariability

List of symbols

Greek symbols		
Symbol	SI units	Name
α	$[\circ]$	Structure seaward slope angle
β	$[\circ]$	Foreshore slope angle
γ	$[-]$	Spectrum enhancement factor
γ_w	$[\text{Kg} / \text{m}^3]$	Specific weight of water
γ_r	$[\text{Kg} / \text{m}^3]$	Specific weight of stones
Δ	$[-]$	Relative mass density, $\Delta = \rho_r / \rho_w - 1$
η_x	$[\text{m}]$	Free surface elevation location
μ	$[-]$	Mean value
ν	$[\text{m/s}]$	Water kinematic viscosity
ξ_m	$[-]$	Surf similarity parameter using H_{m0} and T_m
$\xi_{m-1,0}$	$[-]$	Surf similarity parameter using H_{m0} and $T_{m-1,0}$
$\xi_{m-1,0,c}$	$[-]$	Critical surf similarity parameter in EA formula
$\xi_{s-1,0}$	$[-]$	Surf similarity parameter using H_s and $T_{m-1,0}$
$\xi_{s-1,0,c}$	$[-]$	Critical surf similarity parameter in vdM formula
π	$[-]$	Pi Greco number
ρ_w	$[\text{kg/m}^3]$	Mass density of the water
ρ_r	$[\text{kg/m}^3]$	Mass density of the armor stone
ρ_a^B	$[\text{kg/m}^3]$	Bulk density of material on the slope
σ'	$[-]$	Coefficient of variation
σ	$[-]$	Standard deviation
σ_s	$[-]$	Standard deviation of damage
ϕ	$[\circ]$	Angle of repose

Roman symbols		
a, b, c, d	$[-]$	Regression coefficients for new polynomial single equation
a_m	$[-]$	Composite term in the MK stability equation
A	$[\text{m}^2]$	Exposed area
A_e	$[\text{m}^2]$	Average eroded area
B	$[\text{m}]$	Berm width
BLc	$[\%]$	Blockiness coefficient
C_D	$[-]$	Coefficient of drag
C_p	$[-]$	Permeability coefficient
C_{pl}, C_{su}	$[-]$	Stone shape coefficients
c_o	$[-]$	Coefficient in the Courant number
D	$[\text{m}]$	Probe diameter
D₅₀	$[\text{m}]$	Nominal sized spherical armor stones

D_{n50}	[m]	Armor nominal median stone size, $D_{n50} = \left(\frac{M_{50}}{\rho_r}\right)^{\frac{1}{3}}$
D_{n50,core}	[m]	Core nominal median stone size
D_{n50,filter}	[m]	Filter nominal median stone size
D₈₅/D₁₅	[-]	Grading uniformity coefficient
D₈₅	[-]	Mass exceeded by 85% of a sample by weight
D₁₅	[-]	Mass exceeded by 15% of a sample by weight
E_i	[-]	Error, $E_i = y_{\text{pred}} - y_{\text{obs}}$
f	[Hz]	Frequency
f_p	[Hz]	Peak frequency
Δf	[Hz]	Frequency bandwidth
ff	[-]	Bottom friction coefficient
F_c	[N]	Resisting frictional force
F_D	[N]	Drag force
F_N	[N]	Structure normal wave force
F_p	[N]	Structure parallel wave force
F_w	[N]	Fluid force
g	[m/s ²]	Gravitational acceleration
G	[-]	Model factor
G_c	[m]	Width of the crest
h	[m]	Local water depth
H	[m]	Design wave height
H_{m0}	[m]	Significant (spectral) wave height in frequency domain, $H_{m0} = 4(m_0)^{0.5}$
H_{m0,i}	[m]	Incident spectral wave height
H_{m0,r}	[m]	Reflected spectral wave height
H_{m0,IG}	[m]	Infragravity component of the spectral wave height ($f < 0.7$ Hz)
H_s	[-]	Significant wave height in the time domain, $H_s = H_{1/3}$
H_{1/50}	[m]	Average wave height of the 50 highest waves in time domain
H_{1/20}	[m]	Average wave height of the 20 highest waves in time domain
H_{1/10}	[-]	Average wave height of the 10 percent highest waves in time domain
H_{2%}	[m]	Average wave height of the 2 percent highest waves in time domain
H_{max}	[m]	Maximum wave height in a time series
i	[-]	<i>i</i> -th component of the sample
k	[m ⁻¹]	Wave number, $k = 2\pi/L$
K_a	[-]	Parameter incorporating K_r and K_m
K_D	[-]	Tabulated empirical stability coefficient
K_r	[-]	Empirical constant
K_m	[-]	Constant of proportionality
K_{m1}	[-]	Regression coefficient for plunging
K_{m2}	[-]	Regression coefficient for surging
K_R	[-]	Bulk reflection coefficient, $K_R = m_{0,r}/m_{0,i}$
dl	[m]	Spacing between gages
ΔL	[m]	Profiler soundings spacing

L	[m]	Wavelength
L_m	[m]	Mean wavelength based on T_m
L_{m-1,0}	[m]	Spectral wavelength based on $T_{m-1,0}$
LT	[-]	Length-to-thickness ratio
m	[-]	Foreshore slope, $m = \tan\beta$
m_n	[-]	N th moment of the frequency spectrum
M	[-]	Total number of observations
M₅₀	[kg]	Median mass of the armor stone grading
M_A	[N m]	Moment of a force
M_f	[N/m]	Wave momentum flux
M_{f,1/3}	[N/m]	Significant wave momentum flux, $M_{f,s} = M_{f,1/3}$
N	[-]	Total number of observations
N_d	[-]	Number of displaced stones
N_m	[-]	Stability number using wave momentum flux, $N_m = \left(\frac{(M_f)_{\max}}{\rho_w g h^2 \Delta} \right)^{1/2} \frac{h}{D_{n50}}$
N_s	[-]	Stability number, $N_s = H_s / \Delta D_{n50}$
N_w	[-]	Number of waves, $N_w = t / T_m$
N_Δ	[-]	Erosion damage parameter
p	[-]	Porosity of the structure
p_d	[mwc]	Dynamic pressure
P	[-]	Notional permeability factor
q	[-]	Damage curve exponent
R	[m]	Width of the armor layer
R²	[-]	Correlation coefficient
R_c	[m]	Relative crest freeboard above the still water level
R_f R_b R_s	[-]	Coulwave additional terms for bottom friction, wave breaking and subgrid lateral turbulent mixing
R_{sg}	[-]	Eddy viscosity coefficient
Re_{armor}	[-]	Reynolds number at the armor layer
Re_{core}	[-]	Reynolds number inside the structure core
Re_{crit}	[-]	Critical Reynolds number at the armor layer
s	[-]	Wave steepness
s_m	[-]	Wave steepness using H_{m0} and T_m
s_{m,c}	[-]	Critical wave steepness parameter in MK formula
s_{m-1,0}	[-]	Wave steepness using H_{m0} and $T_{m-1,0}$
S	[-]	Mean of the damage
S[*]	[-]	Normalized damage $S^* = (S - \bar{S}) / \sigma_s$
S_d	[-]	Damage value, $S_d = A_e / D_{n50}^2$
S_e	[-]	Damage value obtained using the virtual net method
S_l	[-]	Damage value obtained using the image processing method
S_{max}	[-]	Maximum damage value
S_{md}	[-]	Damage value obtained averaging damage indexes from each profile

S_p	[-]	Damage value obtained using the section profiling method
S_r	[-]	Specific gravity on the armor units relative to the water, $S_r = \gamma_r / \gamma_w$
S_v	[-]	Damage value obtained using the visual counting method
S_{xx}	[N/m]	Radiation stress
t	[s]	Time
Δt	[s]	Time step
t_Δ	[-]	Armor layer thickness
t_r	[s]	Duration of the test
T	[s]	Wave period
T_m	[s]	Mean wave period in the time domain
$T_{m-1,0}$	[s]	Negative spectral energy wave period, $T_{m-1,0} = m_{-1} / m_0$
T_p	[s]	Peak wave period
u	[m/s]	Wave velocity in the x-direction
\bar{u}	[m/s]	Depth-integrated wave velocity
u_b	[m/s]	Velocity at the seafloor
$u_{1/3}$	[m/s]	Significant wave velocity in the x-direction
u_{max}	[m/s]	Maximum wave velocity in the x-direction
V_e	[m ³]	Eroded volume
V_{50}	[m ³]	Eroded volume calculated with spherical armor stones, $D_{50} = V_{50}^{1/3}$
W'	[N]	Submerged weight force
x	[m]	Longitudinal horizontal coordinate positive in the wave propagation direction
dx	[m]	Grid mesh numerical model along the x-coordinate
Δx	[m]	Spatial grid discretization along the x-coordinate
X_0	[m]	Wave generator x-coordinate in the numerical model
y	[-]	Quantity
y_{obs}	[-]	Observed value
y_{pred}	[-]	Predicted value
\bar{y}_{obs}	[-]	Mean of the observed values
Y	[m]	Transversal coordinate
Δy	[m]	Spatial grid discretization along the Y-coordinate
z	[m]	Vertical coordinate positive in the upper direction

CHAPTER 1

INTRODUCTION

1. Introduction

1.1. Background and motivation of the research

Coastal zones host a variety of natural ecosystems and economic and social activities, which require protection from the actions of the sea. The design of coastal and harbor defense solutions is a complex task due to the challenge of predicting the built environment's response to hydraulic loads and incorporating the stochastic nature of climate forcing. In the present-days, alongside the construction of new coastal and harbor defense solutions, there is an urgent need for planning sustainable maintenance programs for aging infrastructure and adaptation to climate change ([1], [2]).

The evolving hydraulic conditions resulting from sea level rise (SLR) induced by climate change demand continued research efforts for a comprehensive understanding of wave-coastal structure interaction. These changing hydraulic conditions can impact the functionality of both newly constructed and existing structures, potentially causing them to be unable to meeting design requirements. In particular, SLR and wave climate variability (WCV) are expected to intensify shoreline retreat and coastal erosion ([3], [4], [5]), flooding ([6], [7], [8]), and reduce port operability ([9], [10], [11]). Current SLR projections encompass various scenarios (IPCC [12]) characterized by significant uncertainty (Figure 1.1). Moreover, mean SLR ([13], [14], [15]), increases extreme surge height and frequency of occurrence ([16], [17]), inter-annual variability of wave characteristics ([18], [19], [20]), and reduces extreme sea level return intervals [21], directly influencing the hydraulic performance of coastal structures. Given the

considerable uncertainties associated with these input variables, coastal structures risk incurring unnecessarily high costs if a too conservative SLR is assumed, or they may reach the end of their functional lifetime prematurely if SLR is underestimated.

SLR can result in heightened wave loading on sea defenses, particularly affecting coastal defenses in shallow waters where waves at the toe of the structure become larger due to rising water levels. Consequently, this dual impact not only increases the vulnerability of sea defenses to wave overtopping but also compromises the stability of their armor layers.

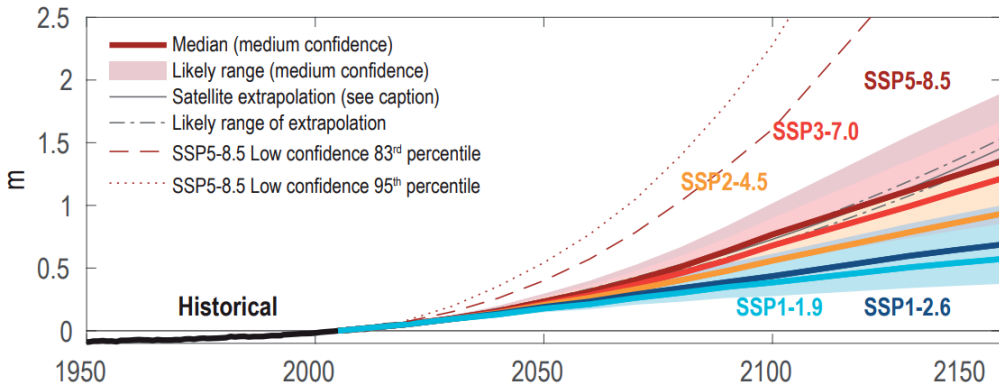


Figure 1.1. Projected global mean SLR under various climate scenarios (source: [12]).

In this context, it is crucial to appropriately consider uncertainties related to the characteristics of historical or adapted structures and the effects of climate change on marine conditions during the design process. Traditional deterministic design methodologies do not consider such uncertainties, whereas probabilistic design methods utilize probability distribution functions of the involved variables to estimate the failure probability of systems.

Presently, only a limited number of national design guidelines have embraced probabilistic approaches, mainly focusing on newly constructed structures (e.g.,

Coastal Engineering Manual (CEM) 2002 (USA) [22], TECH-JAPAN 2009 (Japan), ROM 1.1-2019 Articles (Spain)). Meanwhile, the consideration of climate change impacts and current design methods is often oversimplified. For instance, in Italy, technical recommendations for maritime dikes and coastal defense solutions date back to the 1990s [23], and despite revisions in 2018 [24], they still rely on a deterministic approach. However, climate-aware engineering design is now mandated, as exemplified by UE guidelines for public works funding. The integration of modern probabilistic design and simulation methodologies serves as a driver for deepening our comprehension of physics and uncertainty. This initiative aims to establish a novel probabilistic protocol for designing coastal structures within the context of climate change and poses an impending challenge for the coastal engineering community. Therefore, it is desirable and urgent to review and update the current state of uncertainty knowledge in stone armor stability to provide updated tools for designing rubble mound structures to safeguard human properties along coastlines.

1.2. General overview to stone armor stability

Stone-armored mound structures, such as breakwaters, jetties, and revetments, represent the most common, effective, and widely adopted solutions in harbor construction and coastal defense against waves, currents, and coastal flooding. These structures protect coastal areas by dissipating wave energy through turbulent wave breaking on the outer slope, external flows over the rough surface of the armor layers, and internal flows inside the porous body of the mound. When available in suitable unit sizes and quality, stone armoring may offer a more economical alternative to concrete. Additionally, stone is often preferred for its more “*natural*” appearance.

Coastal structure failure can occur due to several different failure modes (Figure 1.2). Among these, the stability of seaside armor is crucial to the structural integrity and is, therefore, the primary focus of the present study. Stone-armor layer stability differs from other structural designs due to its high variability, which is complex and difficult

to quantify given the wide range and numerous permutations of the involved variables. The engineering interest lies in the loading on armor units primarily caused by incident storm waves, which vary with storm intensity and location. Waves can dislodge seaside armor units through uplifting, rolling, sliding individual units or by causing a mass movement of the entire armor layer. The response of the armor layer to armor movement is highly variable and uncertain. The variability in both loading and boundary conditions demands consideration of randomness associated with each stochastic parameter [25].

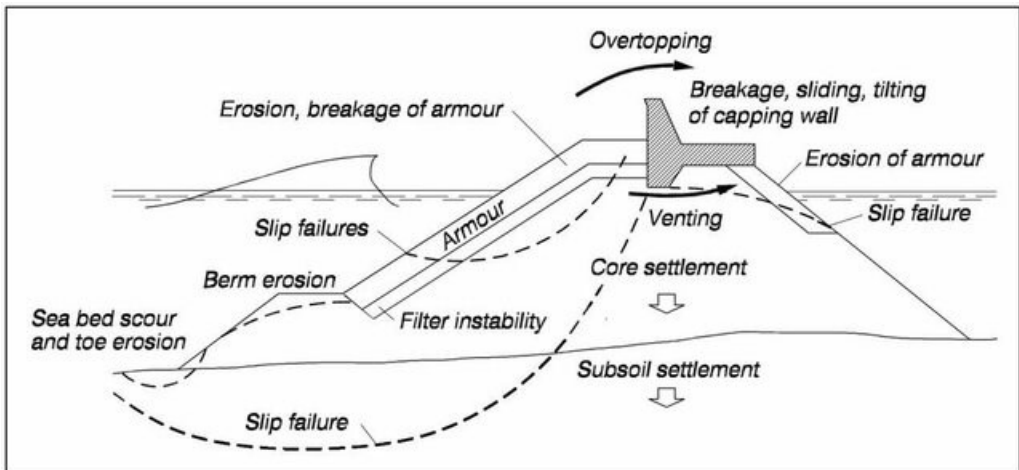


Figure 1.2. Standard rubble mound structure failures modes (source: [26]).

The estimation of hydraulic stability for stone armor units is a standard practice among coastal engineers. Formulae found in design manuals, such as the CEM [22] and the Rock Manual [26], are semi-empirical and predominantly derived from datasets obtained through small-scale physical model experiments conducted at various coastal laboratories worldwide or by employing numerical modeling and machine-learning techniques, or some hybridization of these methods. However, armor damage may be influenced by numerous uncertainties. While new relationships have been introduced to broaden the applicability of the equations, little progress has been made in recent

decades to reduce equation uncertainty. A distinction is generally made between intrinsic (aleatory) and epistemic uncertainty [27]. The former is irreducible and is associated with the random occurrence of processes in time and space. The latter concerns current knowledge regarding processes, observations, and methods and is, in theory, reducible with appropriate resources [28]. Effects of aleatory uncertainty in hydraulic stability have often been assumed dominant over epistemic uncertainty. However, the magnitude of both contributions has not yet been explicitly quantified to validate this assumption. Therefore, it remains a major knowledge gap in coastal structure design and optimization, posing an impediment to understanding related risks.

In recent decades, some progress has been achieved, although more details of the sources of uncertainties in stability and damage formulae are warranted. These semi-empirical formulae have been applied within probabilistic frameworks that consider the concurrent effects of intrinsic and epistemic uncertainty (e.g., [29], [30], [31], [32]). However, combining epistemic and intrinsic uncertainty within the same probabilistic framework is mainly a practical choice rather than an intentional one. Many clients now demand a risk-based analysis as part of effective breakwater design [33, 34]. This requirement integrates economically- and performance-optimized alternatives with extremal probabilistic assessment [35]. The engineering performance study forming the basis of the risk analysis is often accomplished using reliability analysis, where the reliability, or, conversely, the probability of failure, is quantified for each alternative [36].

1.3. Statement of the problem

The design of new solutions, adaptation of existing structures, and maintenance activities must adhere to a probabilistic approach capable of managing uncertainties related to the stochastic nature of external forces in a changing climate. Indeed, modern probabilistic design and simulation methodologies demand a deeper understanding of uncertainty in stone armor stability. Therefore, the comprehensive investigation into the

relative importance of epistemic versus intrinsic uncertainty remains a literature gap and an ongoing challenge that would guide studies toward improving physics research.

1.4. Research objectives

The principal objective of this manuscript is to collect and synthesize data from a wide range of international studies to quantify and improve understanding of uncertainty in stone armor stability. The attention is particularly on investigating hydrodynamic uncertainty associated with laboratory studies and comprehending the relationships between hydrodynamic forces acting on the armor slope and the stone displacement. Furthermore, the thesis aims to provide insights into the advancement of probabilistic methods for designing stone armor layers, comparing data and stability equations, and proposing initial attempts for new stability equations, in combination with uncertainty quantification identified during the research.

Specifically, the focus is solely on upslope seaside armor stability for uniformly sloping fully emergent rubble mound structures and randomly placed equant blasted armor stones. For this class of structure, under most conditions, minimum stability will coincide with higher water levels and higher wave heights.

1.5. Methodology

Efforts to describe complex wave-structure interaction phenomena have prompted new experimental campaigns, generating comprehensive datasets from diverse laboratories, individuals, and methodologies. However, scarcity of experimental data across all water depth conditions, particularly in shallow waters, mixing of non-homogenous laboratory-based data from disparate sources and historical periods, and the utilization of diverse methods and techniques represent just some examples of the gaps evident in the literature and sources of uncertainty in stone armor damage. Although methods have been developed and applied to account for epistemic and aleatory uncertainty in coastal structure design and performance assessment [36-41],

the uncertainty associated with the underlying empirical equations remains poorly understood. This is exemplified by the fact that each new laboratory study yields entirely different formulae for similar physical phenomena, often prioritizing their own dataset. Consequently, further research is imperative to extend the application of existing probabilistic methodologies to coastal structures with a more physically based approach, shifting the attention on the uncertainty inherent in data and stability equations and providing designers with tools to deal with it.

To achieve this goal, the initial phase of this thesis entailed gathering and synthesis existing experimental data in the literature, leading to the formation of a new extensive database encompassing varied water depth conditions. Data synthesis was accomplished by collecting and analyzing data from 7 distinct studies and homogenizing parametric characteristics to the extent possible, considering the disparate nature of the native data.

Benefiting from this unique database, the second step involved comparing data with the most widely used armor stability formulae within the framework of quantifying uncertainty. However, it became evident at the end of this step that the raw data cannot be fully synthesized without further modeling due to the disparate modeling approaches, the non-homogenous nature of the parametric data, and a limited understanding of the detailed laboratory techniques and data analysis.

Consequently, as a third step, an in-depth overview of the principal sources of uncertainty in stone armor stability was presented and detailed to delineate the contribution of each source of uncertainty to the total uncertainty.

Subsequently, the fourth step addressed the simulation of the studies using a numerical high-fidelity phase-resolving wave transformation model to further enhance the synthesis and homogenization of data from an hydrodynamical perspective. A one-dimensional fully nonlinear Boussinesq numerical model (Coulwave) was implemented

to replicate incident and reflected wave conditions throughout each facility, from which stone stability data were obtained. Wave parameters were matched near the wave generator and the structure toe to facilitate a consistent comparison of laboratory and numerical studies. This approach enables the separation of the evaluation of errors caused by stability formulae and the wave transformation model/stability formula (combined), allowing assessment of the effect of wave prediction errors on stability prediction errors.

In the final step, profiting from the new synthesized and homogenized data, a deeper study of the physics and forces influencing structure stability was conducted. Subsequently, the stability equations were re-evaluated using the newly synthesized homogenized database, and preliminary efforts were made to propose new stability equations.

1.6. Organization of the work and thesis outline

The thesis has been structured as follows:

- **Chapter 2:** literature review focusing on the main hydraulic stability formulae employed in the design of stone armor structures.
- **Chapter 3:** synthesis and formation of a new extensive database, comprising over 800 data in different wave and water depth conditions.
- **Chapter 4:** analysis and comparison of data with the most widely used stability formulae within the framework of quantifying uncertainty.
- **Chapter 5:** description and discussion of the principal sources of uncertainty in stone armor stability.
- **Chapter 6:** simulation of each test with a high-fidelity phase-resolving wave transformation numerical model and analysis and discussion of the hydrodynamic uncertainty.

- **Chapter 7:** discussion of results and attempts to propose new stability equations.
- **Chapter 8:** conclusions and identification of future research lines.

CHAPTER 2

Literature review

2. Literature review

The hydraulic stability of a rubble mound structure has been a crucial topic in coastal engineering, extensively studied over the last 80 years. Its complexity arises from the stochastic nature of wave loading and structure response, influenced by the random armor shape, orientation, and contact/interlocking between armor units, as well as the wide variation in structure and armor characteristics. Consequently, the initiation of armor unit movement and subsequent armor damage progression are also stochastic in nature. The development of stability formulae has its roots in experimental results and has potentially been refined through prototype observations. [42-44] give a historical review of damage models.

Numerous empirical stability models have emerged from extensive research on stone armor stability. Typically, a stability formula is derived by assuming the incipient instability of an armor unit subjected to certain wave forces. Early relations describing seaside armor stone incipient motion were formulated by [45], [46], [47], and others. These relations exhibited similarities but primarily differed in the parametric description of the structure slope and internal friction angles.

In particular, the well-known Hudson formula has been the most widely used formula for many decades. The equation in stability number form is given in Eq (1):

$$N_s = \frac{H}{\Delta D_{n50}} = (K_D \cot \alpha)^{\frac{1}{3}} \quad \text{Eq. (1)}$$

where N_s is the dimensionless stability number, $\Delta = \frac{\rho_r}{\rho_w} - 1$ is the relative buoyant density of the stone armor, with ρ_r and ρ_w being the density of stone and water, respectively, H^1 is the design wave height at structure toe, $D_{n50} = \left(\frac{M_{50}}{\rho_r}\right)^{\frac{1}{3}}$ is the nominal median stone size, with M_{50} being the median mass of the stone grading (50%-value by mass), α is the structure seaward slope angle, and K_D is a tabulated empirical stability coefficient associated with the start of damage. K_D varies primarily with the structure type, location on the structure, wave breaking, shape of the armor units, roughness of the armor unit surface, sharpness of edges, and degree of interlocking obtained in placement [48].

The Hudson damage assessment was based on eroded area on an average section and considered a “no damage” condition, allowing for the removal of as much as 1% of the total number of armor units in the cover layer or 0-5% of volume, measured between $1H$ from toe to crest. Damage measurement was conducted using soundings with a sphere rod. The foot was circular, and for each test, the diameter of the foot was equal to one-half the average size of the armor units. An increase in stability number indicates a decrease in the weight of the armor unit for the same wave height.

The early stability works were all deterministic, with the equations intended to be conservative fits to laboratory data. Epistemic uncertainty was addressed by enclosing the data cloud within an envelope, and the equations were not mean fits. Hudson highlighted that the resistance to movement due to wave forcing, characterized by the wave height, is primarily resisted by the stone weight, and affected by factors such as

¹ The original Hudson equation was developed for monochromatic waves and was validated using the average of the highest three waves in a short monochromatic burst. In the Shore Protection Manual (SPM) of 1984 [48], $H_{1/10}$ was introduced for design purposes, but K_D was still quantified for the lower envelope of stability. $H_{1/10}$ represents the average of the highest 10 percent of the waves in a time series.

friction between armor units, stone shape, upslope armor layer weight, and armor slope angle.

In the late 1970s and early 1980s, a series of large rubble mound structures experienced catastrophic failures [49], prompting extensive research to enhance the design and construction of mound breakwaters. Substantial progress in breakwater hydraulic stability research was achieved by [50], [51], and [52], hereafter referred to as TS. TS introduced irregular waves and recognized the significance of factors such as the type of breaking, stone placement, and storm duration. Later, [53] introduced a new damage parameter, $S_d = A_e / D_{n50}^2$, where A_e is the average eroded area.

The results obtained by TS were reanalyzed by [30] and, more recently by [54], referred to as vdM. VdM conducted a large laboratory experimental campaign, including both small- and large-scale tests, quantifying the influence of various parameters (e.g., wave period, damage level, permeability, number of waves (duration), wave steepness, type of armor layer, etc.) on the hydraulic stability of stone armor units. The author derived two different formulae, one for plunging waves (Eq. (2a)) and one for surging (Eq. (2b)) waves, which are widely employed in design practice and research but are mainly limited to deep (nonbreaking) water conditions and specific fields of application.

$$\frac{H_s}{\Delta D_{n50}} = 6.49 c_{pl} P^{0.18} \left(\frac{S_d}{\sqrt{N_w}} \right)^{0.2} \xi_{s-1,0}^{-0.5} \quad \begin{array}{l} \xi_{s-1,0} < \xi_{s-1,0,c} \\ \text{and } \cot \alpha \geq 4 \end{array} \quad Eq. (2a)$$

$$\frac{H_s}{\Delta D_{n50}} = 0.97 c_{su} P^{-0.13} \left(\frac{S_d}{\sqrt{N_w}} \right)^{0.2} \cot \alpha^{0.5} \xi_{s-1,0}^P \quad \begin{array}{l} \xi_{s-1,0} \geq \xi_{s-1,0,c} \\ \text{and } \cot \alpha < 4 \end{array} \quad Eq. (2b)$$

P is the notional permeability factor, g is the gravity acceleration, N_w is the number of waves, $H_s = H_{1/3}$ is the significant wave height in the time domain, $\xi_{s-1,0} = \tan \alpha / \sqrt{2\pi H_s / g T_{m-1,0}^2}$, is the surf similarity parameter (SSP) [55] computed using H_s and the negative first moment spectral wave period $T_{m-1,0}$ at the breakwater toe,

and c_{pl} and c_{su} are stone shape coefficients ([56], [57]). The range of applicability of Eq. (2) depends on the transition value assumed by the critical SSP $\xi_{s-1,0,c}$ (Eq. (2c)).

$$\xi_{s-1,0,c} = \left(\frac{6.49c_{pl}}{0.97c_{su}} P^{0.31} \sqrt{\tan \alpha} \right)^{\frac{1}{P+0.5}} \quad Eq. (2c)$$

The vdM dataset was almost entirely limited to flat bathymetry and relatively deep waters. Therefore, these formulations are not applicable in shallow waters and heavy wave-breaking conditions [19]. A correction was proposed by vdM [30], to extend the formulae to depth-limited water conditions with limited wave breaking if $H_{s,toe}/H_{s,deep} > 0.70$, where $H_{s,deep}$ is in a location before depth-induced wave breaking occurs and $H_{s,toe}$ is at the structure toe. VdM suggested replacing the significant time-domain wave height at the toe (H_s) with the average on the 2 percent highest waves that reach the breakwater ($H_{2\%}$), stating that the significant wave height does not consider the effect of wave breaking on the foreshore.

[58] conducted several laboratory small-scale tests to gain insight into shallow water conditions. Their results indicated that vdM empirical formulae were very sensitive to the choice of input parameters, such as statistical or spectral wave characteristics. The work by [58] was later extended by similar experiments of [59], hereafter referred to as VSK, who introduced new stability data acquired in shallow water conditions, aiming to re-calibrate the vdM formulae. Similar equations for plunging (Eq. (3a)) and surging (Eq. (3b)) waves were derived.

$$\frac{H_s}{\Delta D_{n50}} = c_{pl} P^{0.18} \left(\frac{S_d}{\sqrt{N_w}} \right)^{0.2} \xi_{s-1,0}^{-0.5} \left(\frac{H_{2\%}}{H_s} \right)^{-1} \quad \xi_{s-1,0} < \xi_{s-1,0,c} \quad Eq. (3a)$$

$$\text{and } \cot \alpha \geq 4$$

$$\frac{H_s}{\Delta D_{n50}} = c_{su} P^{-0.13} \left(\frac{S_d}{\sqrt{N_w}} \right)^{0.2} \cot \alpha^{0.5} \xi_{s-1,0}^P \left(\frac{H_{2\%}}{H_s} \right)^{-1} \quad \xi_{s-1,0} \geq \xi_{s-1,0,c} \quad Eq. (3b)$$

$$\text{and } \cot \alpha < 4$$

Here, $c_{pl}=8.4$ and $c_{su}=1.3$ are the new coefficients for plunging and surging waves, respectively. The authors proposed to consider the measured ratio $\frac{H_{2\%}}{H_s}$ in Eq. (3) instead of replacing it with a fixed coefficient equal to 1.4 [58] because, in shallow water conditions, wave heights are not Rayleigh distributed ([60], [61], [62]). The range of applicability of Eq. (3) is broader than Eq. (2) and depends on the value assumed by the critical SSP $\xi_{s-1,0,c}$ computed using different coefficients. However, it was noted that there were unexplained differences between the vdM data and the new VSK data, specifically within the area of application where they were expected to be similar.

In [63], an alternative stability formula (Eq. (4)) was reported, not depending on the spectral wave period ($T_{m-1,0}$) or the notional permeability factor (P), but simply including both the armor stone (D_{n50}) and core stone ($D_{n50,core}$) nominal sizes, respectively.

$$\frac{H_s}{\Delta D_{n50}} = 1.75 \sqrt{\cot \alpha} \left(1 + \frac{D_{n50,core}}{D_{n50}} \right) \left(\frac{S_d}{\sqrt{N_w}} \right)^{\frac{1}{5}} \quad Eq. (4)$$

In [26], a minor correction (addition of a 2/3-power exponent) was considered to better describe the new permeability factor.

[42], hereafter referred to as VML, conducted physical model tests and proposed a new stability formula by suggesting the use of the parameter $H_{1/50}$ (i.e., the average wave height of the 50 highest waves attacking the structure) to characterize the wave height. They replaced H_s with $H_{1/50}$ and re-calibrated the vdM formulae, aiming to design structures in intermediate and shallow waters. The authors claimed that VML formulae are independent of storm duration and can be used for non-Rayleigh-distribution cases, such as regular waves and shallow waters if $H_{1/50}$ is used instead of H_s .

Most stability formulae traditionally do not explicitly include water depth. The influence of depth, bathymetry, and wave breaking on armor stability is still not entirely clear,

because past studies have not yet differentiated the impact of wave breaking on destabilizing and stabilizing forces. The references cited incorporated complex wave-structure interaction by empirically relating the SSP to the stability number. However, this approach does not explicitly incorporate water depth or consider the effect of nonlinear wave transformation on the nearshore bathymetric slope. In addition, in most of the equations herein, the SSP and related wave breaking criteria are given in terms of the structure slope suggesting that the nearshore bathymetric slope is of relatively less importance. However, vdM used deep water and a flat bottom for nearly all tests and this data set is influential in this research area. There is still a question about the relative importance of structure slope to nearshore bathymetric slope in shallow water.

[64] and later [65], hereafter referred to as MK, developed a stability formula based on the maximum wave momentum flux and concluded that incorporating water depth results in a better description of stability for both plunging (Eq. (5a)) and surging (Eq. (5b)) waves:

$$N_m = 5.0P^{0.18} \sqrt{\cot \alpha} \left(\frac{S_d}{\sqrt{N_w}} \right)^{0.2} \quad S_m \geq S_{mc} \quad \text{Eq. (5a)}$$

$$N_m = 5.0P^{0.18} \cot \alpha^{0.5-P} \left(\frac{S_d}{\sqrt{N_w}} \right)^{0.2} S_m^{-P/3} \quad S_m < S_{mc} \quad \text{Eq. (5b)}$$

where $N_m = \left(\frac{(M_f)_{\max}}{\rho_w g h^2 \Delta} \right)^{1/2} \frac{h}{D_{n50}}$ is the stability number that depends on water depth (h) and the nonlinear maximum wave momentum flux $(M_f)_{\max}$ computed at the toe. s_m is the wave steepness at the toe of the structure using the mean period in the time domain, T_m , and the spectral wave height in the frequency domain, H_{m0} . The range of applicability depends on the value of the critical wave steepness $s_{m,c}$ (Eq. (5c)).

$$s_{m,c} = -0.0035 \cot \alpha + 0.028 \quad \text{Eq. (5c)}$$

The formula involves a nonlinear wave momentum flux using a numerical Fourier solution approximated by [66] with the relations reported in Eq. (6).

$$\frac{(M_f)_{\max}}{\rho_w g h^2} = A_0 \left(\frac{h}{g T_m^2} \right)^{-A_1} \quad \text{Eq. (6a)}$$

$$A_0 = 0.639 \left(\frac{H_{m0}}{h} \right)^{2.026} \quad \text{Eq. (6b)}$$

$$A_1 = 0.180 \left(\frac{H_{m0}}{h} \right)^{-0.391} \quad \text{Eq. (6c)}$$

The formula was calibrated using only the vdM data. [65] established a formula for plunging and one for surging waves, but these formulae do not intersect at the defined transition point. Such formulation lacks validation for shallow waters because no data in such conditions were available at the time. However, ERDC researchers have been using the criterion $s_{m,c} = (\cot \alpha)^{-3}$ for over 5 years as it represents the analytical intersection between the equations. Using this value, the separation between surging and plunging better agrees with [55].

[67] attempted to unify the stability formulae for deep and shallow waters, considering the effects of mild and steep foreshore slopes, as well as stone roundness on stability. They re-calibrated the vdM formula using SwanOne to estimate $H_{2\%}$ and $T_{m-1,0}$ at the structure toe [68]. According to their work, stability in shallow waters depends on the phase lag between velocity and acceleration, with the phase lag decreasing for steeper foreshore slopes, maximizing the total (inertia + drag) destabilizing force exerted by waves on the armor stone. Afterward, [69] proposed a formulation that incorporated the effect of the foreshore by adding a correction factor based on the SSP for the foreshore slope. The structure slope in the SSP relation is considered appropriate in deep water, but in shallow water, wave breaker type is influenced by the bathymetry

slope. Therefore, it seems unlikely that the wave height statistic alone would provide consistency for this equation formulation between deep and shallow water conditions.

Recently, [70], hereafter referred to as HGM, introduced a new design formula for breaking waves (Eq. (7)) using a combined experimental-numerical approach with SwanOne.

$$S_d = 0.066 \left(\frac{H_{m0}}{\Delta D_{n50}} \right)^{\frac{1}{6}} \quad \text{Eq. (7)}$$

In this formula H_{m0} is measured at three times the water depth far from the structure toe ($3h$), similar to the recommendation by [71]. Experimental wave measurements were compared to SwanOne estimations to establish a rational procedure for determining wave characteristics in the depth-induced breaking zone.

[63] and [70] did not include tests with highly nonlinear non-breaking or slightly breaking waves characterized by $H_{1/3}$ significantly larger than H_{m0} . In [72], the hydraulic stability of a conventional rubble mound breakwater in shallow waters was investigated, with a focus on the effects of nonlinear and very low steepness waves characterized by a high and narrow crest and a wide wave trough. The authors revisited the vdM stability design formulae and proposed a new formulation (Eq. (8)) based on the newly acquired data and the dataset provided by VSK [63].

$$\frac{H_{m0}}{\Delta D_{n50}} = 4.5 \left(\frac{S_d}{\sqrt{N_w}} \right)^{0.2} 1.6^P \xi_{m-1,0}^{(0.4P-0.67)} \quad \xi_{m-1,0} < \xi_{m-1,0,c} \quad \text{Eq. (8a)}$$

$$\frac{H_{m0}}{\Delta D_{n50}} = 3.1 \left(\frac{S_d}{\sqrt{N_w}} \right)^{0.2} P^{0.17} \min[\cot \alpha, 2]^{0.23} \quad \xi_{m-1,0} \geq \xi_{m-1,0,c} \quad \text{Eq. (8b)}$$

$s_{m-1,0} = 2\pi H_{m0} / (gT_{m-1,0}^2)$ is the wave steepness at the toe of the structure estimated with the deep water wavelength formula. The critical SSP ($\xi_{m-1,0,c}$) is redetermined by setting (8a) and (8b) equal and solving the SSP as reported in Eq. (8c).

$$\xi_{m-1,0,c} = \left(\frac{0.69P^{0.17} \min[\cot \alpha, 2]^{0.23}}{1.6^P} \right)^{\frac{1}{0.4P-0.67}} \quad \text{Eq. (8c)}$$

Based on previous findings, Eq. (8) was derived using spectral wave parameters computed at the toe of. The formulae achieved a reduction in scatter, and it was concluded that H_{m0} may be better than $H_{1/3}$ or $H_{2\%}$ due to the lower influence of wave linearity. The database by Eldrup and Andersen is not yet available in the literature.

Therefore, there is currently no consensus on the appropriate representative wave height and wave period. Different wave parameters, such as $H_{2\%}$, H_s , H_{m0} for wave height and T_m , T_p , $T_{m-1,0}$ for wave period, have been examined to derive formulae applicable to all conditions. The equations mentioned incorporate both frequency and time domain parameters. In practical applications, spectral wave models are the primary models used for wave transformation. However, determining time domain parameters from spectral parameters requires knowledge of spectral shape and parameter probability distribution, which may not be readily available in shallow water. Authors have attempted to address this gap through the development of empirical analytical relations. For example, in real sea waves, the ratio $H_{1/3}/H_{m0}$ in deeper water is approximately 0.95. In shallow water, the ratio increases due to nonlinear wave transformation until the waves initiate breaking. The maximum ratio of $H_{1/3}/H_{m0}$ is close to 1.1 for typical sea conditions and may reach 1.5 for swell with very low wave steepness. Inside the surf zone, the ratio of $H_{1/3}/H_{m0}$ reduces rapidly to values around 0.95 to 1.0 [73]. Spectral wave forecast models typically predict H_{m0} , and the standard output of most wave gage records is H_{m0} . This is different from the design guidelines for coastal structures, which often use $H_s = H_{1/3}$ or other time domain wave heights ($H_{2\%}$, $H_{1/20}$, H_{\max} , etc.) related to

$H_{1/3}$. However, simple relationships are available if waves are Rayleigh distributed. Different methods allow this conversion within specific limits of application ([60], [73], [74]). Therefore, coastal engineers must be aware of the wave height they are using and determine the estimation needed for their specific application.

More recently, alternative approaches utilizing artificial intelligence computing techniques, such as artificial neural networks (ANN) [75], genetic programming ([76], [77]), and machine learning models [78], have gained attention. For instance, in [79], a multi-variable regression model was employed on an experimental dataset consisting of 791 points from the literature. The aim was to develop a compact and concise formula suitable from deep to shallow water conditions for both plunging (Eq. (9a)) and surging (Eq. (9b)) waves:

$$\frac{H_s}{\Delta D_{n50}} = 4.5 C_p N_w^{\frac{1}{10}} S_d^{\frac{1}{6}} \xi_{s-1,0}^{-\frac{7}{12}} (1-3m) \quad \text{for } \xi_{s-1,0} < 1.8 \quad \text{Eq. (9a)}$$

$$\frac{H_s}{\Delta D_{n50}} = 3.9 C_p N_w^{\frac{1}{10}} S_d^{\frac{1}{6}} \xi_{s-1,0}^{\frac{1}{3}} (1-3m) \quad \text{for } \xi_{s-1,0} \geq 1.8 \quad \text{Eq. (9b)}$$

where $C_p = \left[1 + (D_{n50,core} / D_{n50})^{3/10} \right]^{3/5}$ is the permeability coefficient. These formulae consider the effect of the foreshore slope m (where $m = \tan \beta$ and β is the approach slope angle). They are also valid in depth-limited wave breaking conditions if $\frac{h}{H_s} < 3$. Eq. (9) suggests that stable armor size increases with increasing slope.

To gain more insight into stone armor stability, particularly in very and extremely shallow water conditions with heavy wave breaking on the foreshore, [80] carried out a new 2D physical experimental campaign. One challenge in such conditions is that wave conditions may change drastically as the relative water depth becomes small. Further, if the wave heights in the flume become very small (a few centimeters), the stone size must also be relatively small to show relevant damage. Many researchers

(e.g., [81], [82]) have observed that steep foreshores result in more damage than gentle foreshore slopes.

[25] and [65] confirmed the intra-storm damage relations proposed by TS and vdM. However, they suggested that the equations provided in this section do not effectively capture the progressive damage resulting from successive storms. Instead, they presented equations for time-varying damage progression, which are valuable for life-cycle simulation. In a recent study, [83] carried out new physical model tests to explore the static stability of stone-armored mild slopes ($6 \leq \cot \alpha \leq 10$), demonstrating that milder stone slopes usually encounter more spilling waves than plunging or surging waves, resulting in decreased loads on the armor slopes. The authors proposed a new design formula and provided guidelines for designers to assess the stability of mild stone-armored slopes. [84] delved into the classical methodology employed to study the damage evolution of coastal sloped structures. To address the epistemic uncertainty inherent in the current damage evolution model, Losada proposed a novel predictive method based on a sigmoid function. This new method centers on the role of relative depth in damage evolution, specifically considering the interplay between relative depth, wave steepness at the toe of the breakwater, and structure slope.

Despite the existence of various laboratory-based wave stability formulae, there is no complete certainty about their performance. Engineering manuals such as the Rock Manual [26] describe several stability formulae, each with its own range of validity and specific field of application. The manual offers recommendations on the fundamental approaches for evaluating the stability of stone-armored slopes along a flow path. It provides an overview of the different fields of application for various stability formulae, suggesting when and how to use different equations. However, there is an overlapping area termed “*shallow water*” when $2 < h/H_{s,toe} < 3$, where different stability formulae can be applied, leading to substantially different outcomes concerning the designed breakwater's armor stone size.

CHAPTER 3

Description of new extensive database

3. Description of new extensive database

This chapter describes the process of gathering and synthesis of the existing experimental stability data from the literature, leading to the formation of a comprehensive and unique database that encompasses various water depth conditions. Data synthesis is accomplished by collecting and describing data from 7 different international studies and homogenizing parametric characteristics to the extent possible, considering the disparate nature of the native data. To homogenize laboratory data and minimize epistemic uncertainty, the following test conditions were considered:

- 2D physical model
- Head-on wave attack
- Irregular wave trains
- Multi-layered emerged breakwater or embankment structures
- No to little overtopping
- Absence of a toe berm (if $B^2 < 1-3D_{n50}$)
- Standard rough equant angular shape armor layer
- 2-2.5 D_{n50} thickness of the layers
- Bulk-random placement
- Incipient seaside damage

² B is the berm width.

- Constant wave and water level conditions

Data that did not conform to these specified conditions were excluded from the database. As a result, 890 irregular wave tests were collected and organized for subsequent analyses. The selected and utilized datasets include:

- TS dataset – 134 data
- vdM dataset – 295 data
- VSK dataset – 207 data
- VML dataset – 116 data
- MK dataset – 25 data
- HGM dataset – 44 data
- EUMER dataset – 69 data

within this manuscript, an in-depth analysis of the different datasets was conducted, and efforts were made to standardize parameters as much as possible to facilitate meaningful comparisons. Subsequent subsections delve into detailed discussions of the main aspects of the physical models.

3.1. Thompson and Shuttler (1975) – TS data

TS [18] performed both long-term deterioration and shorter single-storm damage tests using a riprap³-armored embankment with an impermeable core. The physical model study was carried out at the Hydraulic Research Station, HR Wallingford (UK), in a 1.2 m wide, 45 m long flume subdivided into a calibration channel and a test channel 0.65 m wide. Irregular sea waves with a Pierson-Moskowitz (PM) spectrum were generated,

³ *American terms to describe a human-placed rock armor to protect shorelines against scour and water, wave, or ice erosion.*

and short-repeated wave sequences were performed to avoid re-reflection at the wave paddle. All tests were restricted to nonbreaking irregular wave attacks on a flat bathymetry just seaward of the embankment, mostly in transitional depths.

The free surface oscillations were sampled with one resistive wave gage placed in the calibration channel, where a 1V:20H spending rocky beach was constructed to limit boundary reflection at the end of the tank. The acquired time series of free surface oscillations were recorded on ultra-violet paper and digitally on magnetic tape for spectral computations. Wave reflection measurements were made in the test channel in front of the riprap slope using two wave gages and short repeating sequences of waves. The reflection coefficient (K_R) was computed using a method equivalent to that of Kajima [85]. To the authors' knowledge, no information was given about the position of the wave probes and the post-processing analyses.

The damage analysis was performed using a mechanical surface profiler covering a $9D_{n50}$ width of the slope with 10 soundings spaced D_{n50} apart. The foot of the profiler was a hemisphere rod equipped with a circular foot with a diameter of $0.5D_{n50}$. The damage analysis procedure consisted of a first sounding of the filter layer (only for the first test), a survey of the riprap, a survey after 1000 waves, and further survey after successive sequences of 1000 waves up to a cumulative total of 5000 waves. The 10 sections were summed to give a mean profile, which was then used to compute the eroded volume (V_e) by differencing with the initial average profile and using the trapezoidal rule to obtain the erosion damage (N_{Δ})⁴ assuming a spherical armor shape.

⁴ N_{Δ} stands for the equivalent number of D_{50} sized spherical stones eroded from a $9D_{n50}$ width of slope (i.e., it is the theoretical number of round stones removed from an area with a width of 9 diameters). $N_{\Delta}=20$ is for start of damage and $N_{\Delta}=80$ is the average for filter exposure.

However, this parameter differs from the damage described by [53], where S_d ⁵ represents the number of square units (width D_{n50}) fitting the eroded area A_e . To facilitate a comparison of the TS dataset with others, the following approximate conversions (Eq. (10a,b)) were made [69, 86]:

$$D_{n50} = 0.82D_{50} \quad \text{Eq. (10a)}$$

$$N_{\Delta} = \frac{\rho_a^B V_e}{\rho_a \frac{\pi}{6} D_{50}^3} = \frac{\rho_a^B 9D_{50} A_e}{\rho_a \frac{\pi}{6} D_{n50}^2} = \frac{\rho_a^b 54 \cdot 0.82^2 A_e}{\rho_a \pi D_{n50}^2} \quad \text{Eq. (10b)}$$

where ρ_a^B is the bulk density of material⁶ on the slope, ρ_a is the mass density of armor stones, $D_{50} = V_{50}^{1/3}$ is the size of stones that exceeds the 50% value of the sieved curve, N_{Δ} is the damage parameter, and A_e is the erosion area in the cross-section. This damage descriptor provides a rough estimation of the number of displaced stones. Additionally, it presents some shortcomings that reduce its applicability. For example, the measurement of bulk density in prototype might be difficult, and D_{n50} is preferable for construction purposes than D_{50} because it allows the straightforward consideration of the weight of the stones [44].

Eq. (10) allows the conversion from N_{Δ} to S_d [86]. [87] showed that Eq. (9b) yielded very different results if a slightly different method is used to compute the average eroded area. The difference between different methods ranged from 2 to 82 percent. In general, the differences decreased as the damage level increased. So, variations in profiling and

⁵ S_d represents the number of removed stones in a row with a width of $1D_{n50}$.

⁶ For Thompson and Shuttler's tests, the density ratio was $\frac{\rho_a^b}{\rho_a} = 0.552$.

data analysis methods produce significant uncertainty that is yet to be entirely quantified and reintroduced into the empirical coefficients.

The stone were placed in a bulk-random manner, and the thickness of the armor and filter layers were $2D_{n50}$ and $0.5D_{n50}$, respectively.

In conclusion, 134 data points were considered for the analysis, and Table 3.3 reports the main characteristics. In [52], only short wave periods were investigated, limiting the applicability range. Uncertainty in wave parameters is a consistent theme and will be discussed throughout this manuscript.

3.2. Van der Meer (1988) – vdM data

The well-known physical model described in van der Meer's Ph.D. thesis [30] was performed at the Scheldt flume WL, Delft Hydraulics (Netherlands) in a 1.0 m wide, 1.2 m deep, and 50 m long wave flume. The test section was installed at 44 m from the random wave generator. Some additional tests were carried out in the large-scale Delta flume, scaled up according to Froude's law by a length scale factor of 6.25. Irregular sea waves were generated using an in-house system developed by Delft Hydraulics to measure and compensate for the re-reflection at the wave board. All tests were conducted using different types of PM wave spectra in relatively deep water conditions with a flat bottom, except for the test series with a 1V:30H foreshore.

The incident waves were measured with the structure in the flume (except for the 1V:30H test series) using two resistive wave gages placed about a quarter of a wavelength apart ($L/4$), considering the reflection analysis described in Goda and Suzuki [88]. No information was given about the post-processing analyses and the reflection method. In addition to the Ph.D. thesis and the several papers, it is mentioned that more information can be found in Delft Hydraulics' project reports M1983 (8 reports, in Dutch).

Damage measurements were conducted using a mechanical surface profiler with a probe diameter D of 4 cm and 9 probes placed 0.10 m apart⁷ on a computer-controlled carriage, with 10 cm left on the lateral boundaries of the wave flume to avoid laboratory effects. For most tests, $D_{n50}=3.6$ cm, so $D/D_{n50}=1.11$. Depending on the slope angle, each survey consisted of between 500 and 1600 data points. Successive soundings were taken at the same points using the repositioning of the profiler. The damage measurement procedure included a pre-sounding, an intermediate survey after 1000 waves, and a final survey after 3000 more waves. After each test with damage, armor layers were removed and rebuilt. A total of 9 profiles were averaged to obtain a mean profile, and finally, A_e was calculated by differencing the damaged average profile from the initial average profile and integrated using Simpson's rule. Van der Meer did not include all the measured A_e but avoided settlement (when $f(y)\leq 0.1D_{n50}$). The fixed values of 1000 and 3000 waves were reported as the number of waves (N_w), defined as $N_w=t_r/T_m$, where t_r is the total run duration.

Van der Meer used 5 types of stones, categorized as equant stones [56]. Construction employed bulk-random placement, and the thicknesses of the armor and filter layers were $2-2.25D_{n50}$ and $0.5D_{n50}$, respectively. In [30], only the categories permeable, impermeable, and homogeneous were plotted, excluding tests with a small number of low-density stones and wide-narrow wave spectra.

⁷ All tests conducted by van der Meer have armor layers with $D_{n50}=0.0360$ m except for the test with a different stone density with $D_{n50}=0.0332$ m and low-crested tests with $D_{n50}=0.0344$ m (large-scale tests in the Delta flume are not considered in this manuscript). Therefore, the foot of the surface mechanical profiler used to evaluate the damage S had a diameter $1.11D_{n50}\leq D=4$ cm $\leq 1.20D_{n50}$, and the spacing ΔL between the soundings related to the nominal size of the armor layers was in the range of $2.78D_{n50}\leq \Delta L\leq 3D_{n50}$.

VdM conducted experiments for only one foreshore slope and used a very narrow range of wave periods. Therefore, the effect of varying approaching bathymetry or breaker type was not determined. For breaking waves, as the approaching slope steepens, the wave breaking becomes more vigorous [55], and the slamming forces increase dramatically as the waves start plunging to collapsing [89]. VdM's spilling breakers were not very severe with respect to stability relative to plunging or collapsing breakers.

In conclusion, 295 data points were considered in the analysis, and Table 3.3 reports the main characteristics.

3.3. Van Gent et al. (2003) – VSK data

The physical model experiments described in [58], [59], and [63] were performed at the Scheldt flume WL, Delft Hydraulics (Netherlands) in a 1.0 m wide, 1.2 m deep and 55 m long wave flume. Irregular sea waves were generated using a 2nd order wave generation technique, an Active-Reflection-Compensation (ARC) system at the wave board, and a sloping beach to reduce the re-reflection in the flume. The experiments were carried out in depth-limited wave conditions with two different foreshores (1V:100H and 1V:30H). Both single and double-peaked offshore spectra (JONSWAP, TMA) were tested. Additionally, broken waves, characterized by single-peaked offshore and flat wave spectra at the structure, were also investigated.

The incident waves were measured without the structure in place using a three-gage resistive array approximately centered at the structure toe. A reflection analysis was performed using the method proposed by Mansard and Funke [90]. No detailed information about the positions of the wave gages and the post-processing analyses was given in the papers.

The damage measurements were made using a mechanical surface profiler ($D=4$ cm) with 9 soundings spaced 0.10 m^8 apart, following a similar methodology as vdM, but with a different instrument. Ten cm were left from the boundaries of the wave flume to avoid laboratory effects, and the structure height was measured at 4 cm and 2 cm increments for 1:4 and 1:2 slopes, respectively. The damage analysis procedure and post-processing were similar to vdM, except that VSK data considered the entire A_e (including the small settlements) for the evaluation of S_d .

In conclusion, the analysis considered 207 data points, and Table 3.3 reports the main characteristics.

3.4. Vidal et al. (2006) – VML data

The physical model experiments described in [42] were conducted at the Coastal Laboratory, University of Cantabria (Spain) in a 0.58 m wide and 24 m long wave flume. The wavemaker used was a piston-type equipped with an Active Wave Absorption Control System (©AWACS) to prevent re-reflection in the wave flume. Tests were performed using a TMA wave spectrum with a flat bottom in relatively deep water conditions with nonbreaking waves.

Wave measurements were taken with the structure in the flume using a four-gage array located seaward of the structure, and the reflection method proposed by Baquerizo

⁸ [58] carried out 3 test series with 2 different nominal sizes for the armor layers (i.e., $D_{n50}=0.036$ m for T1 and $D_{n50}=0.022$ m for T2 and T3). [59] conducted other 4 test series always with the same $D_{n50}=0.026$ m. Therefore, the foot of the surface mechanical profiler used to evaluate the damage S has a diameter $1.11D_{n50}\leq D=4\text{ cm}\leq 1.82D_{n50}$ and the spacing ΔL between the soundings related to the nominal size of the armor layers was in the range of $2.78D_{n50}\leq \Delta L\leq 4.54D_{n50}$.

[91]. A zero-down crossing method was used to determine the incident time series, wave heights, and wave periods.

Armor damage was measured through three different methods before and after each series of waves, namely: i) profiling over 21 cross-sections using a laser profiler with transects spaced at 2 cm, ii) counting displaced armor stones settled over the original armor layers, and iii) computing the planar eroded area on the outer layer of the armor using a digital image processing technique. The number of displaced stones over the original armor layer was counted after each series of waves. If the number of displaced stones is N_d and the porosity of the armor layer is p , the average eroded A_e area in the width R can be obtained from Eq. (11) [42].

$$A_e = \frac{N_d D_{n50}^3}{(1-p)R} \quad \text{Eq. (11)}$$

Tests were performed modeling a storm with sequential storms with varying hazards keeping the SSP constant and increasing the zero-moment wave height H_{m0} and peak period T_p . Each sea state (with a gradual increase in wave energy) contained 1000 waves. At the end of each sea state, the damage was measured before the initiation of the following sea state. Each test finished when some of the units of the second layer of the armor were displaced (initiation of destruction). A typical test was composed of 8 to 13 sea states, and the model was rebuilt after each test series. Only the “*irregular*” data that can be considered nonstationary conditions with $N_w < 5000$ were used in the processed dataset. However, if energy and hazard increase from series to series without rebuilding, then damage past the first measurement would not be comparable to other experiments where conditions were stationary.

In conclusion, 116 data points were considered in the analysis, and Table 3.3 reports the main characteristics.

3.5. Melby and Kobayashi (2011) – MK data

The physical model experiments described in [31] and [65] were conducted at the U.S. Army Engineer Waterways Experiment Station, WES Laboratory (U.S.) in a 1.52 m wide, 2 m deep, and 61.1 m long wave flume subdivided into 2 identical side-by-side channel, each 0.76 m wide. Irregular waves were generated using a 1st order piston-type wave generator with a TMA spectrum. Waves were run in 15 min bursts, with the water settling completely between the wave bursts to minimize re-reflection in the flume. Tests were performed in depth-limited wave conditions on a 1V:20H foreshore with little to no overtopping on the structure. Incident wave breakers were spilling and plunging on the beach slope and collapsing and surging on the structure slope.

The incident waves were computed through two capacitive wave gage arrays placed offshore and nearshore with the structure in place, using the method of Goda and Suzuki [88] for the reflection analysis. The spectral waves were processed in a frequency bandwidth of $0.5 \text{ Hz} \leq \Delta f \leq 1.4 \text{ Hz}$. An additional dataset by [65] used the same flume setup except that the flume was further subdivided into a section with a structure and one with a 0.30 m wide open flume. Wave generation for this series includes second-order correction. Waves were measured nearshore seaward of the structure toe and at the location of the structure toe in the open flume. Most of the other flume and structure characteristics were identical between the two experiments.

[31] utilized a mechanical profiler for damage analysis, while [65] used an automated laser profiler. Soundings spaced at 0.05 m were reduced to 9 transects to be consistent with the mechanical profiler of [31]. To avoid laboratory effects, 21 cm were left from the boundaries of the wave flume. After each test with damage, the armor layers were removed and rebuilt. The 9 profiles were averaged to obtain an average profile, and A_e was calculated using Simpson's rule. Profiles were measured after every two bursts, every 30 minutes of waves. The whole A_e was considered, including small settlements, despite not having many settlements because of the 30 min low-wave shakedown test

with very little damage at the beginning of each test series. The armor layer thickness was $2D_{n50}$. [31] focused on damage progression over multiple storms with varying hazards, making those data are somewhat unique.

Herein, we only include 25 data points from [65], and Table 3.3 reports their main characteristics.

3.6. Herrera et al. (2017) – HGM data

The physical model experiment described in [70] was conducted at the LPC-UPC Laboratory, Universitat Politècnica de València (Spain) in a 1.2 m wide, 1.2 m deep and 30 m long wave flume. For each test, random wave runs of 1000 waves were generated following a JONSWAP ($\gamma=3.3$) spectrum with a 1V:50H foreshore. The AWACS active absorption system was activated to limit multireflection in the wave flume. Tests were performed in depth-limited wave conditions with breaking waves on the foreshore and a non-overtopping rubble mound structure without a toe berm.

Wave height distribution and spectral moments were estimated from the measured water surface elevations with and without the structure model. Incident and reflected waves were separated in the wave-generating zone for tests conducted with the structure using the LASA-V method [92]. In the depth-induced wave-breaking zone, existing methods to separate incident and reflected waves were not reliable when applied near the structure. Incident waves were estimated close to the model from the total wave gage records (average of H_{m0} or $H_{2\%}$ measured at two close wave probes) considering the reflection coefficient measured at the wave generation zone. To reduce undesired reflection, an energy absorber was placed at the end of the wave flume ($K_R = H_{m0,r}/H_{m0,i} < 20\%$, where the term ‘ r ’ refers to the reflected wave and ‘ i ’ to the incident one). As measurements without a structure are more reliable in estimating actual incident waves, only the values obtained in tests without the breakwater model were considered when referring to incident wave measurements. Numerical

simulations with SwanOne were carried out to estimate the wave characteristics at each location more accurately. The method proposed by [60] was implemented to estimate $H_{2\%}$ in the depth-induced wave-breaking zone.

The armor damage was measured considering the cumulative number of stones displaced (N_d) during the test series having constant h and peak SSP. The damage was characterized using the virtual net method (S_e) developed by [93, 94] and the visual counting method (S_v) described by [42]. Both methods gave similar results, as most armor damage was caused by unit extractions only. The virtual net method was finally used in this study to characterize the armor damage. However, [64] pointed out that significant differences may occur between armor damage measured with profiles and that measured with the visual counting method.

H_s from tests without the structure in place was reported for this study and used in the stability equation derivation, whereas $H_{2\%}$ and $T_{m-1,0}$ were derived from the numerical investigation.

In conclusion, 44 data points were considered in the analysis, and Table 3.3 reports the main characteristics.

3.7. EUMER data

The physical model experiment described by [80] was carried out in the wave flume at the EUMER Laboratory at the University of Salento (Italy). The wave flume is 45 m long, 2 m high, and 1.4 m wide and is equipped with a piston-type wave generator (maximum stroke 0.5 m) able to generate 2nd order irregular waves. The wave generator is supplied with an ARC system to minimize the re-reflection at the wave paddle. A sloping beach made of coarse rocks was placed at the end of the flume. The tests were performed from intermediate water to extremely shallow water conditions with a 1V:30H foreshore with little to no overtopping on the structure. New data in very and extremely shallow water conditions over a wide surf zone led to a complete energy saturation at the

structure toe, showing a reduction of the wave-to-wave variations. Durations included 1000 and 3000 waves for each test following a JONSWAP ($\gamma=3.3$) spectrum.

The same tests were conducted both with and without the structure in place. For tests conducted without the structure, the incident wave was measured through one resistive wave gage placed 0.45 m seaward of the toe of the structure without any filtering. The total (incident + reflected) record of the measured waves almost corresponded to the incident waves if an efficient wave absorption system is used ($K_R < 20\%$). The K_R was calculated for all tests without the structure in place using a 4-gage-array inshore using the method by Mansard and Funke (MF) [90]. The bulk reflection coefficient was applied to the measured wave height as in Goda's textbook ($H_{m0,i} = H_{m0}/(1 + K_R)^{1/2}$).

The damage analysis was performed through an automated high-density laser profiler system sounding 10 transects spaced 0.10 m apart⁹ across the flume width. Twenty centimeters were left from the boundaries of the wave flume to avoid boundary-laboratory side effects. The profiler system was remotely controlled, allowing fixing some parameters, like the starting point and the acquisition frequency. The probe can move with a constant velocity up to 25 mm/s, both along the z -axis and y -axis, to maintain a constant measurement distance (80 mm) above the slope. It can proceed also horizontally (x -direction), up to 50 mm/s. The laser provides a measurement resolution in both y and z directions of ± 0.5 mm, and the same positional accuracy is guaranteed by the traverse laser support system [95]. Profiles were collected with very dense samples in the plane and then averaged onto a gird and then into transects. The eroded area (A_e) was retrieved by measuring the cross-shore profiles of the stone

⁹ [80] carried out an experimental campaign using 4 different nominal sizes for the armor layers (i.e., $D_{n50} = 0.046$ m, $D_{n50} = 0.034$ m, $D_{n50} = 0.024$ m, and $D_{n50} = 0.0138$ m). Therefore, the spacing $\Delta L = 0.10$ m between the soundings related to the nominal size of the armor layers was in the range of $2.17D_{n50} \leq \Delta L \leq 7.25D_{n50}$.

slope before and after each wave test along 0.10 m equally spaced transects. The entire A_e , including small settlements, was considered despite not having many settlements because of a low-wave shakedown test with no damage at the beginning of each test series.

Stone placement was assumed to be bulk-random, and the shape equant herein. The armor and filter layer thicknesses were $2D_{n50}$ and $0.5D_{n50}$, respectively.

In conclusion, 69 data points were considered in the analysis, and Table 3.3 reports the main characteristics.

3.8. Processed database

The new database contains experimental measurements from tests conducted in deep, intermediate, and shallow water conditions, both with and without wave breaking on the foreshore, covering a diverse range of generated wave spectra (TMA, PM, JONSWAP, double). The database includes tests with narrow and wide armor stone gradations.

Stability formulae were compared with data for $500 < N_w < 5000$. Typically, a rectangular hydrograph is assumed for all tests, where all waves and the SWL in a series are constant. However, as N_w increases (say, more than 7000), a rectangular hydrograph becomes less and less valid. [65] demonstrated that this approach produced much more damage than a real storm hydrograph or a sequence of storms with varying SWL and waves. N_w for constant wave conditions is only reasonably accurate for the relatively short duration of the storm peak. Generally, damage transitions from nothing to $S_d > 1$ quite rapidly when stones start to be displaced. Initial stability is more uncertain and has different physics than damage progression. This research focuses on constant single storm wave and water level conditions. VML results are not directly comparable with the other experiments because the wave and water level conditions were not constant. However, VML measurements were still used

to highlight differences in the results. For design purposes, vdM introduced a damage classification for a classical rubble mound breakwater, distinguishing three different levels of damage based on the armor slope of the structure ($\cot\alpha$), as reported in Table 3.1. For example, ERDC researchers normally consider 3 limit states: initiation of failure, underlayer exposure and breaching when designing structures.

Table 3.1. Damage classification for a rubble mound breakwater [30].

Armor slope	Level of damage – $S_d = A_e/D_{n50}$		
	Initial	Intermediate	Failure (under layer visible)
1V:1.5H	2	3 to 5	8
1V:2H	2	4 to 6	8
1V:3H	2	6 to 9	12
1V:4H	3	8 to 12	17
1V:6H	3	8 to 12	17

In the new comprehensive database, only damage data falling within the range $1 \leq S_d \leq 1.5S_{\max}$, where S_{\max} is the proposed failure damage level indicated in Table 3.2, were selected for the analyses. This approach was adopted to reduce the uncertainty associated with too low and high damage values. Data for very low damage ($S_d < 1$) and complete failure of the armor layer when the underlayer became visible ($S_d > 1.5S_{\max}$) were not considered due to concerns about the reliability of measurements. The considered damage S is assumed for a $2D_{n50}$ thick armor layer.

Table 3.2. Damage range considered in the analysis.

Armor slope	S_{\max}	$1.5S_{\max}$
1V:1.5H	8	12
1V:2H	8	12
1V:3H	12	18
1V:4H	17	25.5
1V:6H	17	25.5

To ensure that viscous scale effects are negligible, the Reynolds number at the armor layer, calculated as in Eq. (12) should exceed a critical value typically set at $Re_{crit} = 3 \times 10^4$ [96, 97].

$$Re = \frac{\sqrt{gH_{1/3}} D_{n50}}{\nu} > Re_{crit} \quad Eq. (12)$$

Where $\nu = 1.1306 \times 10^{-6}$ m/s is the water kinematic viscosity and $\sqrt{gH_{1/3}}$ represents the characteristic velocity. VdM stated that the lower range of Reynolds numbers should be $1 \times 10^4 \leq Re \leq 4 \times 10^4$. These two conditions are met for all the selected data.

Table 3.3 and Table 3.4 present the model configuration and damage measurements for the selected datasets, forming the new comprehensive database in the present study. Although some characteristics of each study are unknown, such as certain structure and wave information, we assume in the analysis that the experimental data are generally comparable. It is important to note that in some cases, the absence of specific details may introduce considerable uncertainty in the comparison. Information missing regarding the structure, such as armor and filter thickness, stone shape, layer characteristics, and placement methods, may not significantly impact the comparison. The assumption is based on the understanding that most countries adhere to basic standards, and variations from laboratory to laboratory for generalized studies are typically small. Where the differences are deemed significant, the impacts will be discussed throughout this manuscript.

In our analysis, we make the following assumptions to standardize the comparison: bulk-random placement, stone shape assumed to be equant, armor layer thickness ranging from 2 to $2.25D_{n50}$, and a standard underlayer and core with no filter layers (armor placed directly on core) if no information is given for datasets with a permeable core. It is worth noting that the distinction between impermeable and permeable cores can lead to differences in the results.

However, variations in wave parameters will significantly impact the results. To achieve comparable wave parameters across datasets (TS, vdM, VML), waves are assumed to be Rayleigh distributed in deep water. The absent wave parameters in deep water and flat bottom were approximated as follows: $H_{m0}=H_s$, $H_{2\%}=1.4H_s$, and $T_{m-1,0}=1.1T_m$, assuming the standard conversion for Rayleigh-distributed wave conditions.

For instance, the negative first-moment spectral periods ($T_{m-1,0}$) were not initially published in TS and vdM manuscripts but were later reported in [54]. Spectral wave periods ($T_{m-1,0}=1.095T_m$) were derived by averaging 18 digitized, and probably smoothed, wave spectra from the original work and then generalized. While digitization may have introduced deviations and uncertainty from the actual spectra, the specific details were not provided. Moreover, assuming a fixed ratio instead of direct measurements introduces uncertainty. Another source of uncertainty is related to the wave parameters utilized in the analysis.

Incident mean wave period (T_m) and significant wave height (H_s) were reported as time domain values but were apparently determined using the reflection method of Goda and Suzuki, a spectral method. Thus, it is likely that there are secondary steps involved in generating an incident time series from the resolved incident wave spectrum, followed by conducting a zero-crossing time domain analysis. The computation details of the bulk wave parameters were not fully described in the thesis, contributing to the hydrodynamic uncertainty in the laboratory data.

However, real-time wave observations by [98] and numerical simulations by [71] revealed that the significant wave height measured from a zero-crossing analysis, $H_{1/3}$, may be 5% to 10% lower than the significant wave height estimated from the spectrum, H_{m0} . Goda [71] proposed $H_{1/3}=0.95H_{m0}$. For depth-limited wave conditions, the conversion from H_s to $H_{2\%}$ could be performed using the point model of Battjes and Groenendijk [60] but again is dependent on the details of the spectral shape which are unknown. It is important to possess all the information on the experiments without

relying on assumptions or speculations. However, the details are never fully reported and the impacts on armor stability are discussed in Chapter 5.

Table 3.3. Main model characteristics of the datasets.

Parameter	TS	vdM	VSK	VML
cot (α)	2 - 6	1.5 - 6	2, 4	1.5
cot (m)	Flat	Flat, 30	30, 100	Flat
Δ	1.70	0.92 – 2.05	1.65 – 1.75	1.70
D_{n85} / D_{n15}	2.24	1.25 – 2.25	1.4 - 2	1.31
$D_{n50,core} / D_{n50}$	0	0.0 – 1.0	0.0 – 0.45	0.24
S_d	≤ 17	≤ 24	≤ 26	≤ 10
P	0.1	0.1 – 0.6	0.1 – 0.5	0.45
LT	≤ 2	≤ 2	2.1	Not given
BLC (%)	Not given	50 – 60	Not given	Not given
Number of data	134	295	207	116

Parameter	MK	HGM	EUMER	Total
cot (α)	1.5, 2	1.5	2	1.5 - 6
cot (m)	20	50	30	Flat - 20
Δ	1.64, 1.66	1.68	1.574	0.92 – 2.05
D_{n85} / D_{n15}	1.05 – 1.59	1.14	1.20 – 1.28	1.05 – 2.25
$D_{n50,core} / D_{n50}$	0.15	0.21	0.22 – 0.72	0 - 1
S_d	≤ 12	≤ 12	≤ 20	≤ 26
P	0.5	0.4	0.4 – 0.5	0.1 – 0.6
LT	Not given	1.8	1.35 – 1.46	1.35 – 2.1
BLC (%)	Not given	42	35 – 45	35 – 60
Number of data	25	44	69	890

3.4. Main waves characteristics of the datasets¹⁰

Parameter	TS*	vdM*	VSK	VML*
N_w	1000, 3000	1000, 3000	492 - 5172	1000 - 5000
Spectral shape	PM	PM	JONSWAP (3.3), TMA, DOUBLE	TMA
$S_{m,deep}$	0.007 – 0.049	0.004 – 0.064	0.022 – 0.068	0.036 – 0.087
$S_{m-1,0,deep}$	0.009 – 0.046	0.006 – 0.06	0.023 – 0.056	0.029 – 0.072
$h / H_{m0,toe}$	4.84 – 26.29	1.38 – 17.35	0.35 – 5.60	3.23 – 9.96
$H_{m0,toe} / H_{m0,deep}$	1	1	0.22 – 1.06	1
$H_{2\%,toe} / H_{s,toe}$	1.40	1.40	1.162 – 1.432	1.40
$H_{m0,toe} / H_{s,toe}$	1	1	0.986 – 1.477	1
$T_{m-1,0,toe} / T_{m-1,0,deep}$	1	1	1.012 – 4.924	1
$T_{m,deep} / T_{m-1,0,deep}$	0.929 – 0.956	0.753 – 1.022	0.689 – 0.927	0.880
Number of data	134	295	207	116

Parameter	MK	HGM	EUMER	Total
N_w	1023 - 9455	1000	595 - 3826	492 - 9455
Spectral shape	TMA	JONSWAP (3.3)	JONSWAP (3.3)	PM, JONSWAP (3.3), TMA, DOUBLE
$S_{m,deep}$	Not given	0.022 – 0.059	0.030 – 0.061	0.004 – 0.087
$S_{m-1,0,deep}$	Not given	0.019 – 0.045	0.030 – 0.056	0.006 – 0.072
$h / H_{m0,toe}$	1.19 - 1.58	1.33 – 6.37	0.20 – 2.41	0.20 – 26.29
$H_{m0,toe} / H_{m0,deep}$	0.978 – 1.24	0.82 - 1.05	0.20 – 1.03	0.20 – 1.24
$H_{2\%,toe} / H_{s,toe}$	1.36 – 1.42	1.15 – 1.56	1.20 – 1.43	1.15 – 1.56
$H_{m0,toe} / H_{s,toe}$	1.04	0.905 – 1.086	0.892 – 1.109	0.892 – 1.477
$T_{m-1,0,toe} / T_{m-1,0,deep}$	Not given	0.613 – 0.976	0.996 – 3.404	0.61 – 4.92
$T_{m,deep} / T_{m-1,0,deep}$	Not given	0.739 – 0.916	0.86 – 0.93	0.689 – 1.02
Number of data	25	44	69	890

¹⁰ *Wave parameters $H_{m0}=H_s$, $H_{2\%}=1.4H_s$ and $T_{m-1,0}=1.1T_m$, derived assuming Rayleigh.

The present database was analyzed by separating deep, shallow, very shallow, and extremely shallow water conditions, following the classification outlined in the EurOtop manual [99] (Figure 3.1). The foreshore classification is detailed in Eq. (13) as presented by [100].

$h/H_{m0,deep} \geq 4$	Deep foreshore	<i>Eq. (13a)</i>
$1 \leq h/H_{m0,deep} < 4$	Shallow foreshore	<i>Eq. (13b)</i>
$0.3 < h/H_{m0,deep} < 1$	Very shallow foreshore	<i>Eq. (13c)</i>
$h/H_{m0,deep} \leq 0.3$	Extremely shallow foreshore	<i>Eq. (13d)</i>

Deep water is characterized by waves that do not shoal or break due to depth, although changes may occur due to factors such as bottom friction and refraction ($H_{m0}/H_{m0,deep} = 1$). In shallow water, waves may shoal and start to break. Typically, at $h/H_{m0,deep} = 1$, the deep water wave height has roughly broken down to half its original height. The spectral shape still maintains a resemblance to a single-peaked offshore spectrum, with minor second-order effects leading to increased energy at lower and higher frequencies. Very shallow water is where waves break further, and $T_{m-1,0}$ increases. Typical single-peaked offshore spectra may become flattened, form a second peak, or undergo a complete shift in wave energy from higher (wind sea) to lower frequencies. Wave height is reduced to 50% to 60% of the offshore wave height. The so-called infragravity (IG) waves are defined by wave energy at less than half the deep water peak frequency and may become enhanced in extremely shallow water. Generally, the transition between shallow and very shallow foreshores can be indicated as the point where the original total incident wave height, due to breaking, has significantly decreased. The wave height at a structure on a very shallow foreshore is much smaller than in deep water conditions.

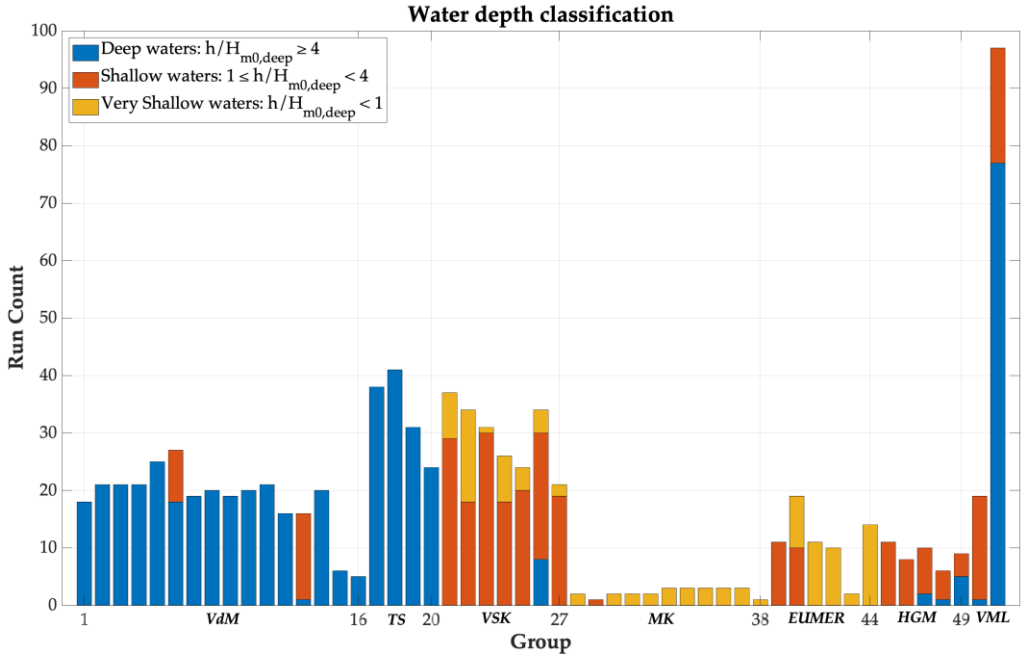


Figure 3.1. Histogram of the water depth classification.

In Figure 3.2 the following parameters are plotted against the relative depth at the toe of the structure:

- 1) Measured spectral wave steepness offshore ($s_{m-1,0,deep} = H_{m0,deep}/L_{m-1,0,deep}$), where the offshore wavelength was calculated using the linear dispersion relationship.
- 2) Relative wave height ($H_{m0,toe}/H_{m0,deep}$).
- 3) Ratio between the wave exceeded by 2% of the waves and the significant wave height in the time domain computed at the toe ($H_{2\%,toe}/H_{s,toe}$).
- 4) Relative wave period ($T_{m-1,0,toe}/T_{m-1,0,deep}$).

In Figure 3.2a, the plot illustrates $s_{m-1,0,deep}$ against the relative depth, indicating that the database encompasses sea (wind waves) and swell wave conditions. The VSK and EUMER datasets cover shallow and very shallow foreshore conditions but not low

steepness waves (swell waves). However, the vdM data supplement them by also covering smaller wave steepness, down to $s_{m-1,0,deep} = 0.01$, which can be considered as a limit for design conditions.

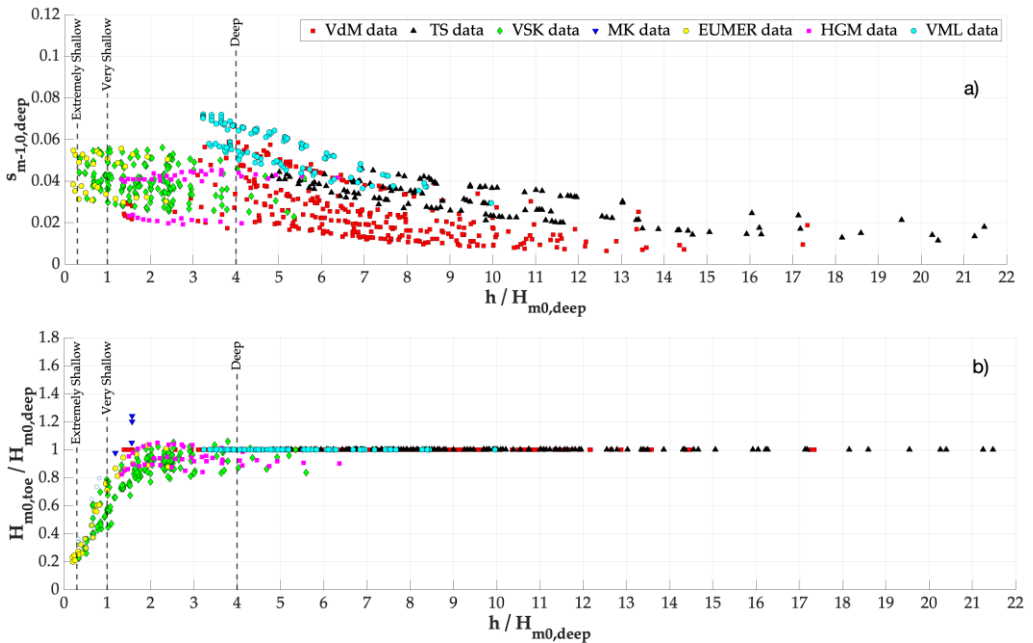
Moving to Figure 3.2b, the relative wave height ($H_{m0,toe}/H_{m0,deep}$) is plotted against the relative depth, revealing an exponential increase as the relative water depth rises. This exponential increase indicates the amount of wave breaking on the foreshore, as detailed in Eq. (14):

$$\begin{aligned} \frac{H_{m0,toe}}{H_{m0,deep}} < 0.7 & \quad \text{severe breaking} & \quad \text{Eq. (14a)} \\ 0.7 \leq \frac{H_{m0,toe}}{H_{m0,deep}} \leq 0.9 & \quad \text{breaking} & \quad \text{Eq. (14b)} \\ \frac{H_{m0,toe}}{H_{m0,deep}} > 0.9 & \quad \text{shoaling} & \quad \text{Eq. (14c)} \end{aligned}$$

in some tests conducted in relatively deep water conditions (EUMER and MK data), waves shoal on the foreshore before reaching the structure toe. However, for all the other tests, the wave height at the toe starts to decay for the lowest water level due to breaking processes occurring over the foreshore. The breaking process begins on the foreshore for $h/H_{m0,deep} < 3$. In extremely shallow water conditions, wave heights at the toe reach up to 20% of the deep water spectral wave height.

In Figure 3.2c, the relative wave period ($T_{m-1,0,toe}/T_{m-1,0,deep}$) is plotted against the relative depth. The trend is similar but inverse. IG waves in the flume are likely to significantly influence the wave parameters, especially $T_{m-1,0,toe}$. The spectral wave period at the toe also reaches four times those observed in deep water, indicating a bore with a flat wave spectrum propagating nearshore with energy saturated. This implies that almost all the energy in the peak area of the spectra has been dissipated due to wave breaking and nonlinear phenomena, but IG energy has significantly increased.

Finally, Figure 3.2d shows the ratio between the wave height exceeded by 2% of the waves and the significant wave height in the time domain computed at the toe ($H_{2\%,toe}/H_{s,toe}$) plotted against the relative depth. Generally, in deep water conditions where no breaking wave occurs, the wave height distribution can be assumed to be Rayleigh distributed, and this ratio is 1.4. However, as waves approach the foreshore and begin to break, $H_{2\%,toe}/H_{s,toe}$ decreases from 1.4 for deep water to 1.2 in shallow water. Eventually, for relative depth smaller than 0.3, namely extremely shallow water conditions, $H_{2\%,toe}/H_{s,toe}$ tends to increase again up to 1.4. These findings align with Goda's textbook [73].



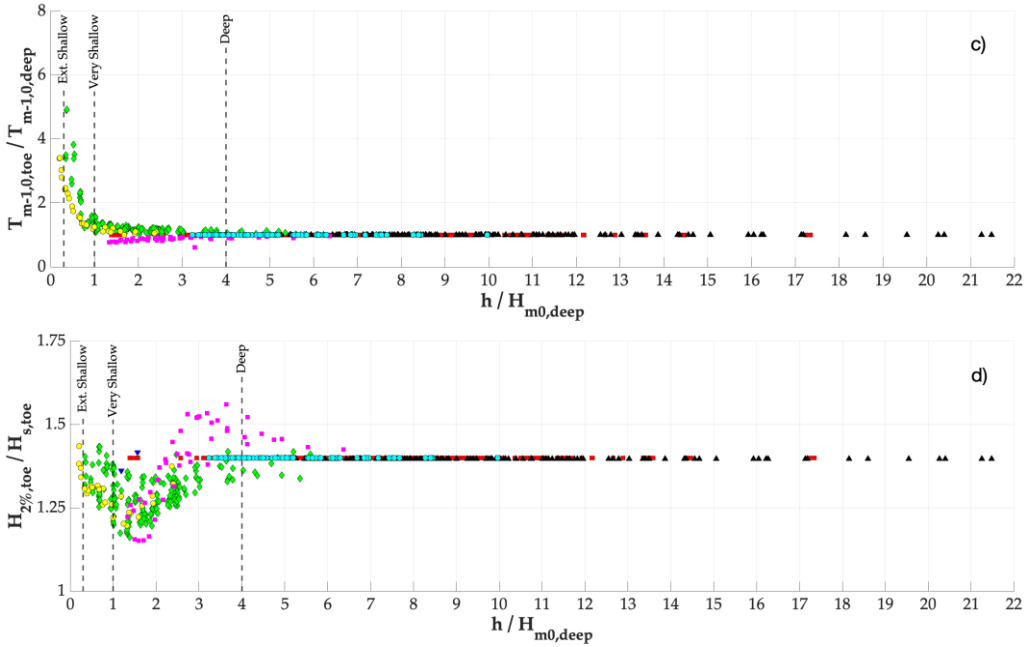


Figure 3.2. Wave characteristics of the database as a function of the relative depth.

3.9. Conclusions

This chapter delineates the process of gathering and synthesizing existing experimental stability data from the literature, leading to the formation of a comprehensive and unique database. The new database encompasses more than 800 data with varied waves and depth regimes from deep to very shallow and will be used for analyses in this thesis.

CHAPTER 4

Data analysis

4. Data analysis

Benefiting from the new extensive database, this chapter compares and discusses data within the framework of quantifying bias and uncertainty. Specifically, the armor stability equation based on wave momentum flux was refit using T_m and $T_{m-1,0}$, with test series separated and each dataset isolated. Finally, a comparison between the most widely used stability equations was conducted, illustrating strengths and weaknesses of the various empirical approaches for deep, shallow, and very shallow waters.

4.1. Physically based derivation of armor stability based on M_r

Armor stability on large coastal rubble mounds has historically been based on empirical equations relating armor stone movement resistance to wave forces. The interaction of wave-induced water motion with the resisting action of armor units in the cover layer becomes highly intricate when wind waves impact an existing rubble mound structure. The resulting forces and their interplay involve a complex scenario. Waves striking the structure can lead to complete wave breaking, projecting a water jet approximately perpendicular to the slope. Alternatively, waves may break partially with a poorly defined jet, or establish an oscillatory motion of the water particles along the structure slope, resembling the motion of a clapotis at a vertical wall. When wind waves impinge on a rubble mound structure, dynamic forces develop, tending to lift and roll the armor units from the structure slopes. These forces comprise a drag force and an inertia force.

Figure 4.1 depicts a representative free-body diagram for the incipient motion of an armor stone. Stone movement is caused by the fluid force (F_w) resulting from the incident wave, while its resistance comes from buoyant self-weight, interlocking between stones, and friction between neighboring stones. F_w can be decomposed into a structure normal force (F_N) and parallel force (F_p). Individual stones can be generally displaced by various mechanisms, including sliding, rolling, lifting, or some combinations of these actions. Consequently, the relationship between stable stone size (D_{n50}), structure slope (α), angle of repose (ϕ), and wave steepness (s) is intricate and varies across the armor layer and construction technique.

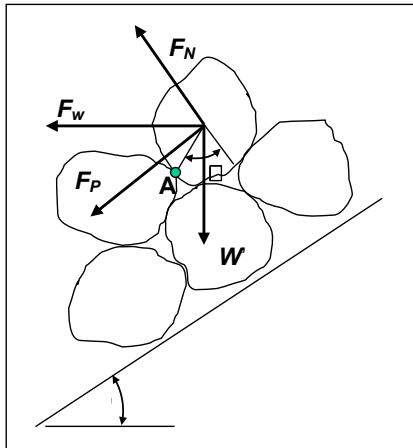


Figure 4.1. Schematic free-body diagram of primary forces influencing stone stability (source: [64]).

[64] noted that nearshore bathymetry plays a significant role in influencing wave forces. Furthermore, wave run-up and run-down on the structure are influenced by its geometry. Hence, the local water depth (h), structure slope (α), and nearshore slope (m) collectively influence wave forces (F_w) on the structure, with this influence being dependent on wave period and wave height (wave steepness).

To determine a physically based stability formula, the free-body diagram was solved to deduce the incipient displacement. The following analyses, taken from [64], specifically

focus on displacement of seaside armor stone on a conventional multi-layer trapezoidal rubble mound subjected to a normally incident wave. The armor stone is assumed to be uniform and composed of angular randomly placed stone armor, with little to no wave overtopping considered.

Instability is conceptualized through three distinct contributions:

- Instability normal to structure slope (Hudson failure): this refers to the potential instability arising perpendicular to the structure slope.
- Instability due to rolling: this pertains to the instability introduced by the rolling motion of the stones.
- Instability due to sliding: this involves instability resulting from the sliding motion of the stones.

These considerations aim to provide a comprehensive understanding of the factors influencing stability and potential failure modes in the context of wave forces acting on the structure.

4.1.1. Instability normal to structure slope (Hudson failure)

The wave force component normal to the structure seaward, F_N , can lift armor units out of the slope, as described by Hudson [46] and [101]. The incipient motion normal condition to the structure face is expressed by Eq. (15a):

$$\sum F_{\text{Normal}} = F_N + W' \cos \alpha + F_c = 0 \quad \text{Eq. (15a)}$$

where F_c is the resisting frictional force mobilized normal to the slope surface, and W' is the submerged weight (see, Figure 4.1). An empirical constant, K_r , is introduced to account for parameters not included in the above relation, such as stone angularity or shape, surface friction, and stone interlocking. F_c is incorporated into this empirical

constant. The normal force component produced by the wave is $F_w \sin \alpha$. Therefore, the incipient motion free-body equation normal to the armor slope becomes Eq.(15b).

$$F_N = F_w \sin \alpha = K_r W' \cos \alpha \quad \text{Eq. (15b)}$$

At this point, depending on the selected proportionality, it is feasible to derive either the stability number based on drag force (N_s) or the stability number based on wave momentum flux (N_m).

4.1.1.1. *Instability normal to structure slope based on drag force*

Starting from Eq. (15b), and noting that the submerged armor weight is given by $W' = (\gamma_r - \gamma_w)V = (\gamma_r - \gamma_w)D_{n50}^3$ and the drag force can be represented in terms of fluid velocity ($F_w \propto \rho_w Av^2$), yields Eq (15c):

$$\rho_w Av^2 \sin \alpha = K_r (\gamma_r - \gamma_w) D_{n50}^3 \cos \alpha \quad \text{Eq. (15c)}$$

where v represents the velocity of the water flowing around or impinging on the armor units in the cover layer, also known as Froude velocity, and A is the projected area of the armor unit perpendicular to the velocity ($\propto D^2$). Assuming that the Froude velocity is proportional to the wave height on the slope ($v \propto \sqrt{gH}$) yields Eq. (15d):

$$\rho_w Av^2 \sin \alpha = K_r (\gamma_r - \gamma_w) D_{n50}^3 \cos \alpha \quad \text{Eq. (15d)}$$

simplifying further:

$$\begin{aligned} \rho_w D_{n50}^2 gH \sin \alpha &= K_r (\gamma_r - \gamma_w) D_{n50}^3 \cos \alpha \\ \gamma_w D_{n50}^2 H \sin \alpha &= K_r (\gamma_r - \gamma_w) D_{n50}^3 \cos \alpha \end{aligned}$$

Finally, Eq. (15d) can be rearranged to form the drag force stability number (N_s), as shown in Eq. (15e), where $S_r = \gamma_r / \gamma_w$.

$$N_s = \frac{H}{(S_r - 1)D_{n50}} = K_r \cot \alpha \quad \text{Eq. (15e)}$$

4.1.1.2. *Instability normal to structure slope based on M_f*

Similarly, assuming that the wave force is proportional to the maximum wave momentum flux per unit width times the armor stone width ($F_w \propto (M_f)_{\max} D_{n50}$), yields Eq. (15f):

$$K_m (M_f)_{\max} D_{n50} \sin \alpha = K_r (\gamma_r - \gamma_w) D_{n50}^3 \cos \alpha \quad \text{Eq. (15f)}$$

where K_m is a constant of proportionality, γ_r is the specific weight of the stone, and γ_w is the specific weight of water. Eq. (15f) can be rearranged to form a momentum-flux-based stability number, as shown in Eq. (15g):

$$N_m = \left(\frac{K_m [(M_f)_{\max} / \gamma_w h^2] h^2}{(S_r - 1)} \right)^{1/2} \frac{1}{D_{n50}} = (K_r \cot \alpha)^{1/2} \quad \text{Eq. (15g)}$$

This formulation can be compared to the Hudson equation in form of W_{50} , and this is why it is also referred to as Hudson failure.

4.1.2. *Instability due to rolling*

Rolling failure is described by summing moments in the contact point A for downward incipient rolling, as depicted in Figure 4.1. This is expressed in Eq. (16a):

$$\sum M_A = K D_{n50} [F_N \sin \phi + F_P \cos \phi - W' \sin (\phi - \alpha)] = 0 \quad \text{Eq. (16a)}$$

Summing the forces normal to the structure slope and assuming F_w is proportional to $(M_f)_{\max} D_{n50}$ as before, we obtain Eqs. (16b,c).

$$F_N = F_w \sin \alpha = K_m M_{\max} D_{n50} \sin \alpha \quad \text{Eq. (16b)}$$

$$F_P = F_w \cos \alpha = K_m M_{\max} D_{n50} \cos \alpha \quad \text{Eq. (16c)}$$

Combining Eq. (16b) and Eq. (16c) and rearranging as before yields Eq. (16d):

$$N_m = \left(\frac{K_m [(M_f)_{\max} / \gamma_w h^2] h^2}{(S_r - 1)} \right)^{1/2} \frac{1}{D_n} = \left(K_r \frac{\tan \phi \cos \alpha - \sin \alpha}{\tan \phi \sin \alpha - \cos \alpha} \right)^{1/2} \quad \text{Eq. (16d)}$$

4.1.3. Instability due to sliding

The sliding failure is analogous to a rolling failure and is determined by summing forces parallel to the structure slope, as expressed in Eq. (17a).

$$F_P - W' \sin \alpha = \tan \phi (W' \cos \alpha - F_N) \quad \text{Eq. (17a)}$$

Again, assuming the wave force is proportional to the maximum wave momentum flux and substituting for submerged weight and nominal size yields Eq. (17b).

$$K_m M_{f_{\max}} D_{n50} (\tan \phi \sin \alpha + \cos \alpha) = K_r (\gamma_r - \gamma_w) D_{n50}^3 (\tan \phi \cos \alpha + \sin \alpha) \quad \text{Eq. (17b)}$$

After some rearranging, the stability relation becomes Eq. (17c):

$$N_m = \left(\frac{K_m [(M_f)_{\max} / \gamma_w h^2] h^2}{(S_r - 1)} \right)^{1/2} \frac{1}{D_n} = \left(K_r \frac{\tan \phi \cos \alpha + \sin \alpha}{\tan \phi \sin \alpha + \cos \alpha} \right)^{1/2} \quad \text{Eq. (17c)}$$

4.1.4. Generalized stability

The stability number equations (Eqs. (15d, 16d, 17c)) share the same form. Although derived from different failure criteria, they differ only in the parametrization of the structure slope and angle of internal friction terms. It is asserted that the angle of internal friction does not vary significantly in coastal structures. Additionally, stone interlocking and friction are assumed to be included in K_r . As the probabilities of lifting, rolling, and sliding are not known a priori and are likely highly dependent on individual wave characteristics and stone boundary conditions, it was reasonable, at the time, to combine K_r and K_m to form a single parameter K_a , incorporating random effects from stone interlocking, slight changes in the angle of internal friction, and the various ways a stone can be stabilized.

Given these assumptions, a generalized stability equation in terms of stability number based on the maximum nondimensional wave momentum flux (N_m) was expressed as Eq. (18):

$$N_m = \left(\frac{K_a [(M_f)_{\max} / \gamma_w h^2]}{(S_r - 1)} \right)^{1/2} \frac{h}{D_{n50}} = f(\alpha, P, S_d, N_w, s) \quad \text{Eq. (18)}$$

where P is the notional permeability factor, $S_d = A_e / D_{n50}^2$ is the normalized eroded area, A_e is the eroded cross-sectional area, $N_w = t_r / T_m$ is the number of waves at the mean period during the event of duration t_r , T_m is the mean wave period, and s is the wave steepness. The momentum-flux-based stability equation was derived from basic principles and is expected to illustrate the wave-structure interaction better than

previous stability relations based on the traditional stability number of Hudson [46] and van der Meer [30], where $N_s = H_s / \Delta D_{n50}$ is used. The most remarkable difference is the inclusion of a maximum momentum-flux-based wave force derived from first principles. N_s and N_m differ only in the parameterization of the maximum wave force and, therefore, differ by only the maximum wave momentum flux, including the local water depth in the formulation.

4.2. Wave momentum flux derivation

The wave momentum flux (M_f) is an appropriate parameter for describing the wave force on a fixed object like a coastal structure. [66] developed a relation for the maximum normalized wave momentum flux and suggested its utility for analyzing rubble mound structures.

Assuming irrotational potential flow on a locally flat bottom in water depth h , the wave-averaged and depth-integrated radiation stress (S_{xx}) is given by Eq. (19a):

$$S_{xx} = \frac{1}{L} \int_0^L \int_{-h}^{\eta_x} (\rho_d + \rho_w u^2) dz dx \quad \text{Eq. (19a)}$$

where L is the wavelength, η_x is the free surface elevation location, ρ_d is the dynamic pressure, ρ_w is the fluid density, u is the velocity in the x -direction, x is the horizontal coordinate, and z is the vertical coordinate. The maximum depth-integrated wave momentum flux is given at the wave crest as in Eq. (19b).

$$(M_f)_{\max} = \int_{-h}^{\eta_x} (\rho_d + \rho_w u^2) dz \quad \text{Eq. (19b)}$$

Using linear wave theory (LWT) values for u and ρ_d yields to Eq. (19c):

$$\left(\frac{(M_f)_{\max}}{\gamma_w h^2} \right)_{\max} = \frac{1}{2} \frac{H \tanh kh}{h} + \frac{1}{8} \left(\frac{H}{h} \right)^2 \left[1 + \frac{2kh}{\sinh 2kh} \right] \quad \text{Eq. (19c)}$$

where g is the acceleration of gravity, H is the incident wave height, and $k=2\pi/L$ is the wave number. Eq. (19c) assumes waves to be periodic and sinusoidal. However, in shallow water, waves are nonlinear and exhibit peaked crests and shallow troughs. Wave forces from these nonlinear waves can differ significantly from those resulting from linear waves. Eq. (19c) will underpredict the wave momentum under a nonlinear wave crest. In Eq. (19c), the first term on the right-hand side is the dynamic pressure term (ρ_d), while the second is the velocity term ($\rho_w u^2$). In general, the pressure term dominates. It is argued that the velocity term will only contribute 5 percent to the maximum momentum flux for low-steepness waves. For waves in shallow water at the steepness limit, the velocity term will provide the maximum contribution, roughly 30 percent of the momentum flux. However, the maximum wave momentum flux is highly nonlinear for nonlinear and steep waves in shallow waters. The maximum wave momentum flux increases rapidly for nonlinear waves, corresponding to the case where armor stability is at its minimum. Therefore, Hughes [66] approximated the nonlinear wave momentum flux using numerical Fourier solutions and provided an empirical equation to determine it (Eq. (6), see Chapter 2) (Figure 4.2).

The nonlinear approximation is crucial because armor stone stability is at a minimum when the incident wave is the most nonlinear. However, potential flow theory is only approximate for breaking waves, and such an approximation introduces significant errors. As $\frac{M_f}{\rho g h^2} > 0.1$, nonlinearity increases and must be considered. The nonlinear approximation results in:

- An error of roughly 10% if $\frac{M_f}{\rho g h^2} \cong 0.2$

- An error of roughly 100% if $\frac{M_f}{\rho g h^2} \cong 0.8$ (typical for breaking wave conditions over a wide surf zone)

The actual wave momentum flux force that a particular armor unit is exposed to will vary from the value given by Eq. (6) due to errors in the numerical approximation, effects of the sloping foreshore, effects of the structure geometry on the wave momentum, armor unit position in the water column, and armor unit extent of the water column. The maximum normalized wave momentum flux could be approximated for irregular waves given the spectral wave height (H_{m0}), the mean wave period (T_m), and the local water depth (h) at the toe of the structure. The author found no noticeable differences if T_p or T_m was used.

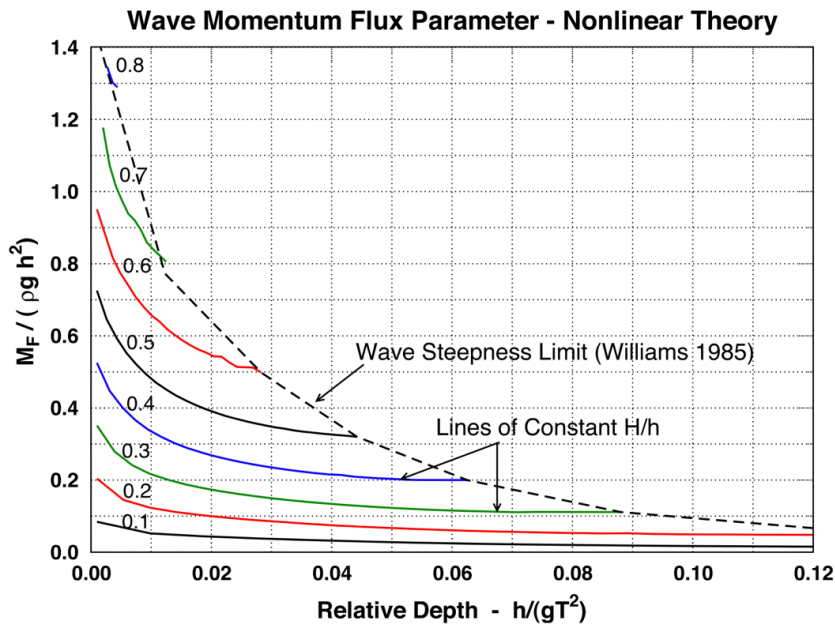


Figure 4.2. Dimensionless wave momentum flux versus h/gT^2 (source: [66]).

4.2.1. Stability equations based M_f with the new database

The stability formula proposed by [64], and subsequently updated by [65], is expressed in general terms in Eq. (20):

$$N_m = \left(\frac{(M_f)_{\max}}{\gamma_w h^2} \frac{K_a}{\Delta} \right)^{1/2} \frac{h}{D_{n50}} \quad \text{Eq. (20a)}$$

$$N_m = K_{m1} \left(S_d / \sqrt{N_w} \right)^{0.2} P^{0.18} \sqrt{\cot \alpha} \quad s_m \geq s_{m,c} \quad \text{Eq. (20b)}$$

$$N_m = K_{m2} \left(S_d / \sqrt{N_w} \right)^{0.2} P^{0.18} (\cot \alpha)^{0.5-P} s_m^{-P/3} \quad s_m < s_{m,c} \quad \text{Eq. (20c)}$$

where K_{m1} and K_{m2} are regression coefficients for plunging (Eq. (20b)) and surging (Eq. (20c)) waves, fitted to small-scale laboratory data. The critical wave steepness ($s_{m,c}$) is determined by setting Eq. (20b) equal to Eq. (20c) and solving for s_m (Eq. (20d)).

$$s_{m,c} = \cot \alpha^{-3} \quad \text{Eq. (20d)}$$

[65] calibrated the stability formulae only using vdM data in mostly nonbreaking waves and relatively deep water conditions, finding $K_{m1}=5$ and $K_{m2}=5$. vdM data show $\frac{M_f}{\rho g h^2} \leq 0.2$, where the dynamic pressure term dominates over the velocity term. The velocity effect is generally more substantial for breaking waves, but vdM conducted very few tests in that condition. More data in shallow waters are required to refit the equations and generalize and validate Eq. (20) for all water depth conditions. Nevertheless, the M_f approach shows considerable advantages compared to other formulations introduced in Chapter 2:

- 1) Derived from basic principles and more physically based
- 2) Uses the maximum depth-integrated wave momentum flux to characterize wave forces on the structure

- 3) Explicitly incorporates water depth h at the toe of the structure
- 4) Expected to be valid for all water depth conditions.

[64] sought a more physical (analytical) description of the stone displacement mechanism on coastal structures attacked by waves, capable of directly relating incident wave forces to the stone movement. Plunging waves should produce direct proportionality because there is more energy absorption and dissipation during the wave-structure interaction. Surging is more complex because run-down may cause instability. If the slope is porous, stability highly depends on how the waves run-up and -down the structure, even though one may think it would be the other way around because velocities are generally higher on a less permeable slope.

4.2.2. M_f stability equations refitting

Given the new comprehensive database, Eq. (20) was refitted, and the regression coefficients K_{m1} and K_{m2} were computed as the mean value of the probability distribution of the error obtained by the difference between the predicted and measured stability numbers. K_{m1} and K_{m2} were calculated for $N_w=1000$, $N_w=3000$, and all damage data according to plunging and surging waves. Results are plotted in Figure 4.3.

The regression coefficients exhibit different variations when obtained by refitting only $N_w=1000$ data or only $N_w=3000$ data. Specifically, for $N_w=1000$, $K_{m1}=4.79$ (std=0.541) and $K_{m2}=4.52$ (std=0.667), whereas for $N_w=3000$, $K_{m1}=5.07$ (std=0.441) and $K_{m2}=4.78$ (std=0.806). This indicates that the mean of the error (bias) does not change significantly due to storm duration (despite being larger for $N_w=3000$), contrary to the standard deviation of the error (uncertainty) for surging waves, which is considerably larger for $N_w=3000$.

Finally, refitting the coefficients using all damage data resulted in $K_{m1}=4.93$ (std=0.522) and $K_{m2}=4.65$ (std=0.806), which are smaller than $K_{m1}=K_{m2}=5$ obtained by the authors using only vdM data. Overall, the plunging equation experiences much

less uncertainty (std=0.522) compared to the surging equation (std=0.806), indicating that the surging equation less adequately captures the physics.

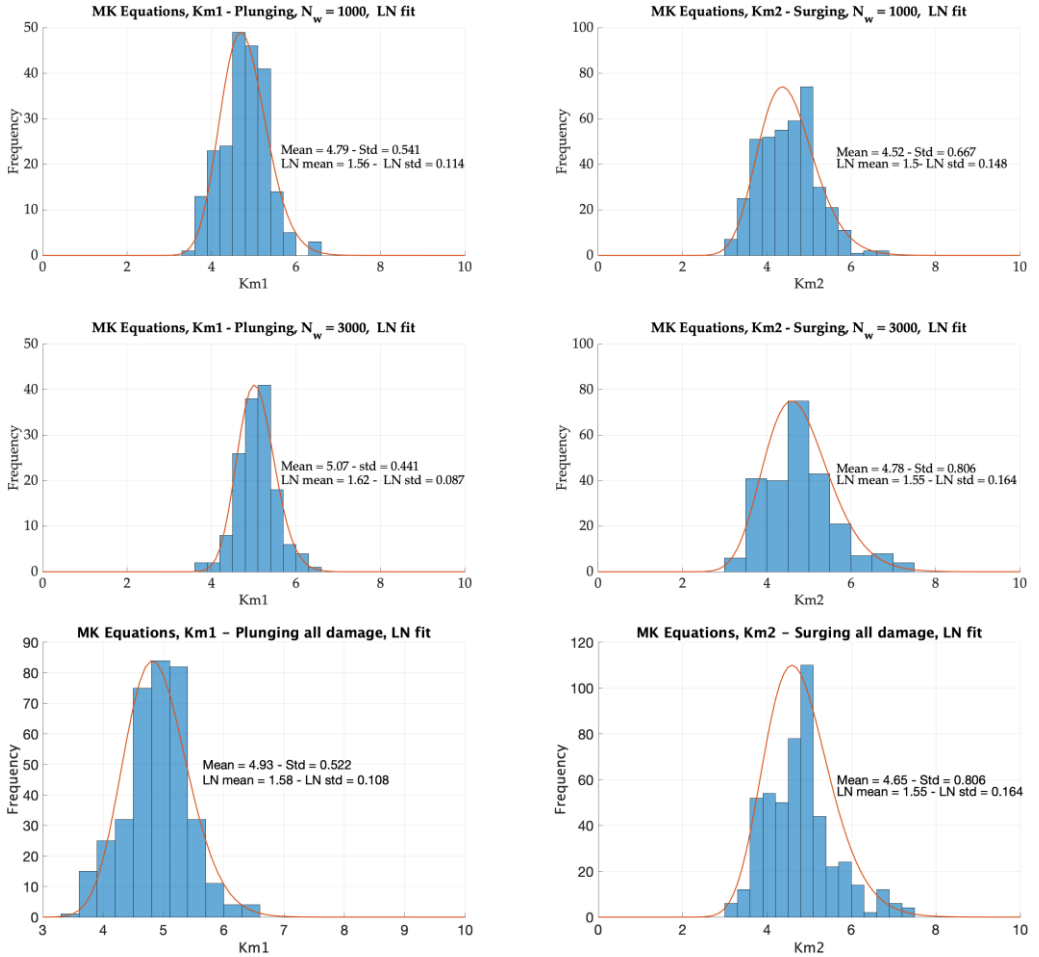


Figure 4.3. Plunging (K_{m1}) and surging (K_{m2}) regression coefficients computed for $N_w = 1000$, $N_w = 3000$ and all damage data.

Using the new coefficients, Figure 4.4 illustrates the refitted Eq. (20), where the mean wave steepness computed at the toe of the structure ($s_m = H_{m0}/L_m^{11}$) and the normalized stability number (N_m), are reported on the x -axis and y -axis, respectively. Data appear to be clustered, showing specific trends for each laboratory experiment. Bias and high uncertainty are evident in the scattering of the data.

Stability equations, in terms of predicted vs. measured stability numbers (N_m) and damage (S_d , in log scale), are also depicted in Figure 4.5. Damage prediction is more uncertain compared to the stability number.

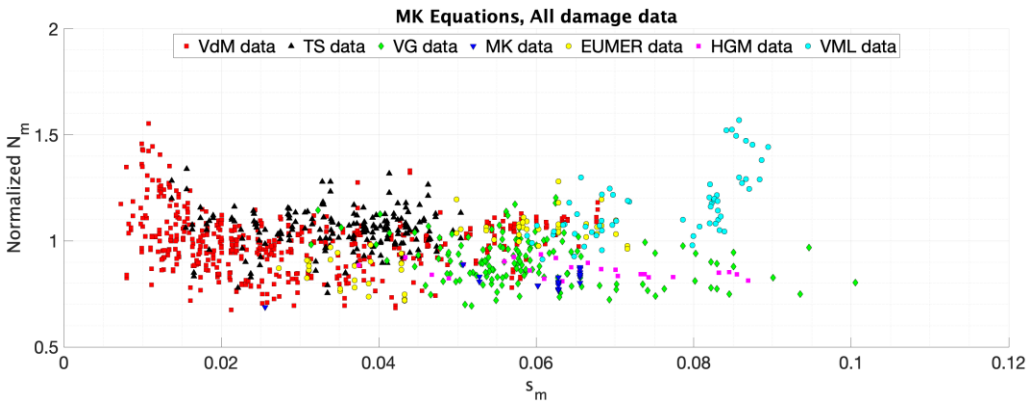


Figure 4.4. M_f refitted stability equations.

¹¹ L_m calculated using the linear dispersion relationship considering the local water level (h) and the mean wave period at the toe of the breakwater (T_m) as $L_m = \frac{gT_m^2}{2\pi} \tanh\left(\frac{2\pi h}{L_m}\right)$

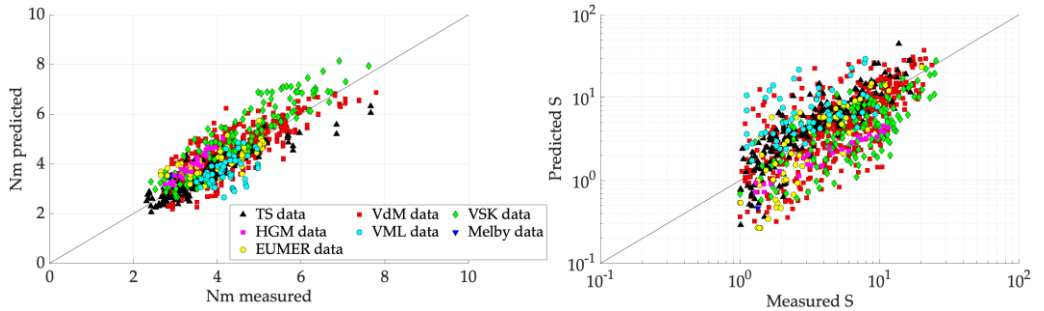


Figure 4.5. Measured vs predicted N_m and S_d .

4.2.3. Test series separation

The refitting of the M_r stability equation, considering the new extensive database, demonstrated a good general performance, although high uncertainty persists in the prediction. To investigate possible reasons for bias and uncertainty, each test series (51 groups) was analyzed and plotted separately in terms of N_m using the newly refitted coefficients ($K_{m1}=4.93$ and $K_{m2}=4.65$). Data were classified into plunge and surge waves according to the breaking criterion adopted by ERDC researchers (Eq. 20d) as reported in Figure 4.6. Groups were named from 1 to 51. This classification aims to identify sources of uncertainty and categorize data based on their specificity, such as permeability, structure slope, shallowness condition, breaking type, etc.

Specifically, Figure 4.7, Figure 4.8, Figure 4.9, Figure 4.10, Figure 4.11 and Figure 4.12 illustrate the comparison between measured vs predicted N_m for each test group series corresponding to vdM, TS, VSK and MK, EUMER, HGM and VML data, respectively. Filled markers represent $N_w=3000$, while open markers represent $N_w=1000$, emphasizing potential differences induced by the storm duration. For the subsequent discussion, structure slopes with $\cot \alpha < 4$ are considered steep slopes, whereas $\cot \alpha \geq 4$ are regarded as mild slopes.

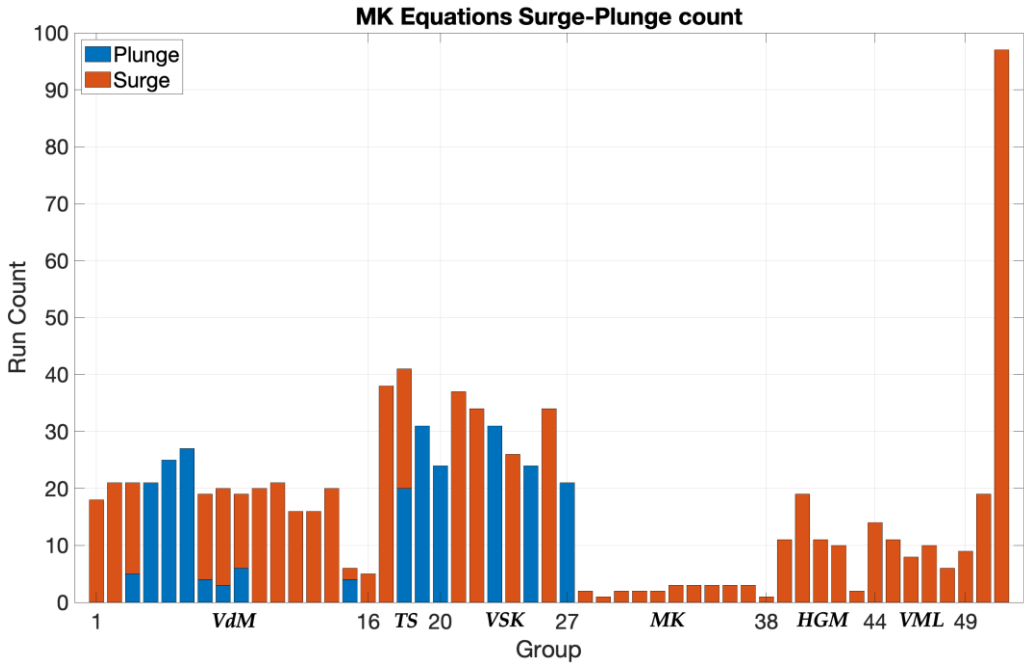


Figure 4.6. Data separation in plunge and surge breaking conditions according to Eq. (20d).

Figure 4.7 displays the results of the stability equation separated into individual groups for the vdM dataset, revealing that:

- 1) N_m tends to bias low (groups 1, 2, 3 – nearly all surge) for steeper impermeable slope.
- 2) N_m tends to bias high (groups 10, 11, 12, 13, 14 – all surge) for steeper permeable slope and shallow waters.

In conclusion, biases are observed for some surge cases and shallow waters but not for plunge cases. Virtually all these tests were conducted in deep water. The plunging equation proves to be more accurate than the surging equation, especially when describing permeability and structure slope. Most series exhibit consistent scatter and bias and trend. If there is a bias, it appears to be consistent for an entire series. In this

dataset, scatter remains consistent across each series, whereas trends are generally favorable, except for G06 (mild impermeable slopes $\cot\alpha=6$).

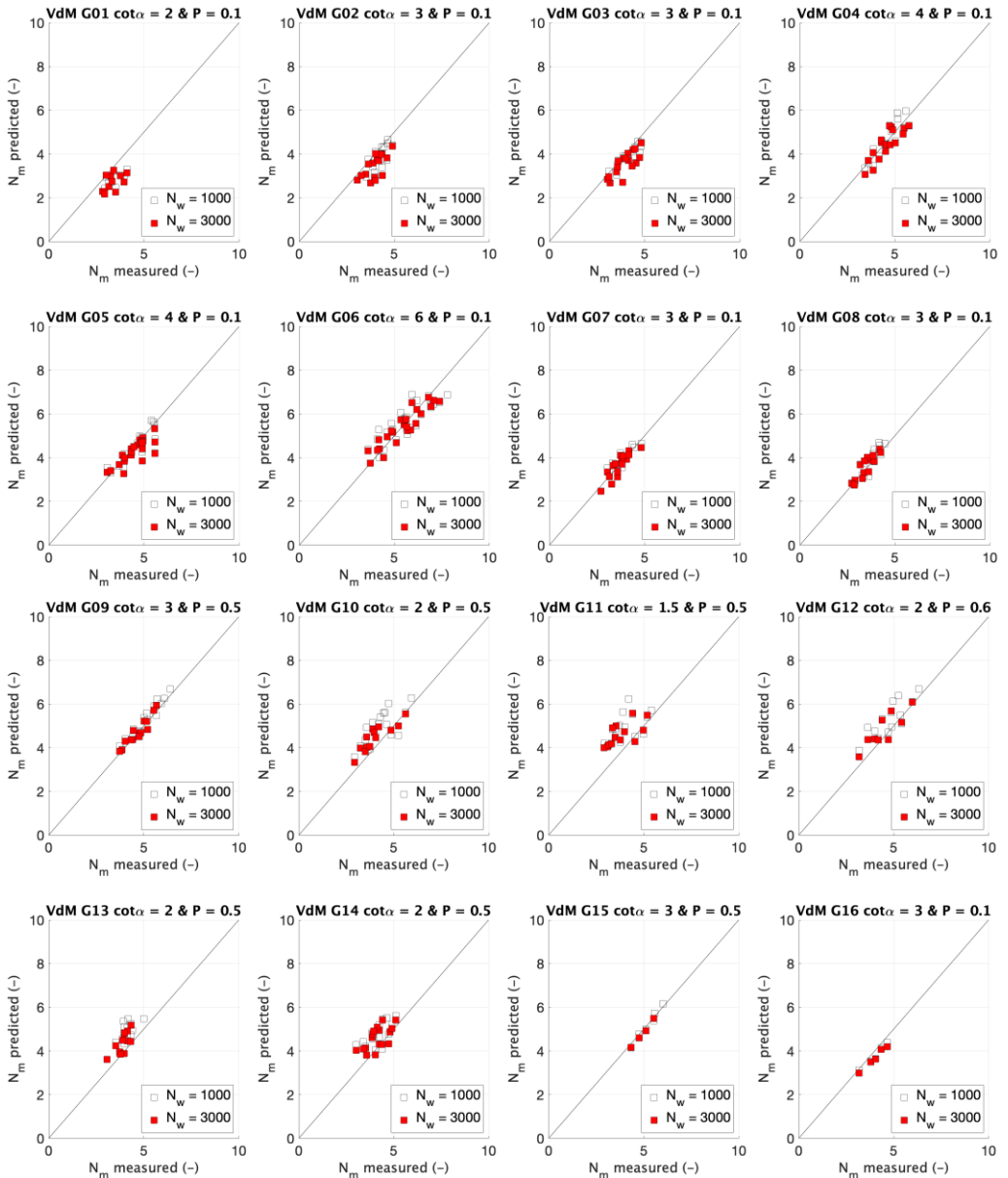


Figure 4.7. Measured vs. predicted N_m for vdM test series.

Similarly, Figure 4.8 shows the results of the stability equation separated into individual groups for the TS dataset, revealing that:

- 1) N_m tends to bias low (group 17 – surge) for steeper impermeable slope.
- 2) N_m exhibits higher uncertainty (groups 19, 20 – all plunge) for milder impermeable slope.

All these tests were in deep water. In conclusion, impermeable structures appeared biased for some surge cases and highly uncertain for plunging cases for milder structure slopes. Once again, all series show similar consistent scatter, bias, and trend, except for TS04, where a different trend is observed. Similarly, a different trend is found for mild impermeable slopes ($\cot\alpha=6$ and $P=0.1$) in this condition.

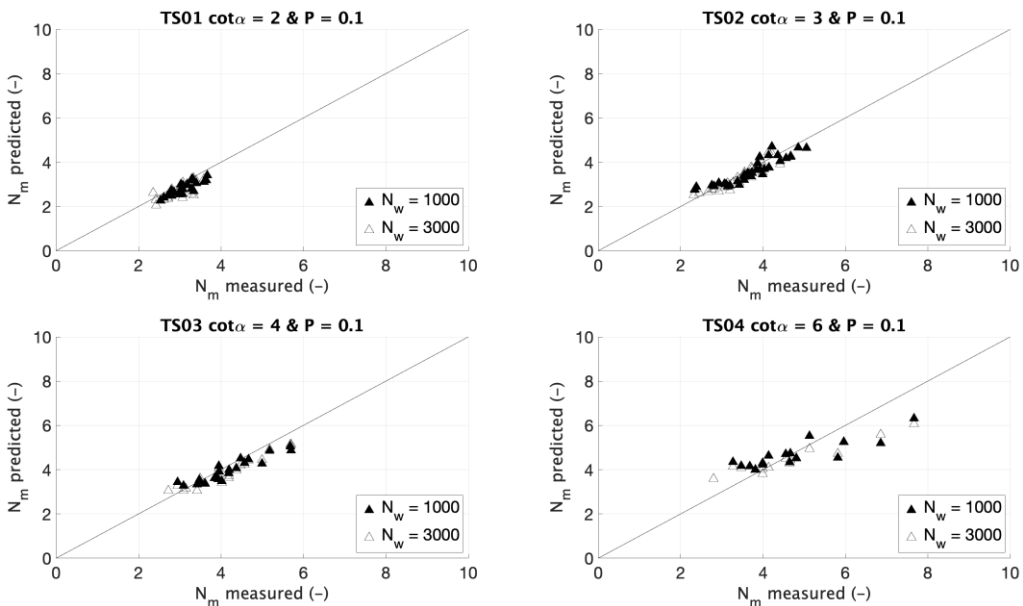


Figure 4.8. Measured vs. predicted N_m for TS test series.

Figure 4.9 illustrates the results of the stability equation separated into individual groups for the VSK and MK datasets. The following observations were made:

- 1) N_m is well predicted (groups 26, 27 – plunge and surge) for steeper impermeable slopes with surge breaking but biases high for milder slopes with plunging breaking.
- 2) N_m biases high (groups 23, 24, 25, 28 and 29 – plunge and surge) for steeper permeable slopes.
- 3) N_m is accurately predicted (groups 21 and 22 - surge) for steeper permeable slopes with surging breaking.

In conclusion, bias occurs for both surge and plunge cases in shallow water conditions. Impermeable slopes are well predicted, whereas permeable slopes are highly biased, indicating that a reformulation related to permeability would be required. Here, no issues with trend are found, only scatter and bias. However, it must be stated that the VSK and MK datasets do not have data with mild slopes.

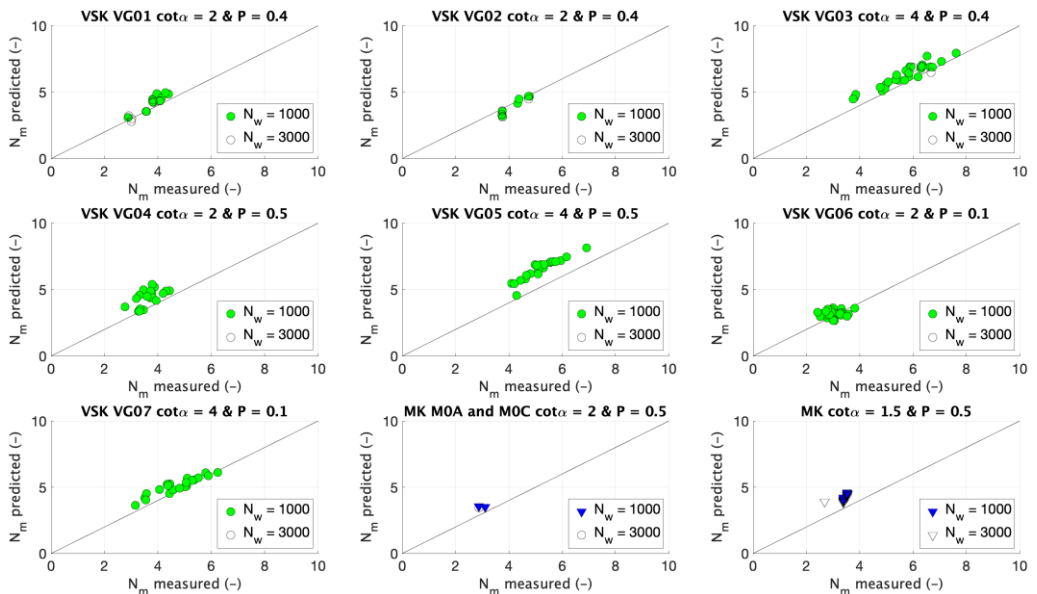


Figure 4.9. Measured vs predicted N_m for VSK and MK test series.

Figure 4.10 illustrates the results of the stability equation separated into individual groups for the EUMER dataset. EUMER data are all surge and in shallow waters except

for group 30 (WL1) in intermediate waters. Groups 34 and 35 are not reported because the data are out of the damage range discussed in Table 3.2 The following observations were made:

- 1) N_m is well predicted in relatively deep water conditions (group 30 - surge) for steeper permeable slopes.
- 2) N_m biases low (group 31 – surge) for steeper permeable slopes in shallow waters.
- 3) N_m biases high (groups 32, 33 - surge) for steeper permeable slopes in very shallow waters.

In conclusion, bias occurs in shallow water conditions and permeable slopes. Very shallow waters appeared to be highly biased and uncertain, indicating that a reformulation related to the water depth classification and permeability is required.

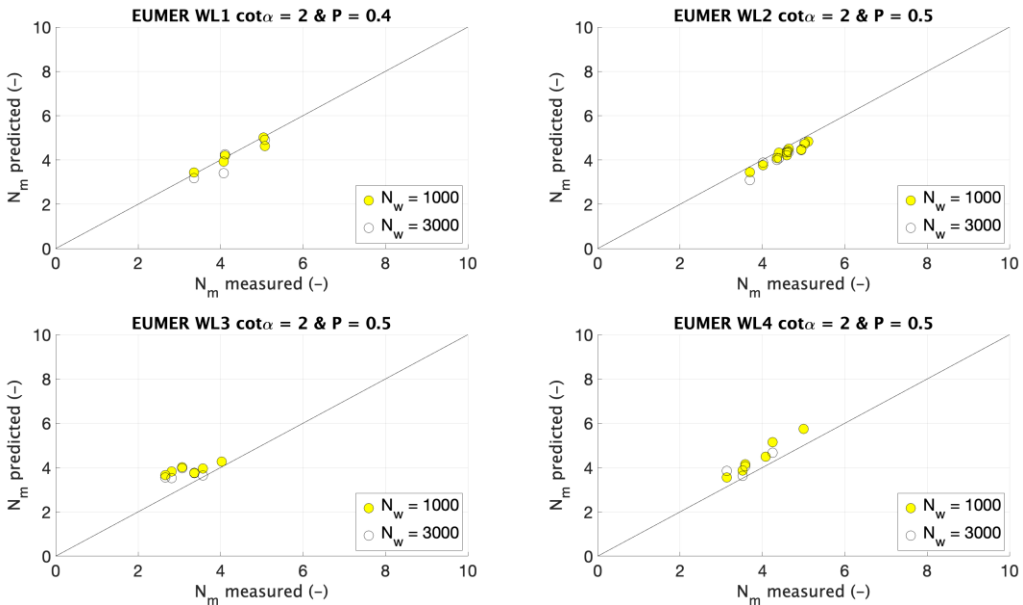


Figure 4.10. Measured vs. predicted N_m for EUMER test series.

Figure 4.11 illustrates the results of the stability equation separated into individual groups for the HGM dataset. HGM data are in shallow waters with a constant structure geometry ($\cot \alpha = 2$, $P = 0.4$). However, this dataset is not consistent with other experiments due to a different method (virtual net method) used to estimate the damage value S_d (see Section 3.6). N_m is systematically biased high for all tests for steeper permeable slopes with surging breaking waves. This observation aligns with EUMER data. However, it is very complex to separate different bias contributions due to non-homogeneity in the damage analysis procedure. Here, the plots suggest both bias and trend that are different from other experiments.

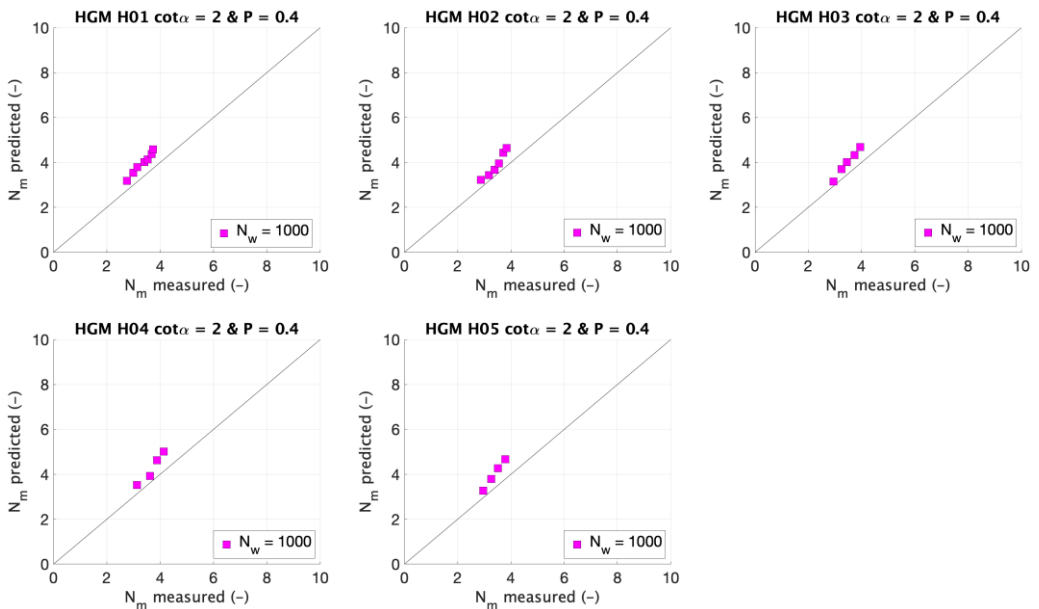


Figure 4.11. Measured vs. predicted N_m for HGM test series.

Figure 4.12 illustrates the results of the stability equation separated into individual groups for the VML dataset. VML data were carried out in relatively deep water conditions and flat bottoms. Data are divided into two groups: (i) Long tests (group 50) and (ii) short tests (group 51) and were performed modeling a storm with sequential storms with varying hazards (see Section 3.4). Tests are all in surging breaking waves,

but structure permeability and damage were estimated differently from the other datasets. The following considerations were deduced:

- 1) N_m is highly biased low for the long tests
- 2) N_m is slightly biased low for short tests ($N_w = 1000$).

In conclusion, such data are not consistent with the others and should be disregarded to better understand the physics of the stability equations because of the increasing amount of uncertainty in the formulations.

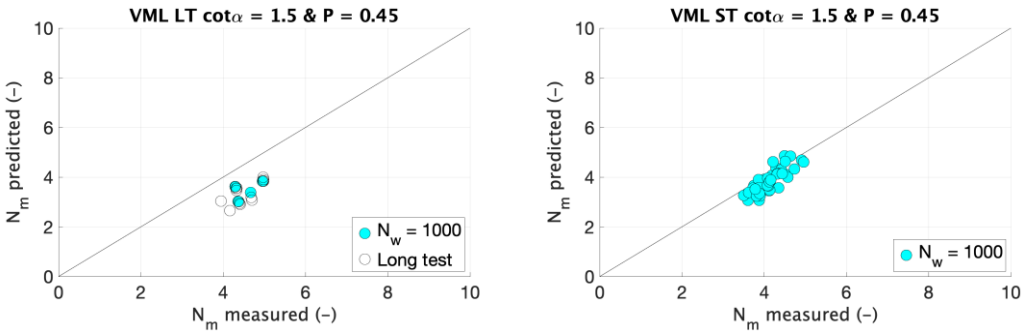


Figure 4.12. Measured vs. predicted N_m for VML test series.

Overall, this section demonstrates how each dataset has specific characteristics and different biases and uncertainties, primarily related to systematic variations in physical model experiments.

4.2.4. M_f stability equations refitting using $T_{m-1,0}$

Recently, $T_{m-1,0}$ has been acknowledged as more consistent than T_p or T_m in describing wave-structure interaction phenomena. $T_{m-1,0}$ is particularly relevant in shallow water conditions where, during propagation, due to nonlinear wave-by-wave interactions, waves superimpose components at different frequencies, shifting part of the energy to low frequencies. In this context, as suggested by [63] and more recently by [54], Eq. (20) was rewritten and partially refitted using $T_{m-1,0}$ computed at the toe of the structure

instead of T_m . $T_{m-1,0}$ was utilized in the evaluation of M_f (Eq. (6a)) and wave steepness. However, it is recommended to always use T_m for M_f approximation and for N_w , as that is how these parameters and equations were derived. However, a recent study by [102] questions the role of $T_{m-1,0}$ in describing the overtopping phenomenon of vertical seawalls under shallow water conditions. The authors highlight that the surf zone's spectral moments are correlated and warn that this phenomenon could result in spurious, unphysical relationships rather than a real physical relationship.

The refitting analysis on all damage data led to $K_{m1}=5.11$ (std=0.479) and $K_{m2}=4.76$ (std=0.825), as depicted in Figure 4.13. The surging equation experiences almost twice the uncertainty of the plunging equation. As previously discussed, the stability equation was plotted in terms of N_m and S_d , as illustrated in Figure 4.14 and Figure 4.15, respectively.

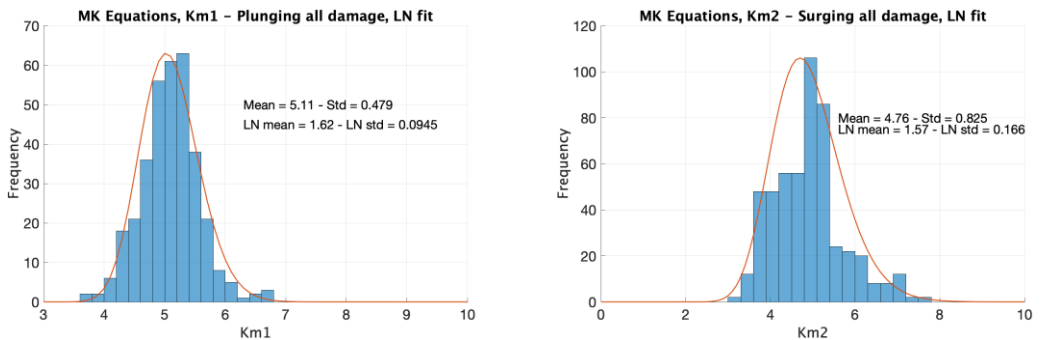


Figure 4.13. Plunging and surging coefficients for all damage data using $T_{m-1,0}$.

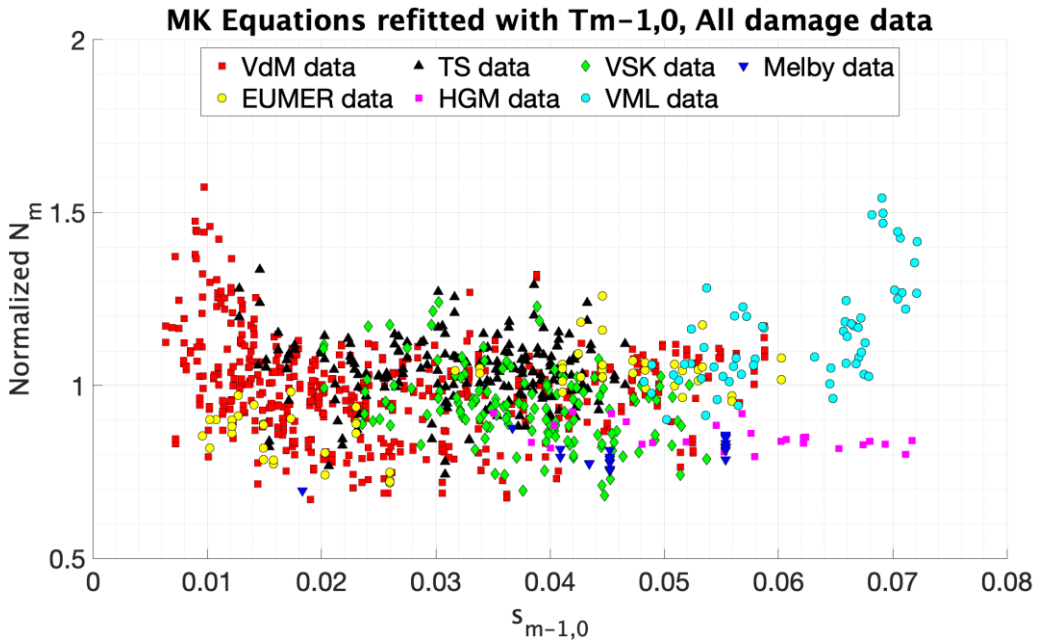


Figure 4.14. M_i refitted stability equations using $T_{m-1,0}$.

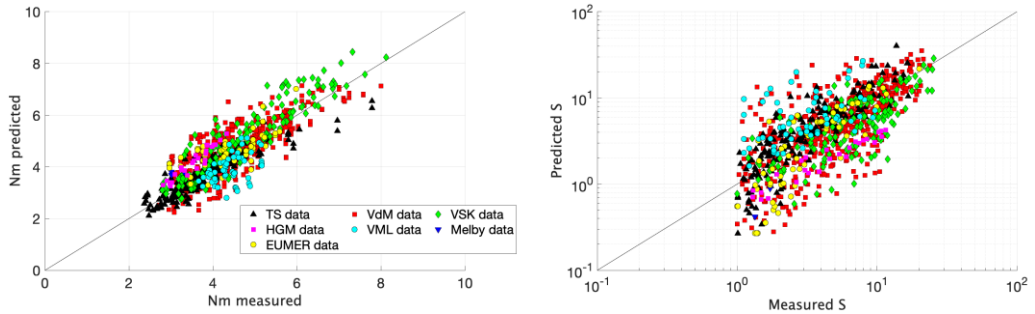


Figure 4.15. Measured vs. predicted N_m and S_d using $T_{m-1,0}$.

Results in Table 4.1 compare the two refitted equations using the mean relative error ($rmse$) and the correlation coefficient (r^2). Overall, no significant improvements could be established using $T_{m-1,0}$. Figure 4.4 is less stretched on the x-axis than Figure 4.14, and thus, more physically representative of the wave steepness range (0.005-0.06). However, high uncertainty is still evident, indicating that uncertainty in laboratory data remains prevalent and obscures the physics of the formulations.

Table 4.1. Comparison between the refitted stability equations.

Name	K_{m1}		K_{m2}		rmse	r^2
	mean	std	mean	std		
MK – Eq. (20) (T_m)	4.93	0.522	4.65	0.806	0.591	0.831
MK – Eq. (20) ($T_{m-1,0}$)	5.11	0.479	4.76	0.825	0.604	0.837

4.2.5. M_f refitting stability equations for each dataset

In Section 4.2.3, the new database was plotted using the refitted stability equation with T_m ($K_{m1}=4.93$ and $K_{m2}=4.65$), separating data for each specific physical model. The VML dataset was excluded from this study to concentrate on investigating and discussing the main differences related to the specificity of homogenous laboratory experiments. Again, Eq. (20d) was used for equation classification. Similarly, this section individually refits the stability equation for each dataset to determine the specific regression coefficients. Specifically, Figure 4.16, Figure 4.17, Figure 4.18, Figure 4.19 and Figure 4.20 show the refitted stability equations for the vdM, TS, VSK, EUMER, HGM and VKM data, respectively.

Figure 4.16 illustrates the refitted stability equation only using vdM data. Results, as expected, led to the same conclusion discussed by [65]. VdM data show a good agreement for the plunging equation ($K_{m1}=5$, $std=0.42$) but less for the surging equation ($K_{m2}=5$, $std=0.768$). VdM data are specific to mostly nonbreaking relatively deep water conditions and flat bottoms. A trend problem is noticeable in the red points (G06), indicating that the trend is off due to the description of structure geometry in the stability equation for homogenous and milder slopes.

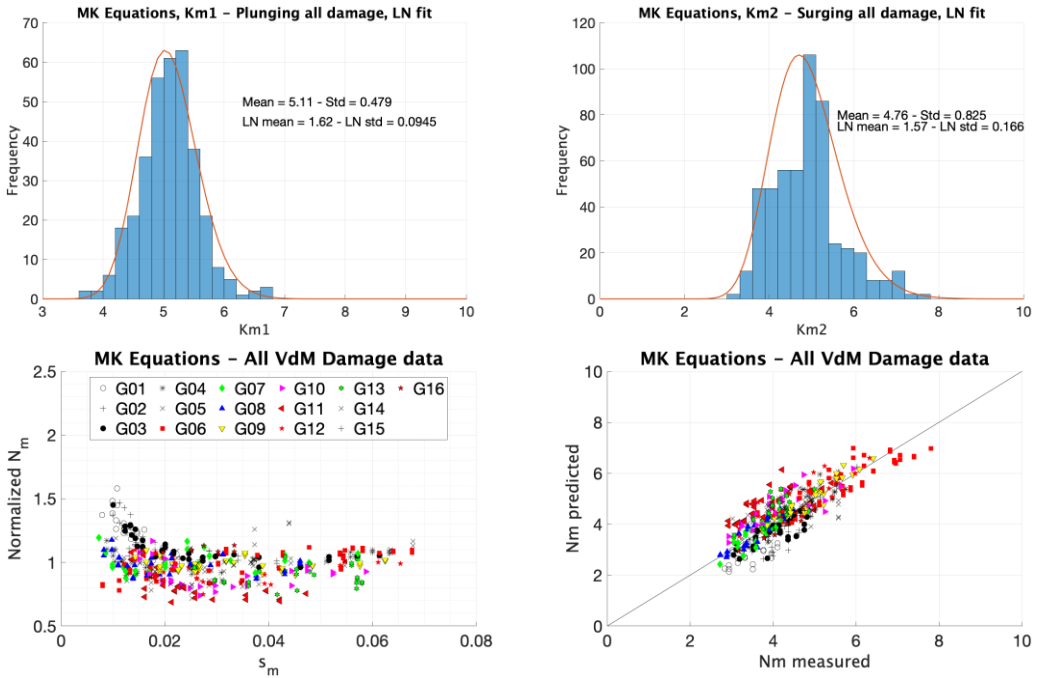


Figure 4.16. M_r refitted stability equation using only vdM data.

On the other hand, TS data exhibit lower uncertainty and a higher coefficient for plunging waves ($K_{m1}=5.11$, $std=0.487$) but an equal coefficient and lower uncertainty for surging waves ($K_{m2}=5$, $std=0.456$) compared to vdM (Figure 4.17). Specifically, K_{m1} is 2% higher than predicted by [65]. The fit appears satisfactory in these plots, except for group 20 (TS04) with plunging waves. Again, a similar trend error (albeit less pronounced than in vdM) is observed for mild slopes ($\cot\alpha=6$). Additionally, it is worth noting that these data are all in relatively deep water conditions and flat bottoms but differ in damage estimation, as discussed in Section 3.1.

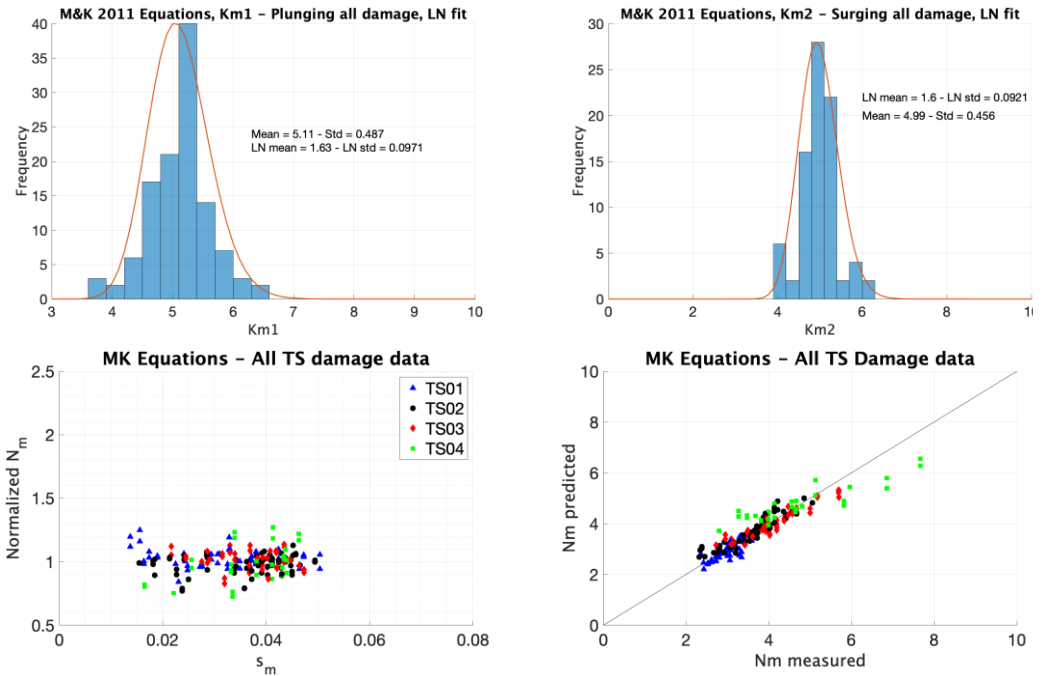


Figure 4.17. M_f refitted stability equation using only TS data.

VSK data encompass both plunging and surging domains. As shown in Figure 4.18, the fit is generally good and resembles vdM (except for VG05 (group 25), which exhibits a notable bias). However, the fit coefficients and uncertainty are lower for both plunging ($K_{m1}=4.47$, $\text{std}=0.422$) and surging equations ($K_{m2}=4.44$, $\text{std}=0.438$). Specifically, K_{m1} and K_{m2} are 10% and 12% lower than predicted by [65]. The stability number and the size of the armor D_{n50} are directly proportional to these coefficients (damage is related to the fifth power in Eq. (20)). Various reasons could account for such deviations, presenting challenges in identification. VSK data are in different water depth conditions than vdM data, implying a need for a more physically accurate reformulation of the stability equation to extend it to all water depth conditions. However, epistemic uncertainty in the laboratory data may also contribute to this difference. This systematic deviation offsets the stability number, suggesting potential factors as older technology

in vdM tests, more reflection in the tank for tests without structure in place, or a cruder damage measurement system.

In this case, the same trend problem is not observed since there are no experiments with mild slopes. Upon closer examination of the data, it is argued that the trend problem lies in the structure part of the stability equation rather than in the experiment. Specifically, it emerges when dealing with mild slopes ($\cot\alpha=6$). Among the entire database, only two test series (TS04 and G06) are conducted under this specific condition, and both exhibit the same trend.

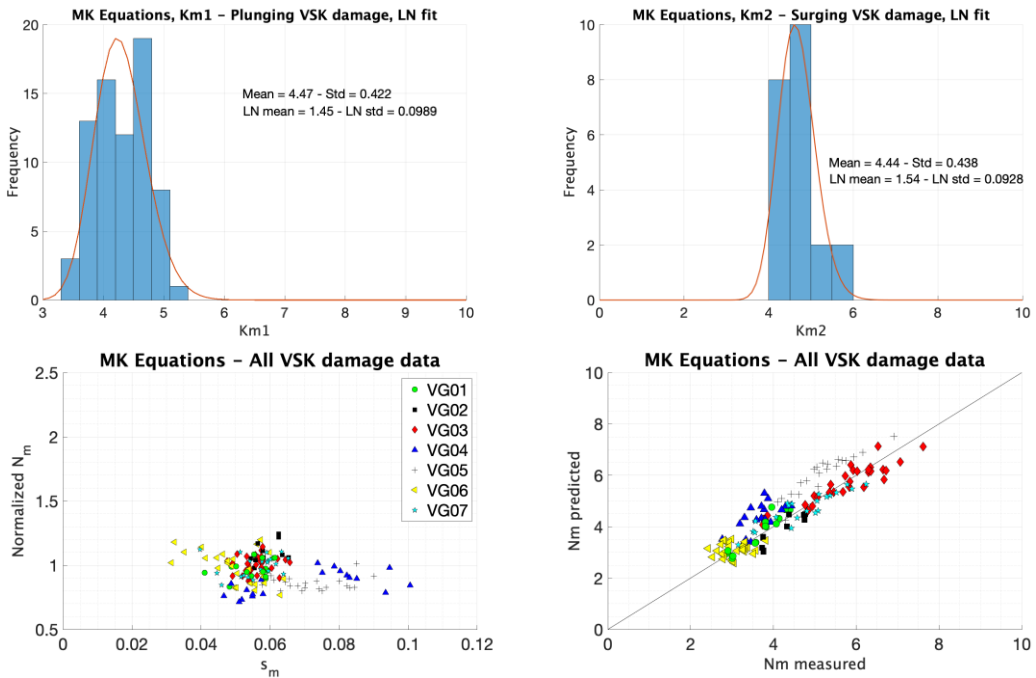


Figure 4.18. M_i refitted stability equation using only VSK data.

EUMER data exclusively fall within the surging domain and share the same slope angle. Variations in test groups are associated with foreshore shallowness. The fit is quite satisfactory and resembles vdM (Figure 4.19), exhibiting a slightly lower coefficient and higher uncertainty ($K_{m2}=4.5$, $std=0.578$). The uncertainty in the surging equation is

comparable to vdM plunging one, meaning that if stability equations were refitted using a uniform type of experiment carried out in the same laboratory and period, data scatter would be reduced. Specifically, K_{m2} is 10% lower than predicted by [65]. EUMER data also align with VSK data in shallow waters.

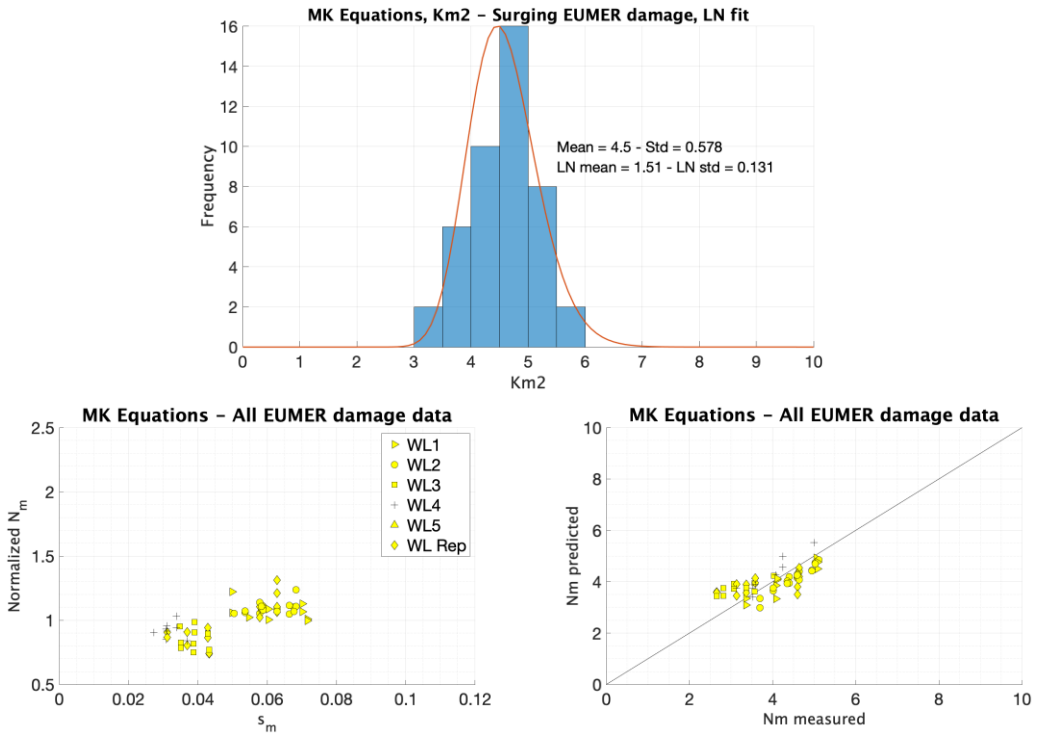


Figure 4.19. M_f refitted stability equation using only EUMER data.

HGM data all fall within the surging domain and share the same structure geometry but differ in shallowness conditions, like EUMER data. The fit demonstrates an excellent prediction of the stability equation in the surging domain (Figure 4.20). The data show a lower coefficient and the lowest uncertainty ($K_{m2}=4$, $std=0.17$). Specifically, K_{m2} is 20% lower than predicted in [65]. HGM data ($K_{m2}=4$) can be compared with those obtained from VSK ($K_{m2}=4.44$) and EUMER ($K_{m2}=4.5$) because data were acquired in similar shallowness conditions. The deviation in the coefficient in HGM compared to

VSK and EUMER is likely related to different damage analysis procedures used in the experiments. Such differences can even lead to a bias of approximately 10% between the data. The VML dataset is not homogenous due to variations in wave and damage analysis procedures. Therefore, despite applying the same procedure ($K_{m1}=5.67$ and $\text{std}=0.609$), leaving out these data from the analysis is recommended.

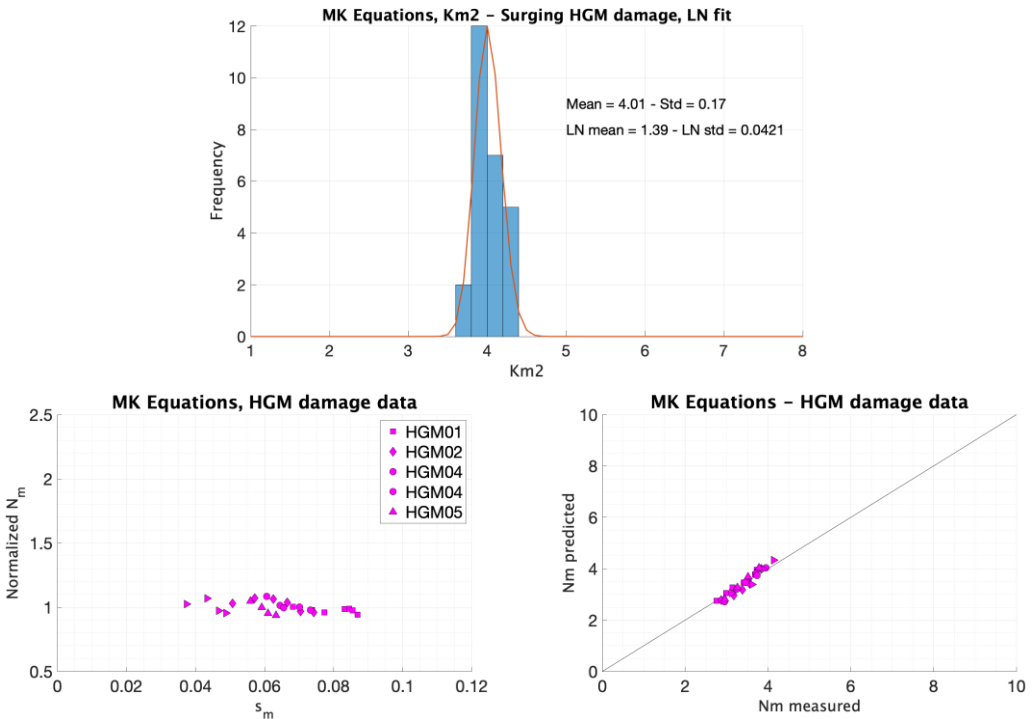


Figure 4.20. M_i refitted stability equation using only HGM data.

4.2.6. Discussion

Table 4.2 presents the coefficients and standard deviations for each laboratory experiment contributing to the new extensive dataset, along with the number of data utilized for each analysis.

Table 4.2. Final comparison between datasets.

Dataset ID	K_{m1} mean	K_{m1} std	K_{m2} mean	K_{m2} std	Number of data
vdM	5	0.419	4.57	0.768	295
TS	5.11	0.487	4.99	0.456	134
VSK	4.47	0.422	4.44	0.438	207
EUMER	-	-	4.50	0.578	69
HGM	-	-	4.01	0.170	44
VML	-	-	5.67	0.609	116
All data	4.93	0.522	4.65	0.806	890

Overall, it can be asserted that the plunging equation (Eq. (20b)) is quite effective with a K_{m1} equal to 4.93 and a low std (0.522), whereas the surging equation (Eq. (20c)) has greater scatter with a lower K_{m2} (4.65) and higher std (0.806). Such uncertainty across different datasets is likely attributed to the lack of physical understanding of the phenomenon and the epistemic uncertainty in the stability laboratory data. Differently, low uncertainty but different regression coefficients highlight a good prediction of the model, but there is some systematic bias in the data. Additionally, different amounts of data used to refit the equations can hide the real behavior of the formulation. The number of data should be equal to assess valid and robust conclusions.

Stability formulae based on the maximum depth-integrated wave momentum flux should be physically reformulated. [25] stated that it is not the total maximum wave momentum flux capable of determining the stone displacement but primarily the drag forces. Indeed, armor near the still water level is more likely to displace than armor in other areas. This occurs because armor is loosened in this area due to high velocities in the breaking wave jet. Once loosened, the motion depends on the armor's shape and position [103]. If the armor shape is flat, the armor unit will flop back and forth until it

rolls out of the armor layer, generally rolling upslope during uprush. If the armor shape is equant, which is usually the case, the armor units would jump vertically under the steep wave face if the waves were severely plunging or collapsing. If the waves are surging, then loose units would only be displaced if exposed. The only displacement mechanism observed for equant stones sufficiently well-interlocked in the armor layer and not poking out of the layer (independently exposed to up and downrush forces) was uplift under the steep wave face.

These observations indicated that a fluid velocity or acceleration component in the vertical direction is normally required to initiate armor motion for well-interlocked armor units. The dominant mode of displacement is due to vertical wave forces, which are shown to occur at the point of maximum vertical velocity under the steep wave front. The maximum vertical convective acceleration is roughly linearly related to the square of the velocity, which puts the inertial force term into the same form as the drag term. The resulting incipient motion stability relation is similar in form to the Shields sediment motion criteria [103]. Therefore, the stability equation based on the maximum depth-integrated wave momentum flux should be reformulated, substituting the maximum wave momentum flux with the maximum velocity-based momentum flux, which is proportional to the drag force. Furthermore, the nonlinear approximated method described by Hughes is only valid and accurate for nonbreaking conditions and is probably not accurate for breaking conditions. Finally, a more accurate and physical description of the permeability of coastal structures should be assessed rather than the notional permeability.

With that said, this thesis argues that, regardless of how close we get to a real physical description, data scatter is likely to persist. The primary reason for this is that armor stability is inherently random, with random stones placed in random configurations exposed to random waves. Data from different laboratories and different historical periods experience bias and uncertainty, as illustrated in this section. Laboratory data exhibit inconsistencies across various laboratories and time periods and cannot be

directly compared without assuming high bias and uncertainty. Therefore, before exploring alternative physical relationships between the stability number and the other parameters, and before refitting the equations, it is necessary to homogenize the laboratory data and reduce epistemic uncertainty (for example hydrodynamic uncertainty), which is very likely obscuring the physics of the phenomenon.

4.3. Comparison between armor stability formulae

This section conducts a comparison between some of the stability formulae described in Section 2. However, a significant complication in comparing the various formula and datasets arises from the disparities between them. For example, vdM data are extensive and influential, predominantly representing deep water with a very tall structure and relying on dated wave and sounding technologies compared to more recent studies. This may introduce offsetting biases that could be challenging to disentangle. Data were classified according to the shallowness criterion reported in Eq. (13) and Figure 3.1, with extremely shallow waters included in the very shallow waters group. The challenge here is that deep water data are likely to involve older technology, while shallow water data are likely to involve more recent technology. One potential remedy is to isolate and compare similar tests from various experiments if such tests exist. The Boussinesq model is also a tool that could be used to ensure that results from one experiment can be compared to another, but this will be addressed later.

The measured vs. predicted stability number was plotted according to the stability equations and separated in deep (left), shallow (center), and very shallow waters (right), respectively (Figure 4.21). The accuracy of the predictions was quantified using accuracy error metrics such as the root mean square error (*rmse*), and the coefficient of correlation (r^2), defined in Eqs. (21a,b). Additionally, bias, and standard deviation, computed as the mean and the standard deviation of the error ($E_i = N_{s_{pred}} - N_{s_{obs}}$), are reported in Eqs. (21c,d) as:

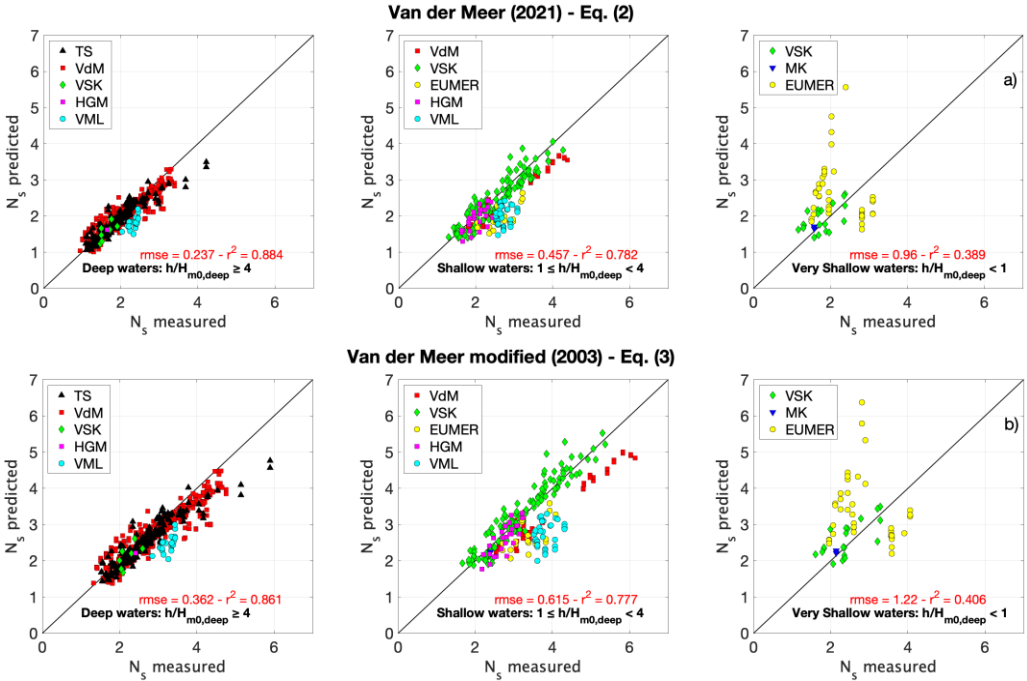
$$\text{rmse} = \sqrt{\frac{1}{M} \sum_{i=1}^M (N_{s_{\text{obs}}} - N_{s_{\text{pred}}})^2} \quad \text{Eq. (21a)}$$

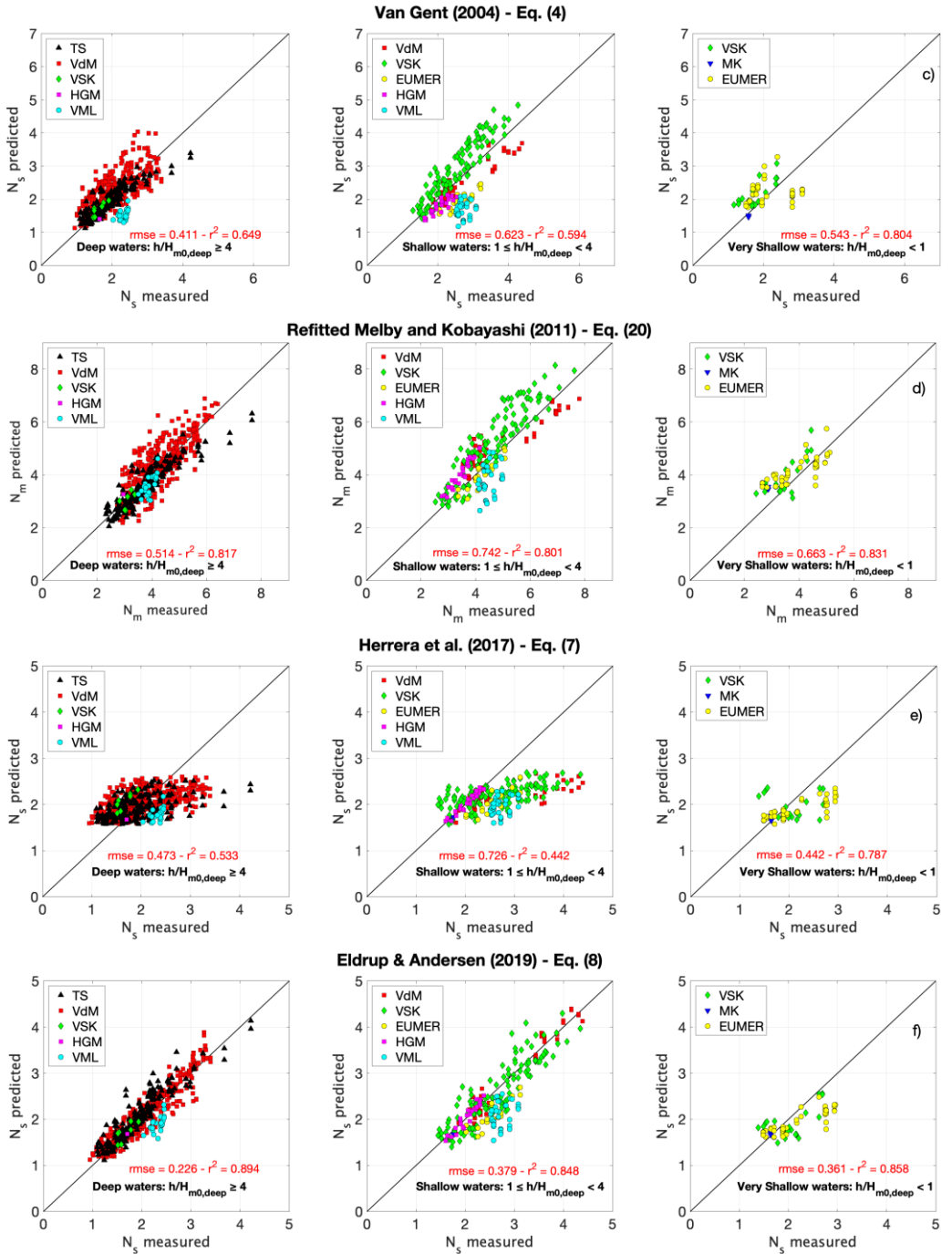
$$r^2 = 1 - \frac{\sum_{i=1}^M (N_{s_{\text{obs}}} - N_{s_{\text{pred}}})^2}{\sum_{i=1}^M (N_{s_{\text{obs}}} - \bar{N}_{s_{\text{obs}}})^2} \quad \text{Eq. (21b)}$$

$$\text{bias} = \mu = \frac{1}{M} \sum_{i=1}^M (E_i) \quad \text{Eq. (21c)}$$

$$\text{std} = \sqrt{\frac{1}{M-1} \sum_{i=1}^M |E_i - \mu|^2} \quad \text{Eq. (21d)}$$

where $N_{s_{\text{obs}}}$ and $N_{s_{\text{pred}}}$ denote the observed and predicted stability numbers, M is the total number of observations, and $\bar{N}_{s_{\text{obs}}}$ is the mean of the observed stability numbers.





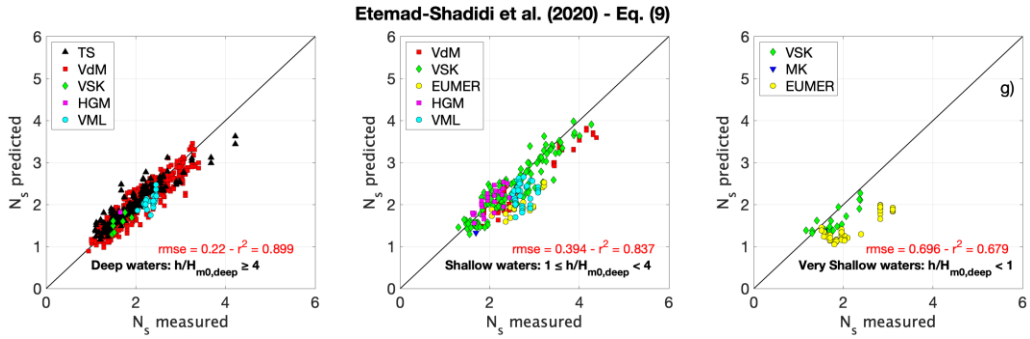


Figure 4.21. Comparison between measured and predicted values of the processed dataset for the most popular stability formulae for deep, shallow and very shallow water conditions, respectively; a) van der Meer (2021) [54]; b) van der Meer modified (2003) [59]; c) van Gent (2004) [63]; d) Melby and Kobayashi (2011) [65]; e) Herrera et al. (2017) [70]; f) Eldrup and Andersen (2019) [72]; g) Etemad-Shahidi et al. (2020) [79].

4.3.1. Discussion

Table 4.3 presents the error measures ($rmse$ and r^2) for each stability formula computed for deep, shallow, and very shallow water conditions. Based on the criteria of the lowest $rmse$ and the largest correlation coefficient, the results identify the stability formulae proposed by Etemad-Shahidi [79], Eq. (9), and Eldrup and Andersen [72], Eq. (8), as the best predictive models for determining hydraulic stability for stone armor slopes in both deep water and shallow water conditions. Specifically, only Eldrup and Andersen equations appear to be also accurate for very shallow waters.

For a wide surf zone (typical design conditions for most U.S. navigation structures), it is speculated that the details of the wave-to-wave variations and their influence on stability are likely reduced due to breaking and energy saturation. If this holds true, the conclusion would be that both the vdM functionality and epistemic variability would be diminished. In wide surf zone conditions, many parameters that are influential in deep water may not exert much influence. The question arises as to whether epistemic uncertainty is dependent on factors such as the relative depth and width of the surf

zone or if it primarily results from one set of factors in deep water and a different set in shallow waters. An answer to this question cannot be given until epistemic uncertainty is first reduced.

Table 4.3. Comparison in terms of rmse and r² between the stability formulae for deep, shallow, and very shallow water conditions.

Stability Formulae	Deep water		Shallow water		Very shallow water	
	<i>rmse</i>	<i>r²</i>	<i>rmse</i>	<i>r²</i>	<i>rmse</i>	<i>r²</i>
Van der Meer (2021) – Eq. (2)	0.237	0.884	0.457	0.782	0.96	0.389
Van der Meer (2003) modified – Eq. (3)	0.362	0.861	0.615	0.777	1.22	0.406
Van Gent (2004) – Eq. (4)	0.411	0.649	0.623	0.594	0.543	0.804
Refitted MK (2011) – Eq. (20)	0.514	0.817	0.742	0.801	0.663	0.831
Herrera et al. (2017) – Eq. (7)	0.473	0.533	0.726	0.442	0.442	0.787
Eldrup & Andersen (2019) – Eq. (8)	0.226	0.894	0.379	0.848	0.361	0.858
Etemad-Shahidi et al. (2020) – Eq. (9)	0.220	0.899	0.394	0.837	0.696	0.679

Now, we can only speculate and refer to the literature to state where most of the bias and uncertainty is coming from. First, it is necessary to investigate the bias magnitude and mean trends. After that, one could look at scatter and uncertainty based on the statistics in Table 4.3 and Table 4.4. Different trends were found only for mild structure slopes ($\cot\alpha=6$). Finally, Table 4.5 summarizes the main characteristics of some of the hydraulic stability formulae compared in Chapter 2.

Table 4.4. Comparison in terms of bias and uncertainty between the stability formulae for deep, shallow, and very shallow water conditions.

Stability Formulae	Deep water		Shallow water		Very shallow water	
	<i>bias</i>	<i>std</i>	<i>bias</i>	<i>std</i>	<i>bias</i>	<i>std</i>
Van der Meer (2021) – Eq. (2)	0.070	0.226	0.276	0.364	-0.313	0.914
Van der Meer (2003) mod. – Eq. (3)	0.180	0.314	0.299	0.538	-0.454	1.142
Van Gent (2004) – Eq. (4)	-0.101	0.399	0.104	0.615	-0.082	0.541
Refitted MK (2011) – Eq. (20)	0.013	0.514	-0.240	0.704	-0.421	0.515

Herrera et al. (2017) – Eq. (7)	0.009	0.474	0.486	0.540	0.145	0.420
Eldrup & Andersen (2019) – Eq. (8)	-0.046	0.221	0.154	0.347	0.178	0.316
Etemad-Shahidi (2020) – Eq. (9)	0.025	0.219	0.226	0.324	0.560	0.416

This section delves into the main factors likely contributing to the differences in the stability equations. It is important to emphasize that the number of tests significantly influences the fitting. A dataset may dominate simply because it has a lot of data, and consequently, an equation may have the best fit even though it does not perform well overall. Additionally, not all equations and datasets are perfectly comparable. Equations should be tested only in their field of application, and data are sometimes not entirely homogenous.

The rewritten vdM equations described in Eq. (2) work well in deep water conditions but less do in shallow waters. There is a progressive increase in bias and uncertainty for shallow and very shallow conditions. The equations were fitted only using vdM and TS datasets, mostly with nonbreaking waves in relatively deep water conditions and flat bottoms, testing them outside their range of application. Specifically, the vdM equations do not recognize the local water depth (h) as a significant parameter in estimating stone armor stability. Moreover, the permeability of the structure is considered with the somewhat subjective “*notional*” permeability factor (P). When dealing with shallow waters, the SSP computed on the structure slope may not be accurate for conditions where waves break over a wide surf zone and not on the structure slope. Finally, the time domain H_s may not be very accurate in shallow waters because it does not consider the nonlinearity of waves. Recently, vdM changed the equations by substituting H_s with H_{m0} and proposed new insights about the vdM formula for stone slope stability at shallow waters [104].

The modified van der Meer formula, Eq. (3), is valid in shallow waters but exhibits an even larger bias and uncertainty than the original vdM equation. The equation was fitted using vdM and VSK data in both deep and shallow water conditions. The

parameterization of the predictive model is identical to Eq. (2) except for the inclusion of $H_{2\%}$. However, as discussed by van der Meer ([54, 104]), and also shown in Figure 3.2d, $H_{2\%}$ cannot be easily predicted. For example, Goda [73] demonstrated on the VSK data that the ratio $H_{2\%}/H_{1/3}$ may decrease from the original 1.4 for deep water to 1.2 in shallow water, but it increases again for very shallow water, up to 1.4. For this reason, the analysis initially used $H_{1/3}$, later $H_{2\%}$, but now H_{m0} has been finally recognized as the best wave parameter. Beyond the same question for the rewritten vdM equation, this should explain why the stability equation is less accurate for very shallow waters.

The van Gent equation, Eq. (4), addresses the shortcomings reported in Eq. (3) by employing a simpler formula without the influence of the wave period and considering the permeability coefficient, $(1 + D_{n50,core}/D_{n50})$, rather than the notional permeability factor, P . The formula was calibrated using the vdM and VSK datasets and exhibits a consistent bias for all water depth conditions. This implies that the main difference in experiments between vdM and VSK, can be attributed to the absence of incident wave period. VSK showed that wave period can soar in shallow water, sometimes by up to a factor of 10, due to energy transfer from swell to IG frequencies. However, waves at IG frequencies are probably much less influential for stability than swell. So, the effect of wave period on stability may be obscured in shallow water if the period at the structure toe is used. Such differences may also be related to the active compensation reflection system, reflection analysis, as well as the damage profiler procedure. The total uncertainty is large but can be explained by the over-simplistic nature of the equation. It is argued that the influence of the spectral wave period (wave steepness) should be included in the equations.

The HGM equation, Eq. (7), was not considered in the discussion due to its too simplistic formulation calibrated only on its own data.

Etemad-Shahidi et al. equation, Eq. (9), can be considered as an updated version of the simple van Gent formula (Eq. (4)). It was derived using a multi-variable regression

model applied to an experimental database of 791 points available in the literature (vdM, TS, VSK, VML) to retrieve a compact formula suitable for both plunging and surging waves valid from deep to shallow water conditions. The formula brings advancements in a more physically based description of the permeability coefficient $(1 + D_{n50,core}/D_{n50})$ and the introduction of the foreshore slope $m = \tan\beta$. Additionally, machine learning algorithms revealed a different dependency (6-power) between the stability number and the damage. However, Eq. (9) omits the local water depth (h) despite the foreshore slope correction term, and it is not physically based. The transition between plunge and surge waves is determined using $\xi_{s-1,0,c} = 1.8$ [55] rather than the intersection between the formulae. Overall, there is an increase in the bias, which becomes relatively high in very shallow waters, and a constant amount of uncertainty. This indicates that the relationship between the stability number and the other parameters is accurately described, but using non-homogeneous data brought high bias. Moreover, the formulation was not calibrated with data in very and extremely shallow water conditions, which causes it to perform poorly for very shallow waters.

The Eldrup and Andersen equation, Eq. (8), can be considered an updated version of the original vdM equation. This equation was fitted using data with nonbreaking, breaking, and very low steepness waves, incorporating both VSK and Eldrup and Andersen (hereafter referred to as EA) datasets. A significant improvement was the inclusion of data from highly nonlinear waves in shallow waters (EA data), along with the use of the formula by [105] to estimate P . However, the relationship between the stability number and the structure slope for the surging equation seems overly simplistic, as it fits equations only considering steep armor slopes. Finally, the SSP was estimated using the wave steepness at the toe of the structure using the deep water wavelength formula $(gT^2/2\pi)$, whereas N_w is considered offshore. This formulation shows a relatively low increasing bias from deep to shallow waters, which remains almost constant in shallow and very shallow waters. A similar form to the vdM equations also guarantees a good prediction in deep water conditions, although Eq. (8)

was not calibrated using vdM data. Moreover, it presents the lowest values of bias and uncertainty in shallow waters among the formulae. This could be explained by the fact that the equations were calibrated using more homogenous datasets acquired in recent years (similar technologies compared to the 1980s). Different hydrodynamic and damage measurements and analyses between the experiments can explain the remaining bias. Uncertainty in the formulations is relatively constant, meaning that the predictive model works well for all water depth conditions, and bias and uncertainty slightly increase in shallow waters.

Finally, the refitted M_f equation by Melby and Kobayashi, denoted as Eq. (20), is theoretically expected to perform better than the other formulations. Eq. (20) was calibrated utilizing the entire database outlined in Section 3.8. It is more physically based and was analytically derived from basic principles. This equation utilized the maximum depth-integrated M_f to characterize wave forces on the structure and explicitly incorporates the local water depth. Despite these advancements, the results presented in Figure 4.4 reveal suboptimal but not worse performance compared to the better models. Bias increases in shallower waters, and the mixing non-homogeneous data may explain this discrepancy. Moreover, uncertainty is notably high, particularly in deep and shallow water conditions. The reasons for this uncertainty can be attributed, in part, to the formulation approximating the nonlinear M_f [66] at the structure toe rather than computing it precisely and rather than computing it at the upslope location of maximum force. This approximation breaks down, especially under nonlinear breaking conditions. Furthermore, it is imperative to consider a comprehensive reformulation of the equation, encompassing both the right- and left- hand sides, as discussed in Section 4.2.6. Such adjustments yield a more precise representation of the forces acting on armor units and introduce a more physically based term for the permeability coefficient.

It is essential to emphasize that all these equations are empirical, tailored to fit within specific limited wave and water level conditions. While some equations prioritize data

fitting, others lean towards elucidating physics. The utmost focus on physical principles is observed in the M_f equations, driven not only by maximum force considerations but also by the incorporation of wave period and depth into the physics, rather than solely relying on mathematical data fitting. Hence, our emphasis here is on these equations.

When equations are considered in terms of damage rather than stability number, a significantly greater level of scatter is observed. Damage is related to a high power of wave height, and that magnifies scatter. We speculate that such uncertainty results from the total uncertainty in the stability laboratory data. There is evidence that disparities in experimental methodologies can yield divergent test results, potentially leading to different design decisions. Achieving standardization in testing procedures to the extent where every laboratory produces identical results is an elusive goal. Intuition and engineering judgment will inevitably differ and remain a major factor in the decision-making process accompanying laboratory test designs. Nonetheless, there is a pressing need to standardize wave parameter definitions and the methods employed for their measurement and computation. This standardization effort holds the potential to alleviate many disparities, thereby reducing bias and uncertainty in the final equations. Moreover, the utilization of numerical simulation methods is essential to validate analysis and synthesis programs applied in laboratory settings. It is proposed that merely attributing apparent discrepancies in results to normal statistical variability is no longer adequate. Instead, there is a need to learn from this comparative analysis and actively work toward minimizing the epistemic uncertainty inherent within laboratory data. This endeavor could facilitate the formulation of a new more physically based stability formula based on the wave momentum flux approach.

Table 4.5. Main characteristics of the stability equations compared in Figure 4.21.

	Stone stability formulae					
	Revisited vdM (2021)	Van Gent et al. (2004)	Herrera et al. (2017)	Eldrup & Andersen (2019)	Etemad Shahidi et al. (2020)	Thesis

Datasets used for stability formulae calibration	TS, VdM	VdM, VSK	HGM	VSK; EA	VdM, TS, VSK, VML	VdM, TS, VSK, MK, HGM, EUMER, VML
Structure slope angle, $\cot\alpha$	1.5 – 6	1.5 – 6	1.5	1.5 – 6	1.5 – 6	1.5 – 6
Foreshore slope angle, $\cot\beta$	Flat, 30	Flat, 30, 100	Flat, 30, 100	30 -100	Flat, 30, 100	Flat, 20, 30, 50, 100
Permeability	P	$D_{n50core}/D_{n50}$	-	P estimated	$D_{n50core}/D_{n50}$	P
Damage analysis	Non homogeneous	homogeneous (profiler)	homogeneous	homogeneous (profiler)	Non homogeneous	Non homogeneous
Shallowness condition	Deep, shallow	Deep, shallow, very shallow	Deep, shallow	Shallow, very shallow	Deep, shallow, very shallow	Deep, shallow, very shallow
Number of tests, N	360	207 (567)	45	68 (635)	1199	69

4.4. Conclusions

This chapter presents a detailed analysis of data, comparing the database with the most widely used stability equations to examine and quantify bias and uncertainty. The main conclusion drawn here is that no stability formula significantly outperforms others due to high uncertainty inherent in the available data. Additionally, it is suggested that the existing stability formulae based on the wave momentum flux should theoretically offer a better description of the physics of stone armor stability but require reformulation for enhanced accuracy. This thesis argues that, regardless of how closely we approximate a realistic physical description, the raw data cannot be fully synthesized without further modeling due to the disparate modeling approaches, the non-homogeneous nature of the parametric data and limited understanding of detailed laboratory techniques and

data analysis methods. There is evidence to suggest that disparities in experimental procedures can yield divergent test results, potentially leading to different design decisions. Therefore, the database needs further synthesis and homogenization before definitive conclusions can be drawn.

CHAPTER 5

Uncertainties in stone armor stability

5. Uncertainties in stone armor stability

In Chapter 4, it was emphasized that the uncertainty inherent in laboratory data is likely to obscure the physics of the formulations. This chapter provides an overview of the primary sources of uncertainty in stone armor stability and aims to elucidate the contribution of each source to the total uncertainty.

5.1. Introduction

Significant progress has been achieved with numerical models, leveraging advancements in informatics expertise, and utilizing models like SPH, OpenFOAM, and FEMDEM. However, despite ongoing evolution in numerical models, physical laboratory experiments remain the preferred and most cost-effective methodology for investigating stone armor stability. The computational demands associated with predicting stone armor stability exposed to irregular waves are still too high, making physical modeling the more practical choice.

Despite numerous efforts to enhance physical modeling in hydrodynamics and damage analysis, some researchers have frequently expressed doubts regarding the reliability of waves generated in laboratory flumes when applied to real structures under real sea waves [106]. Coastal engineering encounters various uncertainties in input parameters and models. The imperfect knowledge of these parameters and related uncertainties may lead to under-design, coastal structure failure, or expensive over-design. Consequently, stochastic parameters and model uncertainties should be considered for

probabilistic coastal structure design. The probabilistic design method aims to initially estimate the uncertainty of design values (parameter uncertainty) and subsequently assess the uncertainty of predictive models (model uncertainty).

5.2. Sources of uncertainty in stone armor stability

Many parameters used in coastal engineering are uncertain, as are the models themselves. Armor stability is a fundamentally random process, with the natural sea state varying randomly in time and space, wave-by-wave interactions on the structure slope varying randomly, and shape and placement of armor stones also varying randomly. Therefore, it should be anticipated that the results of physical model studies in hydrodynamics and damage analysis will yield variability in results, even when employing similar technical approaches.

This class of uncertainty can be classified as inherent or aleatory ($\sigma'_{\text{aleatory}}$), where randomness is intrinsic to the response, and the statistics are reproducible if enough realizations are analyzed. Aleatory uncertainty in stone armor stability constitutes a significant portion of the total uncertainty in predictive models. This fundamental, intrinsic uncertainty is conditioned by the random processes of nature (such as waves and stone displacement) and cannot be reduced or eliminated; it is a general characteristic of the measured laboratory data. For coastal structure experiments, aleatory uncertainty is a consequence of various factors, including environmental parameters and laboratory conditions, wave realization, and material properties of random stones (e.g., placement, orientation, shape, interlocking).

Conversely, there is also an epistemic uncertainty inherent in stability data and resulting predictive models ($\sigma'_{\text{epistemic}}$). This uncertainty depends on various contributions and pertains to uncertainties in data, model, errors, etc. The total epistemic uncertainty results from a quadratic summation of the coefficients of variation of each contribution. These types of uncertainties must be considered during the design of coastal structures

and integrated into predictive models. Concern arises from the possibility that dissimilarities could result from oversights or mistakes in the testing and analysis procedures. Even though different authors and laboratories may adopt similar systems and methods, the design of a stone-armor layer breakwater involves numerous uncertainties. This variability is intricate and challenging to quantify due to the wide range and permutations of the variables involved, especially when comparing non-homogeneous datasets.

Here, aleatory uncertainty is considered irreducible, while epistemic uncertainty is deemed reducible. Although the effects of aleatory uncertainty on hydraulic stability are frequently assumed to be dominant over epistemic uncertainty, the specific magnitude of both contributions has yet to be explicitly quantified to assess the validity of this assumption. Common stochastic engineering approaches incorporate both aleatory and epistemic uncertainty. However, the relative importance and total uncertainty are not yet fully quantified.

The primary objective of this thesis is to quantify the key contributors to epistemic uncertainty. This task is pursued by comparing various datasets against each other and benchmarking them against a high-fidelity phase-resolving numerical wave transformation model. Figure 5.1 outlines the main sources and types of uncertainty, and each contribution will be thoroughly discussed and detailed in subsequent sections.

It is assumed herein that dissimilarities from oversights or mistakes in the testing and analysis procedures are minimal and that the coastal community has fully accepted the selected datasets. However, the acknowledgment is made that mistakes or oversights may still be present in the data, and it is beyond the scope of the present study to resolve these issues.

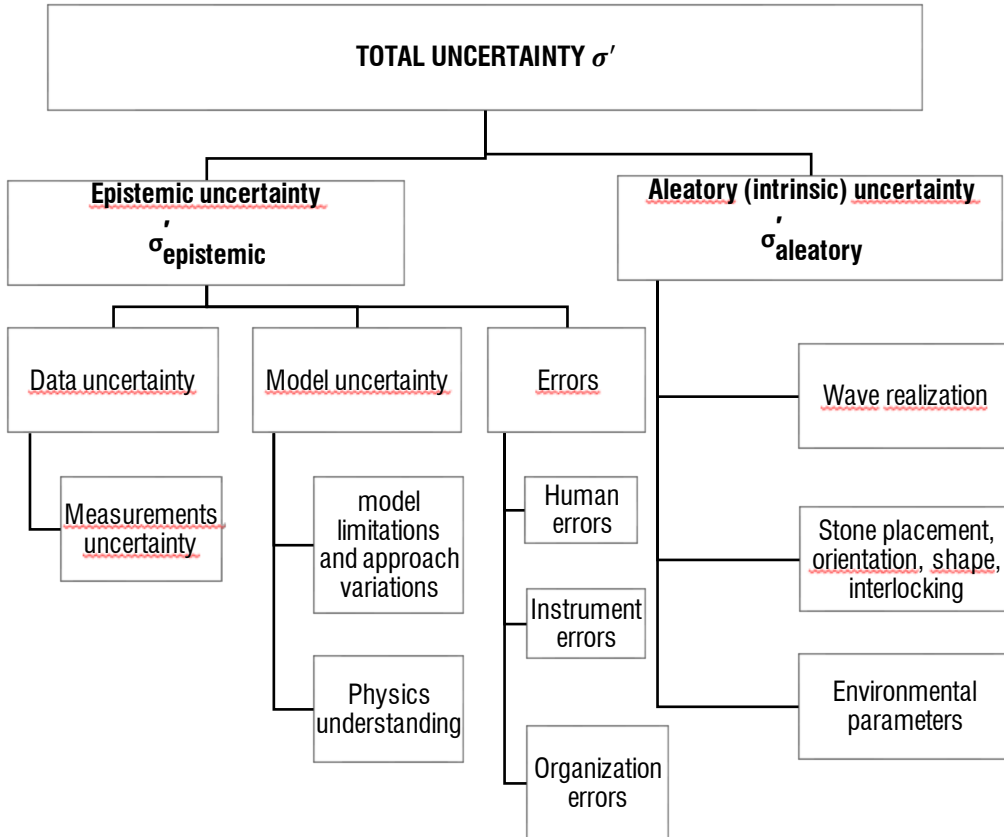


Figure 5.1. Main sources of uncertainty in stone armor stability.

5.3. Definition of uncertainty

This section briefly introduces the concept of uncertainty and outlines its treatment in this thesis. Mathematically, (epistemic) “*uncertainty*” is mainly defined as the relative parameter variation or relative error in the model description. Parametric errors are commonly quantified using normal or log-normal distributions and characterized with

mean (bias) and standard deviation (scatter). In addition, empirical equation fit coefficient errors can be quantified in the same way. It is common to treat error stochastically, assuming a normal distribution for a quantity 'y' with a mean value $\mu(y)$ and a standard deviation $\sigma(y)$. The uncertainty is quantified by the coefficient of variation $\sigma'(y)$ defined as in Eq. (22).

$$\sigma'(y) = \frac{\sigma(y)}{\mu(y)} \quad \text{Eq. (22)}$$

The difference between the mean and the nominal or characteristic value is termed *bias*. Although this definition may be imperfect, it holds practical value and is easily applied. Data used to calculate $\sigma'(y)$ for each parameter must be gathered through various tests, measurements, and investigations. Forming a database of uncertainty is desirable, allowing future contributions to enhance accuracy.

Unfortunately, determining the statistical nature of errors is often challenging in coastal engineering due to different sources of uncertainty and non-homogenous data. The coefficient of variation $\sigma'(y)$ of a design variable 'y' consists of M (statistically independent) individual coefficients of variations $\sigma'(y)_i$ representing different sources of uncertainty (Eq. (23)).

$$\sigma'(y) = \sqrt{\sum_{i=1}^M \sigma'(y)_i} \quad \text{Eq. (23)}$$

An alternative perspective on uncertainties, not used in this thesis, involves presenting the mean and the confidence interval or band. A 90% confidence limit can be achieved by providing the 5%-exceedance on both sides of the mean, calculated as $\mu(y) \pm 1.64 \sigma(y)$ of a normal distribution (e.g., [70], [72]). Designing with uncertainties necessitates careful selection of statistical distributions for most of the parameters.

5.3.1. Parameter uncertainty

As highlighted in previous chapters, the uncertainty of input parameters can signify the natural randomness or inaccuracy with these parameters. These parameters can be derived from model tests or field measurements. As discussed earlier, we quantify this uncertainty using statistical distributions or relative variations in these parameters. The relative variation for most parameters can be taken from various sources, including observed measurement errors, expert opinions derived through questionnaires, and reported errors in the literature. For example, Goda [73] reports coefficient of variations for design parameters related to breakwater design. Similarly, [107, 108] utilized expert elicitation via questionnaires distributed to selected experts in coastal engineering to estimate uncertainties.

This manuscript particularly focuses on sea state parameters computed at the toe of the structure. In cases where statistical distribution or error level information is not available for sea state parameters, such estimation can be drawn from the existing body of knowledge and literature.

5.3.2. Model uncertainty

Model uncertainty refers to the accuracy with which a predictive model can describe a physical process or a limit state function. It essentially captures the deviation of predictions from measured data, attributed to the employed methodology. Difficulties arise from the combination of input parameter uncertainty and model uncertainty.

Model uncertainty can be characterized using a multiplicative approach as expressed in Eq. (24):

$$y_{\text{obs}} = G \cdot f(y_{\text{pred}}) \quad \text{Eq. (24)}$$

where G represents the model factor (-), y_{obs} is the measured output of the model, and $f(y_{pred})$ is the model used for predicting the variable. The model factor is assumed to follow a normal distribution with a mean value of 1.0 and a coefficient of variation explicitly derived for the model.

As in this manuscript, it is also possible that G serves as one of the coefficients in a formula, assumed to be a stochastic variable. In such cases, uncertainty is determined by the standard deviation of this coefficient, as outlined in Eq. (20).

5.4. Epistemic uncertainty

5.4.1. Data uncertainty

Uncertainties in hydraulic stability data are challenging to identify and quantify. The inherent stochastic nature of waves and stones cannot be denied. Data uncertainty arises from various sources, including measurement errors, the frequent use of non-homogeneous data, the application of statistical distributions for database description and extrapolation (data handling and post-processing), and similar factors.

Several authors have provided insights into uncertainties associated with the design of coastal structures. A notable reference is a PIANC report from 1992 [109], which offers a comprehensive summary of variation coefficients.

5.4.1.1. *Hydrodynamic measurement and selected wave characteristics*

The techniques and procedures used in the physical models of rubble mound structures under wave attack have evolved rapidly in recent decades, facilitating more accurate simulation of sea states and comprehensive interpretation of model responses. The quality of wave generation and wave gage measurements has overwhelmingly improved, benefiting from advancements in control system theory and computer

hardware. Technological progress has reached a point where the literature seldom questions or discusses the accuracy of physical model measurement.

However, disparities between laboratory methods and technologies have also grown over the last few decades, partly due to the absence of recent deliberate and multinational efforts towards unification and standardization. Multinational efforts to equilibrate laboratory methods were relatively common in the 1980s and 1990s [110] but are rare now. Hence, some variabilities between results obtained from different lab experiments and periods are expected. These variations can be attributed to many factors such as wave generation systems, wave acquisition systems, wave analysis procedures, etc.

Figure 5.2 illustrates some of the primary sources of uncertainty in the laboratory hydrodynamic measurements, which are fully discussed in this paragraph.

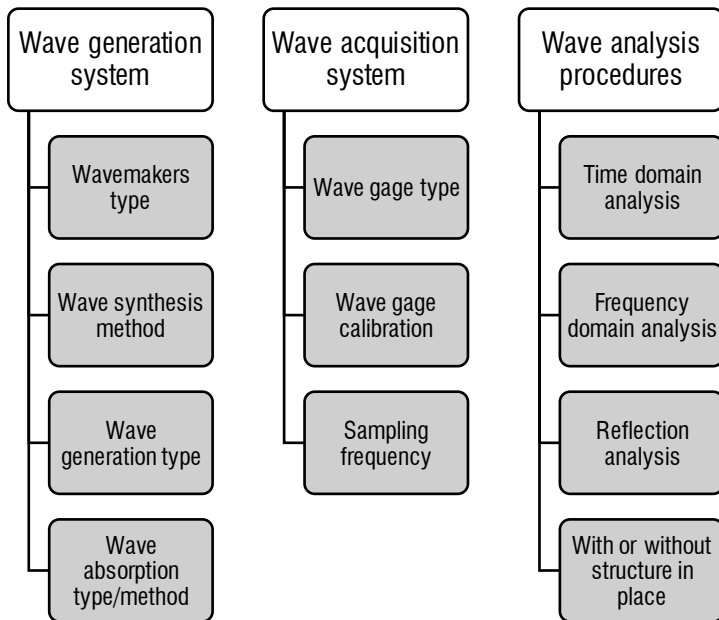


Figure 5.2. Main sources of uncertainty in lab hydrodynamic measurements.

Ocean waves in laboratory wave tanks are generally simulated using servo-controlled wavemakers, where a movable partition is positioned within the wave facility. The oscillation of the partition generates waves, and wave gages measure free surface elevations. Methods can be employed to separate incident and reflected waves at specific points of interest in the wave flume.

Nowadays, wavemakers and wave probes are much more stable and reliable than in the 1980s and 1990s, leading to greater accuracy through a digital acquisition system achieving high fidelity with the natural sea state. In addition, modern computer-based data acquisition can sample at significantly higher rates and for longer duration, both for commanding a generator and collecting measurements, compared to the limitations of the 1980s and 1990s. The extension of simulation durations provides a more precise definition of the low-frequency end of the wave spectrum. Finally, spectra are now defined at higher density than in decades past.

In literature, it is possible to find many different types of wavemakers accompanied by numerous wavemaker theories and synthesis techniques capable of generating irregular waves (e.g., [48], [49], [50]). The dissimilarities in these approaches could contribute to variations in results. For example, some facilities can only operate their wave machine in the piston mode, others exclusively in flapper mode, and some can use any combination of piston and flapper. Wave machines also differ concerning the wave board's driving power and available stroke. An underpowered machine may be unable to generate waves spanning the entire target wave spectrum, while other machines with limited displacement stroke may face constraints in generating or absorbing long waves. Although modern approaches are quite similar across labs, comparing modern simulations with those conducted decades ago is expected to reveal significantly more uncertainty in the older experiments.

Much has also been written about the synthesis of irregular waves. Funke and Mansard's paper [111] cites many significant publications on this topic. The chosen

method of wave synthesis can have a considerable effect on test outcomes. However, it is argued that variations in wavemaker type and wave synthesis method are likely to yield only minor dissimilarities, as they are, to a large extent, very similar ($\sigma' < 1\%$). Furthermore, it is economically and practically impossible to run tests for very long periods of time, run many realizations, and explore all possible combinations of test and wave parameters. Therefore, choices must be made, and it is in these choices that significant differences can emerge.

Efforts to generate waves in a flume using sinusoidally varying wave board motion, as derived from first-order wavemaker theory, may inadvertently produce undesired free secondary waves that move at a slightly slower speed than the primary waves [112]. Combining these primary and secondary waves results in a combined waveform that varies both spatially and temporally. To prevent this, it is necessary to calculate and eliminate various spurious components from the command signal, a procedure commonly referred to as second-order wave generation technique [113].

If the wave generation process does not account for the nonlinear higher harmonic wave activity, distortions in the wave spectrum can be inadvertently generated and exacerbated. Mansard [114] illustrated the differences in generating 1st or 2nd order waves, highlighting that distinct wave generators and control systems can introduce inaccuracies. Classical 1st order wave generation, which neglects for the bounded character of waves, inadvertently generates parasitic waves and gives rise to free error waves at higher orders, both at sub- and super-harmonic frequencies. In contrast, the correct simulation of harmonics in a model is achievable using 2nd order wave generation techniques.

[115] numerically demonstrated that experimental investigations that do not apply second-order corrections correctly may be affected by the presence of second-order error waves, particularly at sub-harmonic frequencies. Ignoring such errors could lead to increased wave-induced run-up and force, resulting in overly conservative design

parameters [112, 116]. In scenarios where the magnitudes of these harmonics could be substantial, say in shallow water, classical 1st order wave generation may produce inaccurate results. However, when second-order generation is implemented, the generation of second-order sub-harmonic bound waves is often incorrect due to constraints on the extent of wavemaker displacement [117, 118].

An additional significant factor contributing to hydrodynamic uncertainty is the ability to absorb most seaward-propagating waves using active reflection compensation systems. In nature, waves reflected by coastal structures generally dissipate in the ocean through diffraction. Conversely, in experimental basins or flumes, waves propagate towards the wave generator and are re-reflected by it, if not absorbed. These re-reflected components alter the statistics of target sea states and can accumulate over a long duration.

Depending on the relative phasing of the incident and re-reflected waves, this phenomenon can lead to either an increase or a decrease in the incident wave conditions, thereby limiting the accuracy with which flume tests can predict the stability of structures such as rubble-mound structures. An active wave absorption control system proves effective in mitigating this issue [119]. Some wavemakers use the second-order wave generation technique to minimize higher-order long waves generated by the wavemaker. However, despite wave generation being limited to wind waves, waves observed in the nearshore zone contain free long waves (not related to local wind waves), that are not considered in laboratory experiments and contingent on the boundary conditions of the wave tank. [120] emphasized the importance of the new active absorption system in compensating for both linear and nonlinear re-reflected waves in the wave flume. It is important to note that systems designed to absorb reflected energy are only partially effective. It is difficult to impossible to absorb waves with frequencies lower than 0.2 Hz due to stroke limitations in small-scale models. Consequently, it becomes virtually impossible to prevent the buildup of wave energy caused by re-reflected waves in stability tests. [121] provided guidelines on the validity

of wave generation theories based on the nonlinearity of the sea state. Free unwanted waves are generated if a wave generation method is used outside its applicability ranges. Therefore, choosing the correct wave generation and absorption types is essential to obtain reliable stone armor stability results. These aspects contribute significantly to the uncertainty of the wave generation system.

[122] discussed the effects of the random variations in the generated seed number and varying armor placement on the stability response of a stone-armored breakwater. They concluded that “*repeat testing is a must*” to ensure the reliability of the test and to capture the range of aleatory variations. Uncertainty arose from differing construction techniques from test to test and the use of different random number seeds to generate the spectra. As expected, the wave height corresponding to the no-damage condition exhibited wide variation. Analogously, [123] suggested that tests should be repeated at least two to four times to establish sufficient statistical certainty in the expected outcome, with more extensive testing conducted if the variance is large.

The correlation between wave groups and damage to the armor layer was controversial for the research community, especially during the 1980s. All the possible wave spectra generations and wave grouping were found to significantly impact the results of the incident wave, as reported by [124] and [125]. This effect is more pronounced in non-breaking areas (deep waters) compared to breaking regions (shallow waters) due to the decrease in wave grouping in shallow waters.

Additionally, uncertainties can arise from differences in pre-processing and wave acquisition systems. It is crucial to regularly calibrate instruments, although modern instruments, being extremely stable, are less affected by temperature or dirt compared to their predecessors. Laboratories typically use capacitive or resistive wave gages and conduct static or dynamic calibrations with various techniques to establish calibration curves and relative errors, ensuring high accuracy in data acquisition. Differences between resistive and capacitive wave gages may emerge when dealing with bore wave

breaking waves in very shallow water conditions over a wide surf zone. Such measurements in shallow waters are likely to contain significant unknown uncertainty.

Another consideration is the sampling rate at which data are collected. A lower sampling rate (i.e., less than 20 Hz) may induce uncertainties due to aliasing, leakage, glitches, or loss of information. This phenomenon is more pronounced in shallow water conditions and poses a more significant issue for data collected decades ago compared to the improved practices in recent times.

Furthermore, analysis techniques and post-processing procedures may vary significantly, leading to different estimates of wave parameters. Smoothing, truncations, detrend functions, and cut-off filters applied to measured time records can introduce remarkable differences in bulk wave parameters. While modern digital signal processing techniques can partially remove these spurious effects, variations in magnitude and different analysis methods can induce uncertainties, especially when utilizing wave data from laboratories in the 1980s.

Spectrally derived wave parameters are contingent on how spectral density is computed, with various algorithms offering several filtering options, weighting windows, and overlapping sub-records for smoothing spectra. Differences in analysis results are not surprising given these variations. Mansard and Funke [110] attempted to evaluate differences in test results caused by experimental conditions by conducting the same experiment in nine different laboratories. They noted that the algorithmic component of variability for significant wave height is not problematic, resulting in variations of $\pm 1.4\%$, which seems acceptable. However, variability in spectral analysis may typically lead to variations of $\pm 2-5\%$, while differences in reflection analysis amount to $5-25\%$.

These findings, though dated, were revisited by [107, 108], who specifically addressed this topic and reported typical variation coefficients for sea state parameters based

primarily on personal experiences, individual projects, and restricted information. They reported that significant wave height (H_s) and spectral wave height (H_{m0}) have $\sigma(y)' = 5-35\%$, whereas peak wave period (T_p) or spectral wave period ($T_{m-1,0}$) have $\sigma(y)' = 5-15\%$. While these variations may be considered relatively large compared to [110], they appear relatively small compared to that proposed by Goda [73] and the EurOtop manual [99]. T_p is a typical example of a very sensitive bulk wave parameter and highly depends on the spectral computation method and smoothing windows. However, in many engineer analyses, integrated periods like T_m and $T_{m-1,0}$ are often preferred to avoid large uncertainty associated with T_p resulting from chaotic shifts in the spectral peak with little change in the underlying wave climate.

In dealing with measured wave spectra, it is common to apply lower and upper cut-off frequencies, and these choices can impact the computed values for wave parameters. Researchers may also place significant importance on higher and lower spectral moments, which are especially sensitive to white noise background or arbitrary cut-off frequencies. In shallow water conditions, applying a high-pass filter may introduce errors and inaccuracies, particularly in not considering the IG waves ([126], [127]). Surf beats occur when deep water waves propagate into shallow water. Entering shallow water, waves exhibit increasingly strong nonlinearities. One substantial nonlinear effect is the emergence of low-frequency energy resulting from the interactions between higher-frequency incident wave components. These low-frequency components, with periods of several minutes, cause water level variations in the surf zone. Compared with wave impact, on average, surf beat has only a minor contribution to the forces acting on the stones, and therefore it is, in most situations, neglectable. However, when wave heights are low (in the order of centimeters), e.g., TS, VdM, and EUMER datasets, the effects of surf beat on stability may not be negligible. The same consideration applies to the effects of wave reflection. Laboratory techniques may introduce even larger variations than those described above. Waves

may be measured with or without the structure in place, or in an open section, and wave reflection may be measured or not.

This section addressed only a portion of the broader non-uniformity problem in the analysis method. Many other parameters, such as wave steepness and asymmetries, are known to be extremely sensitive to specific computational details. Further, information about spectral and statistical analysis, recorded time series, and filtering processes is needed for reproducibility. The determination of proper wave characteristics, such as wave height and wave period, is still an ongoing process. Presently, $T_{m-1,0}$ has been recognized as more consistent than T_p . However, attention must be paid to the spectral wave filtering procedures, especially regarding the impacts of IG on stability ([126], [127]). [70] and [72] focused on H_{m0} because it is less influenced by wave nonlinearity. This observation has been recently confirmed by Van der Meer [104].

Parameters like H_{m0} and $T_{m-1,0}$, resulting from spectral integration are considered robust wave parameters compared to a low exceedance time domain wave height like H_s or $H_{1/10}$, which can vary considerably with small variations in the realization. Moreover, these parameters are typically output from numerical spectral wave models and are usually available for design without relying on empirical relations, unlike time domain parameters that necessitate detailed knowledge of the wave height distribution. Also, if the time domain parameters are determined from an indent wave spectrum, the details of the wave spectrum are relatively more important. The choice of wave characteristics in depth-limited water conditions may introduce inaccuracies between models, as reported by [60] and [61].

Spectral parameters are outputs from commonly used Goda and Suzuki and Mansard and Funke incident and reflected wave resolving techniques. If these methods are not used, total wave energy spectral analysis tends to be very similar across laboratories, whereas time domain analysis techniques may vary. For instance, questions arise

regarding whether zero up crossing or down crossing is used, and whether the zero-crossing is applied to the time series synthesized after applying the incident and reflected wave routine or to the total signal. More often than not, such details are not published.

An additional significant aspect is how and where to compute the incident wave. [128] and [70] have suggested measuring the incident wave at a distance of $5H_s$ and $3h$ seaward from the structure toe, respectively, to account for the plunge distance of the largest breaking waves. Undoubtedly, especially in shallow water conditions, the location of the incident wave may affect the results and will be influenced by the foreshore slope and nonlinear wave transformations (e.g., shoaling and breaking).

Reflection analysis is another major source of uncertainty in lab-based data. To isolate the incident and reflected wave components, it is theoretically sufficient to use simultaneous measurements of the standing wave system at two known positions in the flume, in a line parallel to the direction of propagation, to resolve a narrow frequency range. This technique, known as the 2-point method, is extensively used to determine the reflection characteristics of test structures [88, 129]. However, real wave conditions have a wide frequency range, demanding multiple spacing between gages. Therefore, some laboratories use more than two gages and achieve better estimations by averaging reflection coefficients computed from different pairs of gages [130]. Note that this method results in an averaging of the waves across the space of the multiple gage array. Uncertainty in the incident wave characteristics will increase with wider gage array footprints and steeper bathymetry and this is not addressed in the armor stability literature. Other alternate methods use a least squares technique to resolve the incident and reflected characteristics using simultaneous standing wave measurements at three probe positions [90]. It is important to stress that the most popular methods are based on the assumption of flat sea bottom and LWT, leading to high inaccuracies for shallow water conditions [131]. Besides these fundamentally LWT approaches, there are various advanced techniques to resolve the incident spectrum, differing in the

way phase relationships and reflection coefficients are calculated (some examples are [132], [92], [133], etc.). It is essential to point out that, no matter how hard we try to reduce the reflection within the flume, it is physically impossible to eliminate it completely. Therefore, reflection analysis needs to be considered in the analysis. Furthermore, each reflection routine has limits and optimal probe spacing, which can be challenging to achieve in a physical model. It is crucial to plot the error function and the coherency factor for each pair of wave gages to determine the cut-off frequencies for the reflection calculations. These cut-off frequencies may become necessary when applying the analysis method to real wave data, which usually includes nonlinear long waves. Finally, incident wave parameters determined from the incident wave spectrum may offer a more accurate description compared to those determined by computing the bulk reflection coefficient (K_R). For flat bottom in non-breaking waves, a multi-gage reflection analysis will likely be the optimal approach. However, for a sloping bottom in shallow water, the bulk reflection approach will typically be more accurate, particularly if the reflection coefficient is known based on deep water reflection analysis. Varying reflection analysis techniques could result in differences in results.

Another aspect to consider is whether there is a structure in place, especially if unsuitable absorption systems are present at the wave generator and the end of the flume. Wave reflection compensation is never perfect, so accumulated energy will be different in a flume with a structure compared to one without. Sometimes, a different mean-water level between tests with and without structure may occur because of differing wave setup near the structure or the waves might deviate from those at the toe due to details of depth-induced breaking, shoaling, and wave-structure interaction.

In Table 5.1, an estimation of the uncertainty in terms of coefficient of variation for hydrodynamic measurements is provided based on the literature and the discussed body of knowledge. The numbers in Table 5.1 are somewhat heuristic and assume that each laboratory is using a state of practice system and approaches. Uncertainty in any specific experiment could be much greater than those indicated.

Table 5.1. Sense of hydrodynamic uncertainty (data uncertainty) in terms of $\sigma'(y)$.

Type	Classification		Relative contribution
	Deep	Shallow	
Wave generation	< 1 %	< 5 %	IG waves, absorption system
Wave acquisition	< 1 %	< 3 %	Wave gage type
Wave analysis procedure	< 5 %	< 50 %	Reflection analysis, with or without structure, selected wave characteristics

5.4.1.2. Damage measurement

The term “*damage*” in coastal engineering commonly refers to the degree of reshaping of the armor layer after a wave attack. However, variations in definitions make the concept of damage complex. The Shore Protection Manual (SPM) [48] defined damage as the “*normalized eroded volume in the active region, since [...] the ridge until $1H_s$ below the water level at rest*”. The assimilation of results from different laboratories depends on how damage is defined, parameterized, and measured.

Distinguishing the intrinsic uncertainty of stochastic behavior of stones under random wave attack from the total epistemic uncertainty related to damage measurements is challenging. Reproducibility requires a complete description of the experimental methodology. Despite each laboratory having protocols for evaluating damage, the coastal engineering community claims for a general standardization of the method to ensure comparable results worldwide. There is a need for a uniform decision on when a stone can be considered displaced or not [134]. Typically, a stone is classified as displaced if it moves more than $1D_{n50}$ [48]. However, the new definition of the active armor layer by the CEM [22] complicates this descriptor, as the active layer is extended to the “*reference area*”, such as the complete armor area or, preferably, a specific zone around the sea water level to be defined for each particular case. This means that blocks are not individually differentiated. In other words, if a block is moved but only occupies a gap left by another, no displacement is recognized, considering the unit maintains its

protective role [135]. In the end, counting displaced units is less conclusive than using measured profiles.

Damage measurement comes after selecting an appropriate damage descriptor and is influenced by technical and methodological limitations. Figure 5.3 illustrates some of the primary sources of uncertainty in damage measurements, exhaustively discussed in this paragraph.

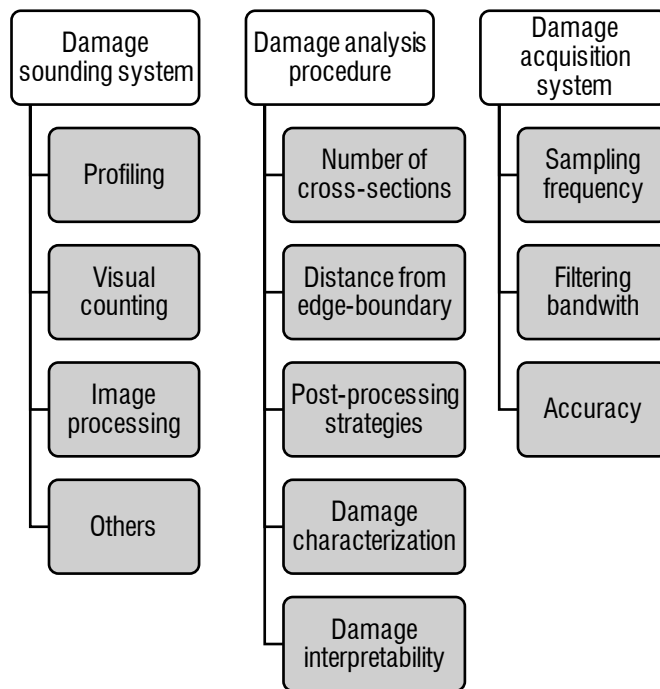


Figure 5.3. Main sources of uncertainty in lab damage measurements.

Different ways exist for measuring the damage level of a mound structure, including profiling the slope before and after the test (the most common method) ([30], [59]), counting the number of displaced stones [136], image processing, LiDAR surveys [137], 3D measuring techniques [95, 138, 139], etc. Although these methods have been improved, automated, and made less sensitive to human mistakes, and have been

compared and validated, some inaccuracies and differences between the procedures still need to be addressed.

In his Ph.D. dissertation, Cornett [140] discussed the differences in determining damage between the profiler procedure and the stone counting method. Differences in damage survey methods are also described in [141], [136], [65], and [44]. The accuracy of these methods depends on several factors, including the type of sounding system, damage analysis procedure, and the damage acquisition system.

Structure damage can be readily estimated at low damage levels by visually counting the number of displaced stones. However, this method becomes tedious and prone to human error when more than a few stones are displaced, or stones moved slightly by one storm condition are moved further downslope by a subsequent storm sequence. Moreover, the number of stones counted using this method may not be the same as those removed from their original position, because many stones can settle in already damaged areas, and these stones may not contribute to the eroded area.

Image processing allows visual techniques to be used at higher damage levels. However, the limitations of these techniques include the need to drain the basin before image capture to allow measurement below the still water line and the fact that image quality can restrict accuracy. Furthermore, most techniques allow an estimation of only the damaged surface area, not the depth of penetration of the damage.

In contemporary coastal structures laboratories, the most prevalent method for damage measurement involves profiling several cross-sections of the structure. The measurement of the cross-sectional profile is often the fastest and most reliable means of damage assessment.

[136] conducted an experimental campaign assessing damage analysis using three methods: (1) counting settled stones in more than two layers S_V , (2) image processing S_i , (3) section profiling S_P . Figure 5.4 illustrates the study by [136], wherein a

comparison of the three S_d values obtained for a conventional breakwater is reported and discussed.

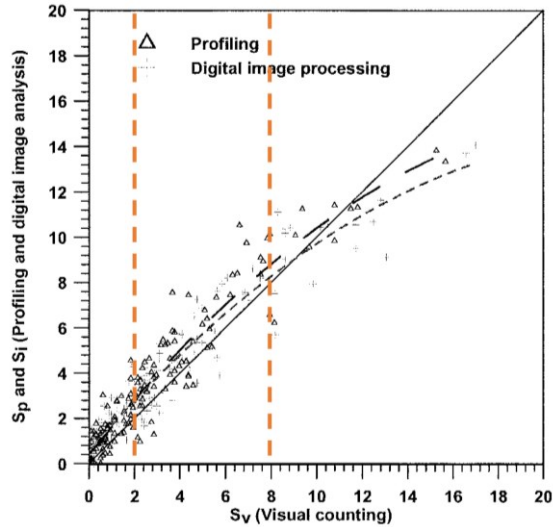


Figure 5.4. Damage estimation comparison between methods (source: [136]).

As shown in Figure 5.4, damages measured through profiling and digital image processing follow a similar trend. For very high damages ($S_d > 8$), S_V tends to be much larger than the values of S_P and S_I . However, S_I is clearly smaller than S_P because the damage starts to affect the second layer of the armor, and this type of damage is not identified by digital analysis. Instead, for $S_d < 8$, the values of S_P and S_I are, on average, larger than the values of S_V .

Although the authors did not provide a coefficient of variation, they reported an average systematic difference (bias) between S_P and S_V of about 0.7. When damage is small, most of the measured damage is due to systematic measurement errors. As damage increases, systematic error is reduced because the non-disturbed area of the armor reduces in size, explaining the parabolic shape of the fitting. For extreme damage bigger than $S_V = 12$, difficulties arise in the counting process because the removed stones can pile-up on more than two layers, making it very difficult to identify the stones located in

the lower layer. This implies that among the three methods of measuring damage, only profiling measures A_e directly, whereas the others require calibration. Many authors derived empirical formulations (for example Eq. (11)) to compute A_e given the number of displaced stones (N_d) and the geometric characteristics of the breakwater. However, such calibration introduces uncertainty ([136], [65]). The number of eroded units depends on the porosity, armor grading, and shape of the stones, but according to vdM, it is equal to 0.7 to 1 time the value of S_d .

However, using the same profiling method may also lead to differences in the results. [141] described the semi-automated profiling strategy used in their experiments and introduced two kinds of profilers: laser and mechanical. The mechanical profiler is significantly different from the laser profiler, and several differences may arise between the two methods, as reported by [142] and [57]. For example, profiling the armor layers with a mechanical probe foot causes several distortions of the transects, such as wider convexities, narrower concavities, and higher surveyed transects, generally cutting out valley rather than peak details. Conversely, high-resolution laser transects effectively provide all the peak and valley information and can be used to calculate roughness parameters and void coefficients [142]. For mechanical profilers, profiles are equal to transects. [31] stated that due to the physical contact, the mechanical profiler is an invasive technique that could even provoke the movements of armor units. After the 2000s, mechanical profilers fell into disuse with the advent of the high-density laser profiler. It is likely that older damage based on mechanical measurements are biased low compared to modern laser measurement.

The literature currently lacks references regarding the optimal accuracy of profiles or the requisite number of transects (i.e., the long-shore distance between chainages and the number of cross sections). The methodology for damage analysis procedure deemed equally important as the chosen damage analysis method. The number of transects is generally a function of armor size and the width of the testing section. In the case of a mechanical profiler, the foot size is roughly equivalent to the sieve size or

D_{n50} . However, this is not the case with a laser profiler, and there is often ambiguity in how a specific study measures and analyzes soundings. Indeed, the strategy for computing S_d from multiple transects across a section differs among authors. Some calculate S_d from an average profile obtained from a small number of transects (vdM), others uniformly profile in a dense grid and then convert to transects, while others do not even use transects at all and derive an averaged magnitude of S_d from the values of S_d on each profile [143]. For instance, [51] measured 6 profiles, [31] measured 8 profiles, [52] opted for 10 profiles, whereas [141], [30] and [63] investigated 9 profiles. Specifically, the number of profiles should be determined based on the size of the armor stones and the width of the structure.

Furthermore, it is important to profile at a sufficient distance from the flume boundary, as the armor units near the flume walls may interlock differently than those in the center of the test section. [57] observed that, due to the edge effect in the wave tank, there still seemed to be significant variation in damage across the width of the structure. In general, there is a tendency for the center of the test section to experience more damage than the outer edges, suggesting a potential model effect causing variation in damage across the width of the structure.

In addition, S_d may be based on the entire eroded area [63], the average transect, the average A_e , or the transect with the highest S [30], and variations among these methods may lead to differences of more than 30% in S_d , especially for low damage values. Including the entire eroded area in the analysis, provides a clearer definition of the damage level without subjectivity [57]. When S_d is calculated from multiple profiles over a section, the strategy may differ from one author to another. As discussed in [57], differences in how damage is evaluated can be significant, especially for the lowest damages, although they tend to decrease with the increase in damage level.

The main numerical distinction in damage measurement between the different methods arises from calculating the damage to a mean profile as opposed to calculating the

mean damage for individually differenced profiles. The method of calculating damage to a mean profile consistently yields lower results (particularly for lower damage levels) despite the consistent method of differencing the profiles. Figure 5.5 illustrates the bias (left) and relative error (right) computed by calculating the dimensionless eroded area of a section from an averaged profile (S) or from averaging damage indexes from each profile (S_{md}) using the experimental data in [57]. Although, in theory, both methods should yield the same results, in this case (shown as an example), the differences appear to be derived from the smoothing method based on cubic splines applied to the profiles by the authors. Indeed, S_{md} is calculated from smoothed profiles, whereas the averaged slope for evaluating S is calculated by smoothing the profile resulting from averaging the measurements at each fixed chainage.

This study estimated a bias of 0.96 and a standard deviation of 1.03. [87] found a difference between the two methods, ranging from 2 to 82 percent.

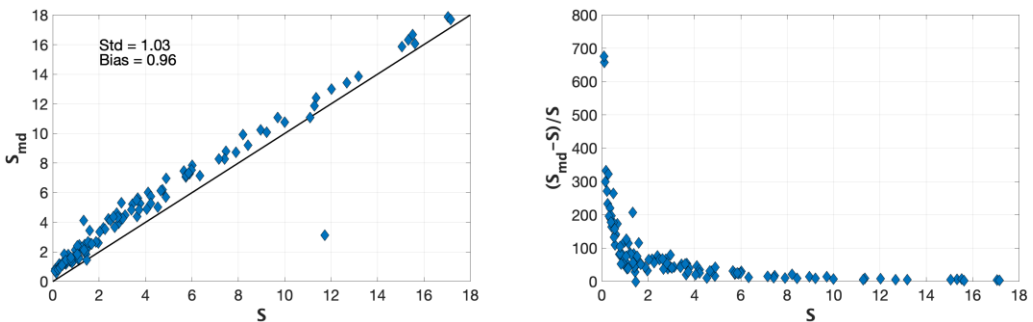


Figure 5.5. Example of uncertainty induced by damage analysis (source: [44]).

Regardless of the techniques employed, the measurement approach necessitates several post-processing strategies that are likely to affect the quantification of the eroded volume. Additionally, none of these methods provide information about the profile shape or the maximum depth of erosion, which is undoubtedly an essential parameter for a multilayer structure [7]. S_d could alternatively be based on the eroded volume (V_e) rather than the eroded area (A_e).

[101] discussed the parameterization of the depth of erosion, thickness of the remaining cover layer, and length of the damaged area. Profiling techniques, the distance between profiles, post-processing strategies, and error estimations typically vary between publications or, in many cases, are not clearly defined and detailed. Furthermore, [144] demonstrated that the normalized damage is in the range of $2.7 \leq S^* \leq 3$, where $S^* = (S - \bar{S}) / \sigma_s$ where \bar{S} and σ_s represent the mean and the std of the damage. The authors provided a formula that offers insight into the variation by considering the std of damage, that was shown to follow the relation $\sigma_s = 0.5 \bar{S}^{0.65}$, indicating that the variability of damage increases with mean damage. This variation is primarily aleatory and is attributed to stone placement. However, repeating a single test may not be sufficient to address this, raising questions about the statistical validity of the conclusions drawn by other authors.

Another significant source of uncertainty lies in the interpretation of damage, which inherently involves a degree of subjectivity, particularly concerning the “*initiation of damage*”. It is necessary to address how different damage levels might affect the functionality of the structure (operational thresholds) and how the deterioration rate is expected to evolve (structural thresholds). Researchers proposed different ways to characterize damage progression ([145], [146], [30] [22] and [26]).

Even for quantitative methods, the dispersion when predicting lower damage values is higher than for larger damage values, relative to the coefficient of variation [32]. Specifically, [32] reported the mean value (μ) and corresponding standard deviation (σ) for the same test repeated 5 times. They demonstrated that μ and σ tend to increase as the water depth increases (the coefficient of variation is higher for shallower water depth conditions). The coefficient of variation (σ/μ), which, in this case, represents a measure of the intrinsic aleatory uncertainty of damage measurement, was found to be $0.04 \leq \sigma/\mu \leq 0.15$.

For example, in the initiation of damage, the SPM suggested an erosion of 0% to 5% of the active armor zone (S_d from 0 to 1.6), vdM considered an erosion of $S_d=2$, and [147] aimed for a value of $S_d=1$. [147] also noted differences in authors' failure points. Similarly, vdM found that failure, defined as exposure of the underlayer by a hole of the size of $2D_{n50}$ for a $2D_{n50}$ thick armor layer, occurred around $S_d=8$. [148] found that there was some healing with variations of SWL across storms, and failure with exposure of the underlayer occurred at $S_d=17$.

These primary shortcomings in the interpretability of S_d stem from two main reasons. Firstly, S_d cannot characterize the spatial shape of damage because it represents a mean eroded area on a complete profile. If failure is defined as exposure of the underlayer, then parameterizing the erosion depth, in addition to S_d , is necessary to understand the vulnerability and resiliency of the armor layer. Secondly, a more concise and standardized methodology must be employed to measure and calculate damage and damage parameters like S_d .

Certainly, the resolution of A_e from the experiments is critical, and differences of $S_d=0.5-1$ may occur, especially when profiling an undamaged layer multiple time. This discrepancy arises from summing many very tiny differences, regardless of the type of instruments used. Consequently, the filtering method plays a very important role in resolving variations on the order of $S_d=1$. Damage measurement error tends to be greater for small damage values, and mechanical systems may not resolve small S_d at all. Lasers, on the other hand, may provide S_d values up to 1 even in the absence of damage, due to the laser hitting different locations on the stones. It has been observed that most errors originate from deep voids where stone faces are steep, causing slight horizontal shifts to produce significant differences in z . Also, water droplets may impact measurements, experiencing diffraction through the water and introducing errors. If S_d is around 1-2, the error could be even 100%. However, as the damage increases, the error tends to decrease.

In general, many aspects need specification for reproducibility, including methods for identifying and filtering erroneous values in raw data, profile/surface reconstruction methods (such as interpolation, fitting, or meshing), types of smoothing methods, methods for filtering possible settlements (such as rocking), and methods for integrating the eroded area/volume (such as the Simpson's method). According to [149], considering laboratory occupation times, a minimum of five repetitions should be carried out to obtain an accurate average damage value.

Undoubtedly, as recursively emphasized by different authors, one of the pending challenges in the parametrization and measurement of damage is the standardization of procedures and protocols for laboratory damage measurements, as for hydrodynamics. This standardization is crucial for characterizing damage dispersion by replicating experiments within the same laboratory, assimilating data from different laboratories, and enhancing the database with normalized results.

The range of variation for damage descriptors spans the range of 30%-100%. This requirement is classified as only partially fulfilled for descriptors with limited available information or an undefined range of variation. The improvement and availability of accurate 3D measuring techniques, coupled with the versatility of artificial vision algorithms, present an opportunity towards more interpretable damage descriptors or combinations between them. With the implementation of advanced measuring techniques, it is anticipated that the traditional "*side view*" of profiling methods and the "*front view*" of visual method will be combined to achieve a more comprehensive characterization the slope reshaping. Standardization the inspection process, utilizing assisting software, and clearly defining thresholds for distinguishing between rocking and displacements are only some of the issues required for reproducibility.

Table 5.2 provides an estimation of the sense of uncertainty in terms of the coefficient of variation for damage measurement based on the literature and the body of knowledge discussed above.

Table 5.2. Sense of damage uncertainty (data uncertainty) in terms of $\sigma'(y)$.

Type	S<2 & S>15	2<S<15	Relative contribution
Damage sounding system	< 100%	< 20%	Type of system
Damage analysis procedure	< 100%	< 50%	Number of profiles, post processing strategies, damage characterization, damage interpretability
Damage acquisition system	< 100%	< 5%	Sampling frequency, filtering, accuracy

5.4.2. Model uncertainty

Model uncertainty can be divided into two primary components: statistical distribution uncertainties and empirical and theoretical model uncertainties. Statistical distribution uncertainty pertains to statistical distributions of random quantities (fixed time parameters) and random processes (variable time parameters). It can be reduced by increasing the volume of data and enhancing the quality of collected data. On the other hand, empirical and theoretical model uncertainties relate to the empirical (data-based) and theoretical relationships utilized to describe physical processes, input variables, and equations. This type of uncertainty can be mitigated by increasing knowledge and refining models.

Specifically, model uncertainty is tied to the current understanding of processes, limitations in modeling, variations in approach, and the extent to which physical processes in nature are inadequately reproduced. Model uncertainty arising from physical model limitations and approach variations often results from the scarcity of experimental data and disparities in techniques and procedures adopted during the setup and construction of the physical model, leading to a mixture of non-homogeneous datasets.

On the other hand, predictive model inadequacy can be caused by missing or overly simplified processes and parameters, as well as the inadequacy of selected parameters and the chosen predictive model. [84] stated that the main sources of uncertainty in stone armor stability could be attributed to the omission of even one independent non-dimensional variable (for example, relative depth), a scarcity of experimental data in shallow water conditions due to limitations in relative wave height ($H_{m0}/h > 0.14$), and the mixing of non-homogeneous data to develop a new formula (for example, mixing vdM and VML data). Furthermore, [150] examined epistemic uncertainty in design formulae for slope breakwaters in terms of experimental design and the method used to select variables influencing the hydraulic performance of the structure. The authors concluded that the data scatter in vdM design formulae comes from the method used to elaborate such formulae, which omits dimensional analysis, and that vdM data are derived from a specific experimental technique.

Figure 5.6 illustrates the main sources of uncertainty in stability formulae associated with model uncertainty. At this point, we are in the process of discerning the relative contributions of missing physics and model uncertainty. Indeed, it is difficult to separate the uncertainty related to each contribution because these are likely to be muddled together.

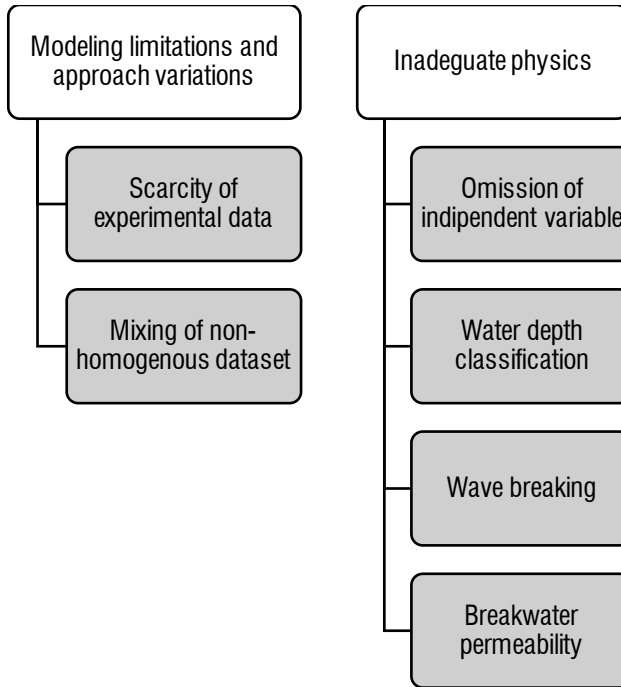


Figure 5.6. Main sources of model uncertainty in stability.

Certainly, a significant source of uncertainty in the predictive models arises from how water depth, wave breaking, and structure permeability are described and incorporated into the equations. The classification of water depth conditions and the type of wave breaking on the structure slope are crucial factors that introduce considerable uncertainty in predictive models. Various classification methods have been proposed by different researchers, such as [151], [30], [152], [64], [65], [100], among others, to classify water depth conditions. Similarly, different criteria are employed to classify wave breaking on the structure slope, including approaches by [55], [30], [153].

It is essential to recognize that the choice of classification methods for wave breaking, and water depth can considerably affect results, potentially leading to different equations for the same data. For example, this aspect is crucial at the discontinuity point between plunging and surging equations, where a slight change in wave

steepness can lead to an entirely different stability prediction. Therefore, careful consideration and standardization of these classification criteria are essential to enhance the reliability and comparability of predictive models.

Figure 5.7 presents vdM data (16 groups) classified and separated into plunge and surge breaking conditions using different breaking classification methods. Specifically, the criteria adopted by Melby (ERDC), van der Meer, and Battjes were used. ERDC's criterion, $s_{m,c} = (\cot\alpha)^{-3}$, relies solely on the structure slope and is derived by analytically intersecting plunging and surging equations (Eq. (21d)). Similarly, vdM criterion, derived in the same way, is based on the mean SSP, as reported in Eq. (3c). Battjes proposed that the SSP using the mean wave period (ξ_m) can serve as the dynamic similarity parameter to analyze the behavior of a wave train over a general slope. According to Battjes, wave approaching slopes can experience four different types of breaking modalities: spilling ($\xi_m < 0.3$), plunging ($0.3 \leq \xi_m \leq 2$), collapsing ($2 < \xi_m < 3$), and surging ($\xi_m \geq 3$). In this section, collapse and surge cases are combined into the "surge" class ($\xi_m > 2$), and spilling breaking is not considered due to the absence of vdM data in such conditions. The same method was also used in Eq. (8) by [79].

The stability equations can cloud the different wave-structure interaction phenomena due to uncertainties related to this aspect. Indeed, vdM data were mainly collected in deep water conditions with a flat bottom, and thus, there should be clarity in determining the actual type of breaking on the structure slope. However, as shown in Figure 5.7, subjectivity arises if different methods are used. Additionally, in shallow waters, waves may break on the foreshore slope rather than on the structure, which introduces complexities in describing stability, especially in a wide surf zone where wave breaking occurs on the foreshore slope, not the structure slope.

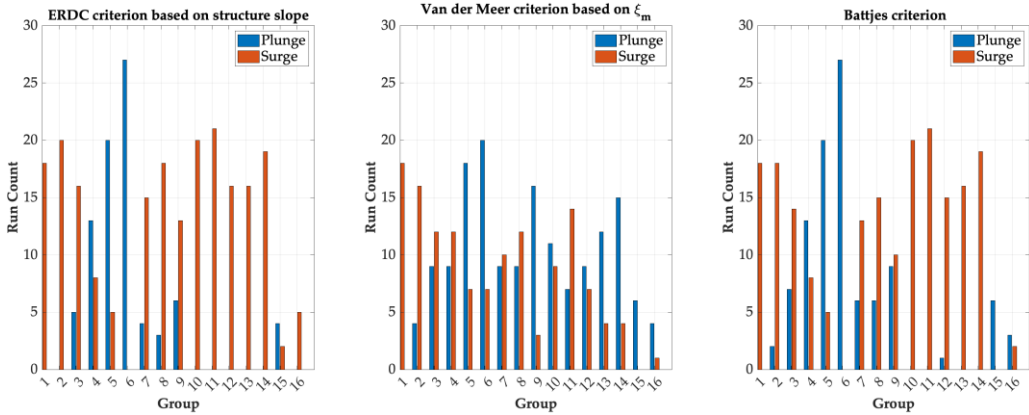


Figure 5.7. Example of breaking classification types using vdM data.

On the other hand, the permeability parameter is also an important variable in the stability equations. It is related to the volume of the water stored/dissipated in the structure during a wave attack [30] and depends mainly on the structure geometry and core and filter characteristics, although other characteristics may also influence it ([154], [94]). The permeability of the structure influences wave-structure interaction processes like the internal set-up of the phreatic surface, wave run-up and wave run-down, and, velocities and pressures around individual stones in the armor layers [155]. Van der Meer empirically estimated three notional permeability values ($P=0.1, 0.5, 0.6$) for the tested layer compositions and introduced $P=0.4$ using the numerical model HADEER. However, P is somewhat heuristic and was introduced to fit stability laboratory data to a (semi) empirical formula.

The armor mass of a coastal structure designed using the vdM equation is very sensitive to the adopted notional permeability factor, as discussed by [105]. Moreover, permeability for a low-crested or reef breakwater in shallow water will affect stability differently from the tall structure in deep water tested by vdM [156]. P ranges from 0.1 for an impermeable core to 0.6 for homogeneous breakwaters. However, [57] suggested that a more realistic estimate of P should begin from 0.05–0.07. Usually, the choice of P is left to the designer's experience, but this is a source of uncertainty.

[105] provided P values and a simple empirical formula ($1 \leq P \leq 0.6$) for seven structure layer compositions. They found good correlation with a typical deviation of 3% between estimated and fitted notional permeability factor.

Different attempts to improve the description of permeability in stability equations have been made over time (e.g., [63], [79], [105]). [59] and later [79] introduced the term $\frac{D_{n50,core}}{D_{n50}}$ as a more physical parameter. This considers the global permeability of the structure, assuming that filter layers have a minor effect. Of course, using a single parameter ($D_{n50,core}$) to characterize the permeability is a simplification, but the size of the core material is likely the most important one.

Finally, concerns arise about computing the incident wavelength in depth-limited wave conditions where LWT may result in a large error. Many authors consider the deep water wavelength with values calculated at the structure toe [66], but for shallow water, this procedure lacks physical meaning [30].

Table 5.3 estimates model uncertainty in terms of coefficient of variation based on the literature and the body of knowledge discussed above. The selection of P , computational approaches for shallow water wavelengths, and other factors contribute to model uncertainty in stability equations.

Table 5.3. Sense of model uncertainty in terms of $\sigma'(y)$.

Type	σ'	Relative contribution
Modeling limitations and approach variations	<10%	Scarcity of experimental data and mixing of non-homogeneous data
Physics understanding	<50%	Omission of independent variable, water depth classification, breaking classification, permeability factor, etc.

5.4.3. Errors

Errors during laboratory experiments represent a considerable source of epistemic uncertainty, encompassing human, instrument, and organizational errors. These errors arise from various factors, including production, abrasion, maintenance, and other human mistakes that may not be fully captured by the model. Contributors to uncertainty in this category also include operators (such as designers), organizations, procedures, environment conditions, equipment, and interfaces between these sources. Improving knowledge and organizational practices can help reduce errors in laboratory experiments.

Inaccuracies and uncertainties can also be introduced during laboratory model set-up, model construction, and modeling procedures. To facilitate meaningful comparisons of results across different laboratories, it is essential to maintain consistency in procedures and methods.

Figure 5.8 illustrates some of the primary sources of uncertainty associated with laboratory experiments. Recognizing and addressing these sources of error are crucial for enhancing the reliability and reproducibility of experimental results in the context of wave-structure interaction studies.

Stone characteristics and breakwater construction are aspects to consider. Parameters such as stone density, stone shape roughness, stone uniformity, layer thickness, stone scaling, placement criteria, packing density, and breakwater geometry can add significant uncertainty to the predictive models. However, several studies have investigated the effects of some of these characteristics on stone slope stability and found that, in specific conditions, uncertainty related to variations in these parameters may not be influential.

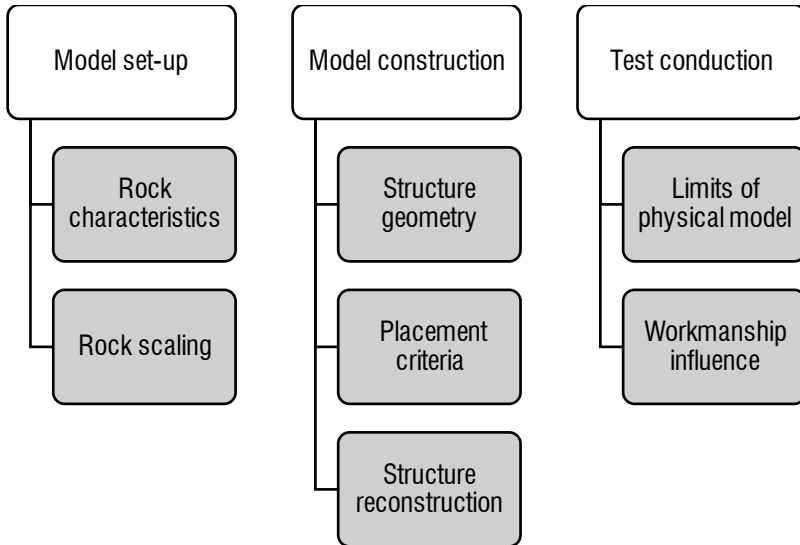


Figure 5.8. Main sources of errors uncertainty.

For example, [157] demonstrated that uncertainty related to relative density does not affect stone slope stability in the range of $0.924 \leq \Delta \leq 2.050$, where the effect of relative density is well described by the stability number term. [87] found that the uniformity coefficient does not affect hydraulic stability if in the range $1.25 \leq D_{85}/D_{15} \leq 2.25$. Similarly, [158] and [159, 160] reported that stone shape, packing density, layer thickness, and placement criteria have minor effects on hydraulic performance if certain conditions are met, such as $LT \leq 2.5$, $50\% \leq BLc \leq 60\%$ (equant stones), $1.8D_{n50} \leq t_{\Delta} \leq 2.25D_{n50}$ and a bulk-random placement criterion is used. LT is the armor length-to-thickness ratio, BLc is the armor Blockiness coefficient, and t_{Δ} is the armor layer thickness, as reported in the Rock manual [26].

According to [161], the thickness of the underlayer and the size of the material if the underlayer can have a slightly impact on stability. Thick filters (filter layer thickness $= 2D_{n50}$) were observed to increase the P value of revetments by up to 0.15-0.20, resulting in an almost 10% decrease in the required stone size. [162] and [163] found that no stone scale effects are present if $1 \times 10^4 \leq Re_{\text{armour}} \leq 8 \times 10^4$ and $Re_{\text{core}} > 300$.

[101] found little difference in ultimate damage after multiple storms for armor layers with uniform and wide stone gradation. [30] stated that the relative freeboard (R_c) has no effect if no or little overtopping conditions occur on the breakwater. However, considering stone stability, taller structures are likely to be relatively more stable for a given wave height due to increased restraining downslope gravity forces. Thus, experimenting with non-overtopped structures with high crest heights may not be conservative regarding damage development.

[32] demonstrated the influence of the width of the test section on the statistical values, showing that the damage values are affected by the width over which the damage is determined. The interaction between stone shape, placement method, void porosity, packing density, and armor stability is complex and not clearly discussed in the literature.

The methodology used for damage analysis, including the type and frequency of tests (e.g., shake-down test, survey, 1000 wave, survey, 2000 wave, survey, etc.) plays a crucial role in comparing damage data. How and how often the structure is reconstructed is another essential element to be considered in investigating the sources of uncertainty. What is more, workmanship errors can be present in the physical model (bathymetry, geometry, stone sieving, stone scaling, etc.), measurements, acquisition systems, and post-processing procedures.

Minor deviation errors may occur due to round-off errors in gravitational acceleration (g) and the number π . Slight differences may occur because of scaling errors in document scanning [69] and the use of less sophisticated software packages and computer programs with analog systems.

There is a great variation in experimental facilities and test basin layouts worldwide. Wave flumes are used with a wide variety of width, depth, and length combinations. The deeper flumes can be used for model studies with larger scale factors than smaller

ones. The length scale factor is a possible cause of some differences in experimental results. There is evidence that differences can result from dissimilar wave flume lengths. Long waves cause the principal problem. These are the group-bound waves and those that are inadvertently produced by the wave generator. These long waves are re-reflected inside the wave tank, increasing their energy based on the flume's length and the test's duration. It is challenging to deal with the long wave components in wave tanks, and there are no simple solutions. Some laboratories have adopted much longer stroke wave generators to better simulate and compensate for long waves, but this introduces another source of disparity between coastal laboratories worldwide.

The most common technological application for improved wave simulation involves minimizing the inadvertent generation of second-order spurious long waves by second-order wave generation. Despite this, second-order waves will be re-reflected and active wave absorption may not be able to deal with this problem due to the limitations of the paddle stroke [164]. Differences in the length of a test flume do not affect the specified first-order sea state parameters; however, flume length significantly affects the presence and magnitude of spurious long-wave [164].

Another interesting cause of the discrepancy in results could be the mean water level set-up behind flume obstacles. The wave activity will produce the set-up against a certain head, but the water must come from somewhere. In the flume, the supply may be limited by the layout of the facility or the test arrangement. In some cases, there could be side channels that absorb waves and become a water source. In another case, the flume area behind the pond may be able to supply water into the test area via side channels. These differences explain many of the discrepancies in the mean level measurements. It is common to employ a return pipe that returns water to the seaside of the structure.

Tracking and isolating uncertainty related to “*errors*” is very difficult, if not impossible. Providing a sense of the coefficient of variations for each aspect is complex due to the

interconnections between all the parameters. However, if data are homogenous regarding model set-up, model construction, and test conduction, it can be assumed that the uncertainty is low ($\sigma' < 5\%$). Human errors are not explicitly considered in the present manuscript, as they tend to be specific to individual problems, and universal approaches are not readily available.

5.5. Conclusion

This section extensively discusses the primary sources of epistemic uncertainty in stone armor stability, categorizing them into data uncertainty, model uncertainty, and errors. Each potential influencer on uncertainty is introduced and discussed within these three categories. Additionally, an estimation of uncertainty (expressed as a coefficient of variation, σ') is provided for each category and class to convey a sense of the magnitude of their influence on the total uncertainty in predictive models.

Table 5.4 summarizes an estimation of σ' and the relative contribution of each category, with some values estimated from the literature and others derived from the collective knowledge of coastal engineering experts.

Table 5.4. Sense of total epistemic uncertainty in stone armor stability in terms of $\sigma'(\psi)$.

Type	σ'	Relative contribution
Data uncertainty	0–50%	Hydrodynamic and damage measurements
Model uncertainty	0–40%	Modeling limitations and approach variations and physics understanding
Errors	0–10%	Human, instruments, and organization errors

In this chapter, it is argued that the largest contributions to uncertainty in stone armor stability lie in the data and model uncertainty. However, upon analysis of the datasets, a significant similarity among them was revealed, with aleatory uncertainty being predominant and closely associated with damage measurements.

Distinguishing between epistemic and aleatory uncertainty, as well as the quantification and separation of their relative proportions to the total uncertainty, presents a complex challenge. The intricate relationship between model uncertainty and data uncertainty adds another layer of complexity to this issue. To tackle this challenge, a primary focus should be on estimating data uncertainty. By gaining a clearer understanding of the uncertainties associated with the available data, researchers can take significant strides in reducing the cloudiness in model predictions.

Improving the accuracy and reliability of data through standardized procedures, consistent methodologies, and enhanced data quality can contribute to a more robust foundation for predictive models. While complete separation and precise estimation of the relative contributions of epistemic and aleatory uncertainty may be challenging, a systematic approach to reduce uncertainties in the available data can serve as a crucial step toward enhancing the overall predictive capabilities of models.

This iterative process of refining data quality can subsequently lead to improvements in model uncertainty, fostering a more accurate representation of the underlying physical processes.

CHAPTER 6

Prediction of waves transformation using Boussinesq model

6. Prediction of waves transformation using Boussinesq model

To minimize uncertainty associated with hydrodynamic measurements of wave and water levels parameters, simulations were conducted using a numerical high-fidelity phase-resolving wave transformation model for 5 out of the 7 studies (excluding TS and VML). This approach aimed to enhance accuracy by improving the synthesis and homogenization of the database from a hydrodynamical standpoint.

6.1. Motivation and objectives

In this section, the setup and calibration of a 1D fully nonlinear Boussinesq numerical model were carried out to investigate the hydrodynamic uncertainties in the stability laboratory data of the new extensive database discussed in Section 3.8. This approach allowed for a comparative analysis of various laboratory studies with consistent waves, facilitating the isolation of the hydrodynamic uncertainty from the total uncertainty in the stability equations. Indeed, certain sources of uncertainty highlighted in Section 5.4.1.1 can be resolved through numerical simulations.

By comparing wave measurements obtained using the numerical model, several sources of uncertainty, such as instrument errors (drift, calibration, sampling), analyses method, reflection analysis, gage location, and structure vs no structure in place, can be avoided. Consequently, data can be homogenized consistently. For

example, given that wave height is a predominant parameter in armor stability and damage formulae, minimizing uncertainty arising from wave observations and limited parametric characterizations (e.g., wave generation, measurements, reflection quantification methods, how and where incident waves are observed, wave analysis procedure, etc.) is crucial.

The objective is to represent incident wave parameters accurately and consistently along the flume and the forces acting on the structure. The motivation behind this effort is to create a homogeneous database, as if all stability tests were run in the same laboratory, by the same individual, and using the identical methods and techniques. This systematic approach is anticipated to aid in resolving uncertainties related to waves and water levels in the laboratory.

6.2. Literature survey and choice of the numerical model

For this reason, selecting an appropriate numerical model is essential. Numerical wave models can be categorized into phase-averaged models and phase-resolving models. Phase-averaged models simulate waves in a stochastic manner and are highly efficient, but they face limitations in predicting IG waves and often yield poor predictions of wave set-up [165]. Various phase-averaged models, such as SWAN [166] and XBeach [167], can reasonably capture wave height variation after tuning wave-breaking parameters. However, they struggle to predict certain aspects of spectral transformation, such as diffraction, wave-wave interactions, and IG wave motions, resulting in potentially poor simulation of wave setup. In XBeach, the phase-averaged solver is employed when the model operates in stationary model. Otherwise, XBeach functions as a phase-resolving model.

In contrast, Navier Stokes models represent the most advanced phase-resolving models, further divided into grid-based and meshfree methods. While both categories can simulate splash-up and plunging due to wave breaking, their computational

intensity limits their practical use for simulating long records and processing hundreds to thousands of simulations. SWASH is an example of phase-resolving [168].

Recently, among phase-resolving models, Boussinesq-type (BT) wave models based on the BT equations ([113], [169], [170]) have emerged as predominant due to their high efficiency and effectiveness compared to the Peregrine formulation [171, 172]. Progress has been made in addressing numerical dissipation, dispersion properties, non-linearity, vorticity, and various numerical formulations over time ([173], [174], [175], [176], [177, 178], [179], [180], etc.). Formulations that include run-up and wave breaking have also been developed (e.g., [181], [182], [183]). The latest developments, utilizing approximate Riemann solvers in combination with TVD limiters ([184], [185], [186], [187]) provide improved model stability and simulation precision using shock-capturing finite volume (FV) methods [188].

[189] conducted a comparison between phase-averaged and phase-resolving mild-slope models, concluding that phase-resolving models offer better predictions. Among phase-resolving models, BT wave models are deemed equally effective and much faster.

Various Boussinesq-type models are commonly employed, including [FUNWAVE-TVD](#) [190], [COULWAVE](#) [191], [NHWAVE](#) [192], designed to model wave hydrodynamics in the surf zone. These models can differ in their governing equations, numerical schemes, and methods for treating wave breaking.

FUNWAVE-TVD (2D) and COULWAVE (1D) utilize BT equations as their governing equations. In one-dimensional cases, both FUNWAVE-TVD and COULWAVE governing equations recover those proposed by [173], and they employ a moving reference level as presented by [181]. The convection terms are discretized using a high-order shock-

capturing FV method for all three BT models, employing a fourth order MUSCL¹² scheme combined with an HLL approximate Riemann.

Wave breaking is a crucial process in the surf zone, necessitating proper treatment in the BT equations. Two main types of waves breaking treatment methods are employed in these models. The first type simulates energy dissipation caused by wave breaking by adding an additional dissipation term in the momentum equation, seen in the roller and eddy viscosity models [181]. The second type, termed a hybrid wave breaking model, discretizes governing equations using shock-capturing schemes, and wave breaking is determined by a user-defined threshold. In this approach, the BT equations are switched to nonlinear shallow water equations in the swash zone, describing the breaking wave as a bore or hydraulic jump. The advantage of the hybrid wave breaking model lies in its relative simplicity and effectiveness, but with fewer adjustable parameters, simulation precision may decrease for different terrains.

A comparison between the different models was carried out by [193]. The results indicated that the eddy viscosity model exhibits greater robustness and stability, when applied to various equations or different meshing selections, providing increased accuracy in simulating wave height and water flow after wave breaking. Overall, it was emphasized that breaking parameters should be calibrated. The only substantial differences between the FUNWAVE-TVD and COULWAVE lie in their wave breaking treatment and the capacity of running 1D simulations. COULWAVE was selected for this research due to its ability to run faster 1D simulations, and because FUNWAVE-TVD lacks nonlinear-dispersive precision in deep waters. Nonetheless, the users must be aware that these methods handle wave breaking using energy dissipation approaches. Therefore, they cannot simulate the splash-up and plunging in the breaking

¹² *Monostone Upstream-centered Schemes for Conservation Laws.*

process. When the basic type of wave breaking is surging or spilling, all models can predict wave set-up with reasonable accuracy. However, significant differences arise between models when the basic wave breaking type is plunging, with FUNWAVE-TVD and COULWAVE tending to underestimate the wave set-up after wave breaking [194].

6.3. The Coulwave

This study utilized a 1D numerical model, specifically the Coulwave, based on fully nonlinear BT equations to study wave transformation over shallow foreshores across a range of water conditions from deep to extremely shallow. Coulwave employs the eddy viscosity model to simulate wave breaking and incorporates various boundary conditions, including bottom friction, wave generation, wave absorption, and wet-dry interface. The model features an internal source wavemaker to ensure mass conservation of water, contributing to accurate simulation of wave-induced set-up. In addition, an internal wavemaker with a sponge layer is incorporated to minimize the influence of wave reflection from the wave generator.

Compared to the original momentum equations proposed by [173], Coulwave introduces additional terms (R_f , R_b and R_s) to address bottom friction, wave breaking and subgrid lateral turbulent mixing, respectively. It is noteworthy that R_b and R_s mainly function as local momentum mixing due to wave breaking and unresolved turbulence. Bottom friction is a run constrain modeled using the quadratic law as shown in Eq. (25):

$$R_f = \frac{ff}{h + \eta_x} u_b |u_b| \quad \text{Eq. (25)}$$

where u_b is the velocity at the seafloor, and ff is the bottom friction coefficient.

In the literature, the types and values of bottom friction can vary significantly. Care should be exercised when selecting bed shear stress coefficients for modeling wave-induced alongshore currents, especially in the swash zone. Under field conditions, due

to the variability in hydrodynamic and morphologic characteristics, spatially variable friction coefficients (e.g., $1.0 \times 10^{-3} < ff < 5.0 \times 10^{-3}$) are likely to be employed, as demonstrated by studies such as [195] and [196]. In this study, a constant friction factor $ff = 5.0 \times 10^{-3}$ was applied uniformly across the entire bathymetry. This value is considered for a smooth concrete bottom, typical of a poured concrete bed in a laboratory setting.

To simulate the impacts of wave breaking, the eddy viscosity model (R_{sg}) proposed by [181] was employed, with some modifications following the approach outlined by [179]. This parameter is proportional to the horizontal velocity gradient and is strongly localized on the front face of the breaking wave. Apart from the energy dissipation term attributed to wave breaking, assumed to be highly localized on the front face of the breaking wave, a parameterization of the Reynolds-like stresses resulting from subgrid-scale turbulent processes associated with surf zone eddies becomes influential in shaping the flow pattern of the wave-generated current field. To address the absence of a subgrid model in the governing equations, which could lead to a chaotic underlying current field generated by wave breaking, a Smagorinsky-type subgrid model [197] was incorporated in the numerical model. This subgrid model aims to account for the effect of resultant eddy viscosity on the underlying flow, and the detailed formulation can be found in [198].

The finite volume (FV) algorithm is employed to solve the model equations, chosen for its stability, although it introduces more numerical dissipation compared to finite difference methods. Spatial derivatives are differenced to fourth-order accuracy, resulting in a model that is numerically accurate to $(\Delta x)^4$, $(\Delta Y)^4$ in space, and $(\Delta t)^4$ in time.

The moving boundary scheme utilized in this model follows the technique developed by [199]. This model is equipped to handle the wet-dry interface using the linear extrapolation method or the wetting-drying scheme. This approach enables the

application of five-point finite difference formulae at all points, including those neighboring dry points, eliminating the need for conditional statements. More detailed information are reported in the Coulwave manual [191].

6.4. Coulwave calibration and validation

6.4.1. Numerical setup

To simulate realistic wave propagation across different shallowness conditions, wave conditions from laboratory experiments were extracted based on measurements offshore in deep water conditions and flat bottoms. These identical conditions were used to drive the offshore wave condition along the flume in the simulation. All tests were run with both the sponge layers activated and without the structure in the flume. This approach isolates the wave transformation along the flume, excluding wave-structure interaction phenomena, providing a clearer comprehension of incident waves and forces on the structure.

It is important to note that when authors use the total wave without the structure in place as "*incident*", two errors are introduced, and this is going to be primarily bias. The first error stems from ignoring the reflection from the back absorber (typically around 15%). The second error is related to the accumulated wave energy in the flume, which differs for scenarios with and without the structure. Wave absorption is only partially effective, and there is usually a published efficiency. Limited absorption of long waves occurs due to stroke limitations. Over a 15-minutes run, significant energy accumulation takes place, resulting in larger waves and a spectral peak shift when the structure is in place.

The numerical model was calibrated and verified against the laboratory EUMER and MK experiments. The goal was not to validate the numerical model but simply to calibrate certain numerical settings to align more closer with real conditions in the lab.

Specifically, the simulations were run with the following settings:

- Sponge layers (0.75 m wide in wavelength)
- Minimum water depth for moving boundary equal to 0.015 m
- Courant number $dx/dt/c_o=0.15$
- Coefficient for vertical eddy viscosity equal to 0.067
- Coefficient for subgrid horizontal eddy viscosity equal to 0.20
- Bottom friction $ff=0.005$

The Coulwave software requires a *bathy.txt* file as input, containing the x - and z -coordinates of the flume bathymetry. The length of the numerical wave tank was extended by 10 m in the vicinity of the wave generator, which was fixed at $x_0=8$ m. The shape function of the incident wave spectrum and the incident wave parameters (H_{m0} , T_p) offshore, near the wave generator, served as input to generate waves. An illustration of the input flume geometry and the energy density spectrum for wave generation in the EUMER flume is depicted in Figure 6.1.

As provided by the respective authors from the various studies discussed herein, incident-measured wave parameters (H_{m0} and T_p) were utilized to synthesize the offshore deep water wave spectrum using the same spectrum shape. It is essential to model the identical flume bathymetry to replicate the exact hydrodynamic conditions. In this thesis, it is assumed that the authors correctly separated incident and reflected wave conditions offshore. Consequently, the related epistemic uncertainty is assumed to be negligible and is considered as part of the aleatory uncertainty of random wave realizations.

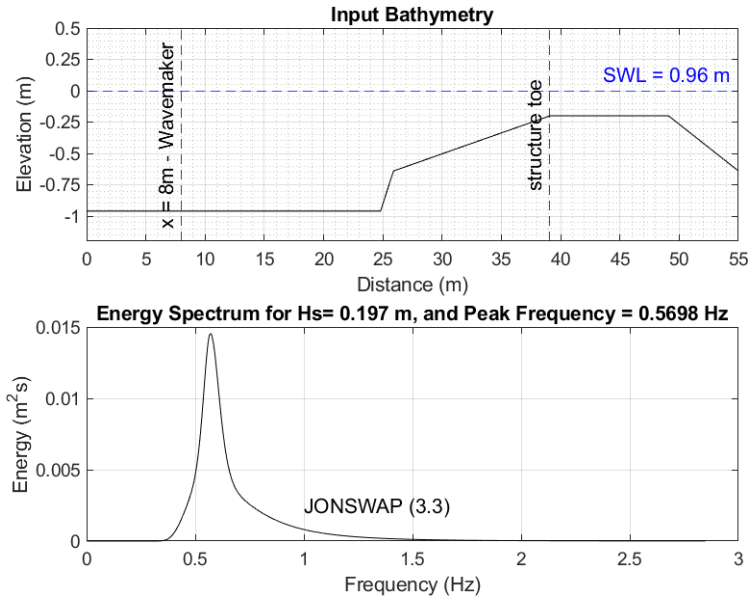


Figure 6.1. Bathymetry and energy spectrum input files for Coulwave simulations (EUMER wave flume).

6.4.2. Convergence

The convergence phase is a fundamental requirement for any numerical model, and it can be assessed through grid refinement tests. These tests involve examining the differences between measured and computed field variables as the grid lengths approach zero. Convergence tests were run for various grid spacings (dx) and simulation durations of 300 s and 600 s. Additionally, a sensitivity analysis of bulk wave parameters (H_{m0} and $T_{m-1,0}$) and spectra shape was conducted offshore, along the foreshore, and at the toe of the structure (inshore).

The grid mesh can influence the breaking point position. Indeed, inaccurate dx values may delay wave breaking compared to natural conditions, resulting in a shift by some wavelength fractions. Therefore, it is important to determine the appropriate dx to ensure negligible differences in bulk wave parameters when using a smaller mesh. This is particularly significant in (very) shallow waters.

For the calibration phase, simulations were performed for two cases in the EUMER flume setup in shallow ($h=0.20$ m) and very shallow ($h=0.10$ m) waters, respectively. The results for case 1 and case 2 are presented in Figure 6.2 and Table 6.1, as well as Figure 6.3 and Table 6.2, respectively.

The convergence tests indicate that results for bulk wave parameters and spectra shape are not significantly influenced by the grid mesh when $dx < 0.05$. Eventually, a grid spacing of $dx=0.04$ m in the (incident wave) x -directions was selected for all tests. This choice represents a good compromise between simulation time and model accuracy.

Table 6.1. Convergence test results - Case 1: $H_{m0,deep}=0.255$ m, $T_{p,deep}=2.78$ s, $h_{,deep}=0.96$ m, $h=0.20$ m, JONSWAP (3.3).

Run	dx	Run Dur (s)	$H_{m0,deep}$ (m)	$H_{m0,toe}$ (m)	$T_{m-1,0,deep}$ (s)	$T_{m-1,0,toe}$ (s)	$H_{m0,IG,deep}$ (m)	$H_{m0,IG,toe}$ (m)
1	0.2	300	0.2572	0.2431	0.1729	3.0341	3.4152	3.6197
2	0.1	300	0.2560	0.2416	0.1700	3.0102	3.1010	3.5961
3	0.05	300	0.2558	0.2361	0.1666	3.0110	3.0700	3.6497
4	0.03	300	OVERFLOW ERROR					
5	0.1	600	0.2576	0.2416	0.1709	3.2301	3.0747	4.0908
6	0.05	600	0.2575	0.2357	0.1672	3.2195	3.0646	4.1829
7	0.03	600	OVERFLOW ERROR					
8	0.04	600	0.2576	0.2351	0.1659	3.2105	3.0600	4.2351

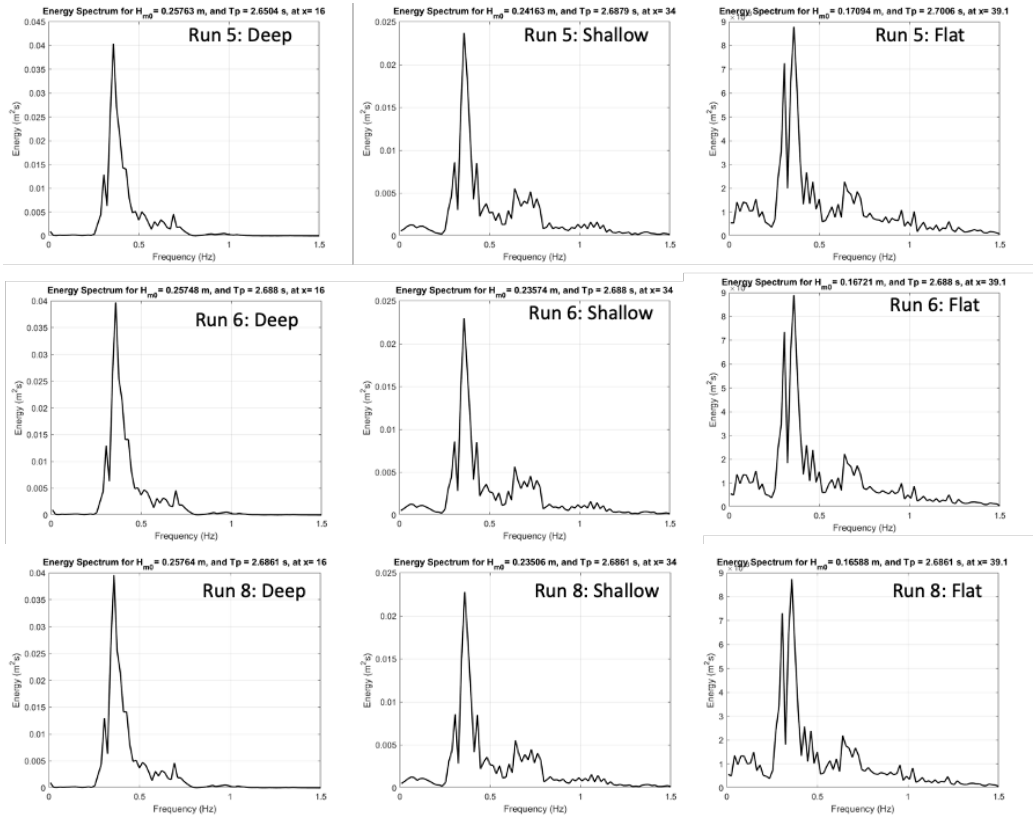


Figure 6.2. Convergence test results - Case 1. Spectra shape offshore, along the foreshore and at the flat bottom for $dx=0.1$ (above), $dx=0.05$ (middle) and $dx=0.04$ (below) with 600 s of simulation.

Table 6.2. Convergence test results - Case 2: $H_{m0,deep}=0.197$ m, $T_{p,deep}=2.38$ s, $h_{,deep}=0.86$ m, $h=0.10$ m, JONSWAP (3.3)

Run	dx	Run Dur (s)	$H_{m0,deep}$ (m)	$H_{m0,toe}$ (m)	$T_{m-1,0,deep}$ (s)	$T_{m-1,0,toe}$ (s)	$H_{m0,1G,deep}$ (m)	$H_{m0,1G,toe}$ (m)
1	0.2	300	0.1994	0.1901	0.1061	2.4536	3.1874	5.0206
2	0.1	300	0.1997	0.1848	0.0977	2.4329	2.9196	5.1216
3	0.05	300	0.1998	0.1807	0.0990	2.4448	2.9026	4.8707
4	0.03	300	0.1998	0.1790	0.0984	2.4451	2.8699	4.8104
5	0.04	300	0.1996	0.1796	0.0983	2.4428	2.8879	4.8415
6	0.1	600	0.2035	0.1879	0.0979	2.5398	2.8893	5.4885

7	0.05	600	0.2035	0.1839	0.0992	2.5494	2.8420	5.4235
8	0.03	600	0.2032	0.1822	0.0985	2.5362	2.8245	5.3235
9	0.04	600	0.2035	0.1828	0.0985	2.5498	2.8358	5.4314
10	0.02	600	OVERFLOW ERROR					

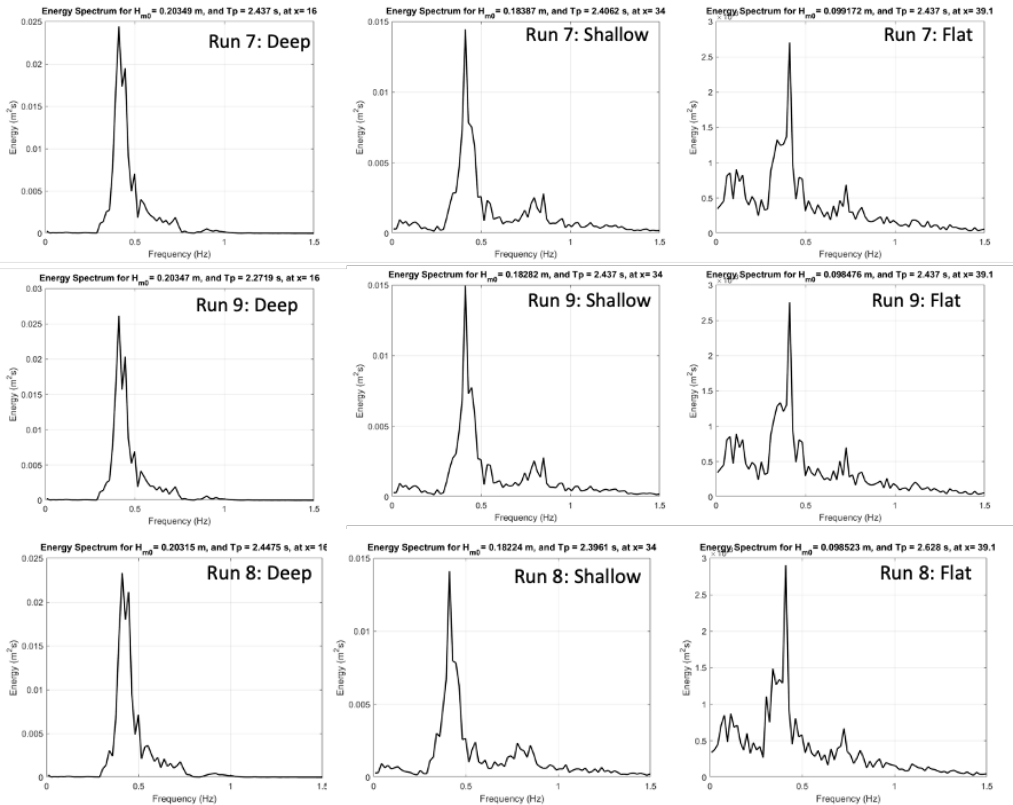


Figure 6.3. Convergence test results - Case 2. Spectra shape offshore, along the foreshore and at the flat bottom for $dx=0.1$ (above), $dx=0.05$ (middle) and $dx=0.04$ (below) with 600 s of simulation.

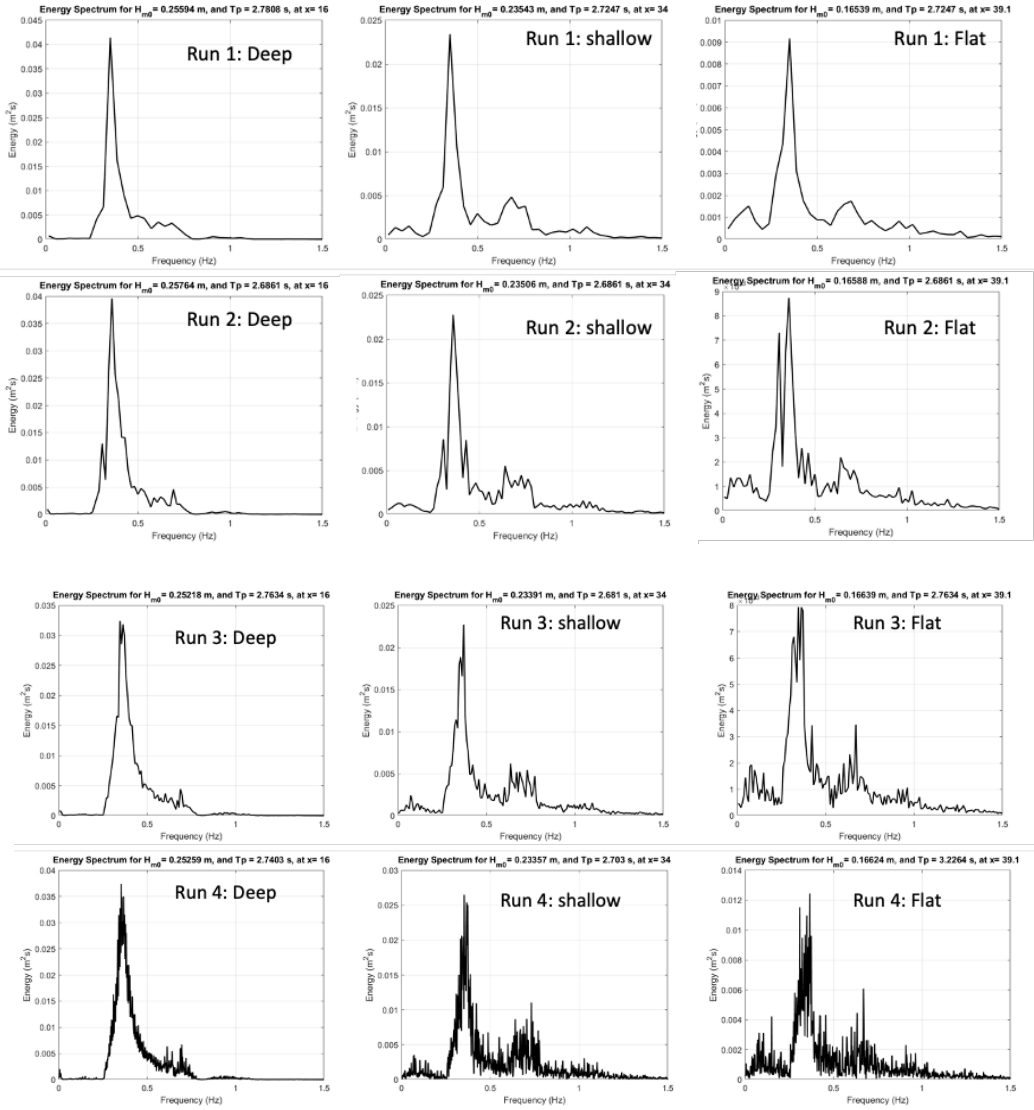
6.4.3. Test duration

A series of tests within the stability database were simulated with different record durations, specifically focusing on the duration corresponding to incipient damage, with $500 \leq N_w \leq 5000$, where $N_w = t_r/T_m$, and t_r is the duration of the test.

Defining the persistence of the sea state is important in stability equations, where the S_d value is normalized by the square root of the duration ($S_d/\sqrt{N_w}$). The calculation of N_w may introduce some potential confusion, such as whether to consider offshore or inshore T_m in the analysis and how reflected waves influence the zero-crossing method and the uncertainty of T_m . Regardless, the uncertainty of N_w is primarily influenced by the uncertainty in T_m only.

This section aims to calibrate and determine an appropriate duration for the numerical tests and investigate the sensitivity of results based on the chosen duration. According to [200], 500 waves constitute a statistically robust sample for ergodicity and stationarity of a sea state. Long waves are better resolved with longer simulations. However, running longer test durations with a small dx in the numerical model can be impractical due to increased computational and analysis time. Therefore, optimizing simulation duration is essential to balance accuracy and computational costs without losing information. A sensitivity analysis of duration was conducted, considering the cases used for convergence testing in Section 6.4.2.

All tests in the dataset were executed, and the results are presented in Table 6.3 and Figure 6.4, as well as Table 6.4 and Figure 6.5, reporting the comparison between bulk wave parameters and spectra shape for different test durations (300 s, 600 s, 1200 s, 5000 s, and 10,000 s) with $dx=0.04$ for case 1 and case 2, respectively.



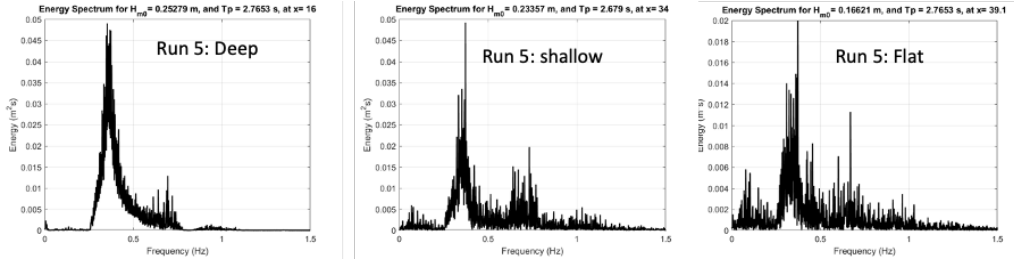
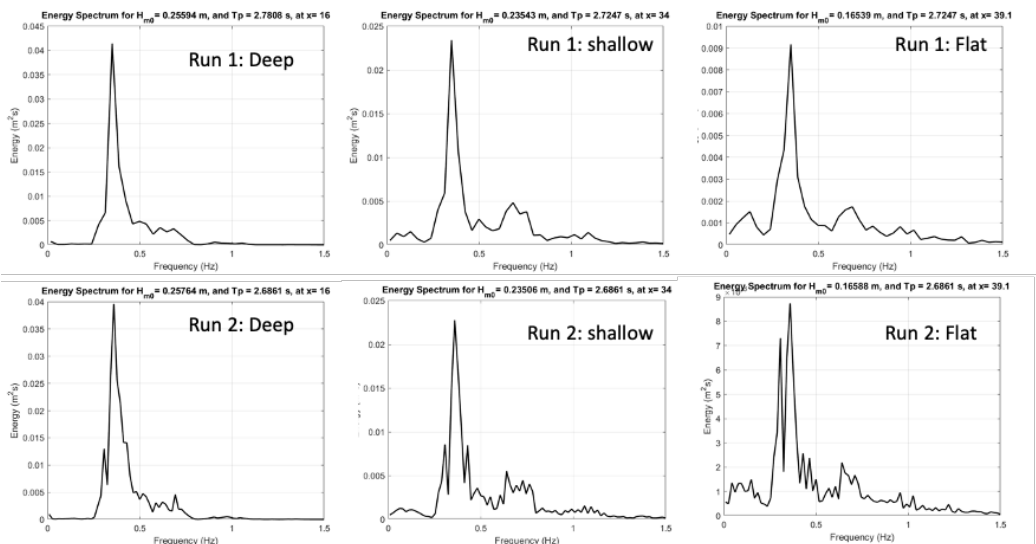


Figure 6.4. Duration sensitivity analysis results - Case 1. Spectra shape offshore, along the foreshore and at the flat bottom for t_r equal to 300 s, 600 s, 1200 s, 5000 s and 10,000 s with $dx=0.04$.

Table 6.3. Sensitivity analysis results of test duration - Case 1.

Run	Dx (m)	Run Dur (s)	$H_{m0,deep}$ (m)	$H_{m0,toe}$ (m)	$T_{m-1,0,deep}$ (s)	$T_{m-1,0,toe}$ (s)	$H_{m0,IG,deep}$ (m)	$H_{m0,IG,toe}$ (m)
1	0.04	300	0.2559	0.1654	3.0031	3.6842	0.0212	0.0283
2	0.04	600	0.2576	0.1659	3.2105	4.2351	0.0189	0.0299
3	0.04	1200	0.2522	0.1664	3.0962	3.9592	0.0167	0.0264
4	0.04	5000	0.2526	0.1662	3.1818	4.1527	0.0167	0.0267
5	0.04	10,000	0.2528	0.1662	3.1926	4.2108	0.0167	0.0269



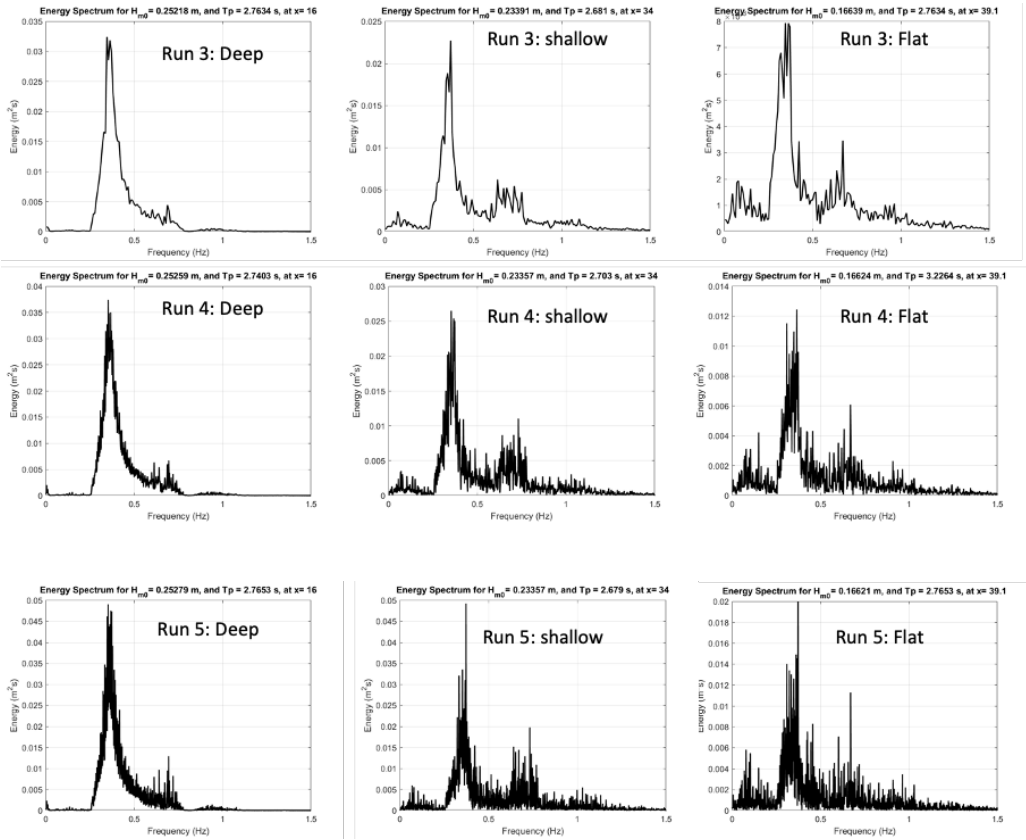


Figure 6.4. Duration sensitivity analysis results - Case 1. Spectra shape offshore, along the foreshore and at the flat bottom for t_r equal to 300 s, 600 s, 1200 s, 5000 s and 10,000 s with $dx=0.04$.

Table 6.4. Sensitivity analysis results of test duration - Case 2.

Run	Dx (m)	Run Dur (s)	$H_{m0,deep}$ (m)	$H_{m0,toe}$ (m)	$T_{m-1,0,deep}$ (s)	$T_{m-1,0,toe}$ (s)	$H_{m0,IG,deep}$ (m)	$H_{m0,IG,toe}$ (m)
1	0.04	300	0.1996	0.0983	2.4428	4.8415	0.0112	0.0242
2	0.04	600	0.2035	0.0985	2.5498	5.4312	0.0109	0.0229
3	0.04	1200	0.1985	0.0988	2.5411	5.1837	0.0100	0.0206
4	0.04	5000	0.1977	0.0992	2.5919	5.4249	0.0099	0.0206
5	0.04	10,000	0.1978	0.1001	2.6669	5.3316	0.0101	0.0208

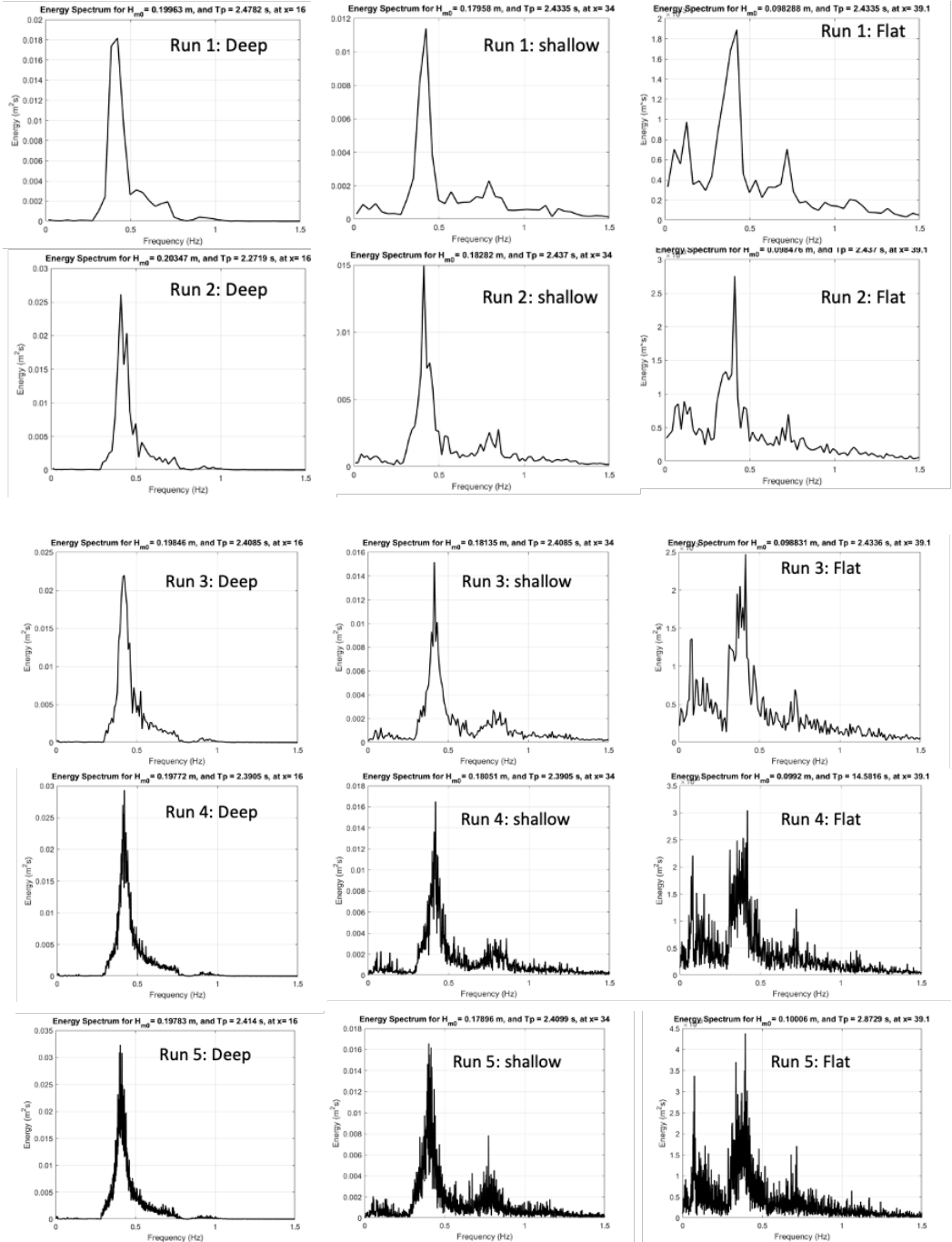


Figure 6.5. Duration sensitivity analysis results - Case 2. Spectra shape offshore, along the foreshore and at the flat bottom for t_r equal to 300 s, 600 s, 1200 s, 5000 s and 10,000 s with $dx=0.04$.

In summary, the results indicate that durations longer than 600 s in the numerical wave tank do not significantly influence the bulk wave parameters. The only notable contribution of longer duration could be the increase in IG waves (arbitrarily defined for $f < 0.07$ Hz). Interestingly, the effect of IG on bulk wave parameters (H_{m0} and $T_{m-1,0}$) remains negligible even for longer test durations, contrary to laboratory conditions. This discrepancy is attributed to the re-reflection condition in the laboratory flume, which differs significantly from the numerical model. The laboratory flume is more susceptible to the buildup of IG energy due to inefficiencies in passive and active reflection compensation, leading to continuous re-reflection.

Uncertainty (σ') was calculated for each bulk wave parameter offshore and inshore, considering a sample of five tests mentioned above. This approach gives a sense of the uncertainty related to the test duration (t_r). Results are presented in Table 6.5. The uncertainty is higher in very shallow waters than in shallow waters, and specifically, it is higher for $T_{m-1,0}$ compared to H_{m0} , both computed at the toe of the structure. Ultimately, $t_r = 1200$ s was chosen as the optimal duration for the numerical test.

Table 6.5. Estimation of the uncertainty σ' related to the test duration.

	$H_{m0,deep}$ (m)	$H_{m0,toe}$ (m)	$T_{m-1,0,deep}$ (s)	$T_{m-1,0,toe}$ (s)	$H_{m0,IG,deep}$ (m)	$H_{m0,IG,toe}$ (m)
Shallow $h=0.20$ m	0.0094	0.0023	0.0277	0.0570	0.1113	0.0528
Very Shallow $h=0.10$ m	0.0121	0.0072	0.0319	0.0468	0.0565	0.0755

6.4.4. Breaking trigger and stopping

In numerical simulation with the sponge layer on the opposite end of the flume from wave generation, a boundary is created with the SWL = 0 at the end of the flume. This setup results in a numerical model effect where the SWL from the structure location to the end of the flume slope down, creating a current. In contrast, in the laboratory, there is a wave set-up that tends to increase in the proximity of the sloping spending beach. This difference can alter the SWL inshore, introducing variations in physics between numerical and laboratory tests. The SWL inshore may be slightly different in the numerical model compared to the lab, and this small difference can induce a systematic bias between numerical and laboratory experiments. The location of the breaking condition may also shift due to different water levels, which can be related to the mesh grid. Lower resolution with a larger dx may push the breaker location shoreward, leading to an underestimation of breaking losses and introducing bias.

In Coulwave, there are two key parameters for evaluating the breaking simulation in the model:

- 1) **Breaking point (breaking trigger)**; this parameter initiates the breaking phenomenon when $d\eta/dt > \text{trigger} \cdot \sqrt{gh}$. The default value is 0.65. Lowering this value triggers breaking sooner, and vice versa.
- 2) **Energy dissipation by wave breaking (breaking stopping)**; this includes breaking stopping and the distance over which breaking occurs. Breaking ends when $d\eta/dt < \text{stopping} \cdot \sqrt{gh}$. The default value is 0.40. Lower values result in longer-lasting breaking events. Coulwave employs a breaking-transport model, so even after breaking ends, both local and advected dissipation are associated with the transport of the breaking eddy viscosity.

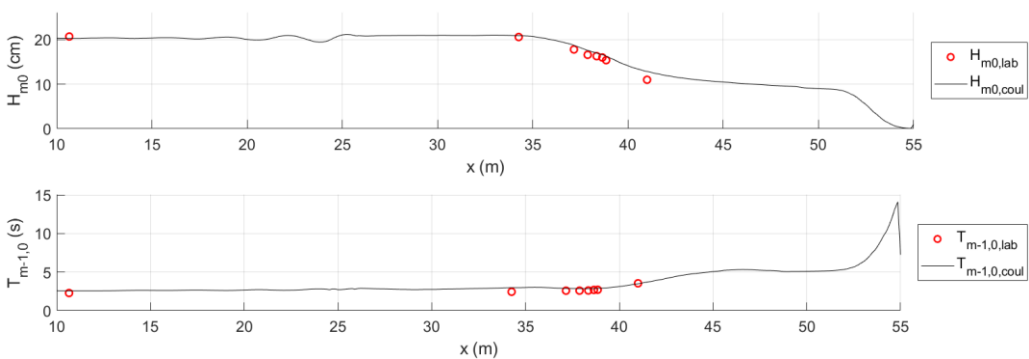
A cursory calibration of these parameters was performed, recognizing that wave laboratory measurements can be inaccurate for propagating breaking bores, and no

existing numerical model can provide zero error. The calibration involved running the entire EUMER dataset from deep to extremely shallow water conditions. The EUMER wave gage layout, with 7 wave gages located inshore, helped in tracking the wave decay along the foreshore.

Figure 6.6, Figure 6.7 and Figure 6.8 illustrate three examples under different water conditions (shallow: $h=0.20$ m; very shallow: $h=0.10$; extremely shallow: $h=0.05$ m), and these examples are representative of all test results. All tests were run with $dx=0.04$, $ff=0.005$, and a duration of 1200 s.

Initially, the default parameters (trigger=0.65 and stopping=0.40) were employed. Results indicated a bias for very and extremely shallow water conditions compared to the lab (see Figure 6.7 and Figure 6.8). Consequently, the breaking trigger was calibrated using values of 0.65, 0.60 and 0.55. A sensitivity analysis aimed at accurately capturing breaking initiation guided the choice of trigger=0.60 (less than default 0.65, indicating breaking sooner). Subsequently, stopping was tuned to 0.35.

The figures show the cross-shore variation of H_{m0} and $T_{m-1,0}$ along the flume, with laboratory measurements denoted by red circles and numerical computations represented by solid line. These figures demonstrate the accurate reproduction of laboratory measurements by the numerical model across all water depth conditions.



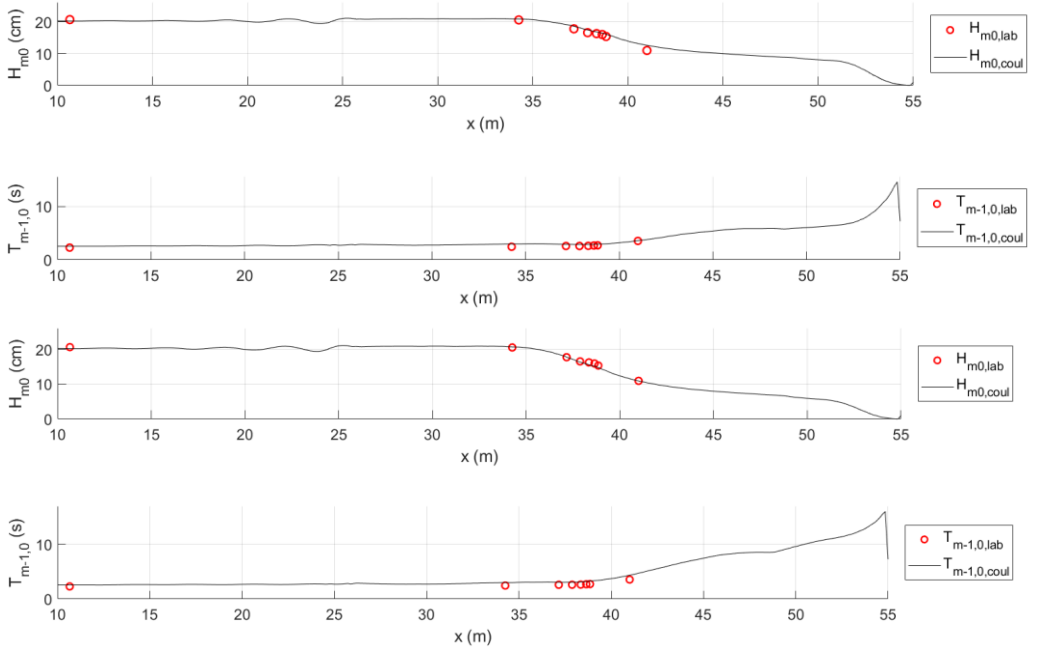
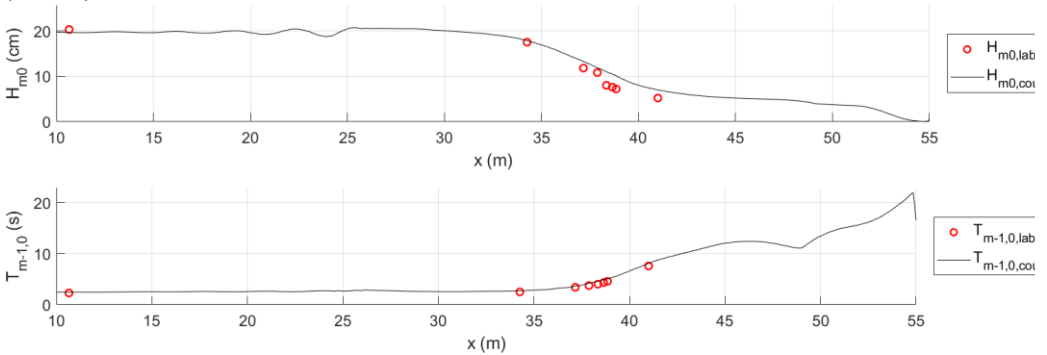


Figure 6.6. Lab measured (red circle) and numerical computed (solid lines) cross-shore variation of H_{m0} and $T_{m-1,0}$ along the wave flume – Case 1 ($h=0.20$ m, $H_{m0,deep}=0.20$ m, $T_{p,deep}=2.38$ s). $\text{Trigger}=0.60$ and $\text{stopping}=0.40$ (above), $\text{trigger}=0.60$ and $\text{stopping}=0.35$ (middle), $\text{trigger}=0.60$ and $\text{stopping}=0.30$ (below).



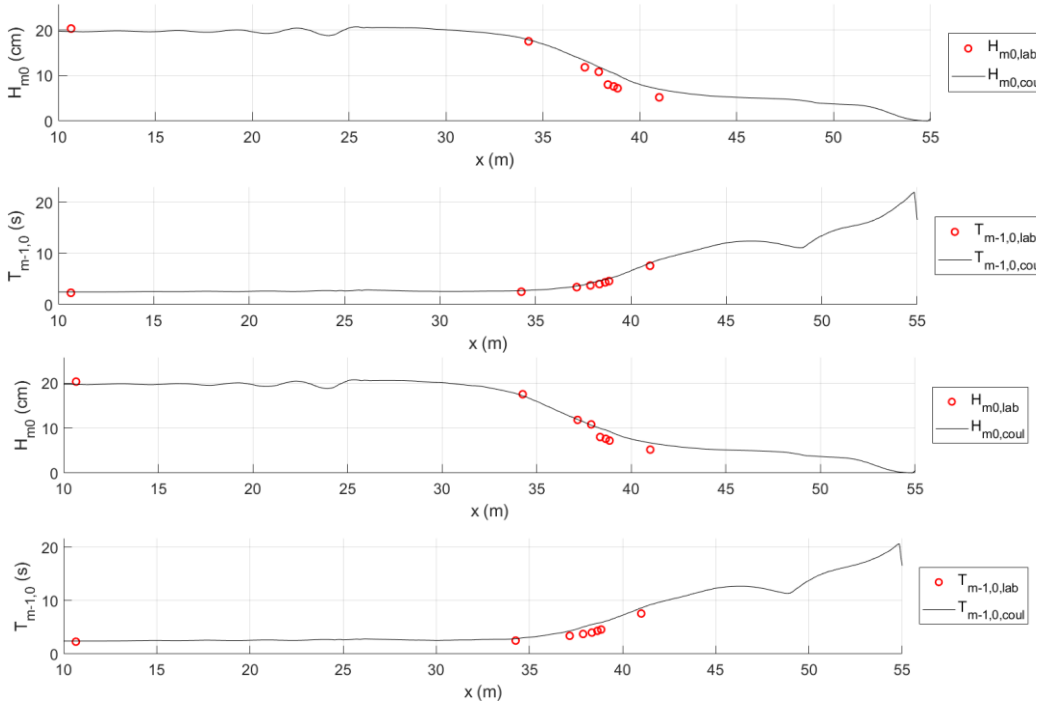
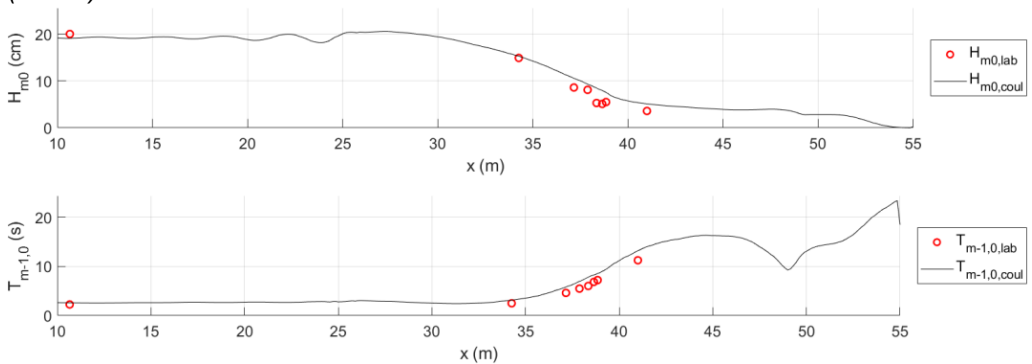


Figure 6.7. Lab measured (red circle) and numerical computed (solid lines) cross-shore variation of H_{m0} and $T_{m-1,0}$ along the wave flume – Case 2 ($h=0.10$ m, $H_{m0,deep}=0.20$ m, $T_{p,deep}=2.38$ s). Trigger=0.60 and stopping=0.40 (above), trigger=0.60 and stopping=0.35 (middle), trigger=0.60 and stopping=0.30 (below).



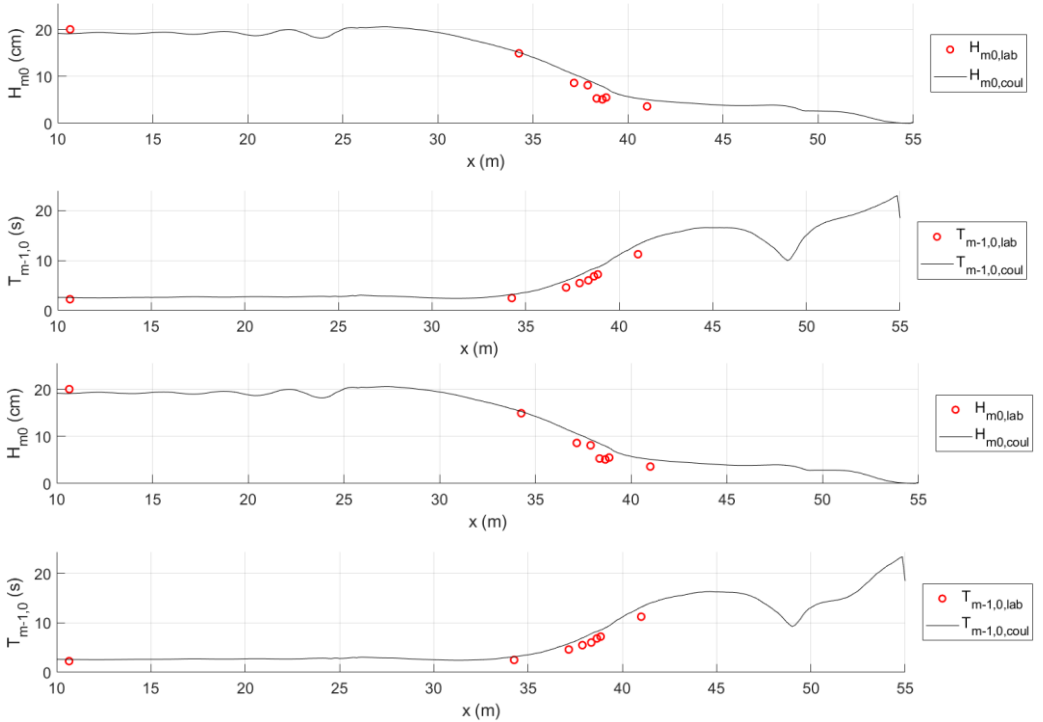


Figure 6.8. Lab measured (red circle) and numerical computed (solid lines) cross-shore variation of H_{m0} and $T_{m-1,0}$ along the wave flume – Case 3 ($h=0.05$ m, $H_{m0,deep}=0.20$ m, $T_{p,deep}=2.57$ s). Trigger=0.60 and stopping=0.40 (above), trigger=0.60 and stopping=0.35 (middle), trigger=0.60 and stopping=0.30 (below).

It is important to acknowledge that the comparison between the laboratory and the numerical model is not direct. In the laboratory, incident wave parameters were compared with the total wave parameters (incident + reflected) from the numerical model. This comparison was feasible because the reflection coefficient in the numerical wave tank was negligible, thanks to the sponge layers. Therefore, the total wave parameters are nearly equal to the incident wave parameters in numerical simulations.

However, in the laboratory, incident H_{m0} was determined using $H_{m0,i}=H_{m0}/(1+K_R)^{1/2}$, based on measured total H_{m0} . Here, $K_R=0.05$ was used, determined from measured reflections in a multi-gage array offshore near the generator. The uncertainty in

estimating $H_{m0,i}$ in the numerical model is likely negligible, while that in the physical model is probably on the order of at least 10% more likely manifesting as bias than scatter. This might explain the consistent small overprediction of H_{m0} and underprediction of $T_{m-1,0}$ in very shallow waters.

It is important to state that if the model is tuned, matching H_{m0} and H_s simultaneously is challenging because spectral energy distribution behaves differently compared to time domain analyses. So, the calibration of the breaking parameters has been conducted considering only the spectral wave parameters (H_{m0} and $T_{m-1,0}$). Finally, breaking trigger equal to 0.60 and stopping equal to 0.35 were chosen for the analysis (default are trigger=0.65 and stopping=0.40).

6.4.5. Coulwave simulations

After calibrating all the parameters, the simulations were conducted using fixed settings (i.e., $ff=0.005$, $t_r=1200$ s, trigger=0.60, stopping=0.35, etc.). The post-processing analyses were standardized for all the experimental datasets using fixed protocols and in-house MATLAB routines.

Considering COULWAVE as the appropriate numerical model for this research and having conducted a proper calibration of the numerical settings, generating numerically identical wave conditions offshore (close to the wave generator) as in the laboratory experiments allows for a comparison of various laboratory data with consistent and comparable wave parameters. This facilitates determining complete wave spectra along the flume length. Thus, obtaining identical wave spectra offshore near the wavemaker regarding spectral shape and bulk wave parameters (H_{m0} and $T_{m-1,0}$) is essential. Figure 6.9 shows an example comparison between the synthesized target

wave spectra (single and double¹³ JONSWAP ($\gamma=3.3$)) and incident measured offshore, demonstrating that the simulated wave spectra are almost identical to the target ones, as expected.

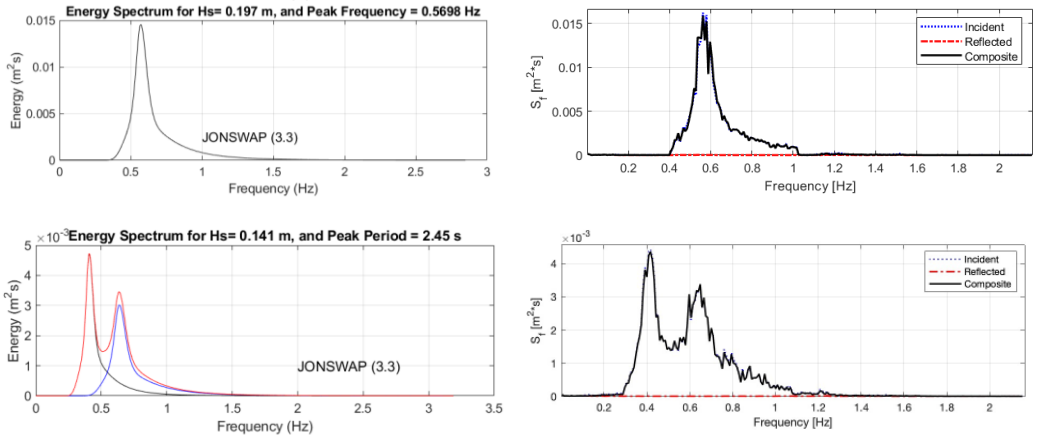


Figure 6.9. Comparison between target (left) and measured (right) wave spectra offshore.

Random wave generation can introduce uncertainty due to the limited number of wave phase realizations. In the laboratory, low-frequency IG waves are very long, and only a very small number of instances are recorded by the wave probes in any realization. The presence of a long wave crest at the gage location may result in a larger wave height at that instant, and vice-versa. Additionally, the bulk parameters can be influenced by the phase of these waves. To address this, it is necessary to run long duration simulations with variations in realization. Smoothing wave spectra is another technique to obtain more stable wave parameters. For example, T_p can be very sensitive if wave spectra are not smoothed, and the run duration is short. While these aspects are likely

¹³ Double-peaked wave energy spectra were obtained by superposition of two single-peaked wave energy spectra of which the ratio of the peak wave periods (T_{p2}/T_{p1}) is known.

to influence wave runup and overtopping on structures, they may not significantly affect armor stability. It is important to note that the end condition treatment may influence long wave generation, and IG energy is likely to be greater for the case with no sponge layer. Furthermore, numerical and real wave flumes with very different dimensions may be influential, as discussed in Section 5.4.3. Therefore, it is important to have wave generation in the same position as the lab physical model because deep water waves are dispersive and simulating something more like real life is essential for determining a more realistic wave state.

6.4.6. Post-processing analyses

Standard laboratory wave analyses were applied to the numerical time series, incorporating various methodologies. These analyses included testing scenarios with and without the structure in place, examining frequency vs. time domain relationships, exploring variations in reflected wave analysis, conducting single-gage frequency analysis, evaluating different statistics for wave momentum flux, and assessing contributions spanning the entire spectrum. The implementation of standardized routines on the entire database resulted in collected results stored in spreadsheets for further analysis.

6.4.7. Reflection analysis

In the numerical simulations, the resolution of incident and reflected waves was achieved using the technique proposed by Goda and Suzuki [88]. This approach was subsequently modified by [130] for determining incident and reflected wave spectra in shallow waters. The modification considered the optimal spacing between a multi-gage array in variable depths. It is noted that due to low signal-to-noise ratios, the reflection analysis technique may provide poor estimates at frequencies with little energy. The determination of cutoff frequencies was essential to maintain coherence above 0.3 in

the cross-correlation between gage pairs. Low coherence in these regions indicated the presence of noise or unreliable data.

In this research, a flexible cutoff filtering method ($0 < f < 3f_p$) was chosen to avoid numerical problems in the analysis. Sensitivity analysis demonstrated small errors and supported this assumption. Utilizing a numerical wave tank provides the flexibility to set up as many wave gages as desired. Following the work by [130], a 9-gage-array was considered an optimal layout for separating incident and reflected waves, and it was implemented in the numerical wave tanks.

The standard Goda and Suzuki (GS) method was applied to separate incident and reflected spectra by analyzing the time series from two gages. Frequencies that can be resolved from the time series depend on the gage spacing, and attention must be paid to the risk of resonance. Frequencies for a given spacing, as utilized in the analyses program, can be determined from the dispersion equation as:

$$\frac{dl}{0.45} < L < \frac{dl}{0.05} \quad \text{Eq. (26)}$$

where dl is the spacing between the gages, and L is the wavelength. The optimal suggested gage spacing is provided as an integer multiple of 0.5 ft in [130], i.e., $x_{12}=0.5$ ft, $x_{13}=1$ ft, $x_{14}=1.5$ ft, $x_{15}=2$ ft, $x_{16}=2.5$ ft, $x_{17}=3.0$ ft, $x_{18}=3.5$ ft, $x_{19}=4$ ft. A trial-and-error method was implemented to obtain the frequency ranges using the 9 GS spacing array for test series to check the accuracy of the method in the analyzed frequency bandwidth.

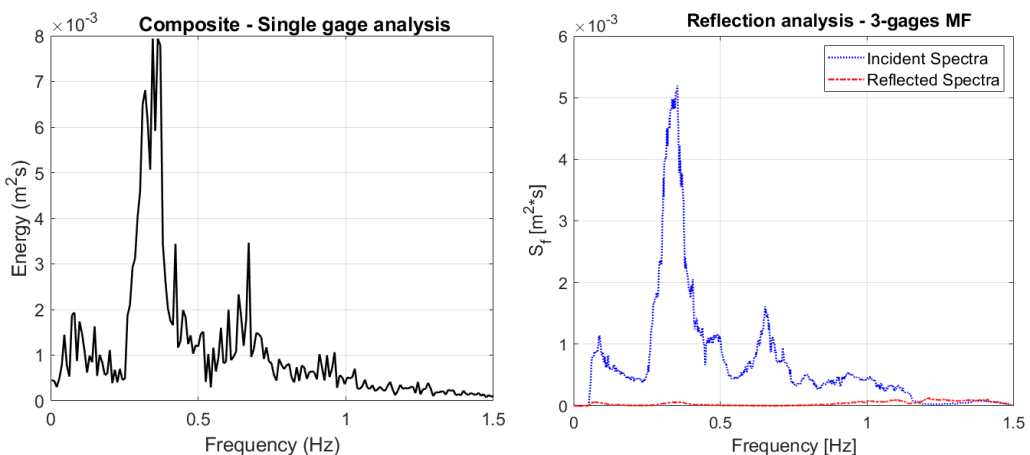
The study conducted a sensitivity analysis to explore the uncertainty associated with different reflection methods in nonlinear wave conditions. Simulations were run without the structure in place and sponge layers activated ($K_R < 10\%$), assuming that the total (incident + reflected) wave was equal to the incident wave. The goal was to assess

bias and uncertainty in shallow waters applying different reflection methods. Three techniques to estimate incident wave parameters were compared:

- 1) Single gage frequency analysis
- 2) GS analysis using a 9-gage array
- 3) Mansard and Funke using a 3-gage array

The same calibrated settings described earlier were used for this study. Multiple gage arrays were always centered at the toe of the structure. For single gage analysis, reflection was determined by simply adding the incident and reflected wave energies calculated offshore ($K_R = m_{0,r}/m_{0,i}$) to the total wave energy, as described in Goda's textbook [73]. Results are reported in Figure 6.10 and Table 6.6 for Case 1 and in Figure 6.11 and Table 6.7 for Case 2.

Table 6.8 presents an estimate of the uncertainty associated with different wave reflection analyses in various water depth conditions conducted in the EUMER laboratory (deep water: $h=0.40$ m; shallow water: $h=0.20$ m; very shallow water $h=0.10$ m). The table illustrates how uncertainty increases when linear reflection methods are employed in nonlinear wave conditions.



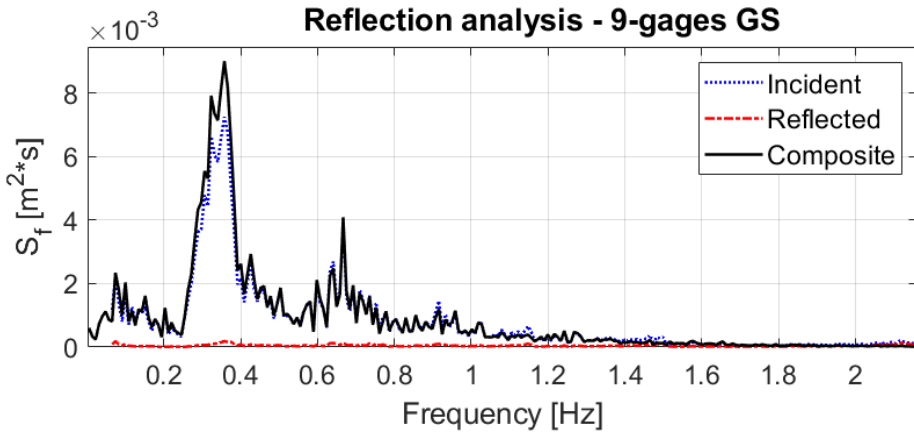
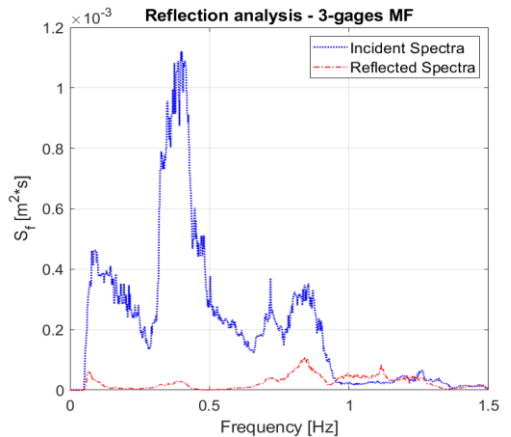
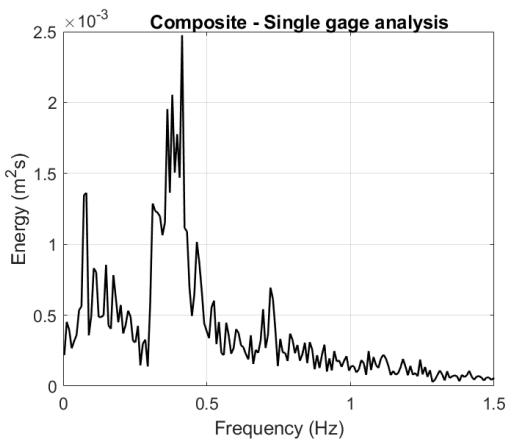


Figure 6.10. Comparison of the wave spectra obtained using different reflection techniques - Case 1 in shallow water ($h=0.20$ m, $H_{m0,deep}=0.255$ m, $T_{p,deep}=2.78$ s). Upper left single gage analysis, upper right 3-gages Mansard and Funke and bottom 9-gages Goda and Suzuki.

Table 6.6. Sensitivity analysis based on reflection methods – Case 1: shallow water ($h=0.20$ m, $H_{m0,deep}=0.255$ m, $T_{p,deep}=2.78$ s).

Reflection method	$H_{m0,i}$ (m)	$T_{m-1,0,i}$ (s)	K_R (-)	$T_{p,i}$ (s)
Single gage	0.1656	3.9593	0.100	2.7634
9-gages GS	0.1671	2.7671	0.234	2.6874
3-gages MF	0.1543	3.1385	0.234	2.7674



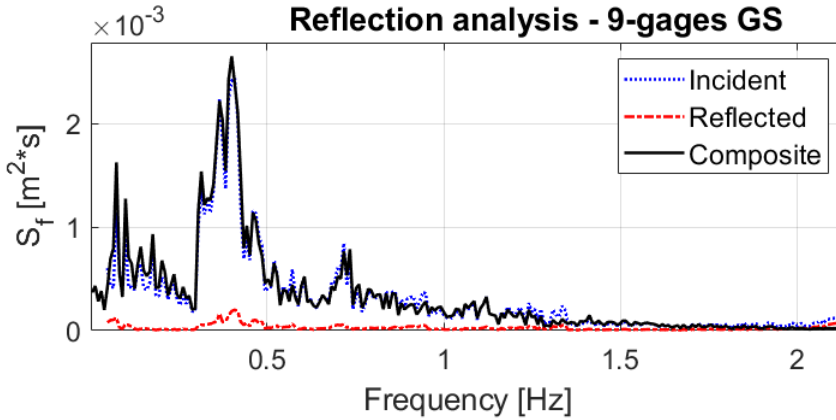


Figure 6.11. Comparison of the wave spectra obtained using different reflection techniques – Case 2 in very shallow water ($h=0.10$ m, $H_{m0,deep}=0.197$ m, $T_{p,deep}=2.38$ s). Upper left single gage analysis, upper right 3-gages Mansard and Funke and bottom 9-gages Goda and Suzuki.

Table 6.7. Sensitivity analysis based on reflection methods – Case 2: very shallow water ($h=0.10$ m, $H_{m0,deep}=0.197$ m, $T_{p,deep}=2.38$ s).

Reflection method	$H_{m0,i}$ (m)	$T_{m-1,0,i}$ (s)	K_R (-)	$T_{p,i}$ (s)
Single gage	0.0988	5.1837	0.087	2.4336
9-gages GS	0.1037	3.0520	0.305	2.4787
3-gages MF	0.0869	3.4649	0.342	3.3349

Table 6.8. Uncertainty σ' related to the use of reflection method in different shallowness conditions.

Test condition	$H_{m0,i}$	$T_{m-1,0,i}$	$T_{p,i}$	K_R
Deep water: $h = 0.40$ m	0.0101	0.1429	0.0112	0.4672
Shallow water: $h = 0.20$ m	0.0431	0.1855	0.0165	0.4085
Very Shallow water: $h = 0.10$ m	0.0896	0.2899	0.1847	0.5626

In this manuscript, the GS method was applied only to the measured signals outside the surf zone, where the incident significant wave height is less than at least half of local water depth. This approach was chosen because applying LWT reflection methods to separate incident and reflected wave spectra in nonlinear wave conditions,

especially in shallow waters, can lead to large errors and significant uncertainty in computing bulk wave parameters. The decision to use the GS method outside the surf zone is based on the understanding that wave nonlinearity increases with decreasing water depth, and BT models become more empirical after wave breaking.

When total wave height measurements are taken far from the structure (at least one wavelength away), it can be assumed that there is little correlation between the incident and reflected waves. Under these conditions, the best option is to simply add the incident and reflected wave energies ($K_R = m_{0,r}/m_{0,i}$), as suggested in Goda's textbook [73]. If $K_R < 30\%$, the reflected wave energy is less than 9% of the incident wave energy and may be neglected within 10% errors. This approach allows for the evaluation of errors in the analysis, acknowledging that the Boussinesq wave model itself has errors of about 10-15% inside the surf zone.

In the numerical tests, the incident wave parameters in shallow water were computed using the formula $H_{m0,i} = H_{m0}/(1 + K_R)^{1/2}$, where H_{m0} was directly taken from the output of the single gage frequency analysis, and K_R was computed with the modified GS method [130] offshore in deep water and flat bottom conditions, where the method is recognized to be accurate. To provide a strong justification for this choice, the GS reflection analysis was performed continuously along the flume for each test to observe where K_R starts to deviate. K_R should be spatially stable in linear wave conditions but may become inaccurate in shallow areas where nonlinear effects (wave breaking) are significant. For example, in Figure 6.12, K_R begins to deviate around $x = 35$ m, which corresponds to the region where wave breaking occurs (around $x = 30$ m). This suggests that the reflection analysis is reasonably accurate for nonlinear waves but not for breaking conditions.

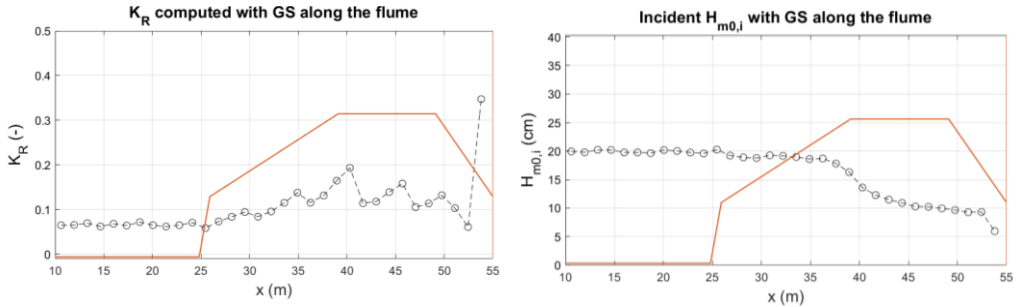


Figure 6.12. Cross-shore variation of K_R and $H_{m0,i}$ along the flume for very shallow water ($h=0.10$ m) where waves break over the foreshore.

6.4.8. Wave momentum flux and IG contribution

The use of a Boussinesq numerical model allows for the computation of the velocity-based wave momentum flux. The numerical model outputs the depth-averaged velocity term \bar{u} at each grid cell, which can be used to calculate the term $(h+\eta)\bar{u}^2$, where $(h+\eta)$ represents the total dynamic local water depth and $(h+\eta)\bar{u}^2$ is proportional to the drag force in shallow water conditions. Conversely, the depth-integrated pressure term p_d is not directly available as an output of the numerical model.

Additionally, the accumulation of IG energy ($f < 0.7$ Hz) impacting the incident spectral wave parameter ($H_{m0,IG}$) can be computed at each grid cell. The majority of research on IG waves and their influence on spectral shape and stability has primarily focused on bound long waves (wave groupiness). However, in the wave tank, long waves may not be part of the incident spectrum initially. Instead, they can be generated by wave-wave interactions in the nearshore and progressively intensify over time. While individual waves may be accurately modeled, the accumulation of IG energy may represent a laboratory-induced effect.

Many laboratories may lack the sufficient generator stroke necessary to absorb these long waves. Consequently, a substantial presence of long wave energy may be observed even when employing wide spectra. To avoid this issue, some laboratories

choose to run their spectra in short bursts, although this approach introduces additional challenges in efficiency.

Figure 6.13 illustrates the cross-shore variations of the maximum depth-averaged velocity term \bar{u}_{\max} , the term $(h + \eta)\bar{u}_{\max}$, and $H_{m0,IG}$ along the tank. These terms approach zero at the end of the tank due to the boundary effect induced by the sponge layer.

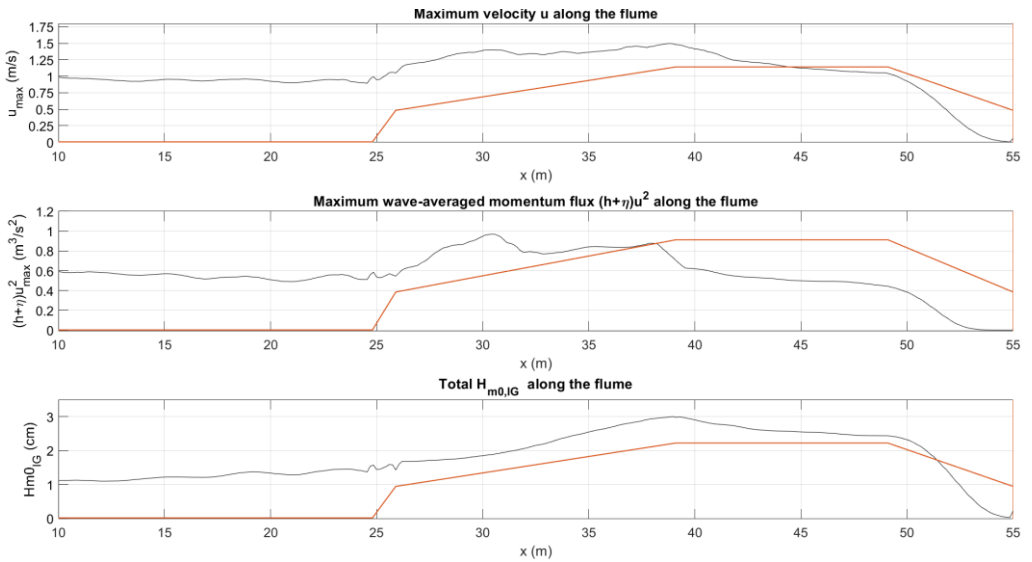


Figure 6.13. Cross-shore variation of \bar{u}_{\max} , $(h + \eta)\bar{u}_{\max}^2$ and $H_{m0,IG}$ along the flume.

Figure 6.14 illustrates the cross-shore variations of $(h + \eta)\bar{u}_{\max}^2$ along the flume in the presence of a mild structure slope (1V:17H). This comparison analysis was conducted to assess the impact of the structure on the variation of the term $(h + \eta)\bar{u}_{\max}^2$, comparing scenarios with or without the structure in place. The results indicate that the presence or absence of a mild structure does not yield significant differences in the computed results at the toe ($x = 39.10$ m), as reported in Table 6.9. A marginal wave setdown is observed at the toe when the structure is present, resulting in a slightly different $(h + \eta)\bar{u}_{\max}^2$, while the term \bar{u}_{\max} remains constant. Nevertheless, steeper slopes should be tested to verify this assertion more comprehensively.

Table 6.9. Structure vs. no structure in place comparison.

Reflection method	h (m)	\bar{u}_{\max} (m/s)	$(h+\eta)\bar{u}_{\max}^2$ (m ³ /s ²)
No structure (SL ON)	0.407	1.011	0.663
Structure in place (SL ON)	0.398	1.007	0.629

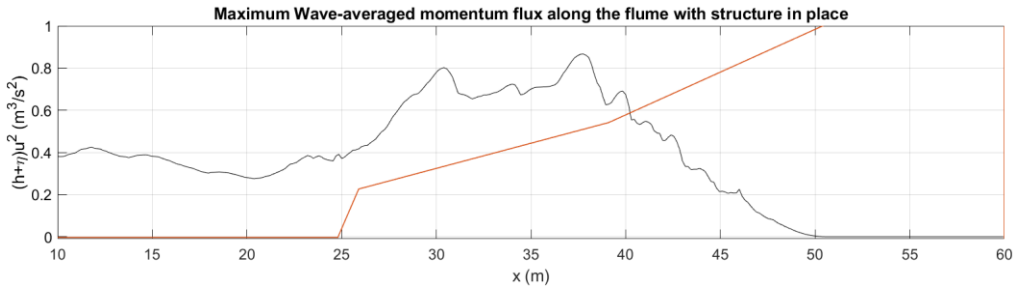


Figure 6.14. Cross-shore variation of $(h+\eta)\bar{u}_{\max}^2$ along the flume with the structure in place.

6.5. Hydrodynamic uncertainty

The use of a calibrated 1D fully nonlinear Boussinesq numerical model was essential to standardize the datasets and replicate the hydrodynamic conditions observed at the structure toe. Wave parameters were carefully matched near the wave generator and the structure toe. Results reveal significant systematic variations when comparing studies conducted across different laboratories and time periods. Notably, all the analyses presented in this study were based on the numerical outputs from the Coulwave model.

6.5.1. Wave parameters uncertainty

Typical incident-reflected wave analysis using LWT introduces a significant bias in shallow water conditions. This bias amplifies as the water depth decreases, attributing a considerable portion of incident wave energy to reflection. In this section, a comparison is made between the incident wave parameters measured at the toe of the structure in the experimental laboratory and the numerical Coulwave tests.

Figure 6.15 plots measured parameters vs. Coulwave simulated values at the structure toe for data in the experimental database. Bias and uncertainty are more pronounced for wave periods (T_m , T_p , $T_{m-1,0}$) compared to wave heights (H_{m0} , H_s , $H_{2\%}$). Wave height from Coulwave is biased and systematically larger than the laboratory data, especially for shallow water tests with sloping bathymetry. On the other hand, the wave period is generally uncertain, particularly for the VSK data and very shallow water tests.

The sources of uncertainty in laboratory wave measurements are diverse. For instance, it is impossible in the laboratory to completely eliminate wave re-reflection due to inherent physical limitations. Moreover, classical reflection analysis based on LWT introduces high uncertainty when applied in nonlinear conditions. Studies that incorporate wave measurements without the structure in the flume, utilizing classical reflection analysis methods, have shown relatively lower uncertainty compared to those conducted with the structure in the flume. These uncertainties in the wave laboratory data can obscure the underlying physics of the phenomena.

Coulwave simulations offer a means to address several sources of uncertainty. For example, it is possible to eliminate various measurement errors, including instrument errors (drift, calibration, sampling), analysis method, reflection methods, and gage location relative to the toe, among others.

Ultimately, the uncertainty for each incident wave parameter was estimated in terms of coefficients of variation (σ'). Bias and σ' for each parameter are reported in Table 6.10, indicating that H_s and T_p exhibit the smallest bias, while $H_{2\%}$ and $T_{m-1,0}$ experience minor uncertainty among wave heights and wave periods, respectively.

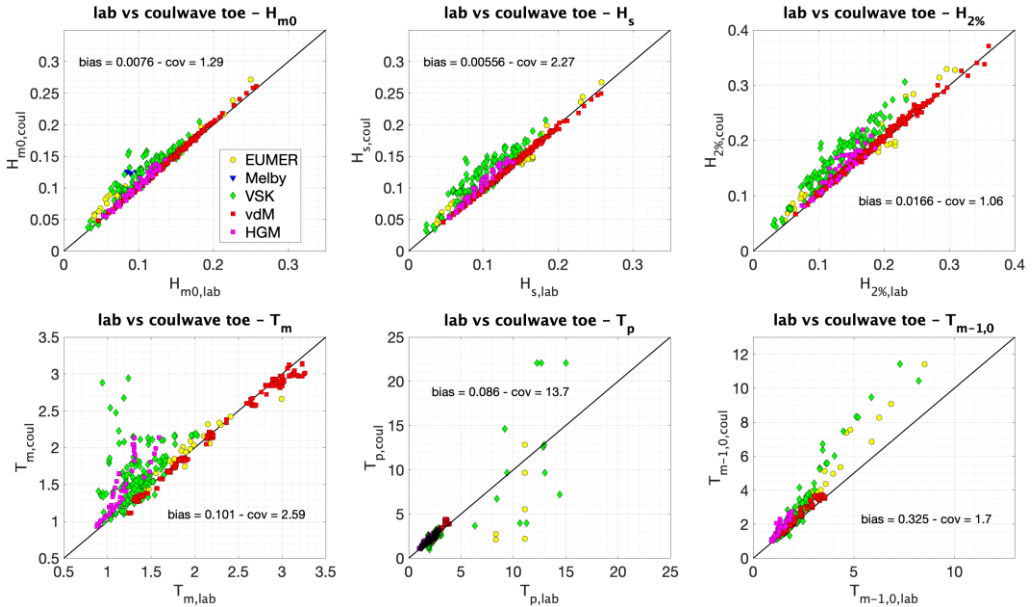


Figure 6.15. Comparison between numerical and laboratory incident wave parameters (H_{m0} , H_s , $H_{2\%}$, T_m , T_p , $T_{m-1,0}$) computed at the toe of the structure.

Table 6.10. Bias and uncertainty for incident wave parameters.

	H_{m0}	H_s	$H_{2\%}$	T_m	T_p	$T_{m-1,0}$
Bias	0.0076	0.0055	0.0166	0.101	0.086	0.325
σ'	1.29	2.27	1.06	2.59	13.7	1.7

Specifically, H_{m0} and $T_{m-1,0}$ were plotted for each dataset as illustrated in Figure 6.16. Bias becomes evident when the data are separated by studies, particularly for shallow water conditions, where the estimated bias is approximately one order of magnitude larger than in deep waters. While the numerical model proved effective in clarifying uncertainty, it also appears to introduce higher bias, likely associated with the numerical dissipation energy model. This bias could be corrected simply by subtracting it to arrive at a final synthesized database.

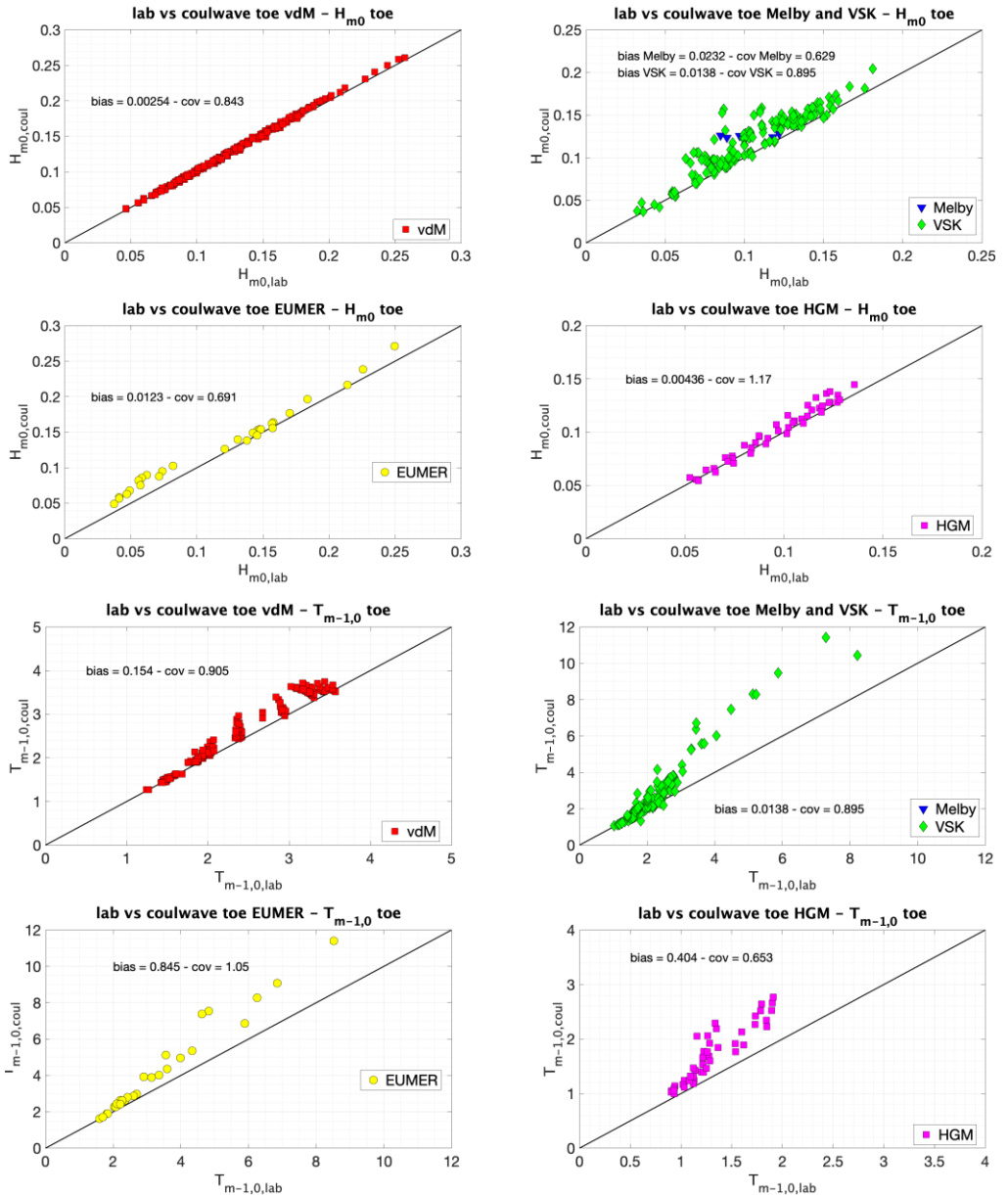


Figure 6.16. Comparison between numerical and laboratory incident wave parameters (H_{m0} , above and $T_{m-1,0}$, below) computed at the toe of the structure.

Figure 6.17 illustrates the ratios of wave characteristics as a function of the relative depth. In general, wave parameters exhibit a robust dataset prediction and demonstrate a close correlation with relative depth. The wave data are now homogenized, directly comparable, and establish continuity among different datasets. Specifically, when compared to experimental wave data, some Melby data (blue triangle) now align with the curve.

Concerning the relative wave height ratio, some uncertainty persists for very shallow water conditions but is less pronounced compared to laboratory data. However, the wave period ratio appears to be even more biased than the lab data in the very shallow waters. A notable divergence is observed in a branch of VSK data with a distinct behavior from that of EUMER. The ratio for numerical data becomes larger compared to laboratory data, reaching almost 8, signifying that $T_{m-1,0}$ from Coulwave is larger than in the laboratory. These specific data, conducted by [58], involve very shallow water conditions with a JONSWAP (3.3) wave spectrum and a 1V:100H foreshore (with around $h=0.10$ m at the toe). No distinctions were identified between single or double spectra.

These findings show that the foreshore slope can significantly influence hydrodynamic parameters and should be considered in the analysis. On the other hand, differences in wave period may be attributed to laboratory effects. Discrepancies in reflection and absorption characteristics could substantially impact the wave period due to potential inefficiencies at different frequencies. Besides, the analysis itself could introduce additional bias, particularly in shallow water and with the use of different analysis filters. Overall, Coulwave simulations inspire greater confidence compared to laboratory data, and in this context, Coulwave outputs are presumed to represent the wave parameters that are closer to the truth.

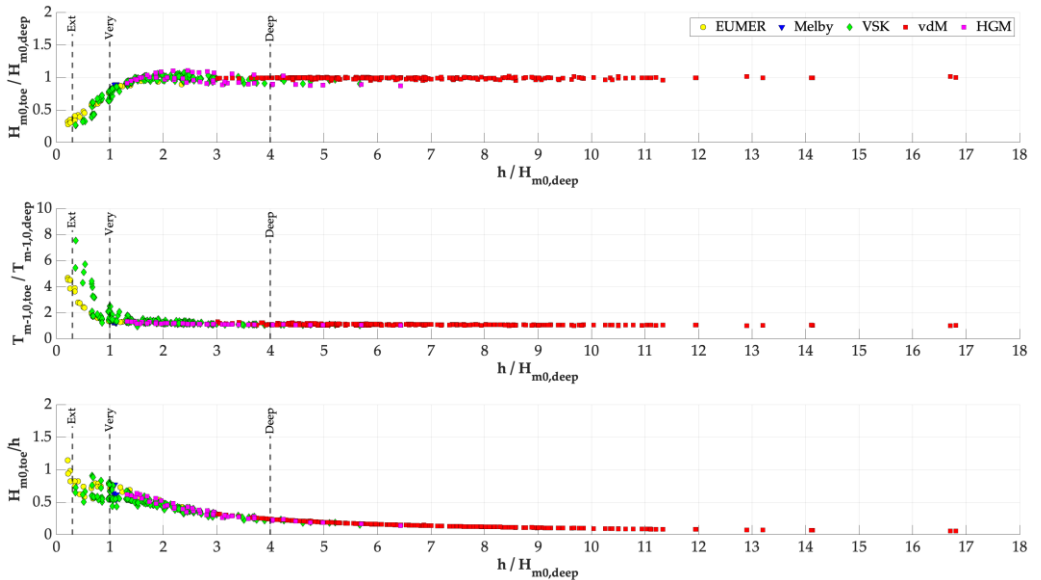


Figure 6.17. Wave characteristics ratios as a function of the relative depth.

6.5.2. Hydrodynamic force uncertainty

The LWT approximation becomes unreliable as waves become very steep, break, and transform into bores. At that point, wave momentum flux becomes primarily a function of the wave bore velocity (u) and typically resembles a drag force. Therefore, we can simply represent wave momentum flux as a drag-like force because they are directly proportional. Only quasi-static component is considered, neglecting slamming coefficients and other complexities, as it eventually culminates in an empirical equation fitted to data. In this context, we propose that the hydrodynamic force exerted by breaking waves on the armor units can be considered proportional to the term u^2 , where $u = \bar{u}$ (depth-averaged velocity) is the output of the numerical model. Thus, the velocity-based wave momentum flux parameter, $M_i = \rho(h + \eta)u^2$, is proportional to the drag force ($F_D = \frac{1}{2} C_D \rho A u^2$) but involves the total local depth ($h + \eta$) rather than the exposed area A . While this parameter shares similarities with a drag force, it is not purely a drag force.

Usually, researchers examining forces on walls and piles focus on the maximum value. However, for our structures, we seek a parameter more likely correlated with damage. Consequently, a procedure analogous to wave force statistics, where authors computed significant wave force and other statistics, was also applied to M_f . It is essential to extract stable statistics on the M_f variable because relying solely on the maximum value, instead of an integrated value, introduces substantial uncertainty. Simply computing maximum value of M_f is essentially akin to computing u_{\max}^2 , comparable to computing H_{\max}^2 . Using H_{\max} in the stability number relation (N_s) instead of integrated values introduces significant uncertainty that obscures the physics.

Numerous questions arise regarding which parameter to employ for statistical analysis, and which integrated statistical value of M_f best represents the force on the armor units at risk. One certainty is that representation of M_f depends on the water depth; depth plays a crucial role here. Therefore, computing statistics separately for $(h + \eta)$ and u is redundant since they are correlated. Consequently, statistics were computed solely on the signed parameter $(h + \eta)u|u|$, which is proportional to M_f (and therefore to F_D) aiming to derive a stability equation with the lowest epistemic uncertainty and the highest correlation with the S_d value.

Indeed, as illustrated in Figure 6.18a, M_f is not a stationary random Gaussian process of time as $\eta(t)$ and $u(t)$ and does not fully conform to a normal distribution due to the term $u|u|$, which tends to narrow the experimental data. What is more, Figure 6.18c, d reveal that the probability density function (PDF) and cumulative density function (CDF) of exceedance of the crest-to-trough heights of the signed time series of M_f , in a non-dimensional form, do not follow a Rayleigh distribution. Assuming a Rayleigh distribution would allow us to use the standard ratios between integrated values, as is done for wave height parameters.

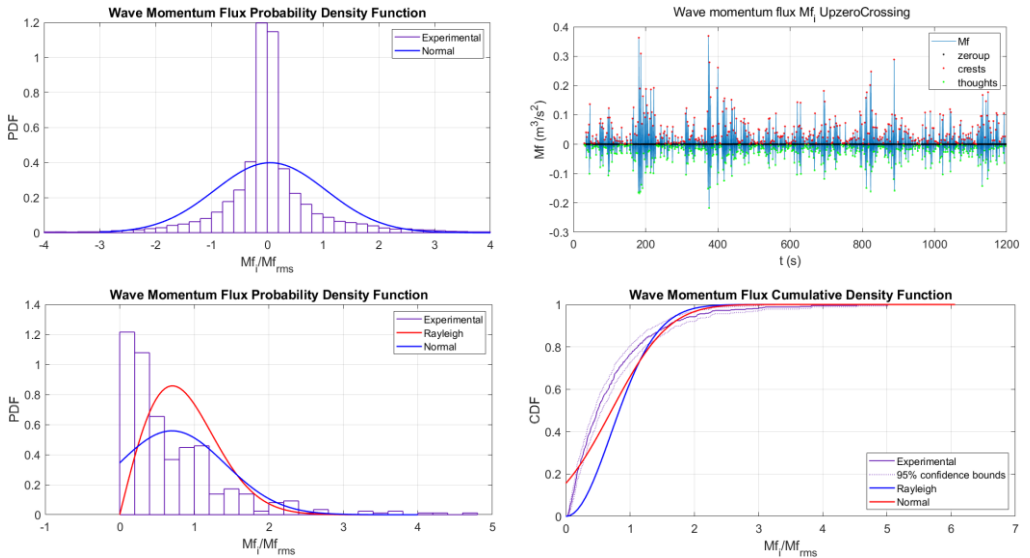


Figure 6.18. Top left) Probability density function for $M_f(t)$; top right) Zero-Up crossing method for M_f ; bottom left) PDF of exceedance of the crest-to-trough heights; bottom right) CDF of exceedance of the crest-to-trough heights.

Results show that the PDFs and CDFs of the instantaneous velocity-based term of wave momentum flux are not fully Gaussian processes, and consequently, the PDF of exceedance of the crest-to-trough heights is not entirely Rayleigh distributed. It aligns more closely with a Weibull PDF. Nonetheless, these outcomes are comparable to the PDF of instantaneous drag force on stone armor units. [201] suggested a slightly different PDF that conserves the sign of the force fluctuation.

In Figure 6.19, Weibull and Lognormal distributions are plotted with the experimental data, demonstrating that the PDF resembles the derived PDF of drag forces (shear stress) found by [201]. Other options considered were computing statistics on the peaks of the normalized $M_f = ((h + \eta)\rho u^2) / \gamma h^2$ or even on $\sqrt{|M_f|}$. Ideally, normalization would remove the offset from h , and distribution should be somewhat closer to Rayleigh. But, in conclusion, the “significant” wave momentum flux

$(M_{f,1/3} = ((h + \eta)u^2)_{1/3})$ was selected as the most suitable for reformulating the stability equations.

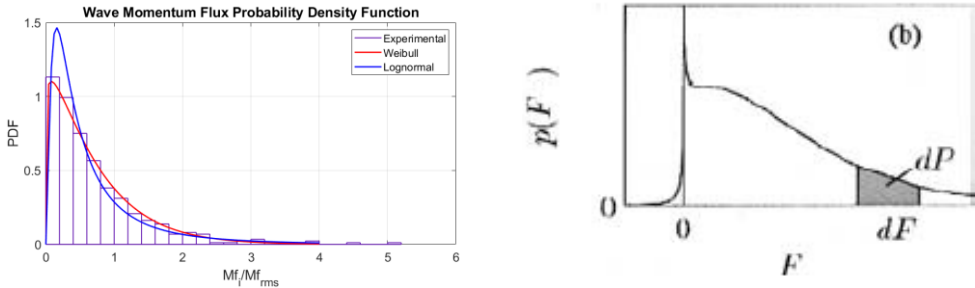


Figure 6.19. Comparison between the M_f and drag forces PDFs (source [201]).

6.5.3. Wave momentum flux uncertainty

A robust data set was discovered that correlates wave parameters with relative water depth. Subsequently, $M_{f,1/3}$ was defined as the most suitable statistical parameter to characterize the hydrodynamic force acting on armor units. If either u or M_f demonstrates a strong correlation with relative depth, similar to the wave parameters, establishing a relationship between M_f and wave parameters, as Hughes did in Eq. (6), should be straightforward. Figure 6.20 illustrates $u_{1/3}$ and $u_{1/3}^2$, $hu_{1/3}^2$, $M_{f,1/3}$, $M_{f,1/3}/gh^2$ and $((h + \eta)u^2)/gh^2)_{1/3}$ against relative depth for the entire database. Two distinct clusters of data emerge in this Figure. Specifically, vdM data (red squares) exhibit different behavior compared to all the others. This inconsistency is observed across most plots and may suggest an influence from the sloping bathymetry. However, a high level of agreement and correlation is observed when the normalized significant M_f is plotted against the relative depth. This can be attributed to the fact that the u^2 term introduces high uncertainty, but normalization by the water depth reveals a discernible trend.

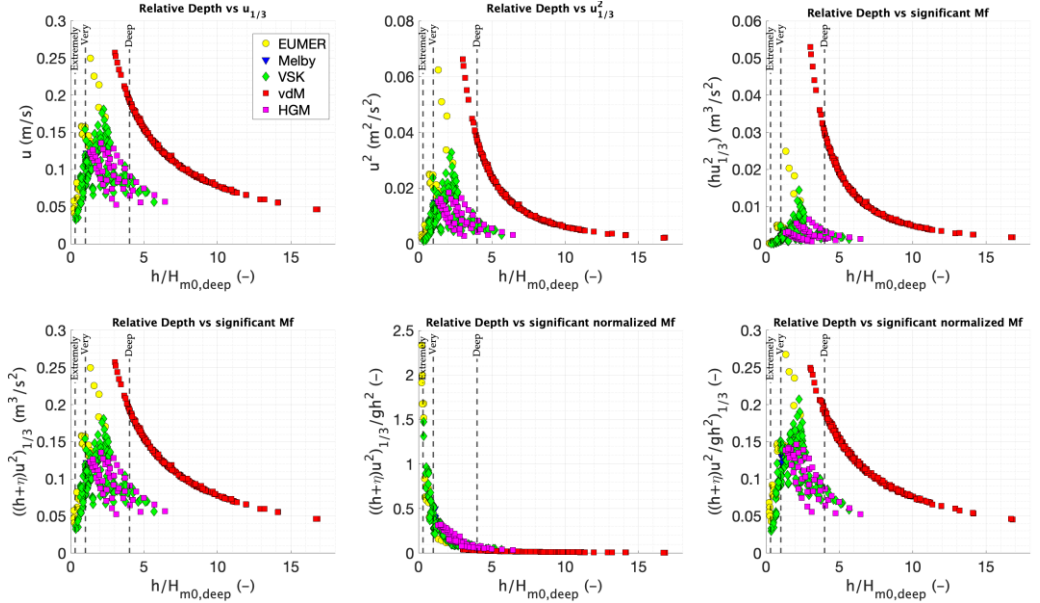


Figure 6.20. $u_{1/3}$ and $u_{1/3}^2$, $hu_{1/3}^2$, $M_{t,1/3}$, $M_{t,1/3}/gh^2$ and $((h + \eta)u^2)/gh^2$ plotted against the relative depth for the entire numerical database.

This conclusion confirms the appropriateness of using the parameter $M_{t,1/3} = ((h + \eta)u^2)_{1/3}/gh^2$ as the ideal descriptor for the correlation between hydrodynamic force and the other variables in stability analysis. Consequently, it would be valuable to assess whether LWT (Eq. (19c)) and the nonlinear approximated Hughes (Eq. (6)) equations fit with the new data. The first-order approximation of wave momentum flux in periodic waves is provided in nondimensional form in Eq. (19c), where the first term represents the pressure term, and the second represents the velocity term. Here, $H = H_{m0}$, k is the wave number using LWT dispersion relation, and T_m is computed at the toe. Figure 6.21 shows the total and the two separate components (i.e., velocity and pressure terms) of linear Hughes M_t plotted against the relative depth to discern their contributions to M_t under different shallowness conditions. In theory, the velocity term should always be much smaller than the pressure term, although there may be conditions where it is significant enough to make a difference. The results in Figure 6.21 demonstrate that the velocity term is always smaller and, in many cases,

almost negligible. The trend of the vbMf (LWT) aligns closely with the one found in Figure 6.20 using $M_{f,1/3}/gh^2$ with a very strong correlation.

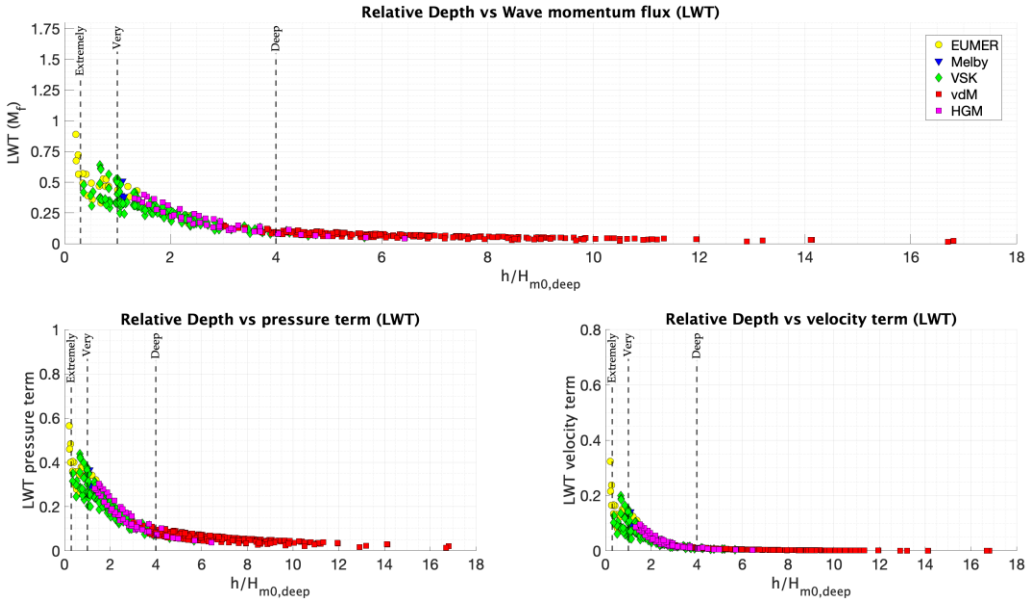


Figure 6.21. Total and velocity and pressure M_f components plotted versus the relative depth.

The same components were plotted as relative percentages of the total linear Hughes M_f to investigate the influence of relative depth on the development of the two components (Figure 6.22). Results consistently show that the pressure term (>60%) always dominates compared to the velocity term (<40%). These findings align with Hughes' observation. The velocity-based M_f (vbMf) term tends to increase in shallower conditions. The relative contribution of the velocity term to the total depth-integrated wave momentum flux varies from about 5% for low-amplitude long-period waves to nearly 30-40% for waves approaching limiting steepness. However, it is important to note that LWT estimates of the maximum depth-integrated wave momentum flux are lower than real values because they neglect the momentum flux above the still water

level. Additionally, it must be acknowledged that LWT introduces large errors in shallow water, providing only a semiquantitative sense of the phenomenon.

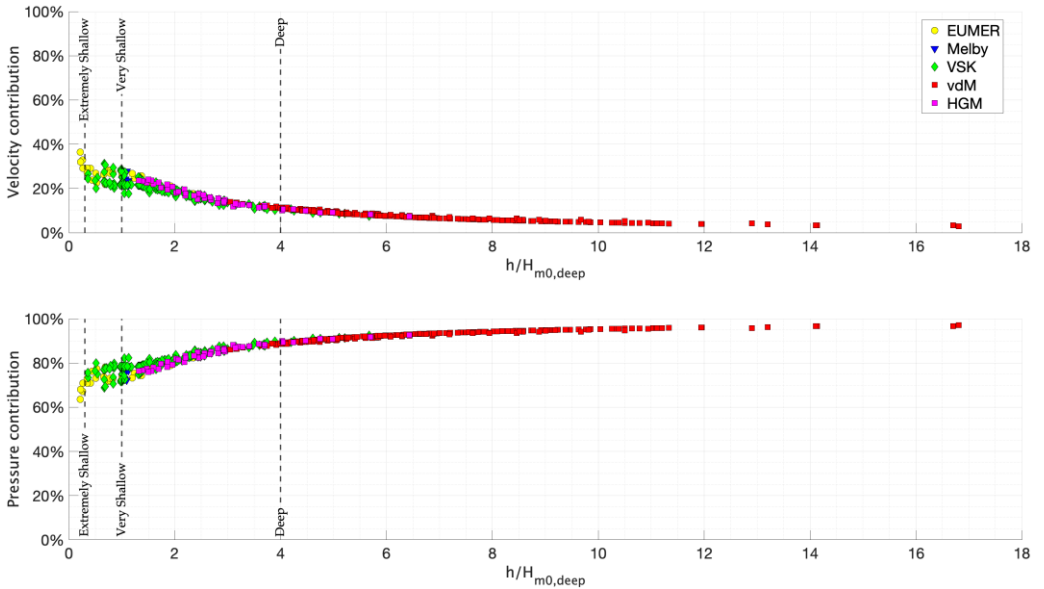


Figure 6.22. Velocity and pressure components to M_f Hughes in percentage with respect to the relative depth for the entire numerical database.

In Figure 6.23, the normalized M_f is plotted against the relative wave height terms ($H_{m0,deep}/h$ and $H_{m0,toe}/h$), revealing that the normalized M_f appears to be primarily a function of H/h . Additionally, the long wave shallow water wave limit is included in the plot. It is possible that, for most cases, the shallow water wave limit assumption holds, and the outliers on the plot represent real cases. If we were to include a broader range of possible wave, depth, and period cases, rare but plausible outliers might become more apparent. It is important to note that Hughes's estimate neglects the velocity in the wave crest. For breaking waves and waves in the swash zone on the structure, this omission is likely significant and may account for most of the difference between Coulwave and Hughes's M_f estimates. The shape and the approximate location of the curve confirm that most tests (almost all the points near the line) involve shallow water

waves. The location of the curve relative to the points is somewhat arbitrary and depends on the statistical measures used to represent the plotted variables. This suggests that most, if not all, of the outliers correspond to very shallow water tests.

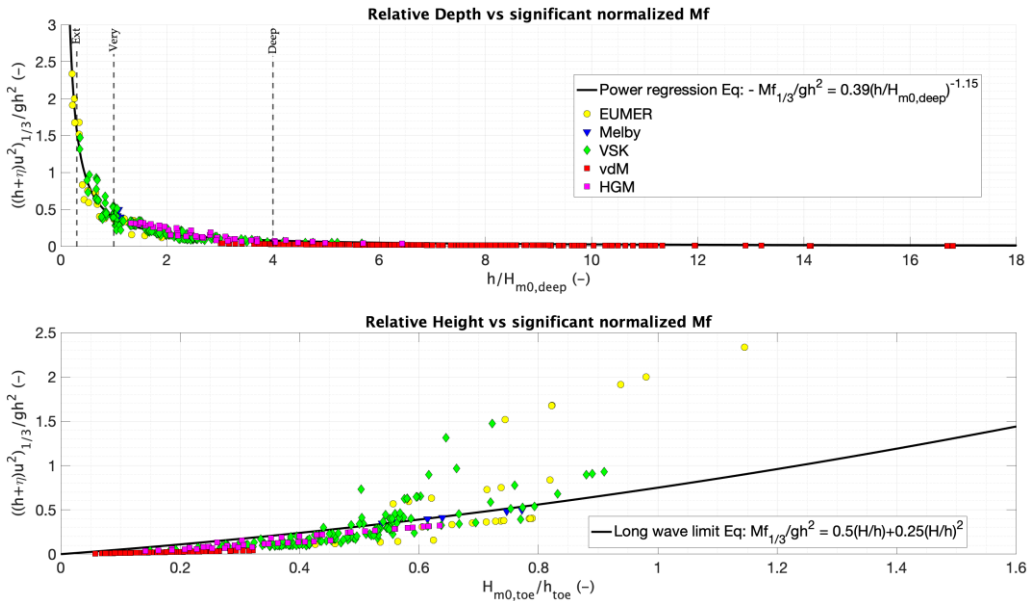


Figure 6.23. Normalized $M_{f,1/3}$ plotted vs. $h/H_{m0,deep}$ and $H_{m0,toe}/h$.

In the final analysis, an examination is conducted to assess the appropriateness of the Hughes equation for fitting the new data. To achieve this, Figure 6.24 illustrates the plotting of the Hughes M_f equation prediction, LWT M_f , and Coulwave M_f , with normalized M_f on both axes with a 45°-degree line. The offshore measured $T_{m-1,0}$ is used to calculate M_f . This approach aims to provide insights into the characteristics of M_f compared to Hughes and LWT. Considering that the stability equation is entirely empirical, this M_f analysis is expected to bring clarity regarding the suitability of confidently using the Hughes equation or, alternatively, propose the development of a revised version that is superior or more straightforward.

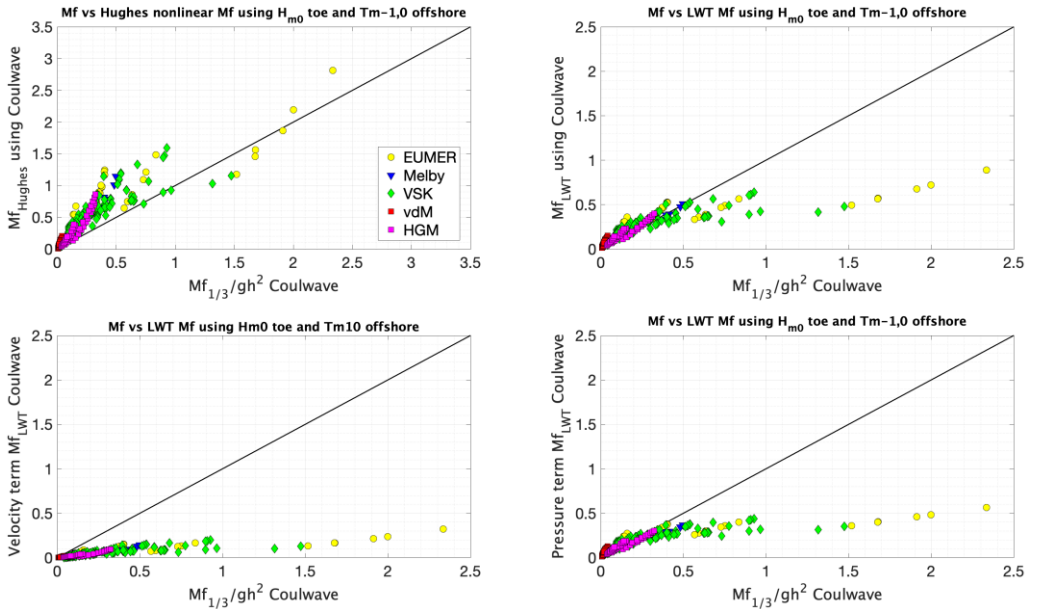


Figure 6.24. Comparison between the measured M_f vs. the Hughes and LWT M_f .

The comparison between Hughes' and Coulwave M_f reveals a significant discrepancy, particularly in the underestimation of nonlinear M_f by Coulwave. The upper right plot is not very informative, as LWT M_f is known to be inaccurate. It can be speculated that this discrepancy may be attributed to the missing pressure term, which represents most of the analytical M_f . Additionally, the M_f vs. H/h plot, combined with observation that the points are almost vertically upward on the M_f vs. M_f plot, suggests that some physics are being lost. There seems to be some functionality missing from the Coulwave M_f computed at the toe, perhaps related to variations in wave steepness. However, this functionality is preserved using the Hughes M_f equation but lost with Coulwave M_f .

The importance of this functionality is questioned, considering that much of it is likely to disappear near the SWL on the structure slope where the forces are highest. Instability typically occurs near the SWL, coinciding with the maximum wave velocity (u_{max}). For shallow water, the depth-integrated velocity at the toe, and thus the M_f at the

toe, is probably a good representation of the maximum force because the wave behaves as a bore. Therefore, Coulwave u at the toe should provide a reasonable basis for the maximum force in shallow water. However, in deep water, the Coulwave depth-averaged u at the toe may not be a suitable basis for the maximum force. It may be that a velocity value up the slope is more appropriate. As we go up the slope from the toe, the flow area narrows, and the flat orbits of the orbital fluid velocity transform into uprush and downrush. Velocity increases to conserve mass and momentum despite turbulent and frictional dissipation. Consequently, the flow force goes from pressure-dominant to velocity-dominant. Thus, Coulwave M_f should be better suited for cases where there is less pressure influence at the toe.

The actual M_f remains unknown, leaving uncertainty regarding the correctness of Hughes or Coulwave. While Hughes' M_f is assumed to be more accurate at the toe, points close to the agreement line suggest that the M_f velocity term is greater, whereas those further away, particularly in deep water, should be dominated by pressure. This reinforces the notion that the differences lie in the pressure term. Coulwave should be more accurate up to the structure slope, near the damaging area, where velocity dominates. Further exploration is needed to elucidate how Coulwave M_f correlates with other parameters such as structure slope, bathymetry slope, permeability, and wave steepness, specifically in the context of instability.

In Figure 6.25, all the stability wave data were plotted using the same approach as Figure 4.2. For breaking waves at high M_f (on the left side of the plot), small changes in T lead to large changes in M_f . There exists a narrow range of potential periods on the left side where M_f is at its peak, representing shallow depths and long waves, likely the worst-case scenario for stability. On the other hand, wave period strongly influences the right side of the plot. Linear theory performs well on the right side but is poor on the left side. In addition, for low relative depth (H/h , lower on plot), linear theory introduces less error compared to high H/h .

Linear theory produces an error of approximately a factor of 2 on the left side of the plot when compared to Hughes' Fourier wave model. This Figure shows that nearly all the very shallow water tests fall outside the long wave steepness limits, indicating that they are not well predicted by the Hughes equation. On the other hand, the velocity-based wave momentum flux from a depth-integrated model $((h + \eta)\bar{u}^2/gh^2)$ differs from the analytical M_f integrated with depth. The numerically computed vbMf lacks the pressure term, possibly leading to inaccuracies compared to the integral form. However, it represents the best approximation for a depth-integrated model like Coulwave.

Hughes' error increases with decreasing depth due to real fluid effects in wave breaking regions. In Hughes's model, wave particle orbits are elliptical for nonlinear waves, but it behaves more like a bore with a velocity predominantly shoreward except for the return current. The physics involved are very different, but Coulwave is likely to be closer to reality. Nevertheless, a reasonable error of 20-30% difference in velocity becomes huge when squared.

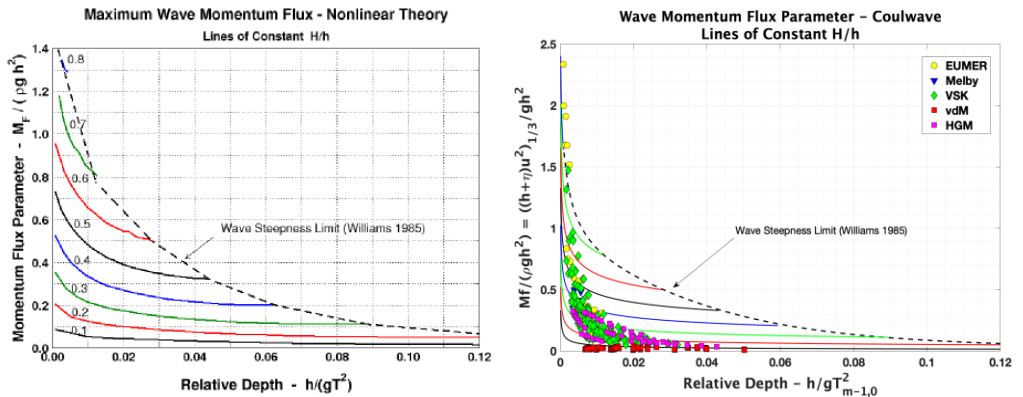


Figure 6.25. New wave stability data plotted in Hughes figure.

Moreover, as highlighted by numerous authors in the past and previously discussed in Section 4.2.6, armor stability is more closely linked to runup (drag force), which can be even more destabilizing than the total wave momentum flux. In this context, we

argue that the pressure term has negligible influence on armor units because the maximum force occurs in a swash regime where waves run up and down the slope, entirely induced velocity. Indeed, numerical Fourier solutions for non-breaking waves with symmetric steep crest may not accurately predict the maximum momentum flux of bores in the inner surf zone. Similarly, the Boussinesq model with empirical wave breaking may not be highly accurate either, showing errors around 10-15% in shallow waters. In our approach, we assume that the maximum M_f at the structure toe is proportional to the maximum force on an armor unit on the slope.

Finally, this thesis proposes a new physical reformulation of the stability equation. Instability is typically caused by specific waves and combinations of waves in a spectrum, often limited to the largest waves, with the wave period and multi-variable combination playing a role. Specific rundown scenarios can cause the next wave to be particularly damaging. Armor stability is highly sensitive to specific wave-wave interaction, yet researchers often employ bulk parameters to describe the wave effect on stability, leading to potential epistemic uncertainty. Variations in wave spectra realization, spectral shape, grouping, and related factors impact stability, and obtaining the necessary data to resolve these issues is very challenging. The problem extends beyond investigating spectral shape and grouping, which have been explored in some referenced papers. Parameters such as H_s vs. H_{m0} and T_p vs. $T_{m-1,0}$, breaking vs. nonbreaking, wide vs. narrow breaker zone, approach slope and structure slope, all influential this topic. Fortunately, comparing results from different laboratories, has allowed us to capture much of this variation.

6.6. Conclusions

This chapter delves into the setup of the numerical high-fidelity phase-resolving wave transformation model utilized to enhance the synthesis and homogenization the data from an hydrodynamical perspective. A one-dimensional fully nonlinear Boussinesq numerical model (Coulwave) was implemented to replicate incident and reflected wave

conditions at the toe of the structure, facilitating a consistent comparison of laboratory and numerical studies.

This approach contributes to a better understanding of hydrodynamic uncertainty by shedding light on the primary sources and magnitudes of intrinsic and epistemic uncertainty in wave parameters. The numerical model proved effective in clarifying uncertainty, although only achieved a marginal reduction in hydrodynamic uncertainty compared to the total uncertainty. This finding reveals that most of the uncertainty is not associated with the wave and water level conditions.

Results conclusively indicate that the wave momentum flux parameter maintains a direct proportionality to the drag force exerted along the structure slope, displaying a discernible correlation with incident wave parameters.

Ultimately, the method also enables the separation of errors caused by the wave transformation mode, thereby facilitating the assessment of the effect of wave prediction errors on stability prediction errors.

CHAPTER 7

Results

7. Results

This section proposes a reformulation of the destabilizing forcing on the armor unit based on the significant momentum flux and wave parameters measured at the toe of the structure through numerical wave simulations. After rewriting the left-hand side (LHS) of the equation, it is recommended to re-define and refit the right-hand side (RHS) using the new database.

Section 4.1 provided a physics-based derivation of the stability equation, outlining the derivation of the maximum M_f using the nonlinear approximated Hughes equation (Eq. (6)) based on the incident H_{m0} and T_m and h . In this context, hydrodynamic forcing was characterized in terms of the “*significant*” wave momentum flux ($M_{f,1/3}$). However, there remains a necessity to introduce empirical relations that describe armor damage, resistance, storm duration, and the influence of wave-structure interaction.

The expectation is that the reformulation and refitting processes will enhance the understanding of physics due to reduced epistemic hydrodynamic uncertainty. Ultimately, this may not necessarily reduce overall uncertainty, but we anticipate a more accurate representation of the physics. Furthermore, there is potential of having a single equation as opposed to two equations, enabling application to a broader range of parameters owing to improved physics.

7.1. General overview on the stability equation

The governing variable for hydraulic static stability is the damage value, denoted as $S_d = A_e / D_{n50}^2$. Several authors have compiled lists of governing variables that influence the performance of rubble mound armors. These lists encompass variables related to environmental conditions, which are typically beyond the control of a designer and influence disrupting forces, as well as variables associated with the physical characteristics of the structure, affecting the structure's response.

A representative list of environmental variables comprises:

- the incident wave field $\eta(x,t)$
- the duration of wave activity, characterized by the number of waves N_w
- the spectral shape
- the angle of wave attack
- the foreshore slope angle β
- the water depth $h(x,t)$ at the toe of the rubble mound structure
- the density of water ρ_w
- the acceleration due to gravity g
- the viscosity of the water μ

In previous studies, the incident wave field was parameterized based on a design wave height and wave period. Physical variables were employed to describe the geometry of a rubble mound and characteristics of its constituent materials. This includes factors such as the size, shape, and grading of armor and filter layers.

The atypical list might include:

- the nominal size of armor stones D_{n50}
- the grading of armor stones D_{85}/D_{15}
- the density of armor stones ρ_r

- the shape of armor stones *LT* and *BLC*
- the quality (mechanical strength) of armor stones
- the surface roughness and packing density of armor stones
- the thickness of the armor layer t_A
- the nominal size of the filter stones $D_{n50,filter}$
- the grading of the filter stones
- the thickness of the sublayers e
- the nominal size of the core stones $D_{n50,core}$
- the permeability of the structure P
- the seaward slope angle α
- the natural angle of repose of stones ϕ
- the construction method
- the relative crest freeboard R_c
- the width of the crest G_c

The shape, roughness, and gradation of armor stones, as well as the construction method, influence the porosity of the armor (ρ). These factors also impact the degree of interlocking between armor stones, commonly parameterized by the internal friction angle (ϕ). Design equations for armor stability are typically semi-empirical relations that incorporate a few dominant environmental and physical variables. Among these variables, wave height stands out as the most influential environmental variable affecting the stability of armor stones. Its direct output from wave buoys or numerical models makes it easily accessible for designers. According to LWT, the average energy density of waves can be expressed in terms of their wave height as $\frac{\rho g}{8} H^2$. In shallow water, the average forward energy flux is $\sqrt{gh} \frac{\rho g}{8} H^2$.

Thus, wave height can be considered a parameterization of the energy density and energy flux of incident waves on a rubble mound. Consequently, using the velocity-

based wave momentum flux (vbMf) as the primary environmental variable to describe armor stability is a straightforward approach.

Moreover, for a rubble mound with a fixed slope angle exposed to waves with constant wave height, the wave period governs the type of wave breaking that occurs. This, in turn, affects the flow within the armor layer and the forces acting on and stability of armor stones. Therefore, adopting the dimensionless wave steepness (s_m) is a valid assumption for describing the impact of wave period on armor stability.

Additionally, insights from the literature reveal that:

- For $Re > 300$, Re is negligible (viscous effect μ).
- For standard rough equant angular shape armor layers ($LT \leq 2.5$ and $50\% \leq BLC \leq 60\%$), the stone shape is considered negligible.
- For $1.25 \leq D_{85}/D_{15} \leq 2.5$, the armor grading is considered negligible.
- For $1.8D_{n50} \leq t_{\Delta} \leq 2.2D_{n50}$, both e and t_{Δ} are considered negligible.
- For non overtopping conditions, R_c and G_c are considered negligible.
- For perpendicular wave attack, the angle of wave is negligible.
- For bulk random placement method, both ϕ and ρ are considered negligible.
- The relative density can be combined as $\Delta = f(\rho_r, \rho_w)$.
- The spectral wave period ($T_{m-1,0}$) and significant wave height (H_{m0}) are functions of the spectral shape.

These considerations provide guidelines for simplifying certain variables and focusing on the most influential factors in the analysis.

7.2. Reformulation of the stability equation

In this section, we want to reformulate the equation for stone armor stability by incorporating the significant wave momentum flux and wave parameters obtained from

the Coulwave model. The primary environmental variables were translated into the dimensionless stability number (N_m) and the dimensionless wave steepness (s).

The tests described in this study involved perpendicular wave attacks, minimal to no overtopping, standard rough equant angular shape stones, and bulk random placement. Moreover, the conditions of the new database allowed for the exclusion of numerous variables within the specified set. Therefore, the stability equation resulting from the following function can be expressed as shown in Eq. (27):

$$N_m = \left(\frac{K_m [(M_f)_{1/3} / gh^2]}{(S_r - 1)} \right)^{1/2} \frac{h}{D_{n50}} = f(S_d, N_w, \alpha, P, s) \quad \text{Eq. (27)}$$

7.2.1. Storm duration N_w

Armor damage is influenced by both the intensity and duration of wave attacks. Once the incident waves exceed the threshold for damage initiation, the extent of damage incurred becomes dependent on the duration of wave attack. Usually, longer test durations are necessary to approach the equilibrium damage level. While an infinite duration of stationary irregular wave attack would eventually establish a true equilibrium damage response, such tests are impractical. Therefore, a relatively short and finite test duration, allowing significant damage to occur, must be selected.

Damage progression is observed over time as long as wave severity remains above the damage initiation threshold, and marginally stable armor stones are exposed to wave action. As the number of marginally stable armor stones decreases (due to shifting and displacement), the erosion rate tends to decrease until an equilibrium condition is reached. In this state, all remaining armor stones are sufficiently stable to resist erosion, regardless of further wave activity.

[52] conducted tests with durations of up to 5000 irregular wave cycles, with intermediate damage surveys every 1000 waves. [30] used test duration corresponding to 1000 and 3000 average wave periods. Based on empirical analyses of their tests, van der Meer suggests a damage relationship with the square root function of the number of waves (N_w) for constant wave and water level conditions as in Eq. (28):

$$S = f(N_w^{0.5}) \quad \text{Eq. (28)}$$

The damage growth rate is initially rapid but diminishes with extended storm durations [31, 144]. The number of waves attacking the structure (N_w) is typically calculated as $N_w = t_r/T_m$, where t_r is the total duration of the record, and T_m is the mean wave period. The square root function is applicable within a limited range ($500 \leq N_w \leq 5000$), as discussed by [52], [31]. It is recommended to measure damage after at least two test durations to validate the square root function's applicability. It is advised to assess the validity of this assumption for any new dataset before application.

[54] proposes a validation check if $(N_{w,3000}/N_{w,1000})^{0.5} = 1.73$ and $(S_{d,3000}/S_{d,1000})^{0.5} = 1.26$, where $N_{w,3000}$ and $N_{w,1000}$ are the number of waves attacking the structure (measured at the toe) corresponding to damage values $S_{d,3000}$ and $S_{d,1000}$, respectively. This check was also conducted on the present database, and the results are outlined in **Table 7.1** for each dataset. The table indicates that, as expected, the square root function accurately describes all the analyzed datasets. Indeed, vdM stated that this function is applicable when the mean ratios of $(N_{w,3000}/N_{w,1000})^{0.5}$ and $(S_{d,3000}/S_{d,1000})^{0.5}$ are approximately equal to the values obtained in his thesis. Therefore, for VSK and EUMER data, it is evident that the mean ratios closely align with vdM, exhibiting a relatively small std.

Table 7.1. Validation for the square root function for N_w as indicated by vdM [54].

	vdM	VSK	EUMER	All
Mean $(N_{w,3000}/N_{w,1000})^{0.5}$	1.73	1.71	1.68	1.73
Std $(N_{w,3000}/N_{w,1000})^{0.5}$	$\cong 0$	0.085	0.102	0.038

Mean $(S_{d,3000} / S_{d,1000})^{0.5}$	1.26	1.25	1.20	1.25
Std $(S_{d,3000} / S_{d,1000})^{0.5}$	0.132	0.087	0.171	0.135

7.2.2. Damage curve

The relationship between the damage values $(S_d/N_w^{0.5})$ and the stability number (N_s) calculated at the toe of the structure is commonly expressed as a 5-power relationship, as illustrated in Eq. (29):

$$\frac{S}{\sqrt{N_w}} = f(N_s)^q \quad \text{Eq. (29)}$$

Here, damage gradually increases according to a power relationship with the exponent “ q ”, which defines the shape of the curve. [30] proposed ‘ q ’=5 as the optimal relationship in the equations, while [70] reported ‘ q ’=6. [54] recommended checking the shape of the damage curve before comparing different datasets. Therefore, the same procedure described by vdM was repeated for this new database to verify if ‘ q ’=5 can still be considered the optimal relationship between the armor damage value and the stability number based on the M_f calculated at the toe of the structure.

In Figure 7.1 the armor slope normalized damage $(S/N_w^{0.5})$ is plotted on the y -axis, along with the incident H_{m0} (on the left) and M_f (on the right) on the x -axis, where a 5-power relationship is also shown. Similarly, in Figure 7.2, $S/N_w^{0.5}$ is plotted against the stability numbers namely N_s and N_m . Overall, values of the exponent ‘ q ’ between 4 and 6 should not be considered significantly deviating from other formulae, indicating that an average value of ‘ q ’=5 can be confirmed for the development of the new stability formula. In this way, it becomes evident that both M_f and N_m are correlated to the fifth power of damage, akin to H_s and N_s . However, it is valuable to isolate data points that do not conform, representing outliers, and attempt to understand the reasons, as these data may not be reliable for use.

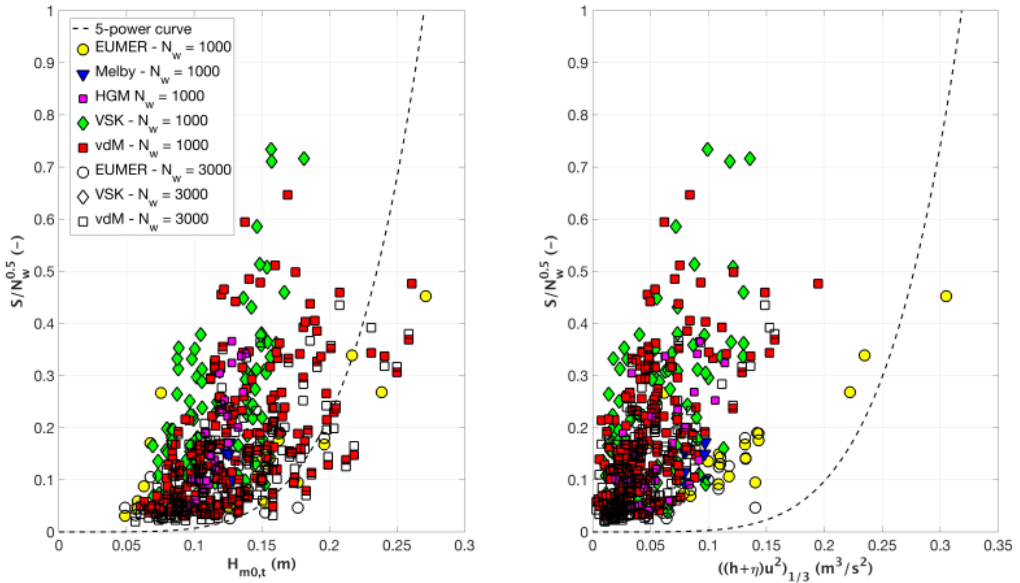


Figure 7.1. Normalized damage plotted vs. H_{m0} and $M_{f,1/3}$.

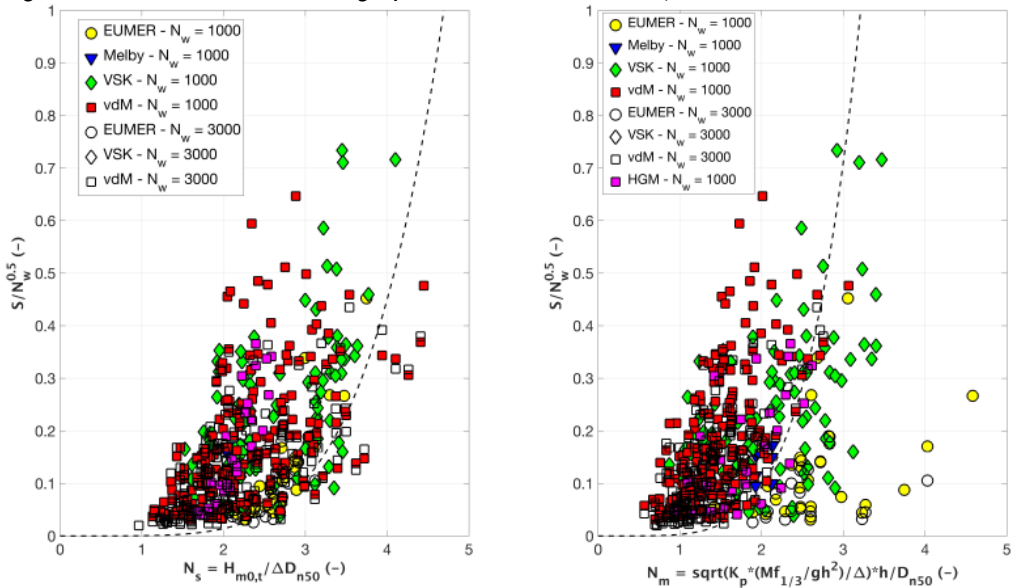
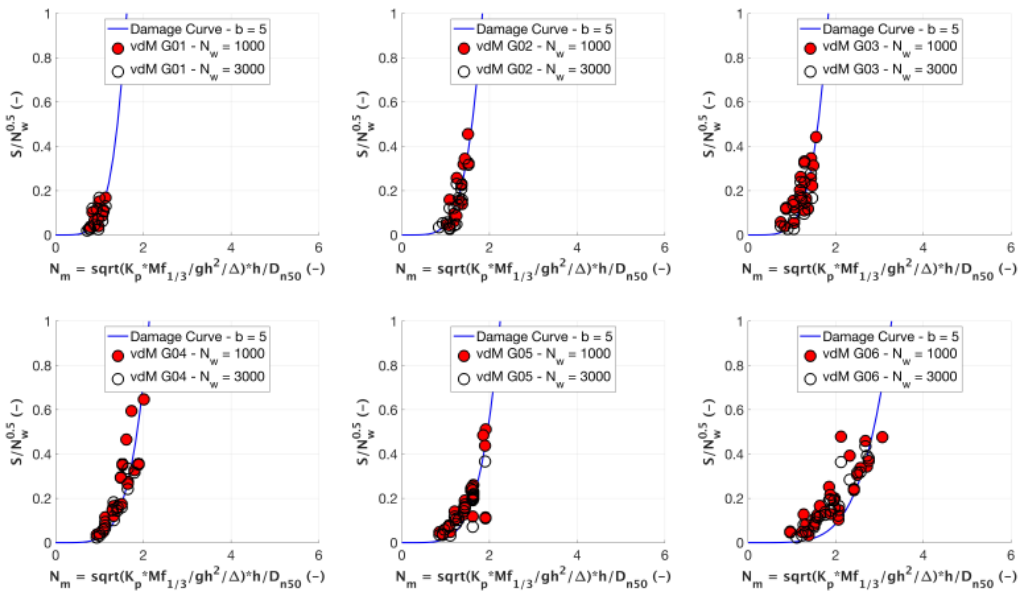


Figure 7.2. Normalized damage plotted vs. N_s and N_m .

Generally, lower levels of damage exhibit greater scatter and often do not adhere to any specific rule. There is a valid reason of this. Minor damage can be influenced by atypical

cases, such as one or more loose stones or poorly shaped (flat) stones that are displaced early in the test. Additionally, subsequent progressive damage may deviate from the rule due to initially poor placement. In addition, overly tight placement may result in an armor layer that is relatively more stable. This could be attributed to aleatory uncertainty, as an intrinsic characteristic of structures, or epistemic as an additional error. To this extent, the most significant data groups (i.e., vdM, VSK, Melby, and EUMER) were selected and plotted in isolation in Figure 7.3, Figure 7.4 and Figure 7.5 as an example to demonstrate that N_m exhibits a clear relationship with the dimensionless damage $(S_d/N_w^{0.5})$ with low uncertainty. Overall, despite some deviations, it can be concluded that the stability number can be effectively combined with the term $(S_d/N_w^{0.5})^{0.2}$ for the entirety of the experiments. In certain instances, some divergencies can occur. The reasons for this divergence can be epistemic and difficult to explain and separate, potentially related to laboratory effects or the inherent stochastic nature of stone displacement.



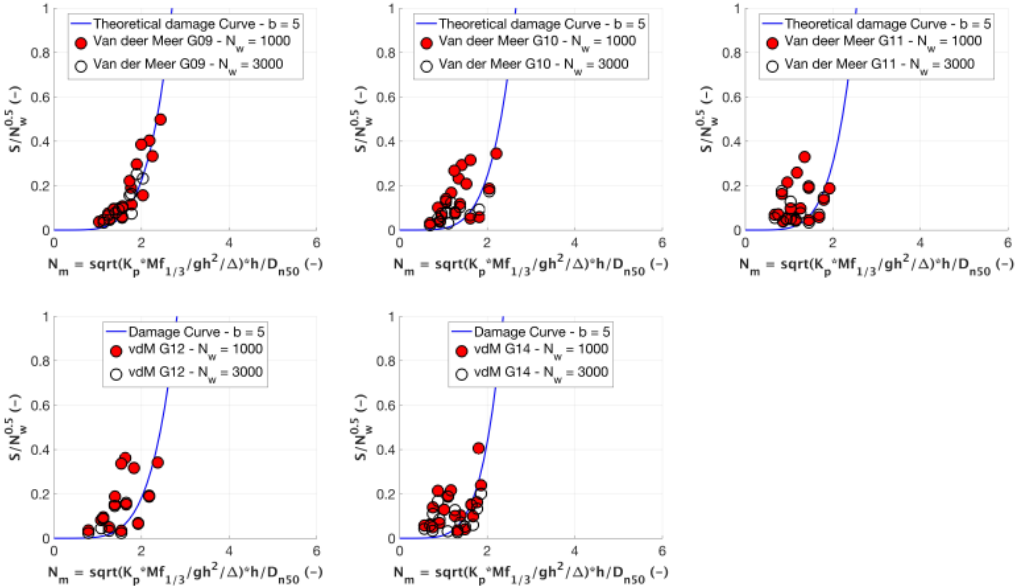


Figure 7.3. Damage curves for vdM data groups.

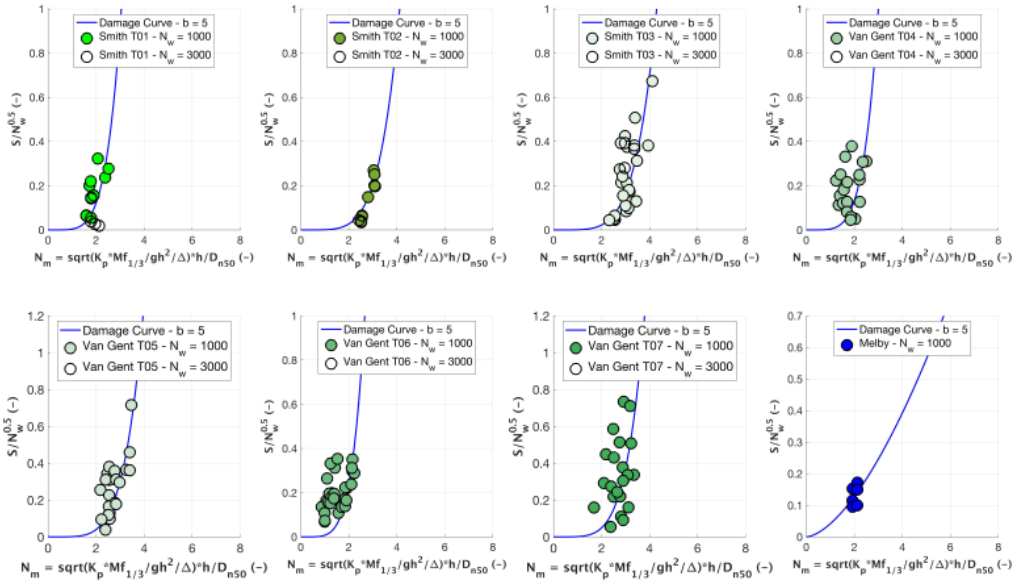


Figure 7.4. Damage curves for VSK and Melby data groups.

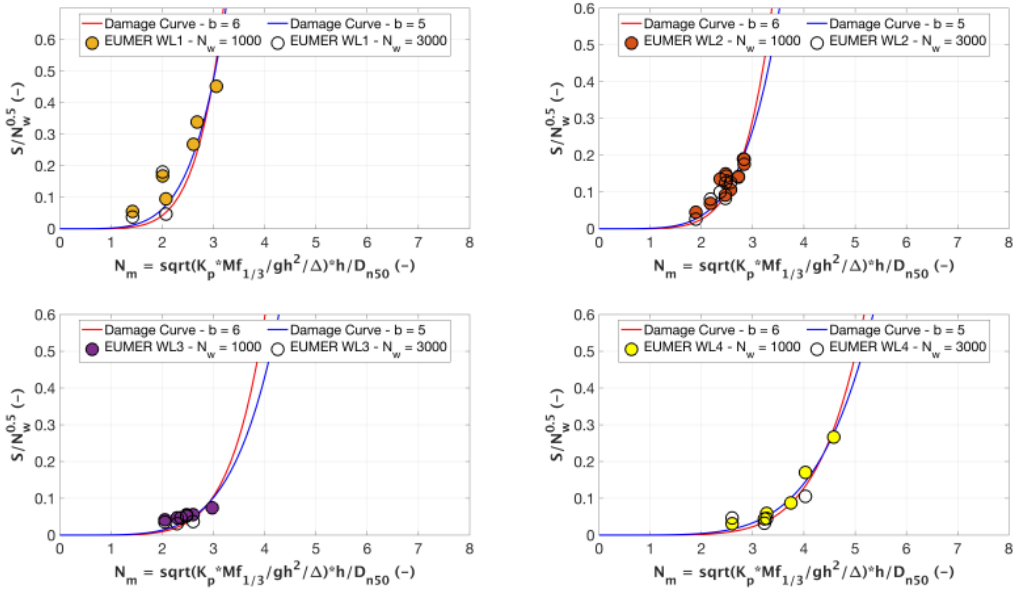


Figure 7.5. Damage curves for EUMER data groups.

7.2.3. Slope angle α

The angle of the seaward slope of a rubble mound influences the stability of armor stones in two primary ways:

1. Effect of wave breaking: the slope angle influences the type of wave breaking that occurs for a given wave condition, affecting the fluid kinematics on and within the rubble mound and the resulting hydrodynamic forces applied to the armor stones.
2. Distribution of stone weight: the slope angle also affects the proportions of stone weight that act normal and tangential to the surface. Stability is compromised as greater proportions of stone weight act tangentially down-slope. As the slope angle (α) approaches the friction angle (ϕ), armor stones become unstable without additional hydrodynamic forcing. Steeper slopes consequently reduce armor stability.

Hudson's design formula, extended to include the damage level, suggests $S_d \propto (\tan\alpha)^{2.22}$, while van der Meer's formulae propose $S_d \propto (\tan\alpha)^{2.5}$ for plunging waves and $S_d \propto (\tan\alpha)^{2.5-5P}$ for surging waves. The Hudson and the plunging wave van der Meer equations predict a similar positive trend between damage and slope angle, without the influence of the permeability on the damage value. However, the van der Meer equation for surging waves predicts a dependence on slope angle that diminishes with permeability to the extent that damage becomes independent of slope angle for a permeable rubble mound with $P=0.5$. In this manuscript, the same relationships found by van der Meer and generalized by MK are initially considered.

7.3. Comparison and analysis of datasets

This section aims to identify and address outliers in the stability number vs. normalized damage plot. Additionally, once the reasons for these outliers are understood, these data will not be used in subsequent analyses but will be addressed in future works. Finally, some plots showing a systematic bias induced by laboratory effects between different clusters of data will be reported and discussed.

7.3.1. Outliers

Once again, in Figure 7.6, the wave momentum flux stability number is plotted against the normalized damage for the entire numerical database. From this figure, it is evident that there are some data that are outliers and do not collapse within the main cluster inside the primary data cloud. These data are mostly associated with EUMER (yellow circles) and VSK (green diamonds) data on the right-hand side of the figure.

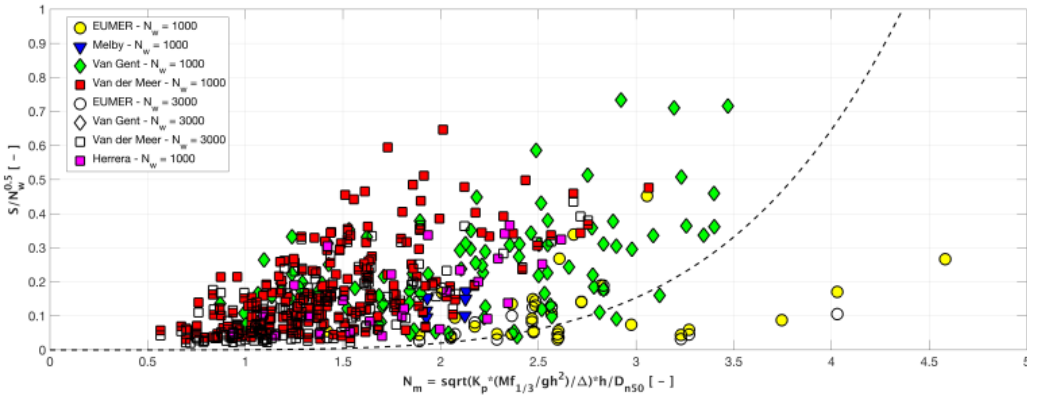


Figure 7.6. N_m vs. normalized damage for all numerical database.

To better visualize the category of data outliers, Figure 7.7 separates the data into deep, shallow, and very shallow waters according to the shallowness classification reported in Eq. (13a). Results show that nearly all the outliers are in very and extremely shallow water conditions, specifically for 1V:30H foreshore tests. Furthermore, it was observed that vdM test series “G06” with $\cot\alpha=6$ is the only vdM group that is clustered in the shallow water conditions and is separated from the other vdM data. This finding, consistent with [83], indicates that a different wave-structure interaction is observed for stone-armored mild slopes ($6 \leq \cot\alpha \leq 10$), and such data needs further analysis. Eventually, only data from deep to shallow water conditions and with $\cot\alpha \leq 4$ have been considered for the following analyses.

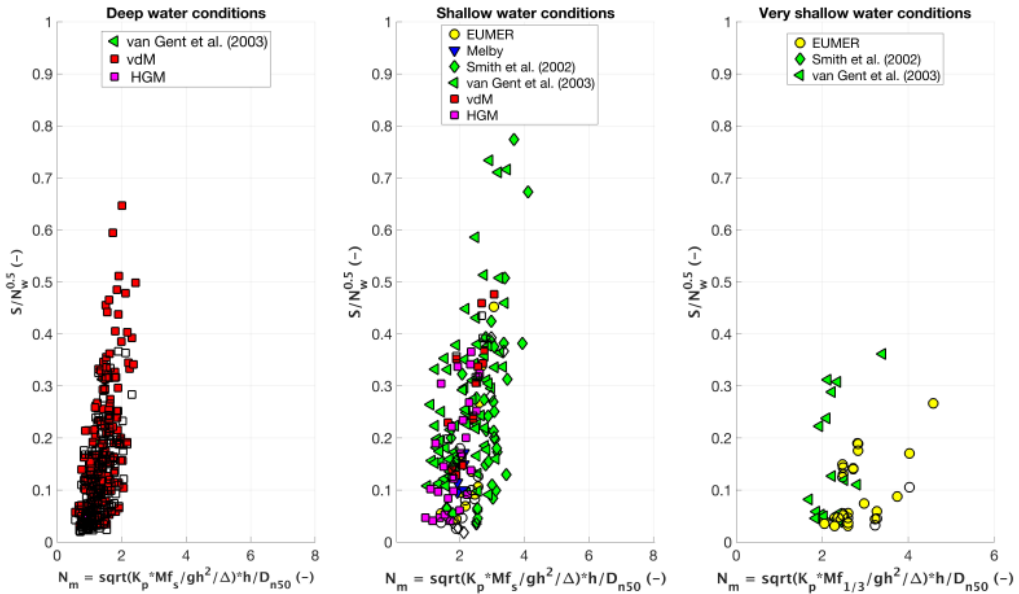


Figure 7.7. N_m vs. normalized damage plotted for deep, shallow, and very shallow water conditions.

7.3.2. Differences in datasets

Figure 7.9 illustrates the damage curves for each group of experiments conducted in the same laboratory, specifically categorized into four experimental groups: EUMER data, HGM and Melby data, VSK data, and vdM data. As discussed in Section 7.2.2, a 5-power function can be assumed as the optimal relationship for the damage curves and can be fixed for the entire dataset.

Several reasons could contribute to such bias, including physical effects like the presence of a foreshore slope and laboratory effects such as variations in damage and wave measurement methods. In the VSK dataset, for instance, the 1V:30H foreshore slopes, on average, exhibit more damage than the 1V:100H foreshore slopes, creating a broader data cloud (Figure 7.9). Tests conducted by a few M.Sc. students in the Laboratory of Fluid Mechanics of TU Delft suggested that identical wave spectra at the toe of the structure can result in different damage to the structure due to differences in

the foreshore slope [69]. Although the wave spectra were identical in these experiments, the varying damage levels cannot be solely explained by the intrinsic aleatory uncertainty of the random behavior of stone displacement. Therefore, this implies that damage is also dependent on other wave parameters not adequately represented by the shallow water wave spectrum.

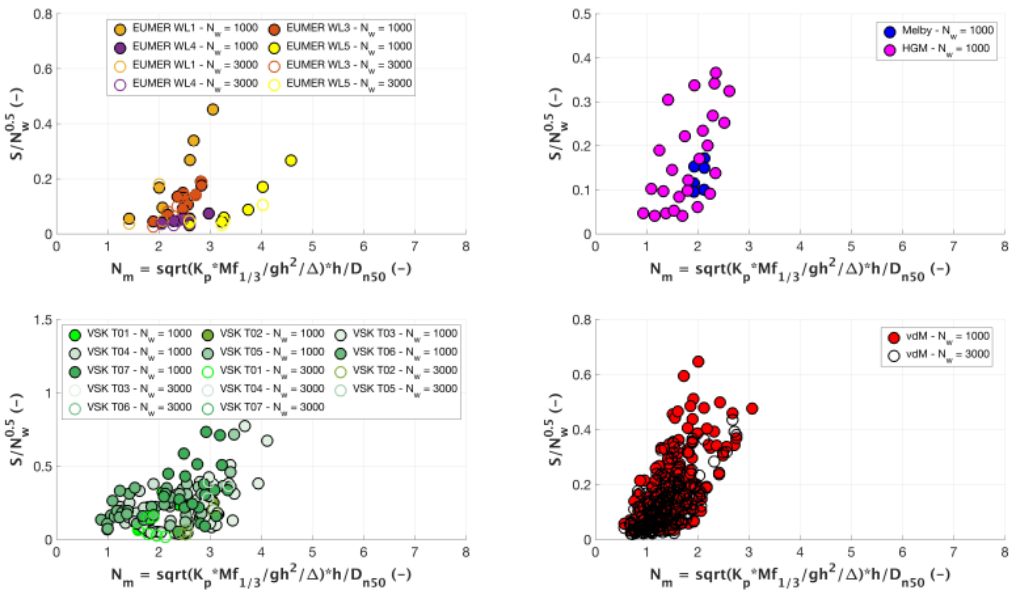


Figure 7.8. N_m plotted vs. normalized S separated for the different laboratory experiments (i.e., EUMER, HGM and Melby, VSK and vdM).

This section addresses the systematic bias observed between the VSK and vdM data. Undoubtedly, differences exist between the two datasets, and the main challenge lies in the inappropriate comparison due to inconsistent parameter format.

For instance, in the vdM graph for surging waves, test results of the low-density material tests, on average, show less damage, while different spectra tests show significantly more damage than average. According to van der Meer, this discrepancy is attributed to the influence of stone roundness, likely caused by the painting process of stones, in which the stones became rounder and less sharp-edged due to the

intensive rolling in the concrete mill and frequent handling between the tests. The wave run-down has a more significant effect on smoother stones as they roll more easily downward with the help of gravity, making them more susceptible to being picked up by flowing water. Therefore, vdM introduced shape coefficients c_{pl} and c_{su} to consider the influence of stone roundness and collapse of the data clouds. The Author presented a table with coefficient values to be used as multiplier for the entire equations, emphasizing that, especially for surging waves, the impact of including the roundness parameter is significant. In contrast, the VSK dataset assumes that the stones are of the standard type ($c_{pl}=c_{su}=1$), requiring no corrections or changes. This discussion emphasized the importance of scrutinizing each group of data singularly, analyzing them in detail to seek explanations for possible biases and uncertainties.

Therefore, beyond the entire database, VSK and vdM data with the same structural (permeability, structure slope) and hydrodynamic (wave spectrum, water depth, wave parameters) conditions have been identified and compared to demonstrate the presence of a systemic bias between the two clusters. Initially, tests with the same structural characteristics were sought, followed by the selection and comparison of tests with similar N_m .

Table 7.2 provides a comparison between three selected pairs of data with similar characteristics. Furthermore, in Figure 7.9, the same data have been plotted together, separated into plunging and surging waves, respectively. This comparison reveals a systematic bias between the two groups, unlikely to be solely explained by the aleatory uncertainty of stone armor stability. In general, the VSK dataset tends to show more damage than the vdM dataset, and this is likely related to the damage measurement method. Ultimately, a semi-quantitative demonstration is provided suggesting it would be reasonable to average-adjust the vdM damage values to mitigate the bias and align the two clusters.

Table 7.2. Comparison between similar data from VSK and vdM datasets.

ID	Spectra	P	$\cot\alpha$	$\cot\beta$	h	N_s	S_d	N_w
VSK	TMA	0.1	4	30	0.375	3.45	25.40	1198
VdM	PM	0.1	4	Flat	0.800	3.50	7.26	1000
VSK	JONSWAP	0.4	2	100	0.400	2.60	6.70	927
VdM	PM	0.5	2	Flat	0.800	2.56	5.90	1000
VSK	TME, double	0.5	2	30	0.300	2.32	6.59	1322
VdM	PM	0.5	2	Flat	0.800	2.33	7.36	1000

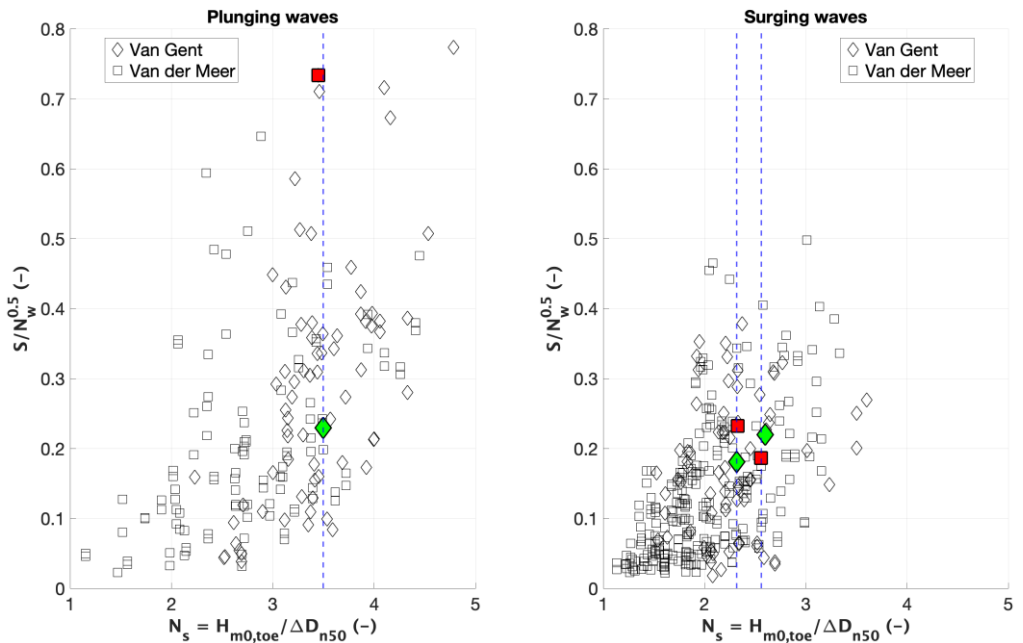


Figure 7.9. Bias in the damage curve for plunging (left) and surging (right) equations between VSK and vdM data.

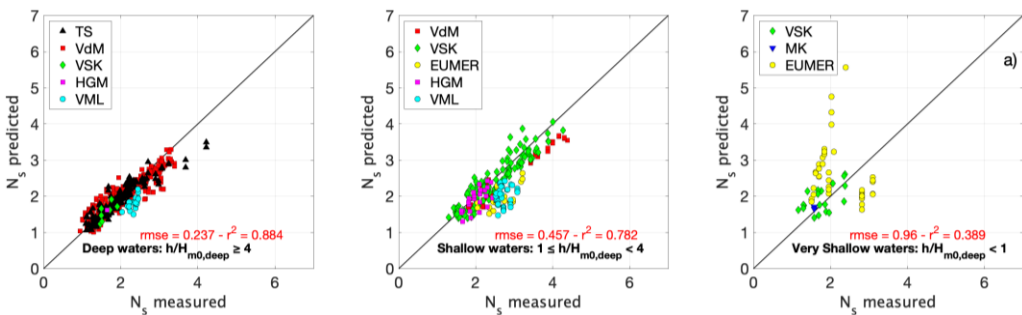
7.3.3. Stability equations using Coulwave data

In this section, we present a comprehensive analysis of the most reliable stability equations, as detailed in Section 4.3. These equations have been plotted using the Coulwave results to ascertain any potential reduction in uncertainty. The primary objective of this paragraph is to discern and discuss the strengths of each equation

under varying water depth conditions. As a result, stability equations from van der Meer (2021) Eq. (2), van Gent (2004) Eq. (4), refitted Melby and Kobayashi (2011) Eq. (20), Eldrup and Andersen (2019) Eq. (8), and Etemad-Shahidi et al. (2020) Eq. (9) have been plotted utilizing the Coulwave wave parameters. Specifically, we present comparisons among equations using laboratory data, Coulwave data with the inshore wave period, and Coulwave data with the offshore wave period.

It is noteworthy that employing a different wave period only influences shallow cases. In shallow water, the spectrum spreads out, and a single period reflects that entire energy frequency bandwidth. However, the portion of the spectrum influencing stability remains fairly narrow, likely centered around the original swell period. High and low IG wave frequencies do not exert a significant influence on armor stability. The application of cutoffs to isolate the swell portion of the remaining spectrum would probably yield a representative period close to the original peak.

Figure 7.10 illustrates the comparisons between the three cases for the van der Meer equation (Eq. (2)). The use of Coulwave wave parameters shows slightly changes and improvements in the fit in deep waters. Conversely, in shallow waters, the fit improves marginally, yet scattering and bias remain apparent. Finally, fits for very shallow waters see substantial improvement, with decreased scatter, and only bias is observable (with a similar magnitude for VSK and EUMER data).



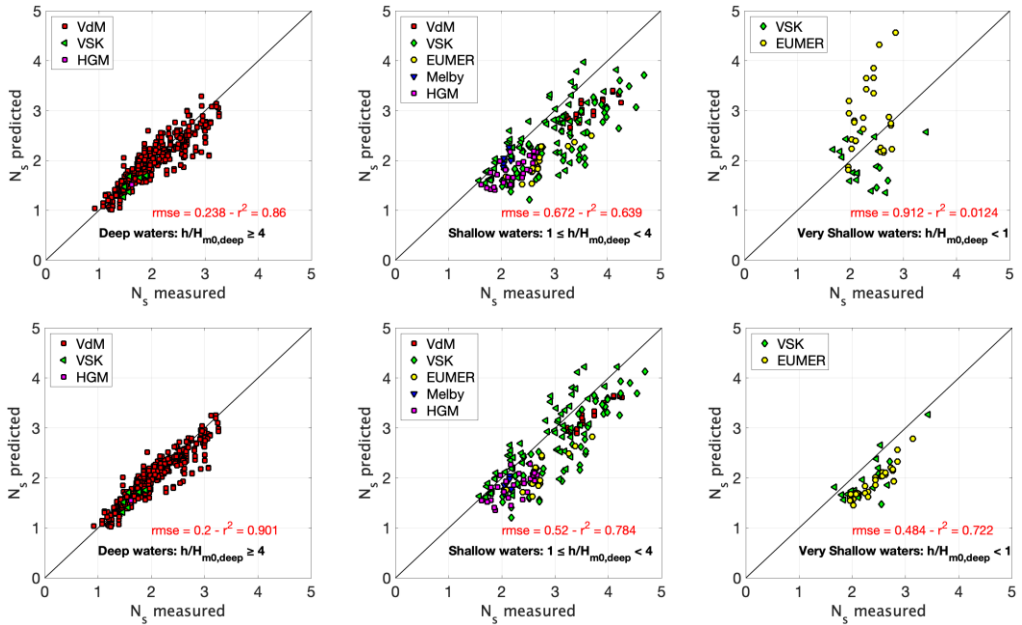


Figure 7.10. VdM stability equation for deep, shallow, and very shallow waters using laboratory data (top), Coulwave data with the inshore wave period (middle), and Coulwave data using the offshore wave period (bottom).

Figure 7.11 illustrates comparisons between laboratory and Coulwave data for the simple van Gent equation (Eq. (4)). The van Gent formula does not incorporate the wave period within it; hence, the use of offshore or inshore wave period is rendered meaningless. The use of Coulwave wave data reveals that the fit in deep water remains unchanged, indicating a potential oversight in this equation. Conversely, the fit in shallow water improves, displaying reduced scatter and bias, particularly for VSK data. Ultimately, the fits for very shallow waters exhibit a notable agreement across all datasets, suggesting that in such conditions, a simple formula without the influence of wave period may outperform more complex ones.

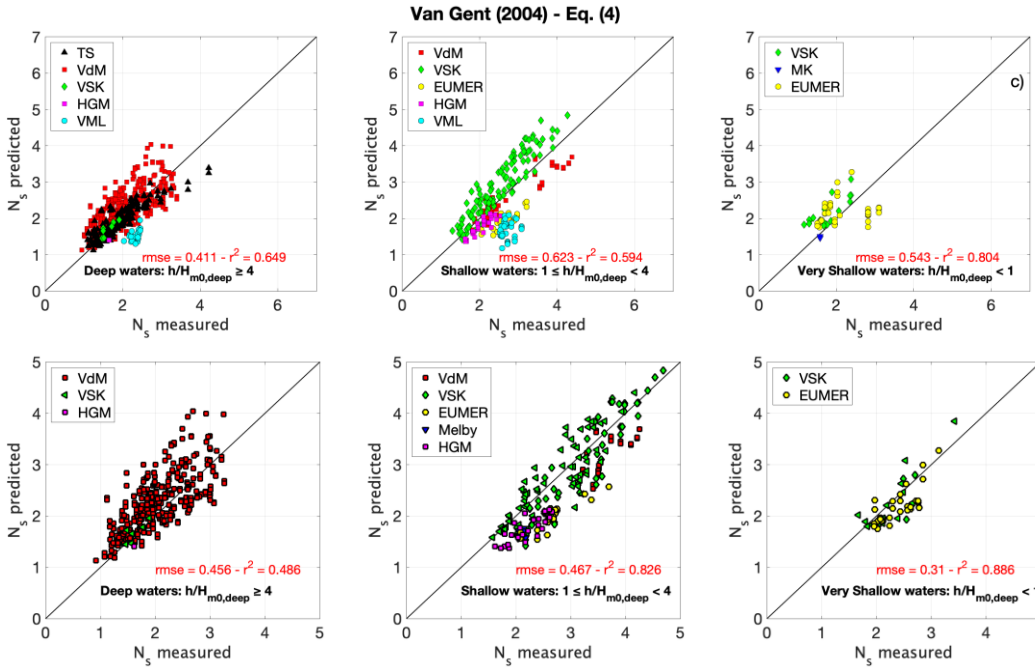


Figure 7.11. Van Gent stability equation for deep, shallow, and very shallow waters using laboratory data (top) and Coulwave data (bottom).

Figure 7.12 illustrates comparisons between laboratory and Coulwave data for the refitted MK equation (Eq. (20)). The use of Coulwave wave data reveals that the fit in deep water remains approximately the same with a slightly worse agreement compared to laboratory data, once again suggesting a potential omission in this equation. Conversely, the fit in shallow water improves, displaying less scatter but a similar bias. Finally, the fits for very shallow waters, employing the offshore wave period, exhibit a very good agreement across all datasets, highlighting the efficacy of this M_f formula in both very and extremely shallow waters.

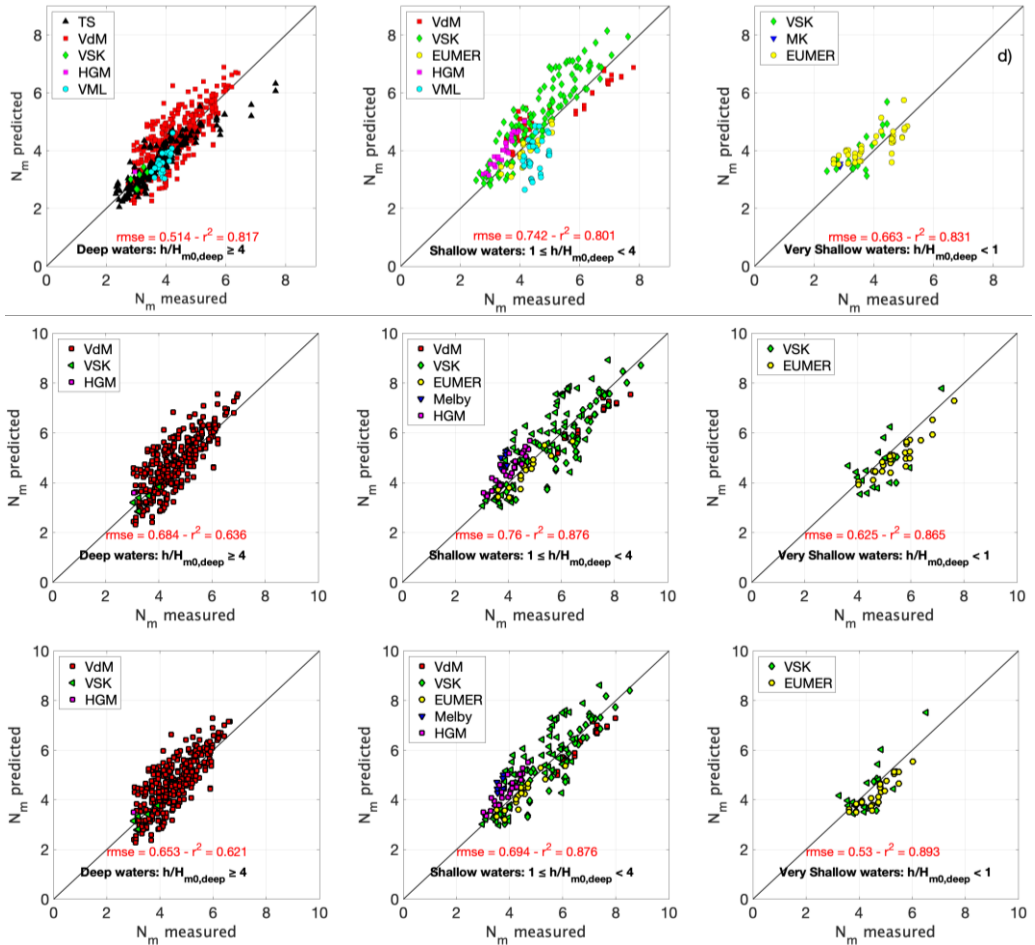


Figure 7.12. Refitted MK stability equation for deep, shallow, and very shallow waters using laboratory data (top), Coulwave data with the inshore wave period (middle), and Coulwave data using the offshore wave period (bottom).

Figure 7.13 illustrates comparisons between laboratory and Coulwave data for the EA equation (Eq. (8)). The use of Coulwave wave data reveals very little changes in the fit in deep water, tending to improve compared to laboratory data. This indicates that the equation accurately represents armor slope stability in deep water conditions. Conversely, the fit in shallow and very shallow waters shows a slight worsening with increased scatter when Coulwave data are employed. A better behavior is observed

when offshore wave periods are utilized in the equation; but, overall, no significant differences are noted except for less scatter and higher bias. It is worth mentioning that bias can be associated with the Coulwave simulations, especially in the wave energy dissipation modality during the breaker propagation.

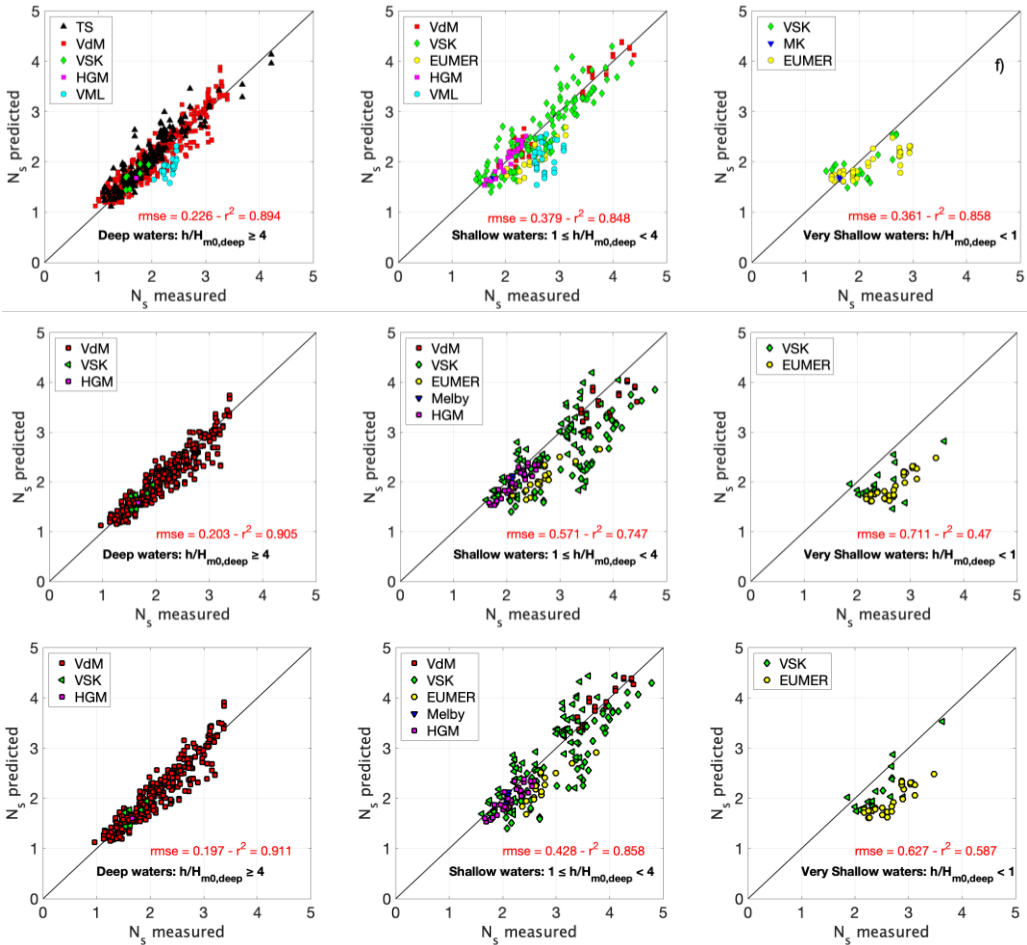


Figure 7.13. EA stability equation for deep, shallow, and very shallow waters using laboratory data (top), Coulwave data with the inshore wave period (middle), and Coulwave data using the offshore wave period (bottom).

Figure 7.14 illustrates comparisons between laboratory and Coulwave data for the Etemad-Shahidi et al. equation (Eq. (9)). The use of Coulwave wave data shows very little changes in the fit in deep waters, tending to slightly improve compared to laboratory data. Conversely, the fit in shallow and very shallow waters worsens with higher scatter and bias when Coulwave data are employed.

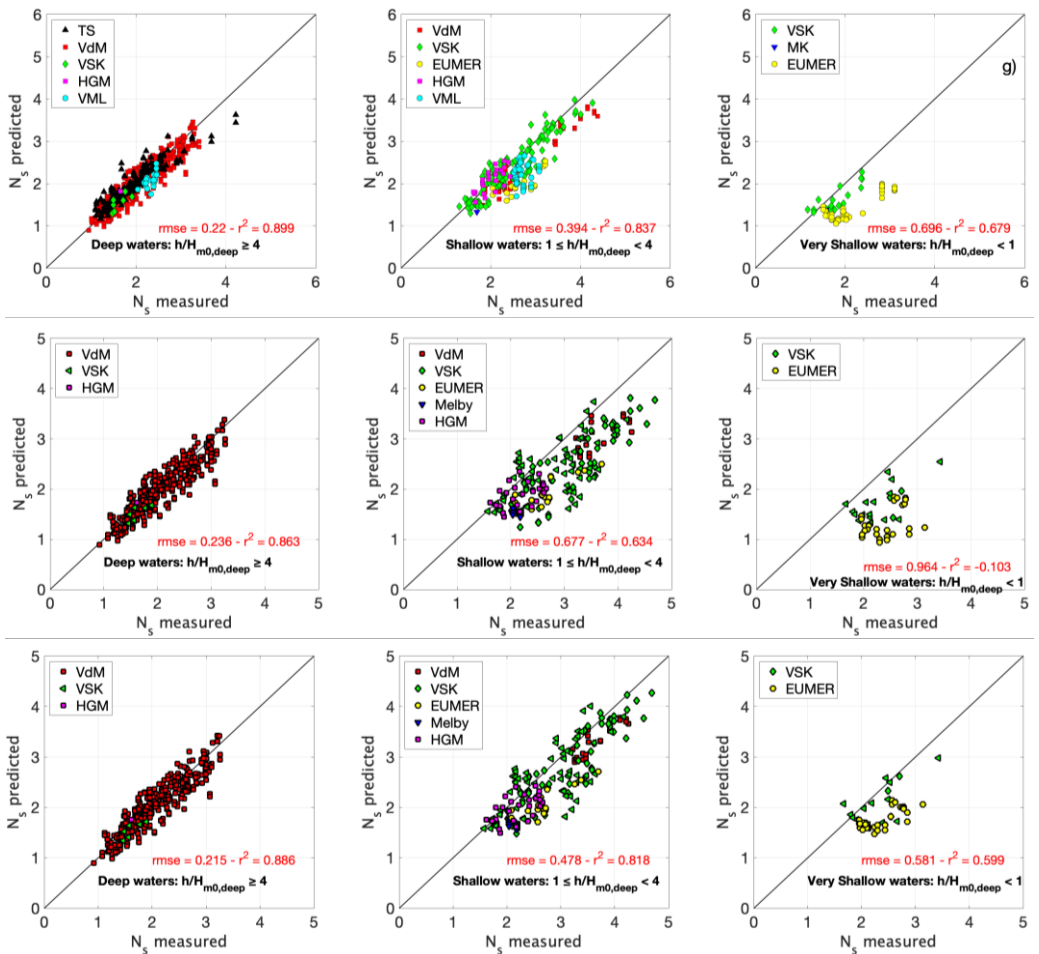


Figure 7.14. Etemad-Shahidi et al. stability equation for deep, shallow, and very shallow waters using laboratory data (top), Coulwave data with the inshore wave period (middle), and Coulwave data using the offshore wave period (bottom).

In Table 7.3 and Table 7.4, a comparison in terms of error statistics ($rmse$, r^2 , bias, std) for the three cases is provided for all the equations presented in this section.

Table 7.3. Comparison in terms of $rmse$ and r^2 between the stability formulae for deep, shallow, and very shallow water conditions using laboratory data, Coulwave data with the inshore wave period, and Coulwave data using the offshore wave period.

Laboratory data using $T_{m-1,0}$ at the toe						
Stability Formulae	Deep water		Shallow water		Very shallow water	
	$rmse$	r^2	$rmse$	r^2	$rmse$	r^2
Van der Meer (2021)	0.237	0.884	0.457	0.782	0.960	0.389
Van Gent (2004)	0.411	0.649	0.623	0.594	0.543	0.804
Refitted MK (2011)	0.514	0.817	0.742	0.801	0.663	0.831
Eldrup & Andersen (2019)	0.226	0.894	0.379	0.848	0.361	0.858
Etemad-Shahidi et al. (2020)	0.220	0.899	0.394	0.837	0.696	0.679

COULWAVE data using $T_{m-1,0}$ at the toe						
Stability Formulae	Deep water		Shallow water		Very shallow water	
	$rmse$	r^2	$rmse$	r^2	$rmse$	r^2
Van der Meer (2021)	0.238	0.860	0.672	0.639	0.912	0.124
Van Gent (2004)	0.456	0.486	0.467	0.826	0.310	0.886
Refitted MK (2011)	0.684	0.636	0.760	0.876	0.625	0.865
Eldrup & Andersen (2019)	0.203	0.905	0.571	0.747	0.711	0.470
Etemad-Shahidi et al. (2020)	0.236	0.863	0.677	0.634	0.964	-0.103

COULWAVE data using $T_{m-1,0}$ offshore						
Stability Formulae	Deep water		Shallow water		Very shallow water	
	$rmse$	r^2	$rmse$	r^2	$rmse$	r^2
Van der Meer (2021)	0.200	0.901	0.520	0.784	0.484	0.722
Van Gent (2004)	0.456	0.486	0.467	0.826	0.310	0.886
Refitted MK (2011)	0.653	0.621	0.694	0.876	0.530	0.893
Eldrup & Andersen (2019)	0.197	0.911	0.428	0.858	0.627	0.587
Etemad-Shahidi et al. (2020)	0.215	0.886	0.478	0.818	0.581	0.599

Table 7.4. Comparison in terms of bias and std between the stability formulae for deep, shallow, and very shallow water conditions using laboratory data, Coulwave data with the inshore wave period, and Coulwave data using the offshore wave period.

Laboratory data using $T_{m-1,0}$ at the toe						
Stability Formulae	Deep water		Shallow water		Very shallow water	
	<u>bias</u>	<u>std</u>	<u>bias</u>	<u>std</u>	<u>bias</u>	<u>std</u>
Van der Meer (2021)	0.070	0.227	0.276	0.365	-0.313	0.914
Van Gent (2004)	-0.101	0.399	0.104	0.616	-0.082	0.541
Refitted MK (2011)	0.013	0.514	-0.240	0.704	-0.421	0.515
Eldrup & Andersen (2019)	-0.046	0.221	0.154	0.347	0.178	0.316
Etemad-Shahidi et al. (2020)	0.025	0.219	0.226	0.324	0.560	0.416

COULWAVE data using $T_{m-1,0}$ at the toe						
Stability Formulae	Deep water		Shallow water		Very shallow water	
	<u>bias</u>	<u>std</u>	<u>bias</u>	<u>std</u>	<u>bias</u>	<u>std</u>
Van der Meer (2021)	0.057	0.232	0.517	0.431	-0.221	0.894
Van Gent (2004)	-0.205	0.408	0.246	0.397	0.142	0.278
Refitted MK (2011)	-0.188	0.658	-0.042	0.761	0.304	0.551
Eldrup & Andersen (2019)	0.063	0.194	0.370	0.435	0.654	0.281
Etemad-Shahidi et al. (2020)	0.069	0.226	0.528	0.424	0.875	0.410

COULWAVE data using $T_{m-1,0}$ offshore						
Stability Formulae	Deep water		Shallow water		Very shallow water	
	<u>bias</u>	<u>std</u>	<u>bias</u>	<u>std</u>	<u>bias</u>	<u>std</u>
Van der Meer (2021)	0.047	0.195	0.340	0.394	0.431	0.221
Van Gent (2004)	-0.205	0.408	0.246	0.397	0.142	0.278
Refitted MK (2011)	-0.160	0.634	-0.105	0.688	0.210	0.492
Eldrup & Andersen (2019)	0.026	0.196	0.167	0.395	0.558	0.289
Etemad-Shahidi et al. (2020)	0.023	0.214	0.298	0.374	0.483	0.327

Overall, the fits for almost all equations do not show improvement for all water depth conditions when using the inshore wave period. In contrast, better performance, compared to laboratory data, is consistently observed when utilizing Coulwave data

and the offshore wave period. Despite a general higher bias in the equations for shallow waters, there is a reduction in scatter. Such bias can be attributed to systematic errors produced by the numerical model in shallow waters (expected to be around 10-15%), which can potentially be adjusted within the equations.

Among the equations, vdM, EA and Etemad-Shahidi et al. exhibit the best performance in deep water conditions, with EA showing an excellent agreement. However, vdM and Etemad-Shahidi et al. tend to break down in shallow waters and specifically in very shallow water conditions, suggesting a missing element in the equations. EA still performs well in shallow waters but requires adjustment to reduce bias for data points in shallow waters. For shallow and very shallow water conditions, van Gent and MK equations prove to be effective and more accurate than others. The conclusion is that in very shallow waters, the influence of the wave period is present and minor on armor stability, and therefore, simpler equations could be more suitable.

7.4. New stability equations based on wave momentum flux

This section presents some preliminary results related to the revisitation and refitting of the MK stability equation (Eq. (20)) using the numerical parameters obtained from the Coulwave simulations. The LHS of the stability equation was revisited with a new version of the N_m based on the velocity-term wave momentum flux. Both the measured Coulwave M_f and the analytically computed Hughes M_f (Eq. 6) are proportional to the drag force on the armor layer, providing better insights into the physics than using only laboratory wave parameters.

Three different attempts using the entire numerical database are proposed herein to demonstrate the potential of the method and inspire future research.

1. Revisited MK equation using measured Coulwave $M_{f,1/3}$
2. Revisited and refitted MK equation using computed Hughes M_f
3. New single equation using computed Hughes M_f

It must be noted that a reformulation of the RHS of the equations is necessary to collapse the data groups with some simplistic changes. Retracing the path undergone in the vdM thesis should help visualize and identify the variability of the trends between N_m and the other parameters.

7.4.1. Refitted MK equation using $M_{f,1/3}$

The first attempt involved substituting the normalized wave momentum flux $M_{if}/\gamma h^2$ computed using the Hughes equation (Eq. 6) with the significant velocity based $M_{f,1/3}$ measured at the exact toe of the structure using the Coulwave wave simulations. Differences compared to Eq. (20) lie in the use of the incident offshore spectral wave period ($T_{m-1,0}$) to compute the incident spectral wavelength ($L_{m-1,0}$) using the linear dispersion relationship. Therefore, the spectral wave steepness ($s_{m-1,0}$) was calculated using the incident spectral wave height (H_{m0}) at the exact toe of the structure and the LWT spectral wavelength using the incident offshore spectral wave period ($T_{m-1,0}$). Instead, for N_w , the numbers of waves given by the authors were used because the duration of the test was not available, and therefore, real N_w could not be computed. Based on the findings in Section 7.3.1, very shallow waters data were excluded from the analyses. As in Section 4.2.1, the new equation was refitted, and the regression coefficients K_{m1} and K_{m2} were computed as the mean value of the probability distribution of the error obtained by the difference between the predicted and measured stability numbers (Figure 7.15). Then, utilizing the refitted coefficients, a qualitative plot of $s_{m-1,0}$ versus the normalized N_m is reported in Figure 7.16. Evident bands of data appear, indicating that a reformulation of the RHS of the equation should be conducted to align the data.

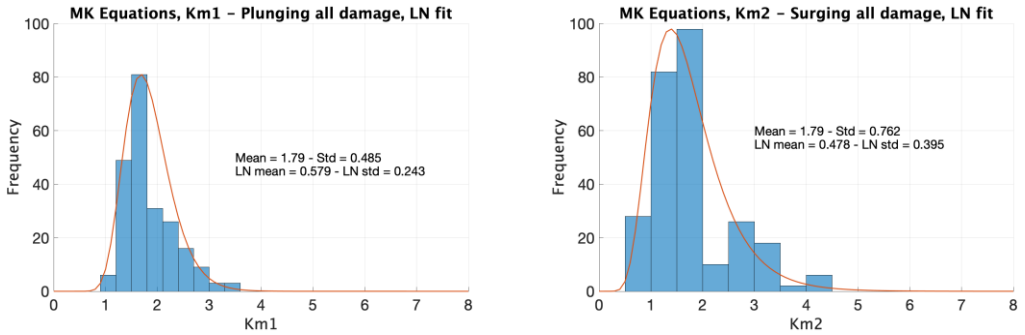


Figure 7.15. Plunging (K_{m1}) and surging (K_{m2}) regression coefficients computed for all analyzed numerical data.

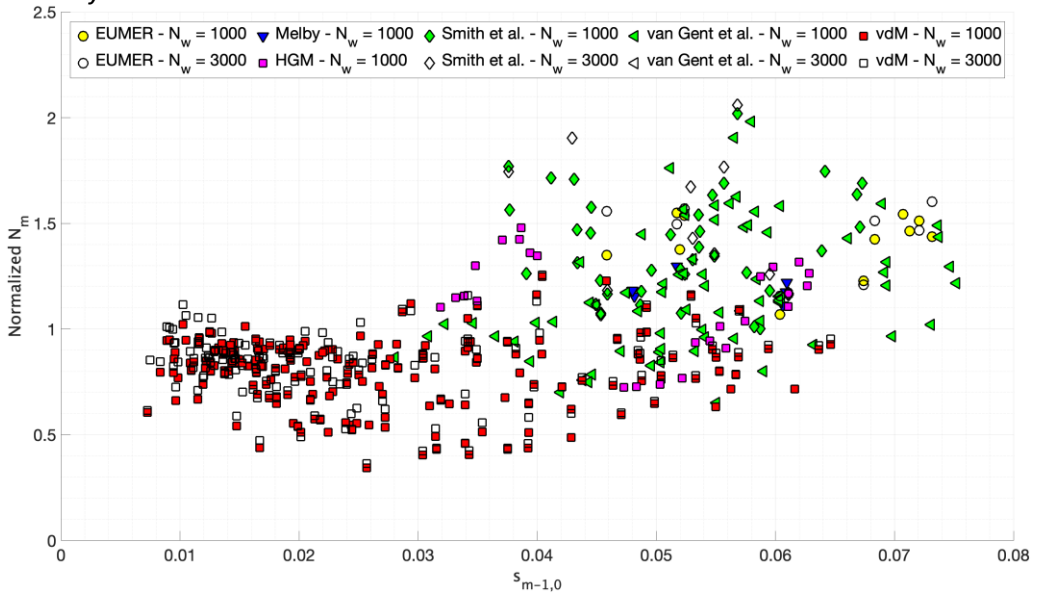


Figure 7.16. Wave momentum flux stability equation using $M_{1,1/3}$.

7.4.2. Refitted MK equation using Hughes M_f with Coulwave data

The second attempt involved refitting the MK equations using the Hughes' nonlinear approximated M_f using Coulwave wave parameters. Coulwave wave parameters exhibit less hydrodynamic uncertainty compared to laboratory wave measurements. The only difference from Section 7.4.1 is the use of the incident offshore spectral wave period ($T_{m-1,0}$) also inside the Hughes equation (Eq. 6), which instead was calibrated using the

incident mean wave period (T_m). It is argued that the use of different statistics on wave period (offshore or inshore) seems to make little difference. However, for very shallow water tests, inshore $T_{m-1,0}$ can be strongly influenced by IG waves, whereas offshore $T_{m-1,0}$ is much more stable and reliable. Figure 7.17 and Figure 7.18 report the regression coefficients and the wave momentum flux stability equation using the Hughes M_f equation with the Coulwave numerical wave parameters. Differently, this time, data bands are less evident, indicating that the nonlinear Hughes approximation introduces a relationship with wave parameters that is better correlated to the RHS of the equations compared to the vbMf.

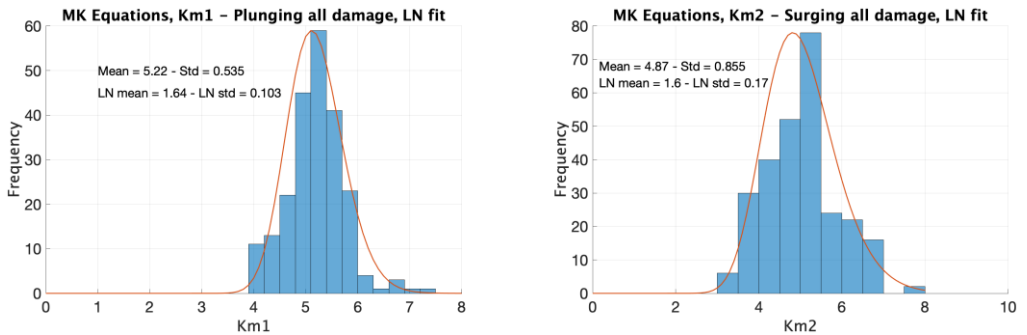


Figure 7.17. Plunging (K_{m1}) and surging (K_{m2}) regression coefficients computed for all analyzed numerical data.

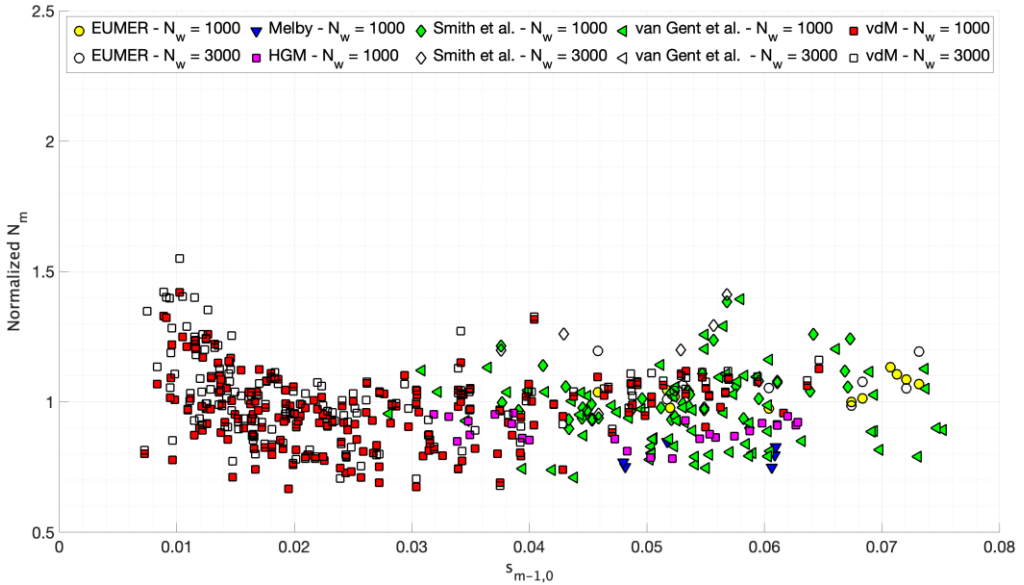


Figure 7.18. Wave momentum flux stability equation using Hughes M_f with Coulwave numerical wave parameters.

7.4.3. New single stability equation

Finally, the third attempt consisted of revisiting the equations presented by Melby and Kobayashi to avoid the discontinuity between plunging and surging waves. This involved developing a new single version of stability relations. The newly formulated equation, expressed in terms of the normalized stability number (N_m') is presented in Eq. (30) as follow:

$$N_m' = \frac{\left(\frac{(M_f/\gamma h^2)_{\max}}{\Delta} \right)^{1/2} \frac{h}{Dn_{50}}}{\frac{1}{a_m} \left(\frac{S}{K_s \sqrt{N_w}} \right)^{0.2}} = f(s_{m-1,0}) \quad \text{Eq. (30a)}$$

$$N_m' = a \cdot \exp(b \cdot s_{m-1,0}) + c \cdot \exp(d \cdot s_{m-1,0}) \quad \text{Eq. (30b)}$$

where 'a'=0.9, 'b'=2.4, 'c'=7 and 'd'=-250 are regression coefficients determined and refined through a trial-and-error procedure fitting a polynomial function. In this case, only simple functionalities for the permeability factor ($P^{0.18}$) and the structure slope ($\sqrt{\cot\alpha}$), are considered in the evaluation of term a_m , similar to the approach for plunging waves. No distinction is made between plunging and surging waves in this case, leading to the calculation of a single regression coefficient $K_m=5.51$ (std=0.748). The significant advantage of this new single equation lies in the elimination of errors and uncertainties arising from the selection of one equation over another. Indeed, by employing a unique equation for each point, an unambiguous representation of the physics is ensured in a straightforward manner, notwithstanding potential higher uncertainties.

Consequently, by combining a_m with the polynomial fit relation, a new factor is derived, as shown in Eq. (31):

$$\text{new } a_m = a_m / (a \cdot \exp(b \cdot s_{m-1,0}) + c \cdot \exp(d \cdot s_{m-1,0})) \quad \text{Eq. (31a)}$$

$$= \left(K_m P^{0.18} \sqrt{\cot\alpha} (a \cdot \exp(b \cdot s_{m-1,0}) + c \cdot \exp(d \cdot s_{m-1,0})) \right)^{-1} \quad \text{Eq. (31b)}$$

Figure 7.19 and Figure 7.20 illustrate the probability function for the regression coefficient and the new single wave momentum flux stability equation, utilizing the Hughes *Mf* equation and Coulwave numerical wave parameters.

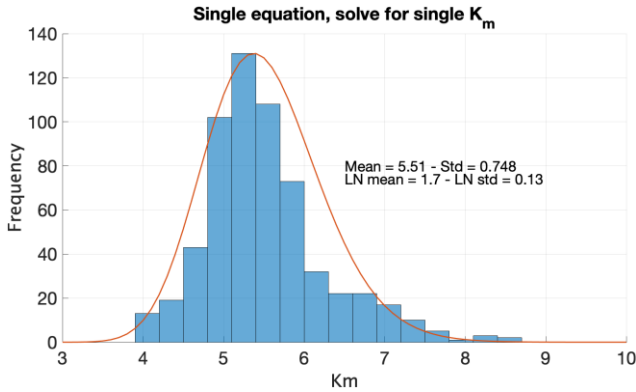


Figure 7.19. Single regression coefficient (K_m) computed for all numerical data.

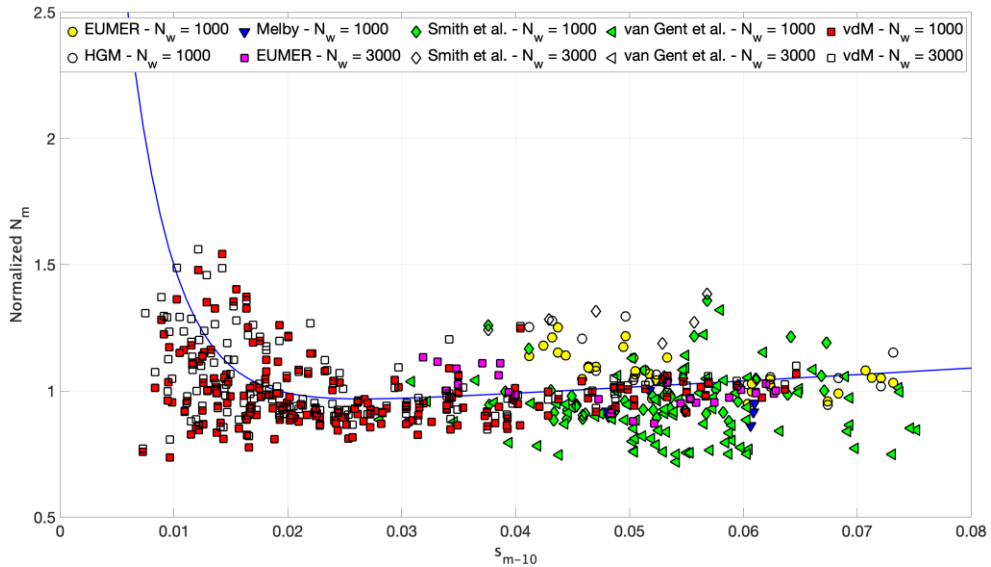


Figure 7.20. New single wave momentum flux stability equation.

7.4.4. Final comparison

In conclusion, the three attempts are once again plotted in terms of the measured vs. predicted stability number, as illustrated in Figure 7.21. Subsequently, Table 7.5 presents a comparison using the primary error statistics for the three cases analyzed.

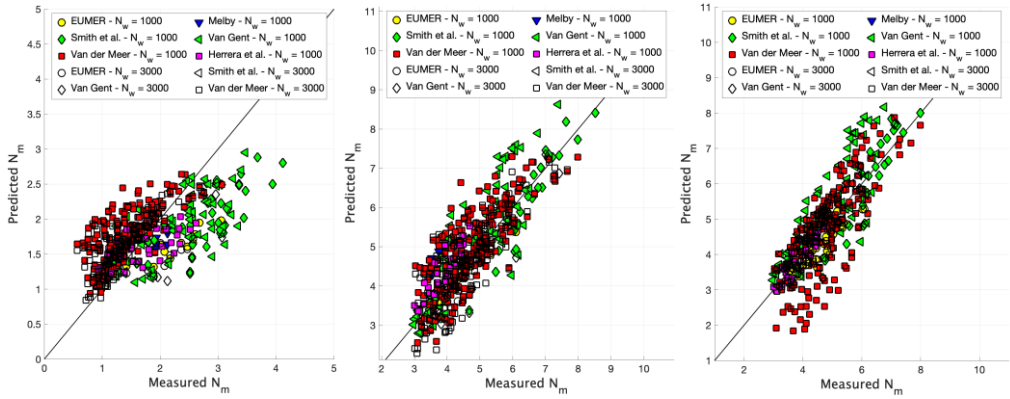


Figure 7.21. Measured vs. predicted N_m for the three attempts.

Table 7.5. Final comparison.

Error statistics	1° attempt	2° attempt	3° attempt
$rmse$	0.597	0.658	0.736
r^2	0.613	0.813	0.696
bias	0.021	-0.113	-0.021
std	0.598	0.648	0.736

According to Table 7.5, the first attempt exhibits the lowest root mean square error, the second one appears with the highest correlation and bias, and the third one shows the largest standard deviation. Based on these statistics, none of these new equations is significantly better than the others and can be considered exhaustive.

In conclusion, assuming a correct use of the LHS of the equation, it is reiterated that there is need for reformulating the RHS of the equations to genuinely enhance and establish a stability equation with improved predictive capabilities. The key lies in investigating the proper relationship between the stability number and the other parameters, aiming to achieve the best correlation. It is argued that through a reformulation of the RHS and by adjusting the systematic bias between the different datasets, a predictive model with reduced uncertainty could be identified. Based this

consideration, some insights are provided following the path outlined in vdM thesis, utilizing only vdM data.

In Figure 7.22, the MK equations were plotted using the computed nonlinear Hughes M_f and the incident spectral wave steepness ($s_{m-1,0}$) based on offshore incident $T_{m-1,0}$, and the inshore incident H_{m0} , where $a_m = 1/K_m P^{0.18}$. Results indicate some data banding which is likely to be collapsible with an opportune reformulation of the RHS of the equations. Data on the right side of the plot represents surge, while the left side represents plunge. All surge groups include G01, G02, G10, G11, G12 and G14 whereas G03 and G09 are mostly surge. Instead, mostly plunge groups consist of G04, G05, G06, G11, G12 and G14.

In Figure 7.23, the same modifications as in Figure 7.22 were implemented, with the only difference being that data were plotted using the spectral SSP ($\xi_{m-1,0}$) instead of $s_{m-1,0}$ on the x-axis.

The conclusion drawn from Figure 7.22 and Figure 7.23 is that data banding is very evident. Groups shift to right in plots with increasing $\cot \alpha$. Plunge groups tend to be on left, while surge groups tend to be on right. In these cases, P and structure slope were considered to compute a_m using the plunge fit equation but with different regression coefficients (K_{m1} and K_{m2}).

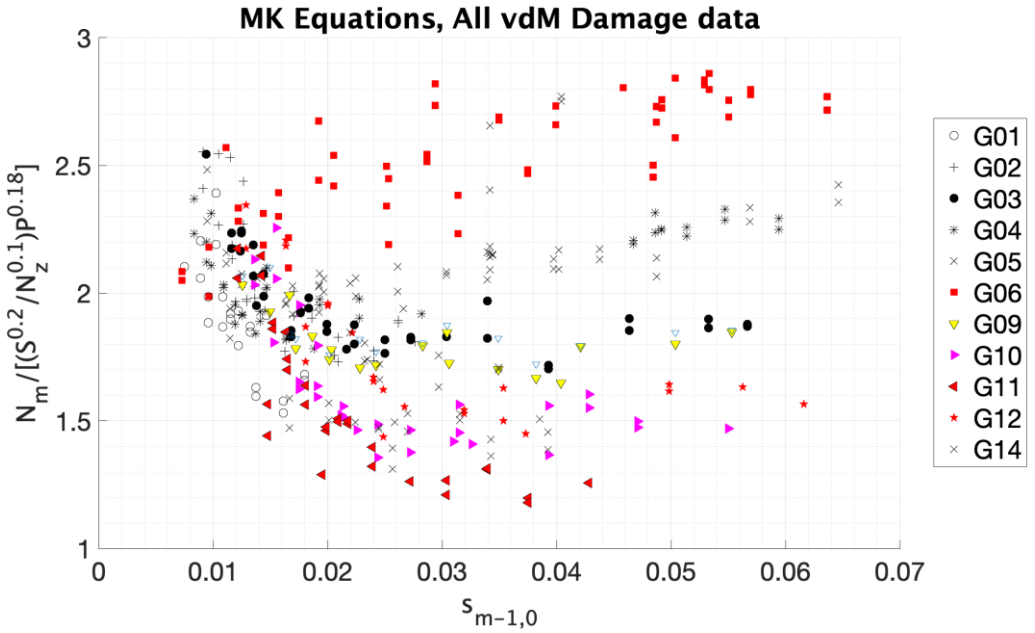


Figure 7.22. Normalized N_m plotted versus $s_{m-1,0}$ where $a_m = 1/K_m P^{0.18}$.

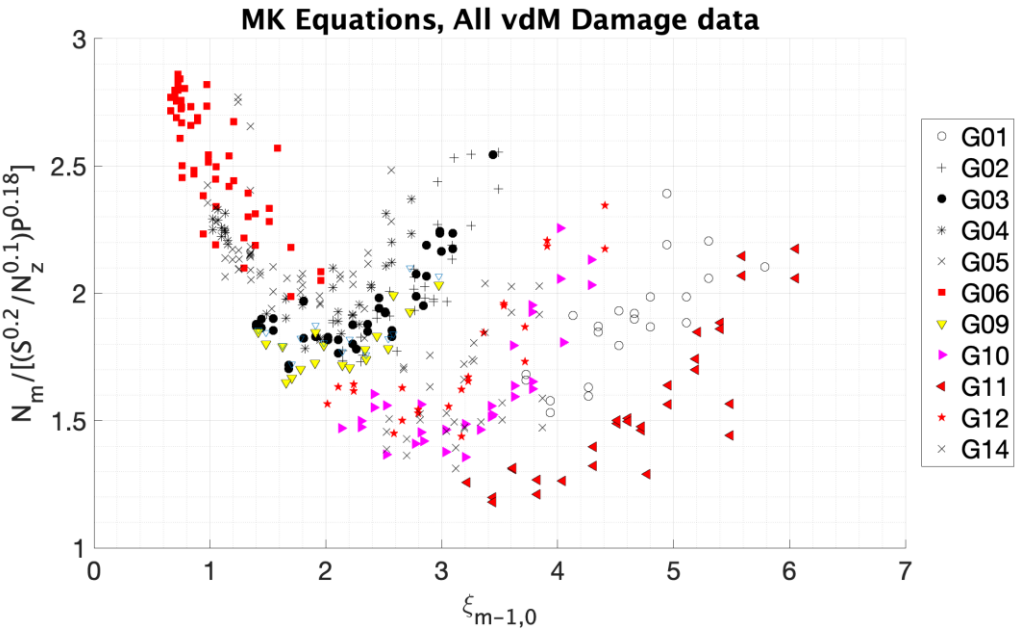


Figure 7.23. Normalized N_m plotted versus $\xi_{m-1,0}$ where $a_m = 1/K_m P^{0.18}$.

Similarly, in Figure 7.24top, the same plot was created, but plunge and surge equations were separated based on SSP discontinuity. However, the plunge fit equation was consistently used, incorporating the effect of the structure slope ($a_m = 1/K_m P^{0.18} \sqrt{\cot \alpha}$). In Figure 7.24bottom, the same plot was made, considering the effect of the P inside the equation as an exponent of the structure slope ($\cot \alpha^P$) for surging waves. Results demonstrate how the groups collapse with this simplistic change.

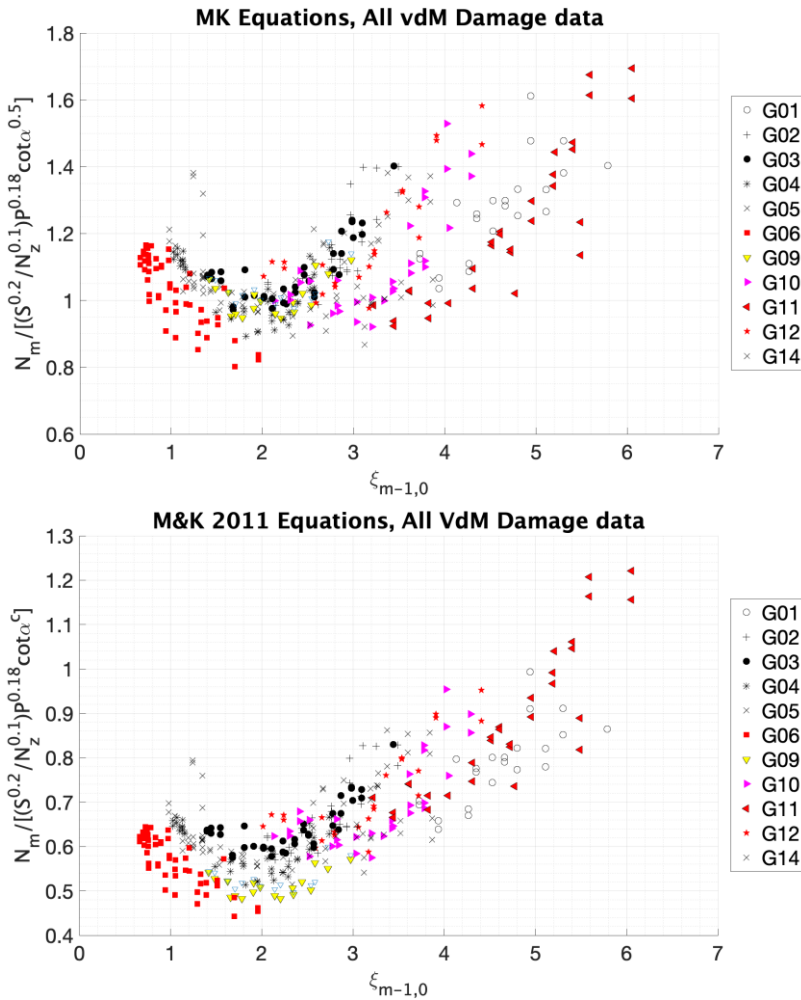


Figure 7.24. Normalized N_m plotted versus $\xi_{m-1,0}$ where $a_m = 1/K_m P^{0.18} \cot \alpha^P$.

Following the same trends observed by vdM would be crucial in determining how the new trends based on M_f vary. Based on this concise analysis, it appears that collapsing scatter is achievable and not a significant challenge. The approach involves plotting data into identifiable groups, observing trends, and subsequently collapsing the data. At an initial assessment, it seems that SSP is more useful than just wave steepness.

Herein, it is argued that variations in the statistics applied in the Hughes equation or distinctions between offshore and inshore wave periods do not exert a significant influence. The overall impression is that these factors collectively make minimal difference. Therefore, to draw a preliminary conclusion, a series of expedient plots were generated to ascertain, through a trial-and-error procedure, what factors indeed contribute to distinctions and what factors do not. The findings are reported in Table 7.6. Identifying the non-influential elements is as crucial as identifying those that are influential.

Table 7.6. Influence of parameters on stability equations.

Parameters	Influence
Wave period statistics ($T_m, T_p, T_{m-1,0}$)	Little to no influence
Wave period inshore and offshore	Little to no influence
$gT^2/2\pi$ or linear dispersion relationship	Little influence
Hughes M_f vs Coulwave M_f	High influence

To conclude, from these concise analyses, it can be stated that, at least for the vdM dataset with data in deep water conditions and a flat bottom, wave period statistics and wave period location (offshore vs inshore) make little to no influence on the stability equations. This outcome could be anticipated, as statistics remain relatively stable for flat bottom flumes. The method employed to calculate wavelength may exert a minor influence on the results. Ultimately, the choice of M_f type significantly impacts the final stability equations.

7.5. Conclusions

This chapter addresses the reformulation of the RHS and LHS of the wave momentum flux stability equation, alongside a re-evaluation of stability equations using the numerically synthesized and homogenized wave parameters.

The results reveal that the equations performed well in deep water conditions, but weaknesses are identified in shallow and very shallow waters. Results suggest that incorporating depth, bathymetric slope, structure slope, and wave steepness/breaking characteristics based on bathymetry, in addition to structure slope, is crucial for improving equations. The relationship between the stability number and the normalized damage is accurately described.

Furthermore, the inclusion of the offshore wave period ($T_{m-1,0}$) and inshore wave height (H_{m0}) into the equations enhances predictive accuracy. However, in very shallow water, the influence of wave period is found to be of minor importance compared to deep water.

An energetic approach based on the wave momentum flux parameter is used to improve understanding of the physics and forces acting on stone armor units. This approach facilitates the search for the optimal relationship between the stability number and other parameters. Additionally, initial attempts are made to propose new stability equations, offering valuable insights, and representing a significant advancement in the exploration of probabilistic methods for designing stone armor layers.

CHAPTER 8

Conclusions and future research lines

8. Conclusions and future research lines

8.1. Summary of the thesis

This manuscript addresses the primary sources of uncertainties in stone armor stability. Specifically, it focuses on the stability of seaside armor layers for uniformly sloping fully emergent rubble mound structures and randomly placed equant blasted armor stones. Updating the existing guidelines for the design of stone-armored structures represents a pressing global challenge, especially in the context of developing short- and long-term strategies to mitigate the impacts of climate change. One primary objective is to create a comprehensive and unique database from a wide range of international studies that cover diverse wave and water depth conditions. Synthesizing and homogenizing the data is a major task accomplished. This database serves to quantify and enhance the understanding of uncertainty in stability equations, with specific attention on addressing hydrodynamic uncertainty related to laboratory data. A second primary objective is to evaluate existing popular predictive stability equations against the synthesized database to understand the strengths and weaknesses and quantify aleatory and epistemic uncertainty. A final primary objective is to propose new empirical relations that better characterize physics and uncertainty. The thesis argues that existing predictive models should be upgraded within a probabilistic framework and supplemented with uncertainty in the equations.

A summary of the thesis is reported in this section as follows:

- **Chapter 1** introduces the topic of rubble mound coastal structures within the context of climate change. Emphasizes the necessity of probabilistic methods supplemented with uncertainties for conducting risk and high-fidelity reliability analyses. Provides motivations, objectives, and methodologies for the research.
- **Chapter 2** addresses the historical literature review on the design stability formulae of stone armor layers and details the most widely used stability equations employed in designing stone-armored coastal structures.
- **Chapter 3** describes the gathering and formation of a new comprehensive database, incorporating historical damage data from 7 different international studies worldwide that span various wave and water depth conditions. Additionally, it thoroughly synthesizes and examines the main characteristics of each dataset and the newly processed database to the extent possible with non-homogeneous parameters and methods. This database serves as the basis for the analysis conducted in this thesis.
- **Chapter 4** presents the analysis and comparison of data and stability equations across varied water depth regimes, ranging from deep to very shallow waters. The study is conducted within the framework of quantifying bias and uncertainty using main error statistics such as $rmse$, r^2 , bias, standard deviation, and coefficient of variation. The aim is to highlight the specific characteristics of datasets and equations, providing insights into their behavior and performance.
- **Chapter 5** fully illustrates and details the main sources of uncertainty in hydraulic stability design formulae. Specifically, uncertainty is categorized into data uncertainty, model uncertainty, and errors. A semi-quantitative estimation of uncertainty, expressed as a coefficient of variation, is provided for each category and class to convey a sense of the magnitude of their influence on the total uncertainty in predictive models.

- **Chapter 6** proposes a new methodology to further synthesize and homogenize the database and reduce the hydrodynamic epistemic uncertainty inherent in the laboratory data. This method uses a numerical high-fidelity phase-resolving wave transformation model to predict incident waves consistently for different laboratory experiments. The setup and calibration steps of a one-dimensional fully nonlinear Boussinesq numerical model (Coulwave), are fully described. This methodology facilitates the reduction of the epistemic uncertainty within wave observations when mixing different laboratory data and clarify hydrodynamic uncertainty in wave bulk parameters and forces exerted on the armor slope.
- **Chapter 7** reformulates the wave momentum flux stability equation and re-evaluates the stability equations using the numerically synthesized homogenized data. Here, the main results and conclusions are stated, along with the primary weaknesses and strengths of existing equations. Additionally, an energetic approach based on the wave momentum flux parameter is discussed, and new stability equations are proposed, aiming to enhance the understanding and predictive capabilities in coastal engineering design.

8.2. Principal findings and conclusions

Despite numerous research efforts and experiments, there remains a need for more systematic research on developing stability design formulae that incorporate uncertainty. Indeed, most existing predictive models fail to distinguish between aleatory and epistemic uncertainty. To the author's knowledge, no proposed methodology in the literature can separate one or more different types of stone armor stability uncertainty. In this context, the present thesis aims to contribute by providing a deeper understanding of uncertainty in stone armor stability, taking a step forward in evaluating the actual uncertainty in prediction models.

A summary of the principal conclusions and new findings of this study is presented below:

- (i) Synthesis and creation of a new extensive and unique experimental database (>800 data points) with stability data carried out in 2D small-scale models across varied waves and water depth regimes, ranging from deep to extremely shallow water conditions.
- (ii) No stability formula demonstrates significant superiority over others due to the high uncertainty present in the available data. Raw data cannot be fully synthesized without further modeling, attributed to the disparate modeling approaches, non-homogenous nature of the parametric data, and limited understanding of detailed laboratory techniques and data analysis methods.
- (iii) The numerical model proved effective in clarifying hydrodynamic uncertainty. A marginal reduction in hydrodynamic uncertainty is achieved compared to the total uncertainty, illustrating that most of the uncertainty is not associated with the wave and water level conditions. This approach enables the separation of the effect of wave prediction errors on stability prediction errors. Analysis of the datasets reveals a significant similarity among them, with aleatory uncertainty being predominantly and closely associated with damage.
- (iv) Existing stability equations perform well in deep water conditions, but notable weaknesses are identified in shallow and very shallow waters. Results suggest that incorporating depth, bathymetric slope, structure slope, and wave steepness/breaking characteristics based on bathymetry, in addition to structure slope, is essential for improved equations. Additionally, the integration of offshore wave period ($T_{m-1,0}$) and inshore wave height (H_{m0}) into the equations enhances predictive accuracy. In very shallow water, the influence of wave period appears to be of minor importance compared to deep water. However, [102] questioned the role

of $T_{m-1,0}$ in describing the overtopping phenomenon of vertical seawalls under shallow water conditions, stating that the use of this parameter could result in spurious unphysical relationships. Similar analyses should be extended also on stone armor stability.

- (v) Wave momentum flux parameter maintains a direct proportionality to the drag force exerted along the structure slope, displaying a discernible correlation with incident wave and depth parameters. Therefore, adopting such an approach enhances the understanding of physics and forces acting on stone armor units, suggesting a promising path forward for optimizing armor stability relationships across all water depth conditions.
- (vi) Initial attempts to propose new stability equations offer insights and, in combination with uncertainty quantification, represents a significant advancement in probabilistic stone armor layer design and assessment. These efforts contribute to a more comprehensive understanding of uncertainty factors and provide a foundation for enhancing predictive accuracy and reliability in coastal engineering applications.

8.3. Limits of the research

The present work is affected by some limitations, whose effects on the validity of the obtained results have been minimized.

A summary of the principal limits of this study is presented below.

- Collection and creation of the new database encountered difficulties in finding the required data. For example, the VML dataset is not homogenous with the other data and was consequently excluded from the analyses. Moreover, detailed information about the original design of the physical models and experiments, such as structural cross sections, flume sections, waves and damage measurements, and reflection analysis, is often unavailable. As a

result, some assumptions and approximations were necessary to synthesis and form the database, potentially introducing uncertainties.

- Comparison between stability equations is influenced by the number and type of data used. For example, van der Meer and Thompson and Shuttler data represent a large proportion of the data but are primarily in deep water with a flat bathymetry and tall structure. Care was taken in this research to minimize, where possible, undue influence from a single experiment. Error statistics such as *rmse*, r^2 , bias, std, and uncertainty can be calculated differently and should be viewed and discussed in a broader context rather than individually.
- Coullwave wave parameters are likely to be closer to the truth than some experimental results and useful in homogenizing the database. However, it is well known that numerical wave transformation models have non-negligible error in shallow waters, primarily due to empirical friction and breaking dissipation and numerical dissipation. Users should always be aware of the limitations of the numerical model. Calibration parameters such as bottom friction, breaking trigger and stopping, can be sophisticated. Overall, errors of approximately 10-15% are expected in the surf zone where breaking waves approach the inshore bathymetry. The numerical model proved effective in clarifying uncertainty but revealed a bias in wave parameters for shallow water conditions.
- The comparison between the laboratory and the numerical model is not always direct, and some uncertainties must be accepted. For this study, measured wave spectra were simulated based on reported bulk spectral parameters. The wave time series were not exactly reproduced. Measured incident wave parameters at the structure are compared with the numerical model's total wave parameters (incident + reflected). The inputs (H_{m0} , T_p , wave spectrum) used to initiate the numerical model are also affected by some uncertainty derived from laboratory measurements. Nevertheless, it is argued that such uncertainty in

deep water conditions close to the wave generator can be assumed negligible compared to the total.

8.4. Future research lines

The present work proposed a methodology for studying the uncertainties of stone armor stability, aiming to reduce the epistemic uncertainty of available laboratory data and stability predictive models through a combined analytical-numerical approach. Applying this methodology to the hydraulic stability of stone armored coastal structures yielded some general findings regarding the epistemic uncertainty concerning wave parameters and wave forces acting on stone armor layers.

The investigations presented here could be extended in several areas.

- Further research is required to investigate the influence of the different sources of uncertainties more deeply on stone armor stability. Additionally, a detailed quantitative evaluation of the magnitude of each significant source of uncertainty should be conducted using focused experiments and the numerical methodology described. High-fidelity numerical models offer valuable insights, potentially overcoming the costs and time constraints associated with physical modeling.
- In this thesis, we address all identified uncertainties and endeavor to reduce hydrodynamic uncertainties. However, armor damage uncertainty is only discussed. Conducting targeted experiments could assist in reducing unquantified damage uncertainty associated with diverse technologies and experimental approaches.
- Momentum flux provides a robust parametrization for stability equations. A comprehensive reformulation of the stability equations by grouping data with similar characteristics is necessary. Optimal correlation relationships between the M_s stability number and various parameters, including different statistics for

M_f , wave parameters, stability number, offshore vs. inshore conditions, and other pertinent factors, should be explored. It is anticipated that Coulwave M_f , based on drag, would exhibit better correlation with maximum forces on the structure near the SWL. A simple extension of the modeling could involve quantifying M_f at this specific location on the slope rather than at the toe. This adjustment is likely to better homogenize the data across the full range of structure water depths.

- There is a need for a quantitative estimation of the bias (which may vary among different studies) when comparing different datasets and adjusting the data to collapse the data clouds from all the studies. This process would ensure a more accurate and consistent analysis by accounting for numerical model-induced bias, facilitating meaningful comparisons and conclusions.
- Define and quantify the base level of uncertainty, primarily consisting of aleatory factors. Uncertainty cannot be reduced below this level. Subsequently, by eliminating bias (for example technological biases), one can focus on examining primarily aleatory factors in the overlap region. The objective of any new formulation would be to estimate the relative contributions of aleatory and epistemic uncertainty by reducing the epistemic component.

The method developed for achieving the aforementioned objectives has been successfully applied to the emblematic case of stone armor stability. However, it can be extended for further applications such as seaside and leeside rubble mound breakwater progression, life-cycle berm regression, rubble mound jetty stability, and damage considering flood currents, low-crested rubble mound structure stability, rubble mound toe stability, and more. This demonstrates the versatility and applicability of the methodology across various coastal engineering scenarios, offering valuable insights and solutions to address stability challenges in diverse coastal structure.

Bibliography

1. Hughes, S.A., *Coastal engineering challenges in a changing world*. Journal of Applied Water Engineering and Research, 2014. **2**(2): p. 72-80.
2. Toimil, A., et al., *Addressing the challenges of climate change risks and adaptation in coastal areas: A review*. Coastal Engineering, 2020. **156**: p. 103611.
3. Zhu, X., M.M. Linham, and R.J. Nicholls, *Technologies for climate change adaptation. Coastal erosion and flooding*. 2010.
4. Antonioli, F., et al., *Relative sea-level rise and potential submersion risk for 2100 on 16 coastal plains of the Mediterranean sea*. Water, 2020. **12**(8): p. 2173.
5. Bagheri, M., et al., *Hazard Assessment and Modeling of Erosion and Sea Level Rise under Global Climate Change Conditions for Coastal City Management*. Natural Hazards Review, 2023. **24**(1): p. 04022038.
6. Kirshen, P., K. Knee, and M. Ruth, *Climate change and coastal flooding in Metro Boston: impacts and adaptation strategies*. Climatic Change, 2008. **90**(4): p. 453-473.
7. Chen, C., et al., *Impacts of sea level rise on future storm-induced coastal inundations over Massachusetts coast*. Natural Hazards, 2021. **106**: p. 375-399.
8. Peter Sheng, Y., et al., *A sensitivity study of rising compound coastal inundation over large flood plains in a changing climate*. Scientific Reports, 2022. **12**(1): p. 3403.
9. Sánchez-Arcilla, A., et al., *A review of potential physical impacts on harbours in the Mediterranean Sea under climate change*. Regional environmental change, 2016. **16**: p. 2471-2484.
10. Camus, P., et al., *Probabilistic assessment of port operation downtimes under climate change*. Coastal Engineering, 2019. **147**: p. 12-24.
11. Izaguirre, C., et al., *Climate change risk to global port operations*. Nature Climate Change, 2021. **11**(1): p. 14-20.
12. IPCC, I.S., *IPCC Special Report*. 2018.
13. Lambeck, K., et al., *Sea level change along the Italian coast during the Holocene and projections for the future*. Quaternary International, 2011. **232**(1-2): p. 250-257.
14. Church, J.A., et al., *Sea level change*. 2013, PM Cambridge University Press.

15. Galassi, G. and G. Spada, *Sea-level rise in the Mediterranean Sea by 2050: Roles of terrestrial ice melt, steric effects and glacial isostatic adjustment*. *Global and Planetary Change*, 2014. **123**: p. 55-66.
16. Lowe, J. and J. Gregory, *The effects of climate change on storm surges around the United Kingdom*. *Philosophical Transactions of the Royal Society A: Mathematical, Physical and Engineering Sciences*, 2005. **363**(1831): p. 1313-1328.
17. Vousdoukas, M.I., et al., *Projections of extreme storm surge levels along Europe*. *Climate Dynamics*, 2016. **47**: p. 3171-3190.
18. Chini, N., et al., *The impact of sea level rise and climate change on inshore wave climate: A case study for East Anglia (UK)*. *Coastal Engineering*, 2010. **57**(11-12): p. 973-984.
19. Hemer, M.A., et al., *Projected changes in wave climate from a multi-model ensemble*. *Nature climate change*, 2013. **3**(5): p. 471-476.
20. Morim, J., et al., *Robustness and uncertainties in global multivariate wind-wave climate projections*. *Nature Climate Change*, 2019. **9**(9): p. 711-718.
21. Vousdoukas, M.I., et al., *Global probabilistic projections of extreme sea levels show intensification of coastal flood hazard*. *Nature communications*, 2018. **9**(1): p. 2360.
22. Engineers, U.S.A.C.o., *CEM: Coastal Engineering Manual*. 2002: U.S. Army Corps of Engineers.
23. dei Lavori Pubblici, M., *Istruzioni tecniche per la progettazione delle dighe marittime*. 1996, GNDCl.
24. MATTM-Regioni, T., *Linee Guida per la Difesa Della Costa Dai Fenomeni di Erosione e Dagli Effetti Dei Cambiamenti Climatici*. Versione Settembre, 2018.
25. Melby, J.A., *Damage Prog [r] ession on Rubble-mound Breakwaters*. Vol. 99. 1999: US Army Engineer Waterways Experiment Station.
26. Ciria, C., *Cetmef (2007)-the rock manual. the use of rock in hydraulic engineering*. Publicaçã, 2007(C683).
27. Van Gelder, P., *Statistical methods for the risk-based design of civil structures*. 2001.
28. Kroon, A., et al., *Ranking uncertainty: Wave climate variability versus model uncertainty in probabilistic assessment of coastline change*. *Coastal Engineering*, 2020. **158**: p. 103673.
29. Burcharth, H.F., *Reliability-based design of coastal structures*. *Advances in coastal and ocean engineering*, 1997. **3**: p. 145-214.

30. Van der Meer, J.W., *Rock slopes and gravel beaches under wave attack*. 1990.
31. Melby, J.A. and N. Kobayashi, *Damage progression and variability on breakwater trunks*. 1999: AA Balkema.
32. van Gent, M.R., E. de Almeida, and B. Hofland, *Statistical analysis of the stability of rock slopes*. *Journal of Marine Science and Engineering*, 2019. **7**(3): p. 60.
33. Salvadori, G., et al., *Practical guidelines for the multivariate assessment of the structural risk in coastal and off-shore engineering*. *Coastal Engineering*, 2015. **95**: p. 77-83.
34. Salvadori, G., G. Tomasicchio, and F. D'Alessandro, *Practical guidelines for multivariate analysis and design in coastal and off-shore engineering*. *Coastal Engineering*, 2014. **88**: p. 1-14.
35. PIANC, *Criteria for the Selection of Breakwater Types and Their Related Optimum Safety Levels: Report of Working Group 196 of the Maritime Navigation Commission*. 2016, PIANC Brussels, Belgium.
36. Melby, J., V. Gonzalez, and N. Nadal-Caraballo, *Uncertainty in Coastal Structure Reliability*, in *Coasts, Marine Structures and Breakwaters 2017: Realising the Potential*. 2018, ICE Publishing. p. 901-910.
37. Melby, J., et al., *Life-Cycle Analysis of Mid Bay and Poplar Island Projects, Chesapeake Bay*. 2005, Maryland. Technical Report ERDC/CHL TR-05-12, US Army Corps of Engineers
38. Melby, J.A., *Time-dependent life-cycle analysis of coastal structures*, in *Coastal Structures 2007: (In 2 Volumes)*. 2009, World Scientific. p. 1842-1853.
39. Melby, J.A., N.C. Nadal, and R.M. Males, *CSsim: Breakwater-Harbor Time-Dependent Life-Cycle Analysis Software*, in *Coastal Structures 2011: (In 2 Volumes)*. 2013, World Scientific. p. 649-658.
40. Melby, J.A., N.C. Nadal-Caraballo, and J. Winkelman, *Point Judith, Rhode Island, Breakwater Risk Assessment*. 2015: US Army Engineer Research and Development Center, Coastal and Hydraulics
41. Stehno, A.L., et al., *Sabine Pass to Galveston Bay, TX Pre-construction, Engineering and Design (PED): coastal storm surge and wave hazard assessment: report 2–Port Arthur*. 2021.
42. Vidal, C., R. Medina, and P. Lomónaco, *Wave height parameter for damage description of rubble-mound breakwaters*. *Coastal Engineering*, 2006. **53**(9): p. 711-722.

43. Campos, Á., C. Castillo, and R. Molina-Sanchez, *Damage in rubble mound breakwaters. Part I: Historical review of damage models*. Journal of Marine Science and Engineering, 2020. **8**(5): p. 317.
44. Campos, Á., R. Molina-Sanchez, and C. Castillo, *Damage in rubble mound breakwaters. Part II: Review of the definition, parameterization, and measurement of damage*. Journal of Marine Science and Engineering, 2020. **8**(5): p. 306.
45. Iribarren, R., *Una Fórmula para el Cálculo de los Diques de Escollera*. Pasajes, 1938: p. 160.
46. Hudson, R.Y., *Laboratory investigation of rubble-mound breakwaters*. Journal of the waterways and Harbors division, 1959. **85**(3): p. 93-121.
47. Losada, M.A. and L.A. Gimenez-Curto, *The joint effect of the wave height and period on the stability of rubble mound breakwaters using Iribarren's number*. Coastal Engineering, 1979. **3**: p. 77-96.
48. Center, C.E.R., *Shore protection manual*. Vol. 1. 1984: Department of the Army, Waterways Experiment Station, Corps of Engineers
49. Scaravaglione, G., et al., *Historical overview of the structural integrity of Concrete Armour Units*. Coast. Offshore Sci. Eng, 2022. **1**: p. 68-98.
50. Ahrens, J.P., *The influence of breaker type on riprap stability*, in *Coastal Engineering 1970*. 1970. p. 1557-1566.
51. Ahrens, J.P. and B.L. McCartney, *Wave period effect on the stability of riprap*. 1975, COASTAL ENGINEERING RESEARCH CENTER FORT BELVOIR VA.
52. Thompson, D. and R. Shuttler, *Riprap design for wind-wave attack, a laboratory study in random waves*. Wallingford report EX707 for CIRIA, 1975.
53. Broderick, L.L. and J.P. Ahrens, *Riprap stability scale effects*. 1982.
54. Van der Meer, J.W., *Rock armour slope stability under wave attack; the Van der Meer Formula revisited*. 2021.
55. Battjes, J.A., *Surf similarity*, in *Coastal Engineering 1974*. 1974. p. 466-480.
56. Latham, J.-P., et al., *The influence of armourstone shape and rounding on the stability of breakwater armour layers*. Coastal engineering group report 1, 1988.
57. Bradbury, A., et al., *Rock armour for rubble mound breakwaters, sea walls, and revetments: recent progress*. 1988.
58. Smith, G., I. Wallast, and M.R. van Gent, *Rock slope stability with shallow foreshores*, in *Coastal engineering 2002: Solving coastal conundrums*. 2003, World Scientific. p. 1524-1536.

59. Van Gent, M.R., A.J. Smale, and C. Kuiper, *Stability of rock slopes with shallow foreshores*, in *Coastal Structures 2003*. 2004. p. 100-112.
60. Battjes, J.A. and H.W. Groenendijk, *Wave height distributions on shallow foreshores*. *Coastal engineering*, 2000. **40**(3): p. 161-182.
61. Goda, Y., *Design wave height selection in intermediate-depth waters*. *Coastal engineering*, 2012. **66**: p. 3-7.
62. Karmpadakis, I., C. Swan, and M. Christou, *A new wave height distribution for intermediate and shallow water depths*. *Coastal Engineering*, 2022. **175**: p. 104130.
63. Van Gent, M.R. *On the stability of rock slopes*. in *Environmentally Friendly Coastal Protection: Proceedings of the NATO Advanced Research Workshop on Environmentally Friendly Coastal Protection Structures Varna, Bulgaria 25–27 May 2004*. 2005. Springer.
64. Melby, J.A. and S.A. Hughes, *Armor stability based on wave momentum flux*, in *Coastal Structures 2003*. 2004. p. 53-65.
65. Melby, J.A. and N. Kobayashi, *Stone armor damage initiation and progression based on the maximum wave momentum flux*. *Journal of Coastal Research*, 2011. **27**(1): p. 110-119.
66. Hughes, S.A., *Wave momentum flux parameter: a descriptor for nearshore waves*. *Coastal Engineering*, 2004. **51**(11-12): p. 1067-1084.
67. Verhagen, H.J., B. Reedijk, and M. Muttray, *The effect of foreshore slope on breakwater stability*, in *Coastal Engineering 2006: (In 5 Volumes)*. 2007, World Scientific. p. 4828-4840.
68. Verhagen, H.J., G. van Vledder, and S.E. Arab, *A practical method for design of coastal structures in shallow water*, in *Coastal Engineering 2008: (In 5 Volumes)*. 2009, World Scientific. p. 2912-2922.
69. Verhagen, H.J. and M. Mertens. *Riprap stability for deep water, shallow water and steep foreshores*. in *Coasts, marine structures and breakwaters: Adapting to change: Proceedings of the 9th international conference organised by the Institution of Civil Engineers and held in Edinburgh on 16 to 18 September 2009*. 2010. Thomas Telford Ltd.
70. Herrera, M.P., M.E. Gomez-Martín, and J.R. Medina, *Hydraulic stability of rock armors in breaking wave conditions*. *Coastal Engineering*, 2017. **127**: p. 55-67.
71. Goda, Y., *Statistical variability of sea state parameters as a function of wave spectrum*. *Coastal Engineering in Japan*, 1988. **31**(1): p. 39-52.

72. Eldrup, M.R. and T.L. Andersen, *Extension of shallow water rock armour stability formulae to nonlinear waves*. Coastal Engineering, 2019. **153**: p. 103536.
73. Goda, Y., *Random seas and design of maritime structures*. Vol. 33. 2010: World Scientific Publishing Company.
74. Muttray, M. and J.G. Martinez, *The Conversion of spectral wave heights to design wave heights*, in *Coasts, Marine Structures and Breakwaters 2017: Realising the Potential*. 2018, ICE Publishing. p. 1167-1176.
75. Lee, A., Z.W. Geem, and K.-D. Suh, *Determination of optimal initial weights of an artificial neural network by using the harmony search algorithm: application to breakwater armor stones*. Applied Sciences, 2016. **6**(6): p. 164.
76. Koç, M.L., C.E. Balas, and D.İ. Koç, *Stability assessment of rubble-mound breakwaters using genetic programming*. Ocean Engineering, 2016. **111**: p. 8-12.
77. Lee, J.-S. and K.-D. Suh, *Development of stability formulas for rock armor and tetrapods using multigene genetic programming*. Journal of Waterway, Port, Coastal, and Ocean Engineering, 2020. **146**(1): p. 04019027.
78. Wei, X., et al., *Stability assessment of rubble mound breakwaters using extreme learning machine models*. Journal of Marine Science and Engineering, 2019. **7**(9): p. 312.
79. Etemad-Shahidi, A., M. Bali, and M.R. van Gent, *On the stability of rock armored rubble mound structures*. Coastal Engineering, 2020. **158**: p. 103655.
80. Marino, S., et al., *Laboratory investigation on armour stability for extremely shallow water conditions*.
81. Allsop, N., N. Durand, and D. Hurdle, *Influence of steep seabed slopes on breaking waves for structure design*, in *Coastal Engineering 1998*. 1998. p. 906-919.
82. Muttray, M. and B. Reedijk, *Reanalysis of breakwater stability with steep foreshore*, in *Coastal Engineering 2008: (In 5 Volumes)*. 2009, World Scientific. p. 3346-3357.
83. Jumelet, D., et al., *Stability of rock-armoured mild slopes*. Coastal Engineering, 2023: p. 104418.
84. Losada, M.Á., *Method to assess the interplay of slope, relative water depth, wave steepness, and sea state persistence in the progression of damage to the rock layer over impermeable dikes*. Ocean Engineering, 2021. **239**: p. 109904.

85. Kajima, R., *Estimation of incident wave spectrum in the sea area influenced by reflection*. Coastal Engineering in Japan, 1969. **12**(1): p. 9-16.
86. Mertens, M., *Stability of rock on slopes under wave attack: Comparison and analysis of datasets Van der Meer [1988] and Van Gent [2003]*. 2007.
87. Wallingford, H., *Rock armouring for coastal and shoreline structures: hydraulic model studies on the effects of armour grading (EX 1989)*. 1991.
88. Goda, Y. and Y. Suzuki, *Estimation of incident and reflected waves in random wave experiments*, in *Coastal Engineering 1976*. 1976. p. 828-845.
89. BRUUN, P., *Design and construction of mounds for breakwaters and coastal protection*. Developments in geotechnical engineering, 1985. **37**.
90. Mansard, E.P. and E. Funke, *The measurement of incident and reflected spectra using a least squares method*, in *Coastal Engineering 1980*. 1980. p. 154-172.
91. Baquerizo, A., M. Losada, and J. Smith, *Wave reflection at beaches*. Doctor of Philosophy PhD dissertation, University of Cantabria, Spain, 1995.
92. FIGUERES, M. and J.R. MEDINA, *Estimating incident and reflected waves using a fully nonlinear wave model*, in *Coastal Engineering 2004: (In 4 Volumes)*. 2005, World Scientific. p. 594-603.
93. Gómez-Martín, M.E. and J.R. Medina, *Damage progression on cube armored breakwaters*, in *Coastal Engineering 2006: (In 5 Volumes)*. 2007, World Scientific. p. 5229-5240.
94. Medina, J.R., J. Molines, and M.E. Gómez-Martín, *Influence of armour porosity on the hydraulic stability of cube armour layers*. Ocean Engineering, 2014. **88**: p. 289-297.
95. Marino, S., R.A. Galantucci, and A. Saponieri, *Measuring rock slope damage on rubble mound breakwater through digital photogrammetry*. Measurement, 2023. **211**: p. 112656.
96. Dai, Y.B. and A.M. Kamel, *Scale effect tests for rubble-mound breakwaters: Hydraulic model investigation*. Vol. 69. 1969: US Army Engineer Waterways Experiment Station.
97. Jensen, O.J. and P. Klinting, *Evaluation of scale effects in hydraulic models by analysis of laminar and turbulent flows*. Coastal Engineering, 1983. **7**(4): p. 319-329.
98. Longuet-Higgins, M.S., *On the distribution of the heights of sea waves: Some effects of nonlinearity and finite band width*. Journal of Geophysical Research: Oceans, 1980. **85**(C3): p. 1519-1523.

99. Van der Meer, J., et al., *EurOtop, 2016. Manual on wave overtopping of sea defences and related structures. An overtopping manual largely based on European research, but for worldwide application.* www. overtopping-manual.com, 2016.
100. Hofland, B., et al., *Prediction formula for the spectral wave period $T_{m-1, 0}$ on mildly sloping shallow foreshores.* Coastal Engineering, 2017. **123**: p. 21-28.
101. Melby, J.A. and N. Kobayashi, *Progression and variability of damage on rubble mound breakwaters.* Journal of waterway, port, coastal, and ocean engineering, 1998. **124**(6): p. 286-294.
102. Buccino, M., et al., *Wave overtopping of a vertical seawall in a surf zone: A joint analysis of numerical and laboratory data.* Ocean Engineering, 2023. **288**: p. 116144.
103. Melby, J.A. and N. Kobayashi, *Incipient motion of breakwater armor units*, in *Coastal Engineering 1996*. 1997. p. 1803-1815.
104. van der Meer, J., T.L. Andersen, and M.R. Eldrup, *The Van der Meer Formula for Rock Slope Stability at Shallow Water.* Coastal Engineering Proceedings, 2022(37): p. 8-8.
105. Eldrup, M.R., T. Lykke Andersen, and H.F. Burcharth, *Stability of rubble mound breakwaters—A study of the notional permeability factor, based on physical model tests.* Water, 2019. **11**(5): p. 934.
106. Losada, M.A., P. Díaz-Carrasco, and M. Clavero, *Do Rock Design Formulas Based on Wave Flume Experiments Reliably Model Their Performance at Sea?* Journal of Marine Science and Engineering, 2022. **10**(4): p. 487.
107. Schüttrumpf, H., et al. *Analysis of uncertainties in coastal structure design by expert judgement.* in *Chinese-German Joint Symposium on Hydraulic and Ocean Engineering*. 2008.
108. Schüttrumpf, H., et al., *Expert judgement of uncertainties in coastal structure design*, in *Coastal Engineering 2006: (In 5 Volumes)*. 2007, World Scientific. p. 5267-5278.
109. I.A.A.R., *Analysis of rubble mound breakwaters*. Vol. 78. 1992: Pianc.
110. Mansard, E. and E. Funke. *Experimental and analytical techniques in wave dynamics, a comparative study.* in *IAHR Seminar on Wave Analysis and Generation in Laboratory Basins*. 1987.

111. Funke, E. and E. Mansard. *A rationale for the use of the deterministic approach to laboratory wave generation*. in *IAHR Seminar on Wave Analysis and Generation in Laboratory Basins, 22nd IAHR Congress*. 1987.
112. Mortimer, W., et al., *Correct generation of the bound set-down for surface gravity wave groups in laboratory experiments of intermediate to shallow depth*. *Coastal Engineering*, 2022. **174**: p. 104121.
113. Madsen, O.S., *On the generation of long waves*. *Journal of geophysical research*, 1971. **76**(36): p. 8672-8683.
114. Mansard, E.P., *Some Recent Advances in Physical Modelling of Rubble-Mound Breakwaters*. *Journal of Coastal Research*, 1990: p. 5-18.
115. Orszaghova, J., et al., *Importance of second-order wave generation for focused wave group run-up and overtopping*. *Coastal Engineering*, 2014. **94**: p. 63-79.
116. Mortimer, W., et al., *Implications of second-order wave generation for physical modelling of force and run-up on a vertical wall using wave groups*. *Coastal Engineering*, 2023. **180**: p. 104259.
117. Whittaker, C., et al., *Extreme coastal responses using focused wave groups: Overtopping and horizontal forces exerted on an inclined seawall*. *Coastal Engineering*, 2018. **140**: p. 292-305.
118. Whittaker, C., et al., *Optimisation of focused wave group runup on a plane beach*. *Coastal Engineering*, 2017. **121**: p. 44-55.
119. Laurich, P., E. Mansard, and M. Davies. *Active wave absorption for improved modelling of breakwater stability*. in *PROCEEDINGS OF THE CONGRESS-INTERNATIONAL ASSOCIATION FOR HYDRAULIC RESEARCH*. 1995. LOCAL ORGANIZING COMMITTEE OF THE XXV CONGRESS.
120. Andersen, T.L., et al., *A new active absorption system and its performance to linear and non-linear waves*. *Coastal Engineering*, 2016. **114**: p. 47-60.
121. Eldrup, M.R. and T. Lykke Andersen, *Applicability of nonlinear wavemaker theory*. *Journal of Marine Science and Engineering*, 2019. **7**(1): p. 14.
122. Carver, R.D. and B.J. Wright, *Investigation of random variations in stability response of stone-armored, rubble-mound breakwaters*. 1991.
123. Hughes, S.A., *Physical models and laboratory techniques in coastal engineering*. Vol. 7. 1993: World Scientific.
124. Okuno, T., H. Uji-ie, and M. Sawamoto, *Effects of Wave Grouping on the Stability of Breakwater Armor Units*. *Coastal Engineering in Japan*, 1989. **32**(1): p. 69-89.

125. Medina, J.R., R.T. Hudspeth, and C. Fassardi, *Breakwater armor damage due to wave groups*. Journal of waterway, port, coastal, and ocean engineering, 1994. **120**(2): p. 179-198.
126. Kamphuis, J.W., *Experiments on design wave height in shallow water*, in *Coastal Engineering 1996*. 1996. p. 221-232.
127. Shah, A.M. and J.W. Kamphuis, *The swash zone: a focus on low frequency motion*, in *Coastal Engineering 1996*. 1996. p. 1431-1442.
128. Seas, R., *Design of Maritime Structures* Goda. Y, 1985.
129. Thornton, E.B. and R.J. Calhoun, *Spectral resolution of breakwater reflected waves*. Journal of the Waterways, Harbors and Coastal Engineering Division, 1972. **98**(4): p. 443-460.
130. Kobayashi, N., D.T. Cox, and A. Wurjanto, *Irregular wave reflection and run-up on rough impermeable slopes*. Journal of Waterway, Port, Coastal, and Ocean Engineering, 1990. **116**(6): p. 708-726.
131. Altomare, C., et al., *Wave overtopping of sea dikes with very shallow foreshores*. Coastal Engineering, 2016. **116**: p. 236-257.
132. Baldock, T. and D. Simmonds, *Separation of incident and reflected waves over sloping bathymetry*. Coastal Engineering, 1999. **38**(3): p. 167-176.
133. Røge Eldrup, M. and T. Lykke Andersen, *Estimation of incident and reflected wave trains in highly nonlinear two-dimensional irregular waves*. Journal of Waterway, Port, Coastal, and Ocean Engineering, 2019. **145**(1): p. 04018038.
134. Lamberti, A. and G.R. Tomasicchio, *Stone mobility and longshore transport at reshaping breakwaters*. Coastal Engineering, 1997. **29**(3-4): p. 263-289.
135. Prevot, G., et al., *Stability of rubble mound breakwaters in shallow water and surf zone: An experimental study*. Coast. Eng, 2012. **1**: p. 85.
136. Vidal, C., et al., *Measurement of armor damage on rubble mound structures: comparison between different methodologies*, in *Coastal Structures 2003*. 2004. p. 189-200.
137. Puente, I., et al., *Novel image analysis approach to the terrestrial LiDAR monitoring of damage in rubble mound breakwaters*. Ocean engineering, 2014. **91**: p. 273-280.
138. van Gent, M.R. and I.M. van der Werf, *Rock toe stability of rubble mound breakwaters*. Coastal Engineering, 2014. **83**: p. 166-176.
139. Musumeci, R.E., et al., *3-D monitoring of rubble mound breakwater damages*. Measurement, 2018. **117**: p. 347-364.

140. Cornett, A.M., *A study of wave-induced forcing and damage of rock armour on rubble-mound breakwaters*. 1995, University of British Columbia.
141. Davies, M.H., E.P. Mansard, and A.M. Cornett, *Damage analysis for rubble-mound breakwaters*, in *Coastal Engineering 1994*. 1995. p. 1001-1015.
142. Latham, J., A. Poole, and M. Mannion, *P2. Developments in the analysis of armour layer profile data*, in *Design of Breakwaters*. 1988, Thomas Telford Publishing. p. 343-361.
143. Campos, A., C. Castillo, and R. Molina. *Analysis of the influence of the different variables involved in a damage progression probability model*. in *Proceedings of the 34th International Conference on Coastal Engineering, Seoul, Korea*. 2014.
144. Melby, J.A. and N. Kobayashi, *Damage development on stone-armored rubble mounds*, in *Coastal Engineering 2000*. 2001. p. 1571-1584.
145. Losada, M., J. Desire, and L. Alejo, *Stability of blocks as breakwater armor units*. *Journal of Structural Engineering*, 1986. **112**(11): p. 2392-2401.
146. Vidal, C., M.A. Losada, and R. Medina, *Stability of mound breakwater's head and trunk*. *Journal of waterway, port, coastal, and ocean engineering*, 1991. **117**(6): p. 570-587.
147. Medina, J.R., *A robust armor design to face uncertainties*, in *Coastal Engineering 1992*. 1992. p. 1371-1384.
148. Melby, J.A. and N. Kobayashi, *Damage progression on breakwaters*, in *Coastal Engineering 1998*. 1999. p. 1884-1897.
149. Marzeddu, A., et al., *Effect of wave storm representation on damage measurements of breakwaters*. *Ocean Engineering*, 2020. **200**: p. 107082.
150. Santamaría, M., et al. *Uncertainties of the actual engineering formulas for coastal protection slopes. The dimensional analysis and experimental method*. in *Proceedings of the 39th IAHR World Congress*. 2022.
151. Le Mehaute, B., D. Divoky, and A. Lin, *Shallow water waves a comparison of theories and experiments*, in *Coastal Engineering 1968*. 1968. p. 86-107.
152. Van Gent, M.R.A. *Wave interaction with permeable coastal structures*. in *International Journal of Rock Mechanics and Mining Sciences and Geomechanics Abstracts*. 1996.
153. Moragues, M. and M. Losada, *Progression of wave breaker types on a plane impermeable slope, depending on experimental design*. *Journal of Geophysical Research: Oceans*, 2021. **126**(5): p. e2021JC017211.

154. Merli, D., et al., *Stability of wide-graded rubble mounds*. Journal of waterway, port, coastal, and ocean engineering, 2013. **139**(3): p. 157-170.
155. Scaravaglione, G., et al. *Experimental study on pore pressure attenuation in rubble mound breakwater in depth-limited water conditions*. in *2022 IEEE International Workshop on Metrology for Living Environment (MetroLivEn)*. 2022. IEEE.
156. Eskafi, M., et al., *Icelandic-Type Berm Breakwater: A Nature-Based Structure with a Low Carbon Footprint*. Journal of Waterway, Port, Coastal, and Ocean Engineering, 2024. **150**(1): p. 05023003.
157. Ito, M., et al., *Stability of high-specific gravity armor blocks*, in *Coastal Engineering 1994*. 1995. p. 1143-1156.
158. Newberry, S.D., et al., *The effect of rock shape and construction methods on rock armour layers*, in *Coastal Engineering 2002: Solving Coastal Conundrums*. 2003, World Scientific. p. 1436-1448.
159. Stewart, T., et al., *Packing and voids for rock armour in breakwaters*. 2003.
160. Stewart, T.P., et al., *The hydraulic performance of tightly packed rock armour layers*, in *Coastal Engineering 2002: Solving Coastal Conundrums*. 2003, World Scientific. p. 1449-1461.
161. van der Meer, J., et al., *New Design Guidance for Underlayers and Filter Layers for Rock Armour under Wave Attack*, in *Coasts, Marine Structures and Breakwaters 2017: Realising the Potential*. 2018, ICE Publishing. p. 1069-1079.
162. Andersen, T.L., H.F. Burcharth, and X. Gironella, *Comparison of new large and small scale overtopping tests for rubble mound breakwaters*. Coastal Engineering, 2011. **58**(4): p. 351-373.
163. Burcharth, H. and O. Andersen, *On the one-dimensional steady and unsteady porous flow equations*. Coastal engineering, 1995. **24**(3-4): p. 233-257.
164. Mansard, E. and B. Pratte, *Moored ship response in irregular waves*, in *Coastal Engineering 1982*. 1982. p. 2619-2640.
165. Buckley, M., R. Lowe, and J. Hansen, *Evaluation of nearshore wave models in steep reef environments*. Ocean Dynamics, 2014. **64**: p. 847-862.
166. Team, S., *SWAN User Manual—SWAN Cycle III Version 41.31 A*. Delft University of Technology, Delft, 2020.
167. Roelvink, D., et al., *XBeach model description and manual*. Unesco-IHE Institute for Water Education, Deltares and Delft University of Technology. Report June, 2010. **21**: p. 2010.

168. Zijlema, M., G. Stelling, and P. Smit, *SWASH: An operational public domain code for simulating wave fields and rapidly varied flows in coastal waters*. Coastal Engineering, 2011. **58**(10): p. 992-1012.
169. Madsen, P.A. and O.R. Sørensen, *A new form of the Boussinesq equations with improved linear dispersion characteristics. Part 2. A slowly-varying bathymetry*. Coastal engineering, 1992. **18**(3-4): p. 183-204.
170. Nwogu, O., *Alternative form of Boussinesq equations for nearshore wave propagation*. Journal of waterway, port, coastal, and ocean engineering, 1993. **119**(6): p. 618-638.
171. Peregrine, D.H., *Calculations of the development of an undular bore*. Journal of Fluid Mechanics, 1966. **25**(2): p. 321-330.
172. Peregrine, D.H., *Long waves on a beach*. Journal of fluid mechanics, 1967. **27**(4): p. 815-827.
173. Wei, G., et al., *A fully nonlinear Boussinesq model for surface waves. Part 1. Highly nonlinear unsteady waves*. Journal of fluid mechanics, 1995. **294**: p. 71-92.
174. Chen, Y. and P.L.-F. Liu, *Modified Boussinesq equations and associated parabolic models for water wave propagation*. Journal of Fluid Mechanics, 1995. **288**: p. 351-381.
175. Madsen, P.A. and H.A. SCHÄFFER, *A review of Boussinesq-type equations for surface gravity waves*. Advances in coastal and ocean engineering, 1999: p. 1-94.
176. Gobbi, M.F., J.T. Kirby, and G. Wei, *A fully nonlinear Boussinesq model for surface waves. Part 2. Extension to $O(kh)^4$* . Journal of Fluid Mechanics, 2000. **405**: p. 181-210.
177. Madsen, P.A., H. Bingham, and H. Liu, *A new Boussinesq method for fully nonlinear waves from shallow to deep water*. Journal of Fluid Mechanics, 2002. **462**: p. 1-30.
178. Madsen, P.A., H. Bingham, and H. Schäffer, *Boussinesq-type formulations for fully nonlinear and extremely dispersive water waves: derivation and analysis*. Proceedings of the Royal Society of London. Series A: Mathematical, Physical and Engineering Sciences, 2003. **459**(2033): p. 1075-1104.
179. Lynett, P.J., *Nearshore wave modeling with high-order Boussinesq-type equations*. Journal of waterway, port, coastal, and ocean engineering, 2006. **132**(5): p. 348-357.

180. Chen, Q., *Fully nonlinear Boussinesq-type equations for waves and currents over porous beds*. Journal of Engineering Mechanics, 2006. **132**(2): p. 220-230.
181. Kennedy, A.B., et al., *Boussinesq modeling of wave transformation, breaking, and runup. I: 1D*. Journal of waterway, port, coastal, and ocean engineering, 2000. **126**(1): p. 39-47.
182. Lynett, P. and P.L.-F. Liu, *A numerical study of submarine–landslide–generated waves and run–up*. Proceedings of the Royal Society of London. Series A: Mathematical, Physical and Engineering Sciences, 2002. **458**(2028): p. 2885-2910.
183. Metallinos, A.S., E.G. Repousis, and C.D. Memos, *Wave propagation over a submerged porous breakwater with steep slopes*. Ocean Engineering, 2016. **111**: p. 424-438.
184. Erduran, K., S. Ilic, and V. Kutija, *Hybrid finite-volume finite-difference scheme for the solution of Boussinesq equations*. International Journal for Numerical Methods in Fluids, 2005. **49**(11): p. 1213-1232.
185. Kim, G., C. Lee, and K.-D. Suh, *Extended Boussinesq equations for rapidly varying topography*. Ocean Engineering, 2009. **36**(11): p. 842-851.
186. Kim, D.-H. and P.J. Lynett, *Dispersive and nonhydrostatic pressure effects at the front of surge*. Journal of Hydraulic Engineering, 2011. **137**(7): p. 754-765.
187. Shi, F., et al., *A high-order adaptive time-stepping TVD solver for Boussinesq modeling of breaking waves and coastal inundation*. Ocean Modelling, 2012. **43**: p. 36-51.
188. Roeber, V. and K.F. Cheung, *Boussinesq-type model for energetic breaking waves in fringing reef environments*. Coastal Engineering, 2012. **70**: p. 1-20.
189. Sheremet, A., et al., *Modeling of nonlinear wave propagation over fringing reefs*. Coastal Engineering, 2011. **58**(12): p. 1125-1137.
190. Shi, F., et al., *FUNWAVE-TVD Fully Nonlinear Boussinesq Wave Model with TVD Solver Documentation and User's Manual*. Center Appl. Coastal Res., Univ. Delaware, Newark, DE, USA, Res. Rep. No CACR-11-04, 2011. **2**: p. 1.
191. Lynett, P.J., et al., *Modeling Wave Generation, Evolution, and Interaction with Depth-Integrated, Dispersive Wave Equations COULWAVE Code Manual Cornell University Long and Intermediate Wave Modeling Package*. 2008.
192. Derakhti, M., et al., *NHWAVE: Model revisions and tests of wave breaking in shallow and deep water*. Center for Applied Coastal Research, Department of

- Civil and Environmental Engineering. University of Delaware. Research Report No. CACR-15-18, 2015.
193. Kazolea, M. and M. Ricchiuto, *On wave breaking for Boussinesq-type models*. Ocean Modelling, 2018. **123**: p. 16-39.
 194. Zhang, S.-j., L.-s. Zhu, and K. Zou, *A comparative study of numerical models for wave propagation and setup on steep coral reefs*. China Ocean Engineering, 2019. **33**: p. 424-435.
 195. Whitford, D.J. and E.B. Thornton, *Bed shear stress coefficients for longshore currents over a barred profile*. Coastal engineering, 1996. **27**(3-4): p. 243-262.
 196. Chen, Q., et al., *Boussinesq modeling of a rip current system*. Journal of geophysical research: oceans, 1999. **104**(C9): p. 20617-20637.
 197. Smagorinsky, J., *General circulation experiments with the primitive equations: I. The basic experiment*. Monthly weather review, 1963. **91**(3): p. 99-164.
 198. Chen, Q., et al., *Boussinesq modeling of wave transformation, breaking, and runup. II: 2D*. Journal of Waterway, Port, Coastal, and Ocean Engineering, 2000. **126**(1): p. 48-56.
 199. Lynett, P.J., T.-R. Wu, and P.L.-F. Liu, *Modeling wave runup with depth-integrated equations*. Coastal Engineering, 2002. **46**(2): p. 89-107.
 200. Frostick, L.E., S.J. McLelland, and T.G. Mercer, *Users guide to physical modelling and experimentation: Experience of the HYDRALAB network*. 2011: CRC press.
 201. Hofland, B. and J.A. Battjes, *Probability density function of instantaneous drag forces and shear stresses on a bed*. Journal of Hydraulic Engineering, 2006. **132**(11): p. 1169-1175.

Acknowledgments

Funding for the research discussed in this manuscript was provided by the Department of Civil, Environmental, Building Engineering and Chemistry (DICATECh), which is part of the University Polytechnic of Bari (PoliBa). The research was also directly funded by CEERD-RM-S at the Coastal and Hydraulics Laboratory (CHL) of the U.S. Army Engineer Research and Development Center (ERDC) with a scholarship grant of \$7000 to cover the expenses of the visiting periods at the CHL of the U.S. Army Engineer Waterways Experiment Station (WES) in Vicksburg, Mississippi (MS).

The studies were conducted under the direct supervision of Prof. Leonardo Damiani (PoliBa). Prof. Giuseppe Roberto Tomasicchio (Unisalento) and Dr. Jeffrey A. Melby (USACE) provided co-tutoring and technical support for this dissertation.

This manuscript is a dissertation in fulfillment of the requirements for the degree of Philosophy from the Polytechnic of Bari, Italy (IT). The author was enrolled in the XXXVI^o cycle of the Ph.D. Doctoral Research in Risk and Environmental, Territorial and Building Development (DRRSATE).

Completing a Ph.D. dissertation is undoubtedly a milestone in a researcher's professional life and offers a moment for reflection. I will dedicate this part to give credit to several people who have contributed to this work in various ways.

First and foremost, I would like to express my sincere gratitude to my Italian supervisors, Prof. Leonardo Damiani (Polytechnic of Bari) and Prof. Giuseppe Roberto Tomasicchio (University of Salento) for affording me the opportunity to pursue a Ph.D. and inspiring the enthusiasm necessary to advance my research. Their unwavering guidance and support were indispensable, and without them, the completion of this doctoral dissertation would not have been possible. Working under their supervision was always stimulating and instructive. I wish to formally acknowledge their generosity

in sharing not only their professional insights but also their personal experiences, invaluable aspects that cannot be found in a textbook. In particular, I want to thank Prof. L. Damiani for his continuous support and encouragement, and for providing me with the tools and fundings necessary to pursue various activities. Additionally, I wish to express my gratitude to Prof. G. R. Tomasicchio for granting me the opportunity to work in the EUMER laboratory (University of Salento) and involving me in numerous experimental research projects, encompassing both 3D and 2D physical models. These experiences represent a key step for a Ph.D. student and have been of fundamental importance in enhancing my practical expertise in the field of coastal engineering.

The author extends his gratitude to the foreign supervisor Dr. Jeffrey A. Melby (USACE), for his tireless contributions to the research. Dr. Melby is sincerely appreciated for providing comprehensive materials, tireless support, and the state-of-the-art insights that served as the foundation and follow-up for this thesis. His encouragement and enthusiasm in advancing his research were instrumental in fostering my own passion for the subject. I really appreciated our informal chats and discussions that were probably even more important than everything else. Furthermore, I am deeply thankful for Dr. Melby and his family for their hospitality and the attention they provided to me during my visiting periods. I never felt alone, and their support enhanced the overall experience. Words cannot be enough.

I am indebted to all my EUMER and poliBa colleagues, who are not just my co-workers but also my friends. Furthermore, I extend a sincere acknowledgment to Prof. Alessandra Saponieri and Dr. Antonio Francone for generously sharing their knowledge and providing invaluable help and support. I appreciated every constructive, work-related discussion and every social experience we had together.

The author gratefully acknowledges and commends the efforts of Prof. Patrick Lynett (University of Southern California) and Prof. Nobuhisa Kobayashi (University of Delaware) for their valuable and priceless comments on this project. The author also

acknowledges Professors Jentsje Van der Meer, Marcel A. Van Gent, Josep R. Medina, and Cesar Vidal for kindly sharing their datasets.

Last but not least, I extend my heartfelt thanks to all my family, with special gratitude to my parents and my grandmother, to whom I dedicate this thesis, for their unwavering and unconditional support and living-by-example. One special person deserves the last word of thanks for her love, support, and patience, especially in those last few months of this research. Thank you, Paola, for bringing so much happiness into my life.

Words will never be enough to express my deep gratitude and thank all those I have mentioned and those, for the sake of brevity, I have not been able to cite.

Giulio Scaravaglione



Curriculum Vitae








Eng. Giulio Scaravaglione

18/03/1996

Mobile: (+39) 3341578606

Email: giulio.scaravaglione@poliba.it; scaravaglione@hotmail.it;

Academic Background

 <p>UNIVERSITÀ DEL SALENTO</p>	<p>University of Salento Lecce, Italy <i>Research Fellowship. – 01/03/2024 – on going</i> <i>PRINN project entitled “PROMETEO”: a PRObabilistic FraMEwork for coasTal and harbor dEfense in the cONtext of climate change.</i> <u>Supervisor:</u> Prof. Alessandra Saponieri</p>
 <p>ERDC</p>	<p>U.S. Army Corps Engineer Research and Development Center (ERDC) Vicksburg, Mississippi, US <i>Ph.D. Visiting Periods – 02/07/2022 – 21/07/2022 and 13/04/2023 – 24/06/2023.</i> <i>Visiting period at the Coastal and Hydraulic Laboratory (CHL) of the U.S. Army Engineer Waterways Experiment Station (WES) in Vicksburg, Mississippi (MS). Supervisor: Dr. J. A. Melby.</i> <u>ERDC Grant of \$7000 provided by USACE finance center</u></p>
 <p>Politecnico di Bari</p>	<p>Polytechnic University of Bari Bari, Italy <i>Ph.D. in “Risk and Environmental, Territorial and Building Development”.</i> <i>01/11/2020 – 08/02/2024.</i> <i>Specialized in Coastal Engineering with a thesis entitled: “On the uncertainties in stone armor stability”.</i> Tutor: Prof. L. Damiani; <u>Supervisors:</u> Prof. G.R. Tomasicchio and Dr. J.A. Melby.</p>
 <p>Politecnico di Bari</p>	<p>Polytechnic University of Bari Bari, Italy <i>Master’s Science degree in Civil Engineering (Curriculum Hydraulic Engineering).</i> 110/110 cum laude. 01/10/2017-18/02/2020. <i>Specialized in Coastal Engineering with a thesis entitled: “Tipologie di blocchi adottate per mantellate di opere a gettata: il Cubipod”.</i> <u>Tutor:</u> Prof. L. Damiani.</p>
 <p>Imperial College London</p>	<p>Imperial College of London London, UK <i>Visiting period for Erasmus Traineeship and Global Thesis program (LM).</i> <i>04/2019 - 07/2019.</i> <i>Traineeship and thesis abroad at the Faculty of Engineering, Department of Earth Science & Engineering.</i> <u>Supervisors:</u> Prof. J.-P. Latham and Dr. J. Xiang.</p>



Polytechnic University of Bari | Bari, Italy

*Bachelor's degree in Civil and Environmental engineering. 110/110 cum laude.
01/10/2014-12/10/2017.*

*Specialized in Hydraulics with a thesis entitled: "Studio dei moti di
filtrazione attraverso mezzi porosi e fratturati". Tutor: Prof. G. Chiaia.*

Awards

- AIOM award prize established by the order of Engineers of the province of Naples **for the best M.Sc. thesis developed between the years 2018-2021** – 18/12/2021
- IEEE award prize established by the 2022 IEEE International Workshop on Metrology for the Living Environment for **the best paper presented by a young researcher**. The awarded paper is titled: "Experimental study on pore pressure attenuation in rubble mound breakwater in depth-limited water conditions" – 27/05/2022.

Publications

Conference papers

- Scaravaglione, G., Melby, J.A., Damiani, L., Tomasicchio, G.R. (2024). On the uncertainties in rock-armoured breakwaters stability. Abstract accepted for the 38th International Conference of Coastal Engineering (ICCE, 2024), Rome.
- Scaravaglione, G., Melby, J.A., Tomasicchio, G.R., Damiani, L. (2023). Uncertainties in rock-armored breakwaters stability laboratory data. In Proceedings of the 10th Short Course/Conference on Applied Coastal Research, Istanbul (Turkey).
- Marino, S., Scaravaglione, G., Francone, A., Valentini, N., Saponieri, A., Damiani, L., Van Gent, M.A., & Tomasicchio, G. R. (2022). Laboratory

investigation on armour stability for extremely shallow water conditions. In Proceedings of the 39th IAHR World Congress Granada (Spain).

- Scaravaglione, G., Marino, S., Damiani, L., Francone, A., Saponieri, A., & Tomasicchio, G. R. (2022). Experimental study on pore pressure attenuation in rubble mound breakwater in depth-limited water conditions. In 2022 IEEE International Workshop on Metrology for Living Environment (MetroLivEn), Cosenza (Italy) (pp. 197-202). IEEE.
- Scaravaglione, G., Marino, S., Saponieri, A., Francone, A., Damiani, L., & Tomasicchio, G. R. (2022). Studio sperimentale del campo di pressioni all'interno di una diga a gettata in condizioni di acque basse. In Proceedings of the XXXVIII Convegno Nazionale di Idraulica e Costruzioni Idrauliche, Reggio Calabria, settembre 2022.
- Marino, S., Scaravaglione, G., Tomasicchio, G.R., Damiani, L., Francone, A., Saponieri, A. (2022). Laboratory study on rock slope stability in depth limited water conditions. In Proceedings of the XXXVIII Convegno Nazionale di Idraulica e Costruzioni Idrauliche, Reggio Calabria, settembre 2022.
- Marino, S., Tomasicchio, G.R., Damiani, L., Francone, A., Scaravaglione, G., Saponieri, A. (2021). The influence of extremely shallow conditions on rock slope stability. In Proceedings of the 2nd IAHR Young Professionals Congress.

Journal papers

- Scaravaglione, G., Marino, S., Francone, A., Damiani, L., Tomasicchio, G.R., & Saponieri, A. (2024). Laboratory investigation on pore pressures inside a rubble mound breakwater in depth-limited waters. *Applied Ocean Research*, 147, 103988.
- Brancasi, A., Leone, E., Francone, A., Scaravaglione, G., & Tomasicchio, G. R. (2022). On Formulae for Wave Transmission at Submerged and Low-Crested Breakwaters. *Journal of Marine Science and Engineering*, 10(12), 1986.

- Scaravaglione, G., Latham, J. P., Xiang, J., Francone, A., & Tomasicchio, G. R. (2022). Historical overview of the structural integrity of Concrete Armour Units. *Coast. Offshore Sci. Eng*, 1, 68-98.
- Scaravaglione, G., Latham, J. P., & Xiang, J. (2021). Numerical Model Study of Prototype Drop Tests on Cube and Cubipod® Concrete Armor Units Using the Combined Finite–Discrete Element Method. *Journal of Marine Science and Engineering*, 9(5), 460.
- Scaravaglione, G. (2021). Studio numerico della resistenza strutturale di elementi di mantellata Cubipod. *Studi costieri N. 29. Dinamica e difesa dei litorali – Gestione integrata della fascia costiera*

Abstract

The present research aims to synthesize data across a wide range of international studies to quantify and improve uncertainty understanding in stone armor stability. Data synthesis was accomplished by collecting and describing data from 7 different studies and homogenizing parametric characteristics to the extent possible considering the disparate nature of the native data. Then all 7 studies were simulated with a numerical high-fidelity phase-resolving wave transformation model (Coulwave) to better homogenize the data. Results were used to quantify hydrodynamic uncertainty and determine the relative contributions of aleatory and epistemic uncertainty and bias in damage measurements, enabling the separation and assessment of the effects of wave prediction errors on stability equations. Five of the studies produced well-known empirical stability equations. These stability equations were refit to the homogenized data illustrating weaknesses and strengths of the various empirical approaches. All formulations work well in deep water but weaknesses are illustrated in shallow and very shallow water. Improved physics are proposed that span the water depth regimes and, in concert with the quantified uncertainty, provide a significant advancement in probabilistic stone armor layer design and assessment.